GRS

Representation of
Inhomogeneities in
the Flow and Transport
Codes d^3f and r^3t

GRS

Representation of Inhomogeneities in the Flow and Transport Codes d³f and r³t

Anke Schneider, ed.

September 2013

Remark:

Acknowledgement

Abstract

The codes d³f and r³t are well established for modelling density-driven flow and nuclide transport in the far field of repositories for hazardous material in deep geological formations. While originally intended to be applied to the overburden of a salt dome they were adapted to alternative host media such as crystalline rock or mudstone by including fractures into an otherwise porous medium. However, only discrete fractures or fracture networks with a rather limited number of fractures could be dealt with. Networks of smaller fractures – so-called background fractures – can easily consist of hundreds and thousands of significant individual fractures in a model domain and were therefore beyond the scope of d³f and r³t. One way to circumvent this problem is to replace a discrete fracture network with an equivalent porous medium. While this is a task in itself the codes had also numerically adapted to be to cope with the new methods. This report describes approaches and results of this work.

In groundwater flow simulation fractures are usually modelled as lower dimensional objects. But especially in the case of density driven flow situations may occur where the validity of this assumption has to be proved. Here a special approach was developed and implemented that allows an adaptive resolution of the layers. Of central relevance in this respect is the development of local refinement or coarsening criteria, an adaptive discretisation that allows an adaptive transition from low-dimensional to equidimensional modelling of the fractures, and an adaptive multigrid algorithm

Furthermore, discretisation methods of higher order for the mixed parabolic-hyperbolic problems were developed. New filtering algebraic multigrid methods as efficient solvers for the large linear equation systems were implemented. The parallelisation was improved by implementation of a **p**arallel **c**ommunication **l**ayer (pcl).

For the estimation of parameters for these systems by inverse modelling, efficient numerical procedures were developed and implemented. These procedures are based on Gauss-Newton techniques that are combined with multigrid methods. Again, implementation on parallel computers was done efficiently as the complexity of the inverse problems may easily exceed the complexity of the simulation itself by one order of magnitude.

Also investigated was the alternative to use reduced 1d-models based on large connected fractures. Here it became clear that this method allows realistic estimations either of breakthrough times or peak concentrations depending on the applied mixing mechanism.

These developments were accompanied by a benchmarking exercise and the development of a user interface for operating d³f and r³t that combines both visual and text-based programming. The highly flexible graphical user interface permits numerical control as well as the input of physical parameters and other model data. It also provides an integrated visualisation.

Zusammenfassung

Die Programme d³f und r³t wurden mit dem Ziel entwickelt, die dichtebeeinflusste Grundwasserströmung und den Transport von Nukliden und anderen Schadstoffen im Fernfeld von Endlagern in tiefen geologischen Formationen modellieren zu können. Standen bei der ursprünglichen Entwicklung ab 1995 Deckgebirge von Salzstöcken im Fokus, so dass ihr Einsatzbereich auf poröse Medien, gespannte Grundwasserleiter und geringe Temperatureinflüsse beschränkt war, wurden die Programme seither in erheblichem Maße weiterentwickelt. Sie können nun auch in Kluftgesteinen, in Gebieten mit freier Grundwasseroberfläche und zur Modellierung des Wärmetransportes eingesetzt werden. So hat sich ihr Einsatzgebiet über das Wirtsgestein Salz hinaus auch auf Endlager im Kristallingestein oder im Ton erweitert. In d³f und r³t werden Klüfte als niederdimensionale Objekte behandelt. Dabei werden Strömung und Transport nicht nur im Kluftnetzwerk selbst, sondern auch in der Gesteinsmatrix modelliert.

Die gewählte Art der Kluftmodellierung wirft – insbesondere im Hinblick auf die Dichteströmung – die Fragestellung auf, bis zu welcher Öffnungsweite eine Kluft als niederdimensionales Objekt dargestellt werden darf, und ab wann man zu einer äquidimensionalen Representation übergehen muss. Diese Fragestellung wurde hier untersucht. Ein Kriterium für die Gültigkeit der niederdimensionalen Darstellung wurde entwickelt. In d³f und r³t wurden eine dimensionsadaptive Diskretisierung für Klüfte bzw. dünne Schichten und ein entsprechendes Mehrgitterverfahren implementiert, so dass während der Laufzeit automatisch – in Abhängigkeit von den Klufteigenschaften, dem Dichtegradienten, der aktuellen Strömungsbedingungen und der Feinheit des Rechengitters – zwischen der niederdimensionalen und der äquidimensionalen Kluftdarstellung umgeschaltet werden kann.

Eine der großen Herausforderungen in Kluftgesteinen stellt die Mehrskaligkeit der vorhandenen Heterogenitäten dar. Die Matrix kann homogene und heterogene Teile, sehr große Einzelklüfte und Netzwerke von Hintergrundklüften enthalten. Auch bei wachsender Leistungsfähigkeit von Hard- und Software bleibt die explizite Modellierung auf Klüfte mit großer Öffnungsweite und Ausdehnung beschränkt: Nur eine begrenzte Anzahl von Klüften bzw. nur eine sehr beschränkte Größe von Kluftnetzwerken kann explizit modelliert werden. Für die Hintergrundklüfte, deren Lage im Einzelnen gar nicht bekannt ist und deren Anzahl leicht in die Tausende gehen kann, müssen andere Strategien gefunden werden.

Ein Weg damit umzugehen ist das Ersetzen von Hintergrundkluftnetzwerken durch äquivalente poröse Ersatzmedien. Hier wird ausgenutzt, dass sich das Feld der logarithmierten hydraulischen Leitfähigkeiten durch selbstaffine Eigenschaften beschreiben lässt. Die Skaleneffekte in heterogenen Medien lassen die longitudinale Dispersionslänge mit der zurückgelegten Weglänge wachsen. Das zeitliche Verhalten unterscheidet sich dabei in Medien mit unendlicher Korrelationslänge (fraktale Medien) entscheidend von dem in Medien mit endlicher Korrelationslänge: Während in letzteren eine ergodische Situation vorliegt und die Ensemble-Dispersionslänge gegen denselben Wert konvergiert wie die effektive Dispersionslänge, konvergiert bei ersteren die longitudinale Korrelationslänge überhaupt nicht. Effektive und Ensemble-Dispersionslänge stellen hier völlig verschiedene Größen dar. Dagegen verhält sich die transversale Dispersionslänge in beiden Medientypen quantitativ ähnlich, wenn auch die Zeitskalen erheblich voneinander abweichen. Die vorliegenden Untersuchungen liefern eine wissenschaftliche Begründung für die erheblich höhere Tortuosität und die wesentlich längere Rückhaltung von Schadstoffen in Medien mit fraktalen Eigenschaften.

Die Dispersionseigenschaften von Modellen hängen vom verwendeten Rechengitter ab. Die Upscaling-Methode des Coarse Grainings erlaubt eine Quantifizierung dieses Effektes in Abhängigkeit von der lokalen Gitterauflösung. Für fraktale Medien konnte gezeigt werden, dass damit künstliche Dispersionseffekte insbesondere für die longitudinale Ensemble-Dispersion stark reduziert werden konnten.

Um die Programme effektiver und genauer zu machen, wurden für die zu lösenden gemischten parabolisch-hyperbolischen Differentialgleichungen Diskretisierungsmethoden höherer Ordnung entwickelt. Die Methode der filternden algebraischen Mehrgitterverfahren wurde weiterentwickelt und in d³f und r³t implementiert. Durch die Implementierung eines **p**arallel **c**ommunication **l**ayer (pcl) wurde die Parallelisierung der Codes vereinfacht sowie effektiver und flexibler gemacht.

Effektive numerische Verfahren zur Parameterschätzung durch inverse Modellierung wurden wurden implementiert. Sie basieren auf Gauß-Newton-Techniken. Da die Komplexität des inversen Problems die des Ursprungsproblems leicht um eine Größenordnung übersteigen kann, werden die resultierenden linearen Gleichungssysteme durch parallele algebraische Mehrgitterverfahren gelöst.

Als eine schnelle Alternative wurden reduzierte 1d-Modelle untersucht. Es wird dargelegt, dass der für eine realistische Abschätzung zu wählende Ansatz für die Dispersion

(effektiver oder Ensemble-Koeffizient) davon abhängt, ob Durchbruchskurven oder maximale Konzentrationen gefragt sind.

Schnelle Voraussagen sind auch durch Particle-Tracking-Methoden möglich. Hier wurden Random-Walk-Particle-Tracking Methoden untersucht und ihre Ergebnisse mit FEM-Rechnungen verglichen. Zudem beinhaltet der vorliegende Bericht eine Reihe vorgeschlagener Benchmarks.

Die VRL-basierte Benutzeroberfläche VRL-Studio wurde weiterentwickelt und an die Neuentwicklungen und den Bedarf der Benutzer angepasst. Auf Java-Basis erlaubt sie sowohl eine visuelle als auch eine textbasierte Programmierung. Auf diese Weise können sowohl physikalische Modellparameter eingegeben als auch die numerischen Verfahren gesteuert werden. Die Benutzeroberfläche wurde um eine integrierte Visualisierungsmöglichkeit erweitert. Auch der Präprozessor PROMESH zum Einlesen und Aufbau von Modellgeometrien und zur Gittergenerierung wurde erweitert und verbessert.

Table of contents

1   Introduction

In Germany, radioactive waste is to be disposed in deep geological formations. Long term safety assessments form a part of the post-closure safety case. According to the German safety case requirements for heat-generating radioactive waste an assessment period of one million years has to be regarded. The assessment is focussed on the proof of a safe containment of the waste in the so-called containment providing rock zone. Nevertheless, scenarios that lead to a nuclide mobilization have also to be addressed in a long-term safety assessment.

In this context, modelling of groundwater flow and nuclide transport in the host rock as well as in the geological formations above play an important role. The performance of these long-term simulations for the different types of host rock regarded requires powerful and qualified tools which need to be checked and verified and continuously adapted to the state-of-the-art of science and technology.

In the period from October 1st, 1994 to August 31st, 1998 under the identification number 02 C 0254 6 (GSF) and later under the identification number 02 C 0465 0 (GRS) and from October 1st, 1998 to December 31st, 2003 under the identification number 02 E 9148 2 both of the computer codes d³f (distributed density-driven flow) and r³t (radionuclides, reaction, retardation, and transport) were developed /FEI 99/, /FEI 04/. From October 2006 to March 2010 these codes were substantially advanced (02 E 10336, /SCH 12/). These works were funded by the Federal Ministry of Education and Research (BMBF) and by the Federal Ministry of Economics and Technology (BMWi), respectively. By means of these two computer codes it became feasible to simulate density driven flow and pollutant transport in porous and fractured media, including heat transport as well as free surface flow. They enable to handle large models with complex hydrogeological structures within convenient processing times.

Both computer codes were successfully used in various qualification projects and subsequently for different applications /BIR 00/, /SCH 04a/, /KEE 05/, /FEI 08/, /FLU 09/, /NOS 13/. Currently they are advanced under 02 E 11062A (H-DuR) and used in different projects such as 02 E 10518 (WEIMAR), 02 E 10750 (URSEL), 02 E 10669 (KOLLORADO), 02 E 10719 (ISIBEL) and 02 E 11213 (QUADER).

A comprehensive system understanding is crucial for the safety assessment of a final repository for radioactive waste or a subsurface disposal of chemo-toxic waste. Instruments used in this context have to be capable of describing the flow and transport processes in the geosphere over long time periods with the required accuracy. Thereby it has to be taken into account that the relevant processes take place on different scales in space and time, whereby scales may differ in some orders of magnitude.

Initially, hard rock offers itself as a location for waste disposal due to its high resistance to being penetrated by any material. It has to be considered, though, that there may be fractures and whole fracture zones in rock formations, facilitating the rapid transport of contaminants.
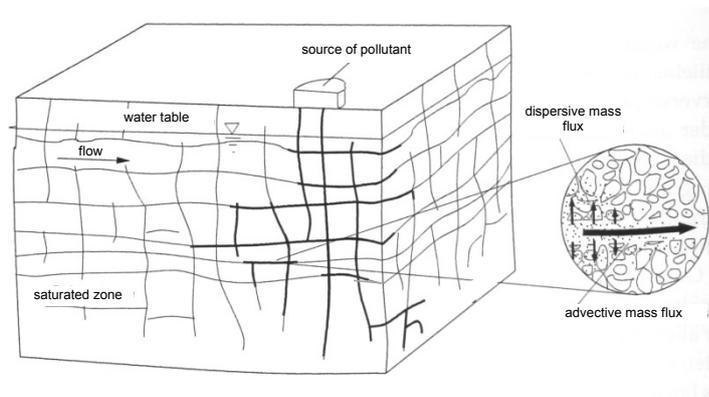
Fig. 1.1   Advective and dispersive transport processes in fractured-porous media /MAC 89/, modified by /NEU 03/

This is why the computer codes that are used should be capable of calculating flow and transport through sedimentary rock formations as well as through dense and fractured porous geological formations.

At present, contaminant transport through dense rock formations is only modelled as a diffusion process in the integrated safety-analytical models of GRS; a possible advective transport of contaminants in fault or fracture zones is either considered separately by way of simplified models or not at all. There are so far no models available in integrated safety analyses for describing the simultaneous transport processes. A further difficulty lies in the determination of the model parameters, which themselves depend on the type of conceptual model.

Modelling flow and transport in fractured porous media such as clay or crystalline rock is a major challenge as fractures exist on different scales and yet require a realistic representation in the model. On the one hand the model must be able to describe local effects in the fractures and the steep pressure as well as concentration gradients at the interface between rock and fracture which may require an equi-dimensional resolution of the fractures and a higher degree of spatial resolution close to the fracture than further away from it. On the other hand there is the need to coarsen the grid where possible to minimise the computational effort. The development of an adaptive multi-scale procedure and its implementation in d³f and r³t was therefore also subject of this project.

With an increasing degree of approximation towards the real, three-dimensional geological and hydrogeological conditions including all relevant processes, the modelling becomes more and more complex. This leads easily to inadmissibly long computing times for the analysis. In such a situation models of reduced dimensions could help. The highly-resolving, complex models serve for understanding the processes involved, while a structuring into compartments is carried out where possible. If these compartments allow a reduction in dimension, the resulting models may be completely or at least in part one-dimensional allowing considerably faster calculations.

For a concrete flow and transport problem concrete values for the corresponding hydrogeological parameters are of course required. Usually they have to be derived directly or indirectly from field data or field observations, and they have to be representative of the area to be modelled. This can be done by solving the inverse problem. Here, the sum oft the squares of the differences between measured and calculated data is minimised. As the complexity of the inverse problems generally exceeds the complexity of the simulation by far, an efficient implementation on parallel computers is particularly important here.

With these extensions of d³f and r³t, the scope of application of the two computer codes is widened considerably, i. e. it is not restricted merely to the area of long-term safety analyses in porous formations and in individual fractures or small fracture networks but has also become applicable to safety analyses in large and complex porous/fractured formations.

2   The project

2.1   State of science and technology

State-of-the-art fundamental priciples can be summarised to the topics flow and transport modelling, numerical procedures, model hierarchies and inverse modelling. These will be described in the following chapters:

2.1.1   Flow and transport modelling

There are in principle two different types of geological hard rock in which a repository could be built (Fig. 2.1). These are on the one hand sedimentary rock formations in whose pores spaces movements of water occur. Typical examples are sandstones and argillaceous types of rock. On the other hand, there are compact types of rock, such as granite. Here, the water can only circulate effectively in (microscopic) cracks, the associated technical term being fractured rock.

sediment   fractured rock

pores   fractures
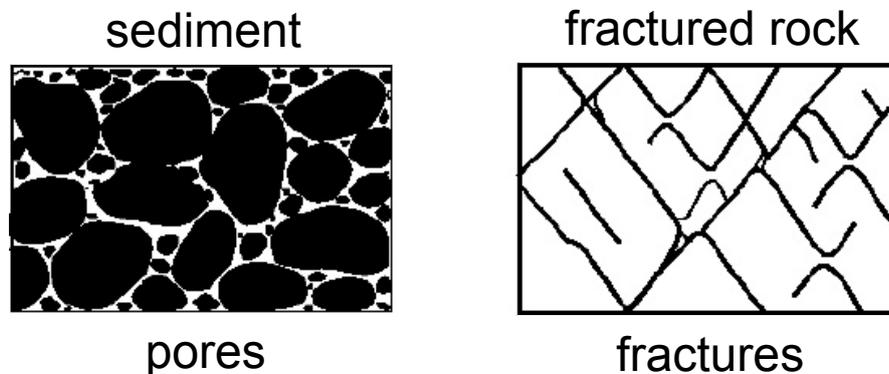
Fig. 2.1   Different types of media

Generally, a large number of spatial scales can be identified in geological media which can be put down to the origin of the media and the different types of parent material. This involves the formation of areas of different characteristics, e. g. spacious geological stratifications or fracture networks, which have a strong influence on the flow and transport through such media.

2.1.2   Sedimentary rock

Flow and transport models in sedimentary rock are derived from balance equations for mass and impulse and can be described as diffusion or advection/diffusion equations using the medium parameters storage coefficient, hydraulic conductivity or transmissivity and dispersivity, which apply on the scale of a representative elementary volume (REV). In the case of density-driven flow, there also exist a system of coupled equation for groundwater flow as well as salt and heat transport /DIE 05/. Sedimentary rocks such as clay are generally characterised by low hydraulic conductivity values and a high adsorption capacity. Sandstones, in contrast, show clearly higher hydraulic conductivity values.

As geological media can vary on many spatial scales, reaching from pore space to aquifer structures and reservoirs, what has to be done first is to define the scale of the model. Heterogeneities in the order of magnitude of the scale of the model have to be represented explicitly, e. g. spatial stratifications. The effect of subscale heterogeneities can be adequately expressed and modelled through so-called upscaling (/REN 97/, /ATT 03/, /HOR 96/) in the form of effective model parameters (see also 3.3).

2.1.3   Fractured rock

The flow and transport processes in fractured rock also develop on very different temporal and spatial scales, reaching from the microscale and individual fractures and fracture networks (centimetre and metre scale) to aquifer structures and reservoirs (hundreds of metres and kilometres). Fractures or fracture zones are generally marked by relatively high humidity and little storage capacity. Thus they can be preferred flow paths that allow fast transport of dissolved contaminants. The surrounding rock matrix in contrast often shows very low hydraulic conductivity and a high storage capacity. Any penetrating contaminants can thus cause long-term contamination caused by the very slow migration through the matrix. or Up-to-date surveys of conceptual models for fractured rock types can be found e. g. in /KOS 06/ and /MCD 06/. Apart from the classic approaches to fracture hydraulics, such as the "cubic law" /WIT 80/, the focus has more recently been above all on the study of scale-dependencies of hydraulic and transport parameters like permeabilities and mixing properties in fractured and fractured-porous media. Similarly as in the section above, the scale of the model has to be defined prior to the actual creation of the model. Subscale heterogeneities such as

small fracture systems (right in Fig. 2.1) are transferred with the help of homogenisation into effective single- or multi-continuum models /LON 82/, /LON 85/, /WOL 90/, /BAR 60/, /WAR 63/, /HUY 83a/, /KOE 00/, /NAR 82/, /HUY 83b/, /PRU 85/, /TEU 88/, /GER 93/, /BIR 94/, /JAN 99/. Heterogeneities in the order of magnitude of the model scale like the large and dominant fracture networks have to be modelled explicitly. In order to model large, hydrogeologically complex areas, the effect of smaller fractures has to be integrated in a continuum model as an effective rock matrix and coupled to the explicit fracture network. /THE 96/ have shown that the consideration of the effective matrix in fractured systems and an explicit description of the interactions between fracture and matrix is necessary also – and in particular – under unsaturated conditions because in this case the fractures may possibly act as barriers and the transport will mainly take place through the porous matrix.

Under certain circumstances, fracture networks can also be strongly simplified with the help of fractal scaling methods and be described as effectively one-dimensional models. Effective hydraulic conductivity values were calculated for two- and three-dimensional fracture networks depending on the size of the model area, the number of fractures, and the distribution of the fracture aperture widths /SNO 65/, /WIL 70/, /LON 82/, /LON 83/, /WOL 90/, /KOS 96/. Equivalent dispersivity values can be determined in a similar way for the transport within the fracture network. One current issue that is presently being debated rather controversially in the literature is the validity of Gaussian distributions for the dispersion models and the resulting non-Fick's transport models /DEN 03/, /BER 06/. For example, fractal Levy distributions (distributions with non-existent first and/or second momenta) will quite often ensue. Corresponding studies were carried out for two-dimensional areas, e. g. by /SCH 83/, /SMI 84/, /WOL 90/, /CAC 90a/, /CAC 90b/, /DEN 03/, /BER 06/. A structural analysis of fracture networks and the integration of these effects on the different scales in spacious fracture networks is proposed by /HES 90/, /BER 93/, /BOU 97/, /MAR 98/.

2.1.4 Numerical procederes

2.1.4.1 Numerical procedures for the modelling of flow and transport through sedimentary rock

The calculation codes d³f and r³t are based on the simulation system UG, /BAS 94/, /BAS 00a/, which as a general parallel and adaptive solver for coupled systems of partial differential equations occupies an island position among the simulation codes to this day. The development of UG, which began as early as in 1990, triggered a number of further developments, among them /DEA 03/, /BAS 05/, and various others, but none of these has reached the level, functionality or scope and depth of application that UG has reached. The treatment of realistic models with adequately fine resolution requires grids with 109 or more unknown variables. These can only be used to any purposeful effect if all possibilities of complexity reduction and efficiency increase, especially massively parallel systems, are utilised. These include adaptive multiple-grid methods /BAS 94/ and their parallelisation. Most recent tests of UG benchmarks on massively parallel computers show the excellent scaling properties of the code system. For example, a scale-up study yielded a scaling difference of 93 % at 2048 CPUs compared to 27 CPUs. Here, systems with more than 109 unknown variables were resolved /LAM 07/. UG thus sets standards.

So far, finite-volume methods have been the standard procedures implemented in UG for discretisation. In recent years, new approaches to discretisation have been developed. These include above all the discontinuous Galerkin methods /ODE 98/. These offer the possibility to handle the order of the initial functions flexibly and thus also to include them in an adaptive concept. Such methods have so far not yet been formulated for density flows and offer an interesting alternative for this as well as for the related transport problems. In this context, we have already done some preparatory work towards fast solvers /JOH 06a/, /JOH 06b/. A combination of algebraic multi-grid procedures is also of interest in this respect.

2.1.4.2 Numerical procedures for the modelling of flow and transport through fracture networks

Based on the data from the DFG-Project: "Festgesteins-Aquiferanalog: Experimente und Modellierung" /NEU 97/, /NEU 99/, /NEU 00/ carried out laboratory- and field-scale

simulations in order to be able to determine the effects of the fracture-matrix interaction on the physical processes. /LAN 95a/ and /LAN 95b/ carried out two-dimensional studies with fracture-matrix models to identify parameters for double-continuum models.

Neunhäuser /NEU 03/ has developed a selection of suitable numerical discretisation methods for equidimensional as well as for low-dimensional formulations of a fracture-matrix model and has studied the solution behaviour of the equidimensional model approach in comparison with the low-dimensional model approach. For the selection of numerical methods that are suitable for the discretisation of flow and transport processes in fractured porous media with consideration of the predetermined conditions, Euler methods from the areas of finite volumes and finite elements were exclusively considered. For the discretisation of flow, the box method and the method of mixed hybrid finite elements was chosen. For the discretisation of transport, the box method was used, which fulfils the requirement of avoiding oscillations even on grids that have been unstructured at will, but is only of the first order and thus introduces numerical dispersion into the system. A determination of the upwinding parameter subject to the Courant and Peclet number and the flow direction (streamline orientation) was therefore established in order to enhance the order of the procedure in dominantly dispersive areas.

In summary, Neunhäuser /NEU 03/ has found that the use of the equidimensional approach, especially in the case of slower systems with a fracture that runs transversal to the main flow direction, shows clear effects on the approximated solutions. The hybrid box method used for transport discretisation with process-dependent upwinding in the matrix and full upwinding in the fractures generates clearly steeper concentration fronts in the matrix area at only little additional calculatory effort. To obtain an improved approximation of the transport equation for the contaminant it is therefore necessary that more complex adaptive discretisation methods are utilised. These also include in particular methods with adaptive order. The heterogeneity of a complex fractured porous medium thus calls for adaptive multi-scale models.

Among the numerical multi-scale models, some areas are already well introduced. This includes the multi-grid technique, which has been established for the design of fast solvers for large systems of equations /HAC 85/, /WES 92/. The d³f and r³t codes are also based on multi-grid solvers. Other multi-scale methods are wavelet procedures, which are used above all in image processing. Further, there continue to appear spe-

cial developments attempting to combine analytical and numerical multi-scale methods. Noteworthy among these are in particular /NEU 95/, /NEU 01/, /ATT 02/.

The inclusion of fractures in the model demands flexibility regarding the dimension of the discretisation. Fractures are typically not modelled as fully three-dimensional objects but are reduced to two- or one-dimensional objects. For multiphase flows, corresponding discretisation methods have already been developed and implemented on the basis of UG /REI 04/. Here, the development of compatible finite-volume formulations of differing dimensions was an essential factor. The current project is to involve the derivation and implementation of corresponding methods for density-driven flow (d³f) and transport (r³t).

For the numerical simulation of multi-scale processes in fractured rock, hybrid methods are used increasingly alongside hierarchical ones. The combination of numerical and hierarchical methods has proved effective for the resolution of the extremely different spatial and time scales, e. g. of advective-dominated channelling effects in fractures and diffusion processes in the rock matrix (matrix diffusion or intra-particle diffusion). Moreover, hybrid approaches are highly suitable for fracture network models /MCD 07/.

2.1.5 Model hierarchies

The physical processes as well as the heterogeneities and material properties of fractured and sedimentary rock on small scales influence the system behaviour on larger scales. If large complex formations are to be modelled, this can generally not be done on the basis of detailed small-scale information since on the one hand the data are not or cannot usually be gathered to the amount that is necessary and on the other hand because the requisite calculation capacity and calculation time is also highly disproportionate to the result. To reduce the complexity of the system it is therefore necessary to identify the physically relevant parameters and processes on the different scales and describe subscale effects with the help of effective models and effective parameters. Examples are the effective hydraulic conductivity or the dispersion that describes the mass flow due to velocity fluctuations in the observation volume. Effective parameters are usually determined by performing an averaging process across the scale volume, with the scale volume having to be a representative elementary volume REV /BEA 72/ regarding the parameter or process to be studied. This averaging process across an REV also corresponds to an asymptotic scaling process. This volume averaging pro-

cess is equivalent to homogenisation methods /PAP 78/ or stochastic averaging methods /GEL 83/, /DAG 84/. These yield the same effective parameters if there is a separation of scales. This means that the scale across which the averaging process is carried out is clearly separated from the large scale on which the effective models and parameters are to be valid. The prerequisite of scale separation is, however, a restriction that does not apply to many practically relevant problems. This is especially true in the vicinity of steep gradients of hydraulic pressure, e. g. near pumping wells or in the case of marked conductivity changes upon the transition from highly conductive to less conductive rock properties or vice versa and/or near steep concentration gradients as they may occur for transient concentration distributions in the vicinity of sources and/or as a result of marked conductivity contrasts. In these cases, the steep gradients in pressure and concentration have to be resolved locally, so that there is a directly ensuing need for adaptive scaling methods. One scaling procedure that allows the possibility of adaptivity is the so-called coarse-graining method. This method is based on the same idea as the method of large-eddy simulations. It represents a filter method that cuts off the high-frequent proportions of the solution in the frequency domain and projects – and thus considers – only their averaged effect on low-frequent proportions of the solution. The high flexibility of this method lies in the free choice of the cut-off frequency which defines the high- and low-frequent proportions. A very small cut-off frequency means that hardly anything is filtered out and the medium and the processes developing in it are still represented at fine resolution, while a high cut-off frequency means that the medium and the associated processes are shown very much coarsened or highly scaled /ATT 03/, /SCH 07a/, /BEC 02/.

Multi-scale methods for discretisation have been developed above all for the equation of hydraulic pressure, e. g. the variation methods /ARB 02/ and /ARB 04/, the multi-scale finite-element methods (MsFEM) /CHE 03/, /HOU 97/, the multi-scale finite volume methods (MsFVM) /JEN 03/, the equation-free computation method /KEV 03/ and the heterogeneous multi-scale method (HMM) /ENG 03/. MsFEM and MsFVM attempt efficiently to calculate a fine-scaled solution, albeit by calculating the solution on a coarser grid and then calculating the basic functions from the solution of a fine-scaled problem which then has the fine-scaled properties of the solution. The calculatory effort is similar to that of a fine-scale solver. (This also works for other methods.) HMM, on the other hand, is best comparable with a coarse-scale solver that presupposes scale separation. Small-scale information is taken into account by solution of small-scale cell problems and the consideration of their flows into the large scales. Numerical multi-

scale models for the advection-dominated transport of contaminants are hardly developed at all. They only exist in the area of two-phase flows in which a pressure equation describes the development of the pressure of the phases, e. g. oil and water, and a transport equation describes the transport of the saturation of the phases. In principle, the pressure shows strongly dispersive properties, so that it can be represented on coarsened grids without any major errors. Advection-dominated transport of phases as well as of contaminants, however, is dominated by small-scale velocities for as long as non-traversal mixing "blurs" these fluctuations in the velocities. This, however, only occurs in the borderline case of long transport times /ATT 99/, /DEN 00a/, /DEN 00b/, /DEN 02/. More recent approaches /AAR 06/ now try to calculate the pressure in a coarse-scaled and the velocities in a fine-scaled manner with mixed hybrid FEMs and to put this fine-scale information to effective use in the transport simulation. Effectively means in this case that the fine-scale information is only used in the vicinity of steep gradients. Apart from that, the transport is only calculated in a coarse-scaled manner. Effective flow and transport parameters for the coarse-scaled proportions are not calculated, though, as the work in /AAR 06/ is solely restricted to a purely advective two-phase problem. The effective model is in turn a purely advective two-phase problem which always has steep gradients at the fronts, which are then calculated at fine resolution. However, an effective multi-scale model for the transport of contaminants requires the inclusion of fine-scaled mixing, which leads to strongly increased mixing in flow direction for longer running times /ATT 99/, /DEN 00a/, /DEN 00b/, /DEN 02/ and therefore to the levelling of steep concentration gradients. Here, there is a need for the development of special subscale mixing models. Strong conductivity contrasts on the other side, as they occur in complex geological formations at the transition between sedimentary layers on the one hand and between rock matrix and fracture system on the other, may in turn generate so-called channelling effects and steep concentration gradients. The levelling and steepening of concentration gradients brings about the need for new adaptive numerical multi-scale methods.

What is decisive for the practical usability of these approaches is their linking to suitable numerical solution procedures. Relevant techniques in this context are the adaptive methods that have been used for many years to overcome numerical scaling problems. These can be used directly as part of multi-scale approaches for discretisation, although refinement criteria and error estimators have to be newly developed for a model hierarchy. Corresponding activities are currently underway within the framework of LES procedures for highly turbulent flows.

2.1.6 Inverse modelling

The estimation of relevant parameters in the differential equation systems is of fundamental importance for the modelling and simulation. The use of fast methods for parameter estimation – as it is only now being developed within the framework of partial differential equations – is of utmost relevance for the practical usability of the models and software. For this purpose there exist a large number of algorithms. However, since inverse modelling brings with it a further level of complexity, common differential equations are typically used in this connection. Typical applications are optimal controls in process engineering, vehicle dynamics of motor vehicles etc. More recent developments that include inverse modelling in partial differential equations are e. g. the SQP multi-grid procedures described in /SCH 98b/, /LOG 01/, /WIT 03/, which are above all suitable for steady-state problems. With its help it was possible to solve the inverse problem with an effort required to solve three to five forward problems, which means an essential reduction in the effort usually required otherwise. A survey of the current status of the research in this area is provided by /BOR 07/, /BOR 05/, /SCH 04b/, /SCH 07b/.

In the case of discrete problems it is more advisable to combine Gauss-Newton methods with multiple-target methods. This was introduced in /HAZ 02/ for a multiphase flow in groundwater and implemented successfully. In /QUE 07/, this approach was used for the estimation of parameters of a model of signal processing in neurons. The inverse modelling for the flow problems in the current project was built on these methods.

Multi-grid procedures are well in place as numerical multi-scale solvers. As they use multi-scale techniques themselves, the can be well combined with multi-scale approaches in modelling and discretisation.

Corresponding work at the SiT Chair has yielded a number of studies /NEU 95/, /NEU 01/, /ATT 02/, /EBE 04/, /EBE 05/. These deal above all with the design of coarse-grid operators for strongly heterogeneous problems and the design of corresponding multi-grid methods. With the exception of the work referred to above, the combination of these methods has not yet been described in the literature. This has been changed with the current project.

2.2   Overall objective

The overall goal of the project was the development of software tools for the multi-scale simulation of flow and advective-dispersive contaminant transport in heterogeneous porous media. Special approaches were developed for thin layers and fractures running through hard rock or clay to allow an adaptive resolution of the layers. Of central relevance in this respect were local dimension-adaptive elements that allow an adaptive transition from low-dimensional to equidimensional modelling of the layers or fractures.

Furthermore, discretisation methods of a higher order were developed for the mixed parabolic-hyperbolic problems and implemented in the simulation software. This was done on the basis of discrete Galerkin methods or finite-volume methods. For the systems thus generated, fast solution methods were developed on the basis of multiple-grid methods. What was furthermore decisive was the efficient implementation of the methods on massively parallel computers. The basis of the implementation were the software tools d³f and r³t.

For the estimation of parameters for these systems, efficient numerical procedures were developed and implemented. These procedures build on the Gauss-Newton techniques that are combined with multi-grid methods. Here, too, it was decisive that the implementation on parallel computers was done efficiently as the complexity of the inverse problems may easily exceed the complexity of the simulation itself by one order of magnitude.

On the basis of the detailed models, reduced models were furthermore prepared allowing a fast, coarse calculation of the problem. For this purpose, compartmentalisation methods were applied. Where possible, it was attempted to speed up the simulation models by reducing their dimensions.

Individual targets:

−   Preparation of a multi-scale reference model

  •   Modelling of flow and transport on the fine fracture network
  •   Scaling of flow and transport on the fine fracture network
  •   Numerical solver for flow and transport on the fine fracture network

−   Development of a numerical solver for the reference model

- Discretisation with finite-volume or discrete Galerkin methods of variable order

- Multi-grid solver for the systems considered

- Parallelisation for massively parallel computers

– Concepts and criteria for multi-scale adaptivity

– Adaptive numerical multi-scale solver for the overall system and implementation in d³f and r³t

– Development of reduced models for coarse simulation

– Algorithms and software tools for the inverse modelling and estimation of the relevant parameters of the flow problem

– Uncertainty analysis, benchmarking and comparative calculations

– Development and realisation of a user interface for operating d³f and r³t

These methods are to be implemented for d³f and r³t.

2.3   The organization

Goethe Center for Scientific Computing (G-CSC), University of Frankfurt

Kettenhofweg 139, 60325 Frankfurt

Prof. Gabriel Wittum

Dr. Alfio Grillo

Michael Hoffer

Dr. Michael Lampe

Dr. Dmitrij Logashenko

Dr. Ivo Muha

Dr. Arne Nägel

Sebastian Reiter

Martin Rupp

Sabine Stichel

Andreas Vogel

Institute for Geosciences, University of Jena, Burgweg 11, 07749 Jena

Prof. Sabine Attinger

Dr. Falk Heße

Dr. Florin Radu

Dr. Jude Musuuza

Katharina Ross

Department Environmental Informatics, Helmholtz Centre for Environmental Research

Permoserstr. 15, 04318 Leipzig

Prof. Olaf Kolditz

Dr. Joshua Taron

Yuanyuan Sun

Gesellschaft für Anlagen- und Reaktorsicherheit (GRS) mbH

Repository Safety Research Division, Th.-Heuss-Str. 4, 38122 Braunschweig

Dr. Eckhard Fein

Anke Schneider

Dr. Judith Flügge

Dr. Klaus-Peter Kröhn

Anne Gehrke

Dr. Sabine Spießl

3 Meso-scale reference model

3.1 Motivation

Solute transport through heterogeneous geological formations is an important research area in hydrology and environmental engineering. An exact quantification of mixing is of particular interest in modelling the fate and transport behaviour of contaminants in the subsurface. The spreading of the solute is strongly influenced by the heterogeneities of the medium through which the groundwater flows.

One of the main challenges in modelling the heterogeneities is how to deal with the different scales of the heterogeneities: the rock matrix can be represented using a continuum model (region A in Fig. 3.1). Large fractures in combination with the surrounding rock matrix (region C in Fig. 3.1) can be modelled in detail using a discrete fracture model combined with a continuum model. An open question is how to model the countless tiny fissures (region B in Fig. 3.1) in which a remarkable part of the water phase flow takes place. Not all the tiny fissures can be modelled in detail because this would be too complex and too time-consuming. A possibility how to treat those fissures would also enable one to handle different scales of heterogeneities (region D in Fig. 3.1). The aim of this study is to model such a situation consisting of tiny fissures and large fractures which would represent a reference model on the fine scale.
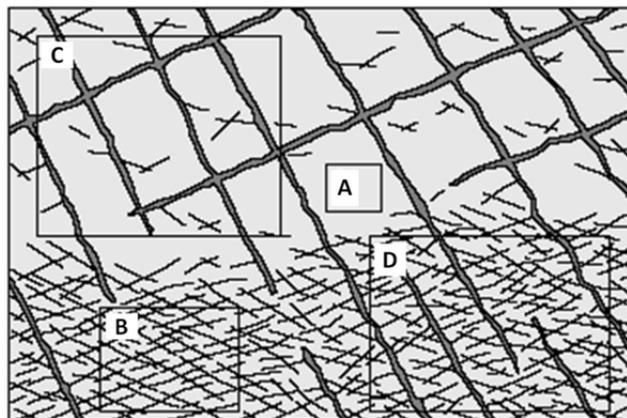
Fig. 3.1   Different scales of the heterogeneities in geologic formations /KRO 91/

In such situations, the background consisting of the tiny fissures can be modelled using a continuum model with correlation lengths which tend to be infinite. But due to computational restrictions, a cutoff-function in the correlation lengths has to be inserted to make sure that the correlation lengths are finite. Large cutoff-values correspond to situations with finite correlations lengths of the heterogeneities in which the different scales are clearly separated whereas small cutoff-values indicate situations with large correlations lengths. The smaller the cutoff-values are, the longer the correlation lengths. Situations, in which the cutoff-value vanishes, correspond to situations with infinite correlation lengths of the heterogeneities which are used to describe media with a "fractal" structure, e. g. /FIO 01/, /NEU 90/, /NEU 95/, /NEU 05/, /ZHA 96a/.

According to /NEU 90/, heterogeneities in natural geological formations are characterised by a complex hierarchy of scales. Whether such a hierarchy is infinite is difficult to assess experimentally. /NEU 90/ argued that with increasing lags, larger scales have to be considered and therefore the semi-variogram of the log hydraulic conductivity increases. Media with this property can be described by applying a scaling assumption /NEU 90/, /BEL 96/. There is no longer a preferential (finite) scale since these media are characterised by "evolving scales" (e. g. /BEL 96/, /FIO 01/, /NEU 95/, /SPO 86/, /ZHA 96a/) due to the absence of clearly separated scales of the heterogeneities. This effect can be compared with a high tortuosity in heterogeneous porous media, where solute particles have to follow longer and branched pathways due to tiny spatial heterogeneities.

The classical dispersion theory on the laboratory scale reveals that homogeneous media dispersivities are constants related to the porous media geometries /SDG 54/, /BEA 72/. Physical heterogeneities include spatial variations in porosity and hydraulic conductivity. Following /ZHA 96a/ porosity variations are treated as a secondary effect and neglected in this study. A spatial variability of hydraulic conductivity is represented by a continuous hierarchy of scales as studied and described e. g. by /PIC 81/, /GEL 86/, /NEU 90/, /NEU 05/, /KEM 94/, /DAG 94/, /DES 94a/, /BEL 96/, /FIO 01/ or /KIM 04/. In the following, fractal media are understood as inhomogeneous fractured media characterized by an infinite correlation length of the heterogeneities which should be modelled with evolving scales.

The dispersion depends not only on the scale, but also on the flow direction. In the following, two directions of the flow are distinguished: The longitudinal component D_{11} fol-

lowing the main flow direction and the transverse one D_{22} in the mutually perpendicular directions.

In order to model the tiny fissures as background medium, the idea of this study is to combine these fissures and treat them as a continuum which is substituted in the context of a multi-Gaussian approach by effective parameters (section 3.3). In this chapter, first the method of generating the subscale heterogeneities is represented using cutoff-functions. Afterwards, the model with special respect to fractal media is described in which the tiny fissures are represented by effective transport parameters. Then, the results are shown and compared with heterogeneous porous media characterised by clearly separated scales and a finite correlation length of the heterogeneities. In the following, vector and tensor quantities are indicated by boldface characters.

3.2 Generation of the random fields

In this section, the role of the variogram will be explained and the derivation of the truncated power-law will be described according to /HES 13/. In addition, the numerical methods used for the generation of random fields are described and compared.

3.2.1 Random fields

Due to the intrinsic complexity of fractured media and the uncertainty of field studies, it is common to use stochastic quantities in order to describe certain geological properties. These quantities are called **random fields** which are basically spatially-dependent random variables. As a result, they can mathematically be described as a set $\{u(\mathbf{x})|\mathbf{x} \in \Omega\}$. In this context, Ω is the support of u, i. e. the spatial region $\Omega \subseteq R^n$ over which u is defined, with n being the spatial dimension (n = 1, 2, 3). In the following mathematical description, random fields and stochastic processes are very similar. Since a stochastic process is a time-dependent random variable, the main difference is the support which is a time interval $T \subseteq R$ instead of a spatial region Ω. The mathematical notation, however, for both random fields and stochastic processes is identical. In this context, they can therefore be considered synonymous.

In order to fully describe random fields, it has to be distinguished between one-point and two-point spatial characteristics. One-point characteristics are the expectation and the variance. These quantities are defined point-wise for every $\mathbf{x} \in \Omega$ in full analogy to

plain random variables. Two-point characteristics describe the stochastic relationship of the random field at two points $\mathbf{x_1}, \mathbf{x_2} \in \Omega$. These functions are the covariance function, the correlation function and the (semi)variogram. They are defined in the following.

The **covariance** function describes the degree of variation of a random field u($\mathbf{x}$) between two points $\mathbf{x_1}$ and $\mathbf{x_2}$:

$$\mathrm{Cov}\big(\mathrm{u}(\mathbf{x_1}), \mathrm{u}(\mathbf{x_2})\big) = \mathrm{E}[(\mathrm{u}(\mathbf{x_1}) - \mathrm{E}[\mathrm{u}(\mathbf{x_1})])(\mathrm{u}(\mathbf{x_2}) - \mathrm{E}[\mathrm{u}(\mathbf{x_2})])] \,. \qquad (3.1)$$

The **correlation** function describes the degree of correlation of a random field u($\mathbf{x}$) between two points $\mathbf{x_1}$ and $\mathbf{x_2}$ which is defined as the covariance between these points normalised by the point-wise variance:

$$\mathrm{R}\big(\mathrm{u}(\mathbf{x_1}), \mathrm{u}(\mathbf{x_2})\big) = \frac{\mathrm{Cov}\big(\mathrm{u}(\mathbf{x_1}), \mathrm{u}(\mathbf{x_2})\big)}{\mathrm{Var}\big(\mathrm{u}(\mathbf{x_1})\big)\mathrm{Var}\big(\mathrm{u}(\mathbf{x_2})\big)} \,. \qquad (3.2)$$

The **variogram** (more precisely semivariogram or structure function according to e. g. /MAJ 99/, /CAM 03/, /KRA 07/) is a function that describes the spatial variability of the random field u($\mathbf{x}$) between two points $\mathbf{x_1}$ and $\mathbf{x_2}$:

$$\gamma\big(\mathrm{u}(\mathbf{x_1}), \mathrm{u}(\mathbf{x_2})\big) = \frac{1}{2}\mathrm{E}\left[\big(\mathrm{u}(\mathbf{x_1}) - \mathrm{u}(\mathbf{x_2})\big)^2\right] \,. \qquad (3.3)$$

All the characteristics described above contain the same information in different forms, i. e. the degree of spatial dependency of a random field u($\mathbf{x}$) between the points $\mathbf{x_1}$ and $\mathbf{x_2}$. It is therefore sufficient to describe only one of these in order to have a full statistic characterisation of a random field.

3.2.2 Variograms and associated spectra of random fields

Hereafter, the variograms will be introduced and the associated spectra of the random fields according to /HES 13/. Special attention will be given to the derivation and description of the truncated power-law due to its central role.

3.2.2.1 Classic variograms and spectra

In geostatistical analysis, a variogram for a specific geologic material is usually acquired by estimation from a sample according to (3.3) and subsequent fitting to a con-

ceptual model function. Typically, such model functions include the exponential variogram

$$\gamma(h, \lambda) = \sigma^2 \left[1 - e^{-\frac{|h|}{\lambda}} \right] \quad \text{with} \quad S(\mathbf{k}, \lambda) = \sigma^2 \lambda^d \frac{\Gamma\left[\frac{d+1}{2}\right]}{\left(\pi(1 + \mathbf{k}^2\lambda^2)\right)^{\frac{d+1}{2}}} \tag{3.4}$$

or the Gaussian variogram

$$\gamma(h, \lambda) = \sigma^2 \left[1 - e^{-\frac{\pi}{4}\left(\frac{h}{\lambda}\right)^2} \right] \quad \text{with} \quad S(\mathbf{k}, \lambda) = \sigma^2 \left(\frac{\lambda}{\pi}\right)^d e^{-\frac{1}{\pi}(\mathbf{k}\lambda)^2} . \tag{3.5}$$

Both models assume a single characteristic length scale λ on which the observed heterogeneities appear. This condition is not met by many porous and fractured materials /RIT 04/. /NEU 08/ argue that the apparent ability of these models to characterise a wide range of porous materials can be seen as an artefact of the finite nature of the sampling process itself.

3.2.2.2   Power-law variogram and spectrum

Exponential and Gaussian variograms assume the existence of a single length scale for the variations of geological media. However, if the estimated correlation lengths λ obtained from sampled variograms on different length scales are compared, a clear scale dependency will be often visible /DIF 97/. If the estimated λ is plotted in these cases versus the length scale of the measuring process, many data will show a linear increase in a logarithmic scale. Such a linear behaviour indicates a power-law for the variogram and the spectrum of the underlying medium

$$\gamma(h) = C_0|h|^{2H} \text{ with } S(\mathbf{k}) = \frac{\Gamma[1 + 2H]\sin(\pi H)}{\pi} C_0|\mathbf{k}|^{-(1+2H)}; 0 < H < 1 \tag{3.6}$$

In this context, C_0 is a constant and H the Hurst coefficient. No characteristic length scales appear in (3.6) indicating that a random field with such a variogram and spectrum is a self-similar fractal field. /DIF 97/ could show that (3.6) can be decomposed into an integral representation with weighted modes consisting of either Gaussian or exponential functions

$$\gamma(h) = C \int_0^\infty \frac{\gamma(h, n)}{n^{2H+1}} dn \quad \text{with} \quad S(\mathbf{k}) = C \int_0^\infty \frac{S(\mathbf{k}, n)}{n^{2H+1}} dn . \tag{3.7}$$

The parameter $n = 1/\lambda$ denotes the wave number, i. e. the inverse correlation length and C is a constant with the dimensions $[L^{-1-2H}]$. The power-law resulting from (3.7) for the case of exponential modes will then follow from (3.6) with

$$C_0 = C\frac{\Gamma[1 - 2H]}{2H}, \qquad 0 < H < 1/2, \qquad\qquad (3.8)$$

and for the case of Gaussian modes respectively (in both cases the variance of the single modes is assumed to be unity i. e. $\sigma^2 = 1$)

$$C_0 = C\frac{\Gamma[1 - H]}{2H}\left(\frac{\pi}{4}\right)^H, \qquad 0 < H < 1. \qquad\qquad (3.9)$$

This decomposition can be interpreted such that fractal geological media are composed of an infinite hierarchy of scales, each of which represented by a classic variogram (see Fig. 3.2 for a schematic representation). The weighted superposition of these modes according to (3.7) is resulting in truly fractal media. The major shortcoming of this approach is the fact that any real medium has an upper length scale λ_u confining the fractal behaviour within an interval of scales. Such a finite-size effect can, however, be implemented by truncating the integral in (3.7), which will result in a so-called truncated power-law variogram.
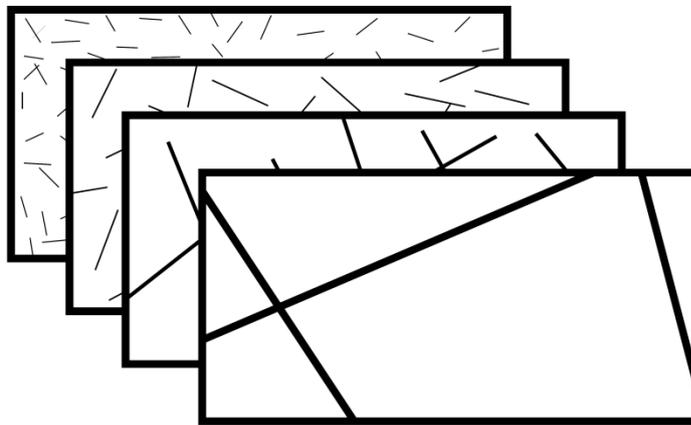
Fig. 3.2   Schematic representation of different scales in multi-scale fractured media /HES 13/

3.2.2.3   Truncated power-law variograms and spectra

The truncated power-law variograms and spectra derived by /DIF 97/ result from truncating the integral from (3.7) at a lower wave number $n_\ell = 1/\lambda_u$

$$\gamma_{n_\ell} = C \int\limits_{n_\ell}^{\infty} \frac{\gamma(h,n)}{n^{1+2H}} \, dn \qquad \text{with} \qquad S_{n_\ell}(\mathbf{k}) = C \int\limits_{n_\ell}^{\infty} \frac{S(\mathbf{k},n)}{n^{1+2H}} \, dn \,. \tag{3.10}$$

Unlike in the case of (3.7), where both exponential and Gaussian modes yielded the same expression, the resulting truncated power-law is different for the two types.

In case of **exponential modes**, i. e. (3.4) are introduced into (3.10) and the resulting variogram and spectrum have the form:

$$\gamma_{n_\ell} = \sigma^2 \left[1 - e^{-|h|n_\ell} + (hn_\ell)^{2H} \Gamma[1 - 2H, |h|n_\ell] \right], \tag{3.11}$$

$$S_{n_\ell}(\mathbf{k}) = \sigma^2 \frac{2H\Gamma\left[\frac{d+1}{2}\right]}{\pi^{\frac{d+1}{2}}(d+2H)n_\ell d^2} F_1 \left[\begin{matrix} \frac{d+1}{2} & \frac{d+2H}{2} \\ \frac{d+2+2H}{2} \end{matrix} \, ; -\left(\frac{|\mathbf{k}|}{n_\ell}\right)^2 \right]. \tag{3.12}$$

In this context, $\Gamma(\cdot,\cdot)$ is the incomplete gamma function, F_1 is known as the Gaussian hypergeometric function and the variance σ^2 is given as

$$\sigma^2 = \frac{C}{n_\ell^{2H} 2H}\,. \tag{3.13}$$

In case of Gaussian modes, (3.5) is inserted into (3.10). Evaluating these integrals, the variogram and spectrum read

$$\gamma_{n_\ell}(h) = \sigma^2 \left[1 - e^{-\frac{\pi}{4}(hn_\ell)^2} + \left(\frac{\pi}{4}(hn_\ell)^2\right)^H \Gamma\left[1 - H, \frac{\pi}{4}(hn_\ell)^2\right] \right], \tag{3.14}$$

$$S_{n_\ell}(\mathbf{k}) = \sigma^2 \frac{Hn_\ell^{2H}\pi^{-\frac{d}{2}+H}}{|\mathbf{k}|^{2\left(\frac{d}{2}+H\right)}} \left(\Gamma\left[\frac{d+2H}{2}\right] - \Gamma\left[\frac{d+2H}{2}, \frac{1}{\pi}\left(\frac{|\mathbf{k}|}{n_\ell}\right)^2\right] \right) \,. \tag{3.15}$$

Comparing (3.11) and (3.14) shows a very similar behaviour for both expressions. Both exhibit a power-law term, which is important for small lengths ($h < \lambda$). In this region, both variograms are similar to a power-law (3.6) which is exemplified by a linear increase in a log-log plot, with a slope of $2H$. Both expressions also exhibit an exponential and a Gaussian term, respectively. As a result the variograms are saturating for bigger lengths ($h > \lambda$). The incomplete gamma function is mediating the transition between these two regimes. Despite similar variograms, the spectra of both models are very different as a comparison between (3.12) and (3.15) shows.

Double Truncation

In the analysis above, the impact of an **u**pper cut-off length λ_u representing the finite size of real geological media was considered. In order to complete this description, a lower cut-off length λ_ℓ, also has to be considered which represents the finite resolution. The variograms and associated spectra are given by

$$\gamma_{n_\ell, n_u}(h) = C \int_{n_\ell}^{n_u} \frac{\gamma(h, n)}{n^{1+2H}} dn = \gamma_{n_\ell}(h) - \gamma_{n_u}(h) \tag{3.16}$$

$$S_{n_\ell, n_u}(\mathbf{k}) = C \int_{n_\ell}^{n_u} \frac{S(\mathbf{k}, n)}{n^{1+2H}} dn = S_{n_\ell}(\mathbf{k}) - S_{n_u}(\mathbf{k}) \,, \tag{3.17}$$

with the variance given as

$$\sigma_{n_\ell, n_u}^2 = \sigma_{n_\ell}^2 - \sigma_{n_u}^2 = \frac{C}{\left(n_\ell^{2H} - n_u^{2H}\right)2H} \tag{3.18}$$

completing the description for the double-truncated power-law variograms and spectra.
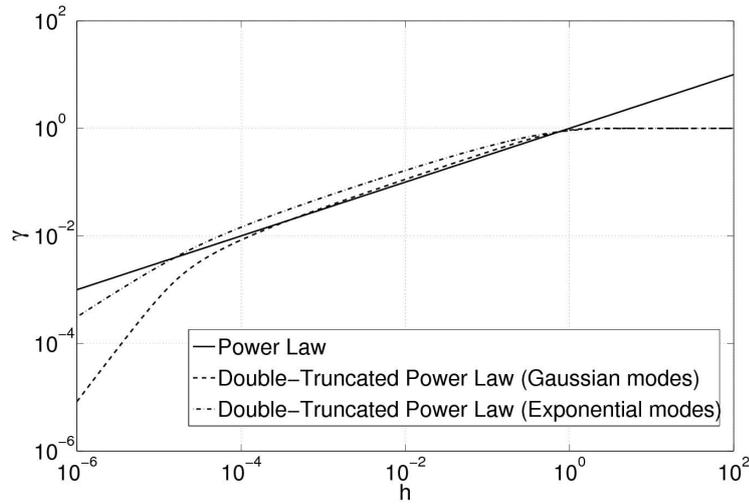
Fig. 3.3   Double-truncated power-law variograms

with Gaussian & exponential modes vs. a power-law variogram (parameters: $\lambda_l = 10^{-5}$, $\lambda_u = 1, H = 0.25$) /HES 13/.

The double-truncated power-law variograms show for high values of h a similar behaviour as described above. For small values of h, it is visible that the double-truncated

power-law is diverting again significantly from the power-law variogram. This exemplifies how the power-law behaviour is confined within $\lambda_\ell \lesssim h \lesssim \lambda_u$ (Fig. 3.3).

3.2.3 Numerical generation of random fields

According to /HES 13/, the different numerical methods used in this study are covered to generate random fields: The Fourier method, the Randomisation method, the Hybrid method and the Fourier-Wavelet method. The derivation of these methods will be laid out for one-dimensional media only. The starting point for the description of these methods must be a mathematic representation of a random field. According to /KRA 07/, a Gaussian random field $u(\mathbf{x})$ can be represented by a stochastic Fourier integral

$$u(\mathbf{x}) = \int_{-\infty}^{\infty} e^{-2\pi i \mathbf{k} \mathbf{x}} \sqrt{S(\mathbf{k})}\, dW(\mathbf{k}) .$$

(3.19)

In this context, $dW(\mathbf{k})$ is a complex-valued white noise random measure. This expression can be rewritten into

$$u(\mathbf{x}) = \int_{-\infty}^{\infty} \cos(2\pi \mathbf{k} \mathbf{x}) \sqrt{S(\mathbf{k})}\, dW(\mathbf{k}) + i \int_{-\infty}^{\infty} \sin(2\pi \mathbf{k} \mathbf{x}) \sqrt{S(\mathbf{k})}\, dW(\mathbf{k}) .$$

(3.20)

Since the spectrum $S(\mathbf{k})$ is the Fourier transform of the covariance function Cov(h) of $u(\mathbf{x})$, which is an even function, $S(\mathbf{k})$ is even, too. As a result, $W(-\mathbf{k}) = -\overline{W(\mathbf{k})}$ holds for the Wiener process. Hence, (3.20) can be rewritten as

$$u(\mathbf{x}) = \sqrt{2\sigma^2} \left(\int_0^{\infty} \cos(2\pi \mathbf{k} \cdot \mathbf{x}) \sqrt{E(\mathbf{k})}\, dW^1(\mathbf{k}) \right.$$
$$\left. + \int_0^{\infty} \sin(2\pi \mathbf{k} \cdot \mathbf{x}) \sqrt{E(\mathbf{k})}\, dW^2(\mathbf{k}) \right) .$$

(3.21)

$W^1(\mathbf{k})$ and $W^2(\mathbf{k})$ are two independent real-valued Wiener processes and $E(\mathbf{k}) = S(\mathbf{k})/\sigma^2$ is the normalised spectrum or spectral density function. In the following, the final form (3.21) is used. A numerical implementation of (3.21) is hampered by two main challenges: (i) The quadrature of the integral and (ii) the numerical representation of the white noise. In the following, it will be laid out how the four considered different methods solve these two problems.

25

3.2.3.1   The Fourier method

The Fourier method is the simplest and most robust discretisation scheme considered in this study. It can be understood as a Riemann sum discretisation of (3.21) It is easy to implement, but suffers from several flaws /ELL 97/ which will be highlighted in the following. The basic idea behind the method is the truncation and discretisation of the integral according to the mid-point rule with equispaced grid points. Using a finite symmetric partition of N intervals having equal widths $\Delta \mathbf{k}$ for the truncation and inserting this into (3.21) gives the following approximation:

$$u(\mathbf{x}) \approx \sqrt{2\sigma^2} \sum_{i=1}^{N} \sqrt{E(k_i)} \left(\cos(2\pi k_i \cdot \mathbf{x})\Delta W_i^1 + \sin(2\pi k_i \cdot \mathbf{x})\Delta W_i^2 \right) \qquad (3.22)$$

yielding a discrete Fourier integral. The calculation of (3.22) is rather straight forward except for the determination of the discretised white noise

$$\Delta W_i^n = Z_i^n \sqrt{\Delta \mathbf{k}} \,, \qquad (3.23)$$

where Z_i^n are independent normal random variables. Introducing this relationship into (3.22), finally gives the representation of (3.21) according to the Fourier method

$$\begin{aligned} u(\mathbf{x})_{\mathrm{Four}} = \sqrt{2\sigma^2} \sum_{i=1}^{N} \sqrt{E(k_i)} \big(& Z_i^1 \cos(2\pi k_i \cdot \mathbf{x})\Delta W_i^1 \\ & + Z_i^2 \sin(2\pi k_i \cdot \mathbf{x})\Delta W_i^2 \big)\sqrt{\Delta \mathbf{k}} \,. \end{aligned} \qquad (3.24)$$

One of the important drawbacks of the Fourier method is the artificially introduced periodicity with length $(\Delta \mathbf{k})^{-1}$. This artifact is due to the finite resolution of the scheme in the Fourier domain and cannot be directly avoided. A workaround would be to simulate a larger domain of which subsequently a smaller part is used. Another problem concerns the applicability of such a truncation of the integral in (3.21) in general. To that end, the integrand has to be zero (or almost zero) outside this interval.

The Randomisation method has been developed by Sabelfeld and his coworkers /KRA 07/. It can be regarded as a modification of the aforementioned Fourier method, whereby the equidistant approximation of the stochastic integral in (3.19) is replaced by a random discretisation. Starting again with (3.21), both terms are treated separately and the first term can be written as

$$u^1(\mathbf{x}) = \sqrt{2\sigma^2} \int\limits_0^\infty \cos(2\pi\mathbf{k}\cdot\mathbf{x})\sqrt{E(\mathbf{k})}\, dW^1(\mathbf{k})\,, \tag{3.25}$$

which is again a random field with zero mean and the variance

$$\mathrm{Var}\left(u^1(\mathbf{x})\right) = \langle|u^1(\mathbf{x})|^2\rangle = 2\sigma^2 \int\limits_0^\infty \cos(2\pi\mathbf{k}\cdot\mathbf{x})E(\mathbf{k})d(\mathbf{k})\,. \tag{3.26}$$

This integral can be approximated by means of a Monte-Carlo integration resulting in the following sum

$$\mathrm{Var}\left(u^1(\mathbf{x})\right) \approx 2\frac{\sigma^2}{N} \sum_{i=1}^N \cos^2(2\pi k_i\cdot\mathbf{x})\,. \tag{3.27}$$

k_i are random numbers following the density distribution function defined by $E(\mathbf{k})$. By virtue of this relationship, (3.25) can be approximated according to

$$u^1(\mathbf{x}) \approx \sqrt{2\frac{\sigma^2}{N} \sum_{i=1}^N Z_i^1\cos(2\pi k_i\cdot\mathbf{x})}\,, \tag{3.28}$$

where the Z_i^1 are again independent Gaussian random variables. If the same procedure is applied to the second term in (3.21), the Randomisation method results

$$u(\mathbf{x})_{\mathrm{Rand}} = \sqrt{2\frac{\sigma^2}{N} \sum_{i=1}^N \left(Z_i^1\cos(2\pi k_i\mathbf{x}) + Z_i^2\sin(2\pi k_i\cdot\mathbf{x})\right)}\,. \tag{3.29}$$

(3.29) is similar to (3.24), but with another manner how the k_i are determined.

In the Fourier method, these equidistant points k_i were sampling the finite interval $[0, k_{max}]$ with N partitions having the width $\Delta\mathbf{k}$ (Fig. 3.4 a). For a spectrum with long tails, such a procedure can be disadvantageous, because k_{max} must be very big to sample a sufficiently large portion of the spectrum. By randomly choosing the sampling points k_i, the Randomisation method can circumvent this problem (Fig. 3.4 b).

a) The Fourier method   b) The Randomisation method   c) The Hybrid method
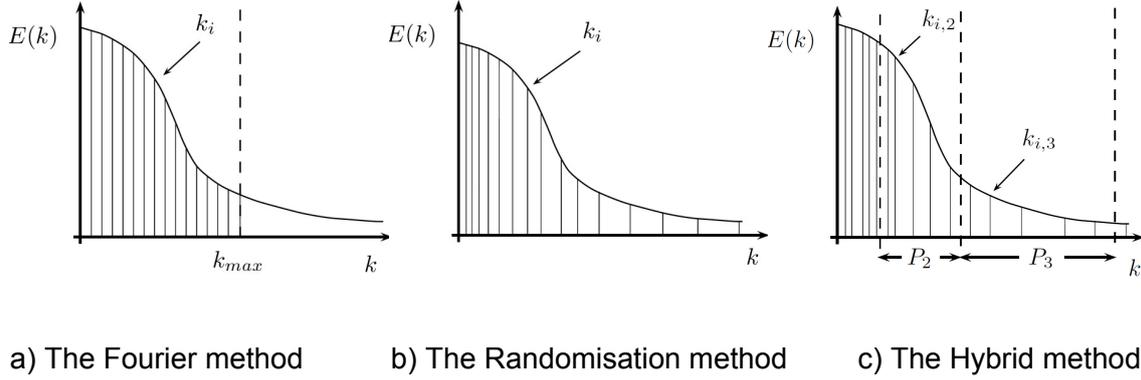
Fig. 3.4   Schematic of the sampling procedure in the different methods /HES 13/

As a result, the interval being sampled is not confined by a finite k_{max} , but is (potentially) the whole support of the spectral density function $E(\mathbf{k})$. For the definitions given above this is the whole domain $[0, \infty)$. Higher regions of the Fourier domain are certainly less likely to be sampled but not discarded completely as in case of the Fourier method.

3.2.3.2   The Hybrid method

The Hybrid method can be understood as a combination of the concepts of the Fourier method (deterministic sampling of the Fourier domain) and the Randomisation method (random sampling of the Fourier domain) by applying a stratified sampling procedure to the latter. To that end, the Fourier domain is partitioned into N_P non-empty and non-overlapping parts $\bigcup_{j=1}^{N_P} P_j = [0, \infty)$. Within each part P_j, having the boundary values $P_j = \left[k_{P_j}, k_{P_{j+1}}\right)$ a random sampling of N points $k_{i,j}$ is applied according to the Randomisation method. The probability density function (PDF) within every part P_j naturally has to be adapted. It now reads

$$E_j(\mathbf{k}) = \begin{cases} \dfrac{2}{\sigma_j^2} E(\mathbf{k}), & \text{for } \mathbf{k} \in P_j, \\ 0, & \text{else}, \end{cases} \qquad \text{with} \qquad \sigma_j^2 = 2\int_{k_j}^{k_j} E(\mathbf{k}) d\mathbf{k}. \tag{3.30}$$

When this partitioning is inserted into (3.29) for the Hybrid method follows

$$u(\mathbf{x})_{\text{Hyb}} = \sum_{j=1}^{N_P} \sqrt{2\frac{\sigma_j^2}{N}} \sum_{i=1}^{N} \left(Z_{i,j}^1 \cos(2\pi k_{i,j}\mathbf{x}) + Z_{i,j}^2 \sin(2\pi k_{i,j}\mathbf{x}) \right). \tag{3.31}$$

The random numbers $Z_{i,j}^n$ are again independent standard Gaussian random variables.

The main advantage of this stratified sampling technique is the possibility of sampling specific portions of the Fourier domain (usually those with high values of $\mathbf{k}$) with higher accuracy. This improves the advantages of the Randomisation method even further. The Fourier method had the drawback of a truncation of the stochastic integral for high values of $\mathbf{k}$ (Fig. 3.4 a). This can be problematic for spectra having long tails. The Randomisation method could circumvent this problem because values from the whole Fourier domain would be sampled according to the PDF given by the respective spectral density function (Fig. 3.4 b). This procedure is a clear improvement but still leaves regions with small values of $E(\mathbf{k})$ with smaller sample size and therefore smaller accuracy. The Hybrid method is countering this tendency by sampling each part P_j with the same sample size (Fig. 3.4 c). The combination of Fourier and Randomisation method improves the representation and hence the overall quality of the sampling procedure.

The crucial question for the application of the Hybrid method is the choice of the partitioning procedure. According to a variety of performed test runs (not discussed here) and in accordance with the results of /KRA 07/ a logarithmic partitioning was found, with doubling interval lengths, gives best results. It is therefore set $P_1 = [0, 1)$ for the first part and $k_{P_{j+1}} = 2k_{P_j}$ for every successive interval boundary. It should be noted, that /KRA 07/ call this specific partitioning strategy for the Hybrid method the 'variant C of the Randomisation method' in their paper.

3.2.3.3   The Fourier-Wavelet method

The Fourier-Wavelet method has been developed by /ELL 97/. As the name implies, wavelets are applied for the discretisation of (3.19) in particular for the random measure $dW(\mathbf{k})$. In contrast (3.23), the following approach is used for the representation of the increments of the Wiener process

$$dW(\mathbf{k}) = \sum_i Z_i \phi_i(\mathbf{k}) d\mathbf{k} .$$

(3.32)

Z_i are again independent Gaussian random variables and the ϕ_i must form an orthonormal basis. The main idea of /ELL 97/ is to use Fourier transformed Wavelets ψ_i or more specifically Meyer Wavelets for $\phi_i = \mathcal{F}[\psi_i]$. The Fourier transform of the Meyer wavelet has the form

$$\phi(\mathbf{k}) = \mathcal{F}[\psi](\mathbf{k}) = -i\,\text{sign}(\mathbf{k})e^{i\pi\mathbf{k}}b(|\mathbf{k}|)\,, \qquad (3.33)$$

with b($\mathbf{k}$) defined as

$$b(\mathbf{k}) = \begin{cases} \sin\left(\dfrac{\pi}{2}v(3k-1)\right), & \text{if } k \in \left(\dfrac{1}{3},\dfrac{2}{3}\right], \\[2mm] \cos\left(\dfrac{\pi}{2}v\left(\dfrac{3k}{2}-1\right)\right), & \text{if } k \in \left(\dfrac{2}{3},\dfrac{4}{3}\right], \\[2mm] 0, & \text{else}. \end{cases} \qquad (3.34)$$

$v(\mathbf{k})$ must be a non-decreasing smooth function with the following properties

$$v(\mathbf{k}) = \begin{cases} 0, & \text{if } k < 0, \\ 1, & \text{if } k > 1, \\ v(k) + v(1-k) = 1, & \text{else}. \end{cases} \qquad (3.35)$$

/ELL 97/ or /CAM 03/ propose the use of spline functions with such properties. With the definition of the so-called mother wavelet Φ, this can be expanded into:

$$\phi_{i,j}(\mathbf{x}) = 2^{\frac{i}{2}}\psi\left(2^i x - j\right), \quad \text{with } i,j = 0,\pm 1,\pm 2,\ldots \qquad (3.36)$$

This set of wavelets is forming an orthonormal basis, a property, which is preserved under the Fourier transform. Hence, a set of functions was found applicable for (3.32):

$$dW(\mathbf{k}) = \sum_{i=-\infty}^{\infty}\sum_{j=-\infty}^{\infty} Z_{i,j}\phi_{i,j}(\mathbf{k})d\mathbf{k}\,. \qquad (3.37)$$

Inserting (3.37) into (3.19) and re-arranging leads to the following representation:

$$u(\mathbf{x}) = \sqrt{2\sigma^2}\sum_{i=-\infty}^{\infty}\sum_{j=-\infty}^{\infty} Z_{i,j}\int_{-\infty}^{\infty} e^{-2\pi kx}\sqrt{E(\mathbf{k})}\,\phi_{i,j}(\mathbf{k})d\mathbf{k} \qquad (3.38)$$

Expression (3.38) is not an approximation of (3.19), but a transformation into a different basis. In order to be used as a numerical algorithm, practical truncations have to be introduced for both sums and a method for the calculation of the Fourier integral.

In order to find an appropriate truncation for the index i, the length scales of $u(\mathbf{x})$ have to be considered, which should be represented. With respect to the single-truncated power-law given by (3.11) and (3.14) as well as the double-truncated power-law given by (3.16) these length scales can be identified with the upper λ_u and lower truncation length λ_ℓ. By virtue of truncating N, the Fourier-Wavelet method provides a very precise

handle for the exact representation of the desired length-scale interval. For the trunca-
tion of the index j, the finite support of the wavelets are used. For the determination of a
single value of the random field $u(\mathbf{x})$ only the $2M$ terms need to be considered, for
which $|j - 2^i x| < M$ holds. For the Fourier-Wavelet method, the finite double sum follows

$$u(\mathbf{x})_{FW} = \sqrt{2\sigma^2} \sum_{i=0}^{N} \sum_{j=1-M}^{M} Z_{i,j} \; c_{i,j}(\mathbf{x}) \text{ with } c_{i,j}(\mathbf{x}) = \mathcal{F}^{-1}\big[\sqrt{E}\Phi_{i,j}\big](\mathbf{x}). \tag{3.39}$$

In order to complete the derivation of the Fourier Wavelet method, a further elaboration
on the functions $c_i(\mathbf{x})$ is needed given by the inverse Fourier transform of $\sqrt{E}\Phi_i$.

3.2.4 Assessing the quality of numerically generated random fields

In order to compare the considered different methods for the numerical generation of
random fields the quality of the generated fields has to be investigated with respect to
several criteria. The criterion for the one-point distribution will be the kurtosis and for
the two-point distribution the variogram is used. Both of these criteria will furthermore
be assessed with respect to a wide interval of decades.

3.2.4.1 Estimating the kurtosis

The kurtosis G_4 is commonly described as a measure for the peakedness or the slope
of the PDF of the random variable. It can be used for assessing the Gaussianity of the
one-point distribution of a random field. The kurtosis is defined as the fourth centralized
moment μ_4 of the random variable X normalised by the square of the variance

$$G_4(X) = \frac{\mu_4(X)}{\sigma^4(X)} \;. \tag{3.40}$$

The kurtosis of a (one-dimensional) random field $u(\mathbf{x})$ with distance h is defined as

$$G_4(h) = \frac{E\big[(u(\mathbf{x}+h) - u(\mathbf{x}))^4\big]}{E\big[(u(\mathbf{x}+h) - u(\mathbf{x}))^2\big]^2} \;. \tag{3.41}$$

A simple method for the estimation of the kurtosis for a given sample of N realisations
$u_n(\mathbf{x})$, is to estimate the second and fourth moment and using the ratio

$$\overline{G}_4(h) = N \frac{\sum_{n=1}^{N} u_n^4(h)}{\left(\sum_{n=1}^{N} u_n^2(h)\right)^2}. \tag{3.42}$$

Since the kurtosis of a Gaussian random variable is always $G_4(X) = 3$, this can be used as a measure for the assessment of the Gaussianity of the random fields.

3.2.4.2 Estimating the variogram

For the assessment of the two-point distribution of the generated random fields, the variogram defined in (3.3) is used. For a given sample of N realisations $u_n(x)$, the variogram can be approximated by

$$\overline{\gamma}(h) = \frac{1}{N} \sum_{n=1}^{N} |u_n(\mathbf{x} + h) - u_n(\mathbf{x})|^2. \tag{3.43}$$

It is clear that, due to the finite resolution of the $u_n(\mathbf{x})$, expression (3.43) can only provide estimates for $\gamma(h)$ on a finite number of points. This is, however, not problematic because the high number of possible permutations between the different points in $u_n(\mathbf{x})$ allows a very fine spatial sampling of h.

3.2.4.3 Estimation of reproduced decades

The generated numerical fields are supposed to exhibit either truncated or double-truncated power-law structures. This means, that the variogram and the kurtosis should be reproduced over a wide range of scales (Fig. 3.3). In order to quantify this statement, the relative error between the expected $\gamma(h)$ and the estimated variogram $\overline{\gamma}(h)$

$$\varepsilon = \frac{|\gamma(h) - \overline{\gamma}(h)|}{\gamma(h)} \tag{3.44}$$

can be used. In order to guarantee that $\overline{\gamma}(h)$ is close to the real variogram of the generated random fields, very high sampling sizes were used (several thousands of realisations). For the derivation of the reproduced number of decades the set h_ε now has to be determined for which the relative error is smaller than a maximally acceptable threshold ε_{max}. Within this study, this threshold was set to 0.1 corresponding to a relative error of 10 %. The set of points, for which the estimated variogram is acceptable, is hence defined as

$$h_\varepsilon = \{h \mid \varepsilon(h) < \varepsilon_{max}\}.\tag{3.45}$$

A contiguous interval Δh has to be determined with the upper boundary of simply $h_{max} = \max_h h_\varepsilon$. The lower boundary h_{min} is defined such that a certain percentage p_h of Δh actually belongs to h_ε (e. g. $p_h = 90\%$). Having determined the boundaries of Δh , the number of reproduced decades d_ε can be computed according to

$$d_\varepsilon = \log_{10} \frac{h_{max}}{h_{min}}.\tag{3.46}$$

This quantity can be used in two different ways, when comparing the different numerical methods: (i) For a single-truncated power-law, the maximum number of reproduced scales (potentially infinite) for a given numerical cost can be measured or (ii) in case of a double-truncated power-law, the minimum numerical cost for the reproduction of a given number of decades can be determined.
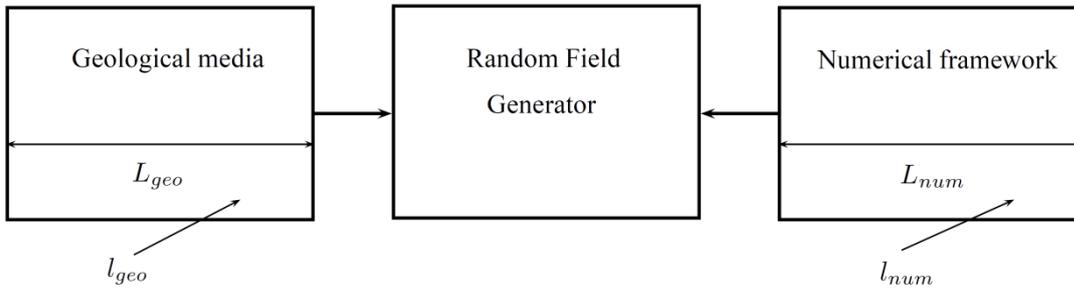
Fig. 3.5   Schematic of the scales influencing the random field generation /HES 13/

It should be noted, that the latter issue involves the numerical framework, too. When deciding on the number of decades, which need to be reproduced by the numerical field generator two different confining frameworks have to be pondered: The geological and the numerical one (Fig. 3.5). As mentioned above, the length scales in any geological medium are confined by the maximum size λ_u (labelled L_{geo} in Fig. 3.5) and the resolution of the medium itself λ_ℓ (ℓ_{geo} in Fig. 3.5). The double-truncated power-law can explicitly account for this fact. In a numerical framework, there are also two confining length scales introduced: the size of the numerical domain (L_{num} in Fig. 3.5) and the minimum grid resolution (ℓ_{num} in Fig. 3.5).

Under regular circumstances, the number of decades that are present in a numerical simulation is rather confined. For a simple finite-difference discretisation, a number of

four decades will result in 10^8 grid points in a 2d system and 10^{12} in a 3-D system. However, with the development of newer techniques this number can be much higher. Such techniques include adaptive grid refinement /TRA 02/ or multi-scale codes /JUT 08/, /NOR 09/.

3.3 Modelling of the effective parameters

In the following, explicit expressions for effective transport parameters in fractal media will be derived, e. g. the effective hydraulic conductivity or effective mixing coefficients. Since the former are already investigated e. g. by /TAR 00/, the focus in this study is on dispersion coefficients which are split in a longitudinal D_{11} and a transverse component D_{22}. As mentioned in section 3.2, randomly distributed heterogeneous fields can be described by the mean value, the variance and the correlation function of the distribution. This correlation function can either be described by a Gaussian function in cases with finite correlation lengths or by an algebraic function in cases where the correlation lengths tend to be infinite. The latter can be characterised by fractal fields, in which the correlation function is described by a power-law /FIO 01/. In the following, it is shown that fractal fields can be reduced to a superposition of Gaussian functions and hence, the results of /DEN 00a/, /DEN 00b/ and /DEN 02/ can be applied.

3.3.1 The transport equation

The temporal behaviour of a mobile solute is given by the standard advection-dispersion equation e. g. in /DAG 89/ or /GEL 93/. The simplified transport model, where only the variations in the flow field are considered, is defined as

$$\frac{\partial}{\partial t} c(\mathbf{x}, t) + \nabla\big(\mathbf{u}(\mathbf{x})c(\mathbf{x}, t)\big) - \nabla \mathbf{D}(\mathbf{x})\nabla c(\mathbf{x}, t) = \rho(\mathbf{x})\delta(t) \tag{3.47}$$

where c [kg m^{-3}] denotes the solute concentration, $\mathbf{u}$ [m s^{-1}] the heterogeneous Darcy velocity, the dispersion tensor is indicated by $\mathbf{D}$ [m² s^{-1}] and the density by ρ [kg m^{-3}] . The right-hand side of this equation gives the initial distribution of the solute

$$c(\mathbf{x}, t = 0) = \rho(\mathbf{x}) \tag{3.48}$$

and a vanishing concentration is assumed as boundary condition. The dispersion tensor $\mathbf{D}$ is assumed to be diagonal in a Cartesian coordinate system and composed of

the molecular diffusion coefficient D_m and the product $\alpha_{ii}|\vec{v}|, i = 1, \dots, d$ of the dispersivities and the absolute velocity $|\vec{v}|$:

$$\mathbf{D} = \begin{pmatrix} D_m + \alpha_{11}|\mathbf{v}| & 0 & 0 \\ 0 & D_m + \alpha_{22}|\mathbf{v}| & 0 \\ 0 & 0 & D_m + \alpha_{33}|\mathbf{v}| \end{pmatrix}. \tag{3.49}$$

The groundwater velocity $\mathbf{v} = \mathbf{u}/\phi$ is given with $\mathbf{u}$ [m s^{-1}] as the Darcy velocity and ϕ [%] as the porosity.

3.3.2   The Darcy equation

According to /BEA 72/, the flow velocity in a saturated macroscopic porous medium is represented by the Darcy equation

$$\mathbf{u}(\mathbf{x}) = -K(\mathbf{x})\nabla h(\mathbf{x}). \tag{3.50}$$

$h(\mathbf{x})$ [m m^{-1}] denotes the hydraulic gradient. Within the stochastic framework, the hydraulic conductivity $K(\mathbf{x})$ [m s^{-1}] is assumed to be a translational invariant random field and from geostatistical investigations it is proposed to be log-normally distributed /FRE 75/, /SUD 86/, /DEN 00a/.

3.3.3   The stochastic approach

The fluctuating Darcy velocity is split into a deterministic and a random contribution

$$\mathbf{u}(\mathbf{x}) = \bar{\mathbf{u}} - \mathbf{u}'(\mathbf{x}), \tag{3.51}$$

where $\bar{\mathbf{u}}$ is the averaged Darcy velocity. The field $\mathbf{u}'(\mathbf{x})$ denotes the fluctuation around the mean value. The corresponding velocity auto-correlation functions are denoted by

$$\overline{u_i'(\mathbf{x})u_j'(\mathbf{x}')} = C_{ij}^{uu}(\mathbf{x} - \mathbf{x}') \tag{3.52}$$

where $u_i'(\mathbf{x})$ is the i-th component of the d-dimensional field $\mathbf{u}'(\mathbf{x}), i = 1, \dots, d$. Without restriction of generality, the mean flow vector $\bar{\mathbf{u}}$ is aligned with the 1-direction of the coordinate system.

3.3.4 Correlation functions for fluctuations with finite and infinite correlation lengths

There are two possibilities to express the correlations of the fluctuations **u'(x)** in a heterogeneous medium: In media with finite correlation lengths, Gauss-shaped functions are an appropriate choice found in the literature (e. g. /DAG 90/, /GEL 93/), whereas in fractal media characterised by infinite correlation lengths algebraic functions are used (e. g. /ZHA 96a/, /NEU 95/, /FIO 01/). According to /DAG 88/, /GEL 93/, /DEN 00a/, the Gauss-shaped correlation functions of the velocity fluctuations $\tilde{\mathbf{f}}'(\mathbf{x})$ have the form:

$$\overline{\tilde{f}'(\mathbf{x})\tilde{f}'(\mathbf{x}')} = C^{ff}(x - x') = \sigma_{ff}^2 \exp\left(-\sum_{i=1}^{d} \frac{(x_i - x'_i)^2}{2\,\ell_i^2}\right). \tag{3.53}$$

The ℓ_i indicate the correlation lengths of the flow field in direction i (with i = 1, …, d in a d-dimensional system) and σ_{ff}^2 is the variance of f'(**x**) /DEN 00a/.

3.3.4.1 Algebraic correlation functions in fractal porous media

According to /BEL 96/, the transport in fractal media is characterised by a heterogeneity of "evolving scales" /SPO 86/. This conceptual approach has been applied by /NEU 95/ and /ZHA 96a/. Since the correlation length is no longer finite, the correlation function has to be adapted accordingly. Quantities, which are related to fractal porous media with infinite correlation lengths, are denoted in the following by a hat.

A possible model for the log-hydraulic conductivity $f = \ln(K)$ is a fractional Gaussian noise (fGn, see /MAN 68/, /MOL 97/).The following isotropic power-law covariance function is adopted:

$$\hat{C}^{ff}(\mathbf{x}) = \sigma_{ff}^2 z^{-\beta}, \quad 0 \le \beta \le 1 \tag{3.54}$$

with the power-law semi-variogram

$$z = \left(1 + \frac{\sum_{i=1}^{d} x_i^2}{\ell^2}\right)^{1/2}. \tag{3.55}$$

x denotes the spatial vector in i directions and ℓ is a physically relevant length scale of the transport problem, for instance the aquifer thickness. Furthermore, there is always a maximum length scale $\ell_{max} < \infty$ while investigating natural formations/ZHA 96a/.

Although geological formations can be separated into a discrete hierarchy of geological units, in the following a continuous hierarchy and infinite ranges of scales are applied (see /NEU 90/). In particular, the summation in (3.55) is replaced by an infinite integral as performed by /PHI 86/ for the Lagrangian correlation function of velocities in the time domain. Such correlation models are often preferred to the exact fGn model (/DAG 94/, /SCU 10/), because their behaviour for large distances with $|\mathbf{x}| / \ell \gg 1$ is similar to that of fGn. In other words, the isotropic correlation function is characterised by a power-law $\hat{C}^{ff}(\mathbf{x}) \sim (|\mathbf{x}| / \ell)^{-\beta}$ that avoids the singularity at $|\mathbf{x}| = 0$.

The exponent β is the same as in /SCU 10/ except of the sign. The model used in this study is equal to $1 + |\mathbf{x}| / \ell$. This corresponds to $-\beta$ in /DAG 94/, /BEL 96/ and /FIO 01/, where β is in the super-diffusion range $0 \le \beta \le 1$. For $1 \le \beta \le 2$ there will be a superposition of sub-diffusion and normal diffusion and for $\beta = 1$ a t ln(t) time behaviour of the ensemble coefficients /SCU 10/. The parameter β is related to the Hurst coefficient as defined in /PEI 88/ and indicates the fractal dimension d_f:

$$d_f = d + 1 - \beta \tag{3.56}$$

with d denoting the Euclidean dimension. Small values of β indicate a larger degree of fractality. A typical range for the value of β is $0 < \beta < 1$ according to /PEI 88/. In order to obtain an appropriate correlation function of the log-hydraulic conductivity field $f(\mathbf{x})$ for fractal media, (3.55) has to be inserted in (7.3). The resulting expression can be redrafted according to /GRA 07/ (p.370, expression 3.478(1.)):

$$
\begin{aligned}
\frac{\hat{C}^{ff}(\mathbf{x})}{\sigma_{ff}^2} = z^{-\beta} &= \frac{2}{\Gamma\left(\frac{\beta}{2}\right)} \int_0^\infty d\lambda\; \lambda^{\beta-1} \exp(-z^2\lambda^2) \\
&= \frac{2}{\Gamma\left(\frac{\beta}{2}\right)} \int_0^\infty d\lambda\; \lambda^{\beta-1} \exp\left[-\left(1 + \frac{\sum_{i=1}^d x_i^2}{\ell^2}\right)\lambda^2\right] \\
&= \frac{2}{\Gamma\left(\frac{\beta}{2}\right)} \int_0^\infty d\lambda\; \lambda^{\beta-1} \exp(-\lambda^2)\exp\left(-\frac{\sum_{i=1}^d x_i^2}{\ell^2}\lambda^2\right) \\
&= \frac{2}{\Gamma\left(\frac{\beta}{2}\right)} \int_0^\infty d\lambda\; \lambda^{\beta-1} \exp(-\lambda^2)\exp\left(-\frac{1}{2}\frac{\sum_{i=1}^d x_i^2}{\frac{1}{2}\frac{\ell^2}{\lambda^2}}\right) \\
&= \frac{2}{\Gamma\left(\frac{\beta}{2}\right)} \int_0^\infty d\lambda\; \lambda^{\beta-1} \exp(-\lambda^2)\exp\left(-\frac{1}{2}\frac{\sum_{i=1}^d x_i^2}{\hat{\ell}^2}\right).
\end{aligned} \tag{3.57}
$$

$\hat{L}$ contains the integration variable λ and represents the new correlation length of the heterogeneities which tends to be infinite. It has the form:

$$\hat{L} = \frac{\ell}{\sqrt{2}\,\lambda} \tag{3.58}$$

Inserting the notation of $\hat{\mathcal{L}}$ in the integral length in x_1-direction gives:

$$\int dx_1 \frac{1}{\left(1 + \frac{x_1^2}{\ell^2}\right)^{\beta/2}} = \frac{2}{\Gamma\left(\frac{\beta}{2}\right)} \int_0^\infty d\lambda\, \lambda^{\beta-1} \exp(-\lambda^2) \int_0^X dx_1 \exp\left(-\lambda^2 \frac{x_1^2}{\ell^2}\right)$$

$$= \frac{2}{\Gamma\left(\frac{\beta}{2}\right)} \int_0^\infty d\lambda\, \lambda^{\beta-1} \exp(-\lambda^2) \frac{\sqrt{\pi}}{2} \frac{\ell}{\lambda} \operatorname{erf}\left(\frac{\lambda X}{\ell}\right). \tag{3.59}$$

Using these notations, the correlation function of $f = \ln(K)$ can be written as a superposition of Gaussian functions. It is now possible to express the dispersion coefficients with power-law correlations of the form (7.3) as linear combinations of the coefficients obtained by /DEN 00a/ for Gaussian correlated fields with finite correlation lengths.

3.4 The methods

For the following steps it has some technical advantages to transform the variables into Fourier space. The Fourier transformed functions are marked by a tilde.

3.4.1 Fourier transforms

The Fourier transform with respect to the spatial variable $\mathbf{x}$ has the form:

$$\tilde{c}(\mathbf{k}, t) = \int d^d\mathbf{x}\, c(\mathbf{x}, t) \exp(i\,\mathbf{k}\cdot\mathbf{x}), \tag{3.60}$$

$$c(\mathbf{x}, t) = \int_{\mathbf{k}} \tilde{c}(\mathbf{k}, t) \exp(-i\,\mathbf{k}\cdot\mathbf{x}). \tag{3.61}$$

$\mathbf{k}$ and $\mathbf{x}$ indicate d-dimensional vectors, and $\mathbf{k}\cdot\mathbf{x}$ is the corresponding scalar product., For the d-dimensional $\mathbf{k}$-integration over the whole space the shorthand notation

$$\int_{\mathbf{k}} \ldots \equiv \int \frac{d^d\mathbf{k}}{(2\pi)^d} \ldots \tag{3.62}$$

is used according to /DEN 00a/. The transport equation (3.47) then has the form

$$\frac{\partial}{\partial t}\tilde{c}(\mathbf{k}, t) + (-i\bar{\mathbf{u}} \cdot \mathbf{k} + \mathbf{k}\mathbf{D}\mathbf{k})\tilde{c}(\mathbf{k}, t)$$
$$= \delta(t)\tilde{\rho}(\mathbf{k}) + \int_{\mathbf{k}'} R'(\mathbf{k}, \mathbf{k}', t)\, \tilde{c}(\mathbf{k} - \mathbf{k}', t) \tag{3.63}$$

with the initial concentration distribution

$$\tilde{\rho}(\mathbf{k}) = \int d^d\mathbf{x}\, \rho(\mathbf{x}) \exp(i\, \mathbf{k} \cdot \mathbf{x})\,. \tag{3.64}$$

The incompressibility condition $\mathbf{k} \cdot \tilde{\mathbf{u}}'(\mathbf{k}) = 0$ is used to write the operator $R'(\mathbf{k}, \mathbf{k}', t)$ as

$$R'(\mathbf{k}, \mathbf{k}', t) \equiv -i\, \mathbf{k} \cdot \tilde{\mathbf{u}}'(\mathbf{k}')\,. \tag{3.65}$$

3.4.2 Fourier-transformed velocity fluctuations

Since there is no closed solution for the equation of the hydraulic head derived from the Darcy equation that reflects all the different boundary conditions, approximative solutions can be constructed by an expansion with respect to the fluctuations of the log-hydraulic conductivity f'($\mathbf{x}$) /DEN 00a/:

$$u_i(\mathbf{x}) = \bar{u}\, \delta_{i1} + \bar{u} \int_{\mathbf{k}} \exp(i\, \mathbf{k} \cdot \mathbf{x})\, p_i(\mathbf{k})\, \tilde{f}'(\mathbf{k})\,. \tag{3.66}$$

According to /DEN 00a/, the functions $p_i(\mathbf{k})$ are projectors which ensure the incompressibility of the flow. In a d-dimensional system ($d \geq 2$) they are defined as:

$$p_i(\mathbf{k}) = \left(\delta_{1i} - \frac{k_1 k_i}{\mathbf{k}^2}\right), \quad i = 1, \dots, d\,. \tag{3.67}$$

According to /ATT 99/, /DEN 00a/ and expression (3.51), the perturbative approximation of the Darcy flow field yields a linear relation between **u(x)** and the fluctuations of the log-hydraulic conductivity f'(**x**). Hence, the flow field **u(x)** is also a stochastically translation invariant Gaussian random field. Therefore, the correlation functions $\tilde{\mathbf{u}}'(\mathbf{k})$ have the form:

$$\overline{\tilde{u}_i'(\mathbf{k})\tilde{u}_j'(\mathbf{k}')} = (2\pi)^d \delta^d(\mathbf{k} + \mathbf{k}')\bar{u}^2 p_i(\mathbf{k})p_j(\mathbf{k})\tilde{C}^{ff}(\mathbf{k})\,. \tag{3.68}$$

The structure of the correlation functions specifies the respective flow model and the delta-function follows from the translation invariance in space.

3.4.3 Dispersion coefficients

The spreading of the solute cloud can be quantified by dispersion coefficients. The available methods include stochastic theory /GEL 83/ and /GEL 86/, spatial moments /DAG 88/, /KIT 88/, /DEN 00a/, /DEN 00b/, /DEN 02/ and homogenisation theory /HEL 05/, /MUS 11b/. In this study, the spatial moments are used and according to /ATT 99/ and /DEN 00a/ two quantities characterising the dispersion are distinguished:

- The **ensemble** dispersion D^{ens} represents the dispersion characteristics of the whole ensemble of aquifer realisations. This quantity generally overestimates the dispersion typically found in one realisation of the medium because it takes into account an artificial mixing effect caused by fluctuations of the centre-of-mass positions of the solute clouds in different realisations of the inhomogeneous medium.

- This effect is suppressed in the **effective** dispersion D^{eff}, derived from the average over the centered second moments of the spatial concentration distributions in every realisation. This quantity characterizes the dispersion in a typical realisation of the medium as a function of time and the characteristic transport properties of the medium fluctuate only weakly around the corresponding ensemble averages. Therefore, this quantity represents indeed "effective" large-scale properties which are characteristic for the single aquifer and are observable experimentally.
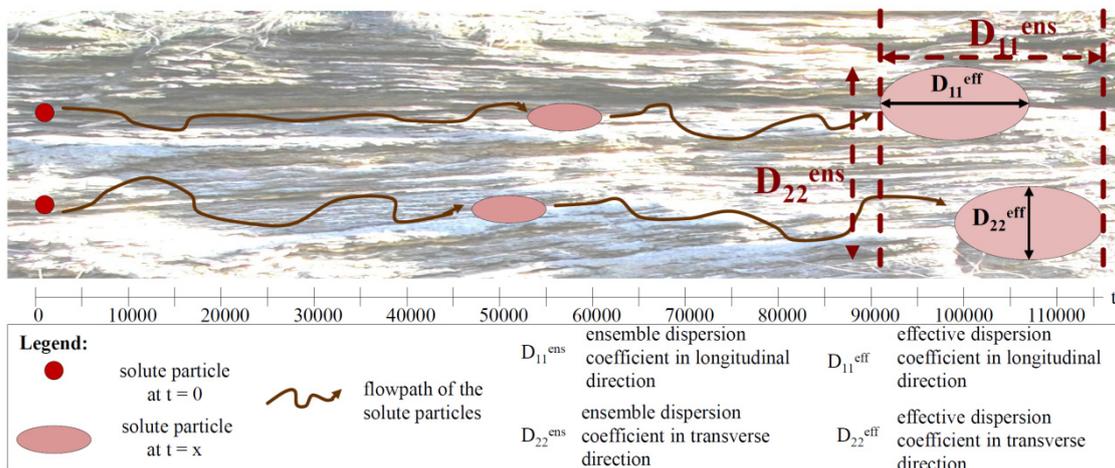
Fig. 3.6 Schematic representation of the ensemble and effective dispersion coefficients

Fig. 3.6 shows the difference between the ensemble and the effective dispersion coefficient schematically and the corresponding legend below the timescale. At the begin-

ning of the injection, a solute cloud consists of single point-like particles which are indicated by the red circles at t = 0. They are moving through the heterogeneous porous and fractured medium and cover with increasing time more and more heterogeneities. These heterogeneities cause the solute particles to spread, therefore the originally point-like particles become more and more the shape of ellipses (indicated in Fig. 3.6 at t = 50 000). With increasing time, these ellipses spread due to more and more heterogeneities which they have covered.

Both quantities are characterised by a longitudinal (named by D_{11}) and a transverse component (D_{22}). The longitudinal component follows the mean-flow direction and is in general larger than the transverse component in the perpendicular direction. In Fig. 3.6 the ensemble quantity is denoted by the dark red dashed arrows around t = 100 000. The longitudinal ensemble dispersion coefficient denotes the whole extension in longitudinal direction which all the single particles cover and the transverse ensemble quantities indicates the extension of all the single particles in transverse direction. On the other hand, the effective dispersion coefficient denotes only the mean extension of the single particles indicated by the black solid arrows within the red ellipses. This quantity is again distinguished in a longitudinal and a transverse component. In the graphs in the results part the ensemble quantities are denoted again by dashed curves, whereas the effective quantities are indicated by solid ones.

The conceptual difference between the two quantities is well known in the literature for quite some time, see e. g. the discussion by /BAT 49/ and /BAT 52/ for the case of diffusion in turbulent flows. The corresponding definitions for static random flow fields are investigated by /KIT 88/, /DAG 90/, /DAG 91/, /RAJ 93a/, /RAJ 93b/, /ZHA 96b/, /ZHA 97/. The two quantities are identical only in the asymptotic limit of infinite times and in media with a finite correlation length of the heterogeneities /MET 99/.

3.4.4   Transport parameters

In uniform flows, the centre-of-mass velocity $u_i(t)$ and dispersion coefficients $D_{ij}(t)$ are given by

$$u_i(t) = \frac{d}{dt} m_i^{(1)}(t) \tag{3.69}$$

$$D_{ij}(t) = \frac{1}{2} \frac{d}{dt} \left\{ m_{ij}^{(2)}(t) - m_i^{(1)}(t) \, m_j^{(1)}(t) \right\} \tag{3.70}$$

where

$$m_i^{(1)}(t) = \int d^d\mathbf{x}\; x_i c(\mathbf{x}, t) \qquad (3.71)$$

$$m_{ij}^{(2)}(t) = \int d^d\mathbf{x}\; x_i\, x_j c(\mathbf{x}, t) \qquad (3.72)$$

are the first two moments of the properly normalised spatial concentration distribution in d dimensions. Corresponding to these equations, the large-scale solute plume now is characterised by

$$u_i^{\text{eff}}(t) = \frac{d}{dt}\overline{m_i^{(1)}(t)}, \qquad (3.73)$$

$$D_{ij}^{\text{eff}}(t) = \frac{1}{2}\frac{d}{dt}\overline{\left\{m_{ij}^{(2)}(t) - m_i^{(1)}(t)\, m_j^{(1)}(t)\right\}}. \qquad (3.74)$$

The over-bar denotes the average over the ensemble of aquifer realisations. The effective dispersion coefficient (3.74) is different from the ensemble dispersion coefficient $D_{ij}^{\text{ens}}(t)$ defined as

$$D_{ij}^{\text{ens}}(t) = \frac{1}{2}\frac{d}{dt}\left\{\overline{m_{ij}^{(2)}(t)} - \overline{m_i^{(1)}(t)\, m_j^{(1)}(t)}\right\}. \qquad (3.75)$$

The ensemble averaged quantities can be expressed with aid of generating functions

$$u_i^{\text{eff}}(t) = \frac{d}{dt}\left(-i\,\partial_{k_i}\right)\overline{\{\ln \tilde{c}(\mathbf{k}, t)\}}|_{\mathbf{k} = 0} \qquad (3.76)$$

$$D_{ij}^{\text{eff}}(t) = \frac{1}{2}\frac{d}{dt}\left(-i\,\partial_{k_i}\right)\left(-i\,\partial_{k_j}\right)\overline{\{\ln \tilde{c}(\mathbf{k}, t)\}}|_{\mathbf{k} = 0} \qquad (3.77)$$

$$D_{ij}^{\text{ens}}(t) = \frac{1}{2}\frac{d}{dt}\left(-i\,\partial_{k_i}\right)\left(-i\,\partial_{k_j}\right)\ln\overline{\{\tilde{c}(\mathbf{k}, t)\}}|_{\mathbf{k} = 0} \qquad (3.78)$$

∂_{k_i} denotes the partial derivative with respect to the $\mathbf{k}$-component in the i-th direction. The difference in these definitions is that for the effective quantities the average is performed over the logarithm of the distribution $\tilde{c}(\mathbf{x}, t)$, whereas for the ensemble quantities first the average is performed over the distribution and afterwards the logarithm is evaluated.

3.4.5   The perturbation theory

In order to solve the transport equation approximately by a second-order perturbation expansion, the transport equation (3.63) is transformed into an equivalent integral expression:

$$\tilde{c}(\mathbf{k}, t) = \tilde{c}_0(\mathbf{k}, t)\tilde{\rho}(\mathbf{k}) - \int_{\mathbf{k}'} \int_{-\infty}^{\infty} dt' \, \tilde{c}_0(\mathbf{k}, t - t') \, R'(\mathbf{k}, \mathbf{k}', t') \, \tilde{c}(\mathbf{k} - \mathbf{k}', t). \qquad (3.79)$$

$\tilde{\rho}(\mathbf{k})$ denotes the Fourier transformation of the initial concentration distribution given in (3.64) and the operator R' is defined in (3.65). The Green-function $\tilde{c}_0(\mathbf{k}, t)$ solves the "unperturbed" problem for the case of a point-like source injection meaning $\tilde{\rho}(\mathbf{k}) = 1$ and $-i\mathbf{k} \cdot \tilde{\mathbf{u}}'(\mathbf{k}') \equiv 0$

$$\tilde{c}_0(\mathbf{k}, t) = \theta(t) \exp(-\mathbf{k}\mathbf{D}\mathbf{k}t + i\bar{u}k_1 t), \qquad (3.80)$$

where $\theta(t)$ is the usual Heaviside-step function. Iterating this equation generates the following series expansion

$$\tilde{c}(\mathbf{k}, t) = \tilde{c}_0(\mathbf{k}, t)\tilde{\rho}(\mathbf{k}) - \int_{\mathbf{k}'} \int_{-\infty}^{\infty} dt' \, \tilde{c}_0(\mathbf{k}, t - t') \, R'(\mathbf{k}, \mathbf{k}', t') \, \tilde{c}_0(\mathbf{k} - \mathbf{k}', t)$$
$$+ \int_{\mathbf{k}'} \int_{\mathbf{k}''} \int_{-\infty}^{\infty} dt' \int_{-\infty}^{\infty} dt'' \, \tilde{c}_0(\mathbf{k}, t - t') \, R'(\mathbf{k}, \mathbf{k}', t') \, \tilde{c}_0(\mathbf{k}$$
$$- \mathbf{k}', t' - t'') \, R'(\mathbf{k} - \mathbf{k}', \mathbf{k}'', t'') \, \tilde{c}_0(\mathbf{k} - \mathbf{k}' - \mathbf{k}'', t'') + \cdots \qquad (3.81)$$

According to /DEN 00a/ this series, truncated after the second order in R' defined in (3.65), is the basis of the given treatment.

3.5   Contributions due to the heterogeneities in the velocity field

The perturbation theory approach of the problem has been investigated in the literature in detail as summarised by /DEN 00a/. The asymptotic long-time values of the ensemble dispersion coefficient in media with Gaussian correlation functions in the limit $t \to \infty$ have been studied e. g. by /GEL 83/ or /DAG 94/. The relevance of the pre-asymptotic behaviour of transport properties is emphasized by /KIT 88/ and /DAG 88/. /DAG 91/ investigated the conceptual difference between ensemble and effective dispersion coefficients using a Lagrangian approach and neglecting the effect of local dispersion corresponding to $D \equiv 0$ in (3.47). The results demonstrate clearly that the two dispersion quantities in general are not equivalent and they get considerably modified when taking

into account the transversal mixing due to the local dispersion. These findings were verified quantitatively by /DEN 00a/ for media with clearly separated scales and they are now extended to fractal media.

3.5.1 The flow situation: Contributions due to the centre-of-mass velocity

Applying the perturbation series as introduced in section 3.4.5 shows, that there are no flow-field-induced disorder contributions to the centre-of-mass velocity (3.73).

$$\delta^{uu}\{u_j^{eff}\}(t) \equiv 0 , \qquad j = 1, \cdots, d. \tag{3.82}$$

This result follows from the incompressibility and the stochastic translation invariance of the fluctuating flow field **u'(x).** It is valid for all orders in the perturbation theory /DEN 97/ and generalises a result by /DAG 84/.

3.5.2 The transport situation: Contributions by the dispersion coefficients

Performing the steps mentioned above, the solute cloud can be characterised by the following integral expressions that contain the contributions due to the dispersion coefficients generated by the heterogeneities in the flow field:

$$\delta^{uu}\{\widehat{D}_{ii}^{ens}\}(t) = \frac{2}{\Gamma\left(\frac{\beta}{2}\right)} \int_0^\infty d\lambda\, \lambda^{\beta-1} \exp(-\lambda^2)$$

$$\cdot \left\{ \bar{u}^2 \int_{\mathbf{k}'>\Lambda} \int_{-\infty}^\infty dt'\, \tilde{c}_0(-\mathbf{k}', t-t')\, p_i(\mathbf{k}')\ p_j(\mathbf{k}')\, \widehat{\widetilde{C}^{ff}}(\mathbf{k}') \right\}, \tag{3.83}$$

$$\delta^{uu}\{\widehat{D}_{ii}^{eff}\}(t) = \delta^{uu}\{\widehat{D}_{ii}^{ens}\}(t) - \frac{2}{\Gamma\left(\frac{\beta}{2}\right)} \int_0^\infty d\lambda\, \lambda^{\beta-1} \exp(-\lambda^2)$$

$$\cdot \left\{ \bar{u}^2 \int_{\mathbf{k}'>\Lambda} \int_{-\infty}^\infty dt'\, \tilde{c}_0(-\mathbf{k}', t) p_i(\mathbf{k}')\ p_j(\mathbf{k}')\, \widehat{\widetilde{C}^{ff}}(\mathbf{k}') \tilde{c}_0(-\mathbf{k}', t') \right\}. \tag{3.84}$$

These quantities are determined by the autocorrelation function $\widehat{\widetilde{C}^{ff}}(\mathbf{k})$ of the velocity fluctuations in fractal porous media defined according to (3.57) as:

$$\widehat{\widetilde{C}^{ff}}(\mathbf{k}) = \frac{2}{\Gamma\left(\frac{\beta}{2}\right)} \int_0^\infty d\lambda\, \lambda^{\beta-1} \exp(-\lambda^2) \left\{ \sigma_{ff}^2 \left(2\pi\, \widehat{L}_1^2\right)^{\frac{d}{2}} \exp\left(-\frac{1}{2}\sum_{i=1}^d k_i^2\, \widehat{L}_i^2\right) \right\}. \tag{3.85}$$

$\hat{L}_1$ denotes the correlation length of the flow field in the mean flow and $\hat{L}_i = \ell_i/(\sqrt{2}\,\lambda)$ are the corresponding transverse ones in the d-1 remaining directions. By substituting $\hat{L}$ in the integral length in x_1-direction according to (3.59), the advective timescale in fractal porous media can be derived:

$$\int dx_1 \frac{1}{\left(1 + \frac{x_1^2}{\ell^2}\right)^{\beta/2}} = \frac{2}{\Gamma\left(\frac{\beta}{2}\right)} \int_0^\infty d\lambda\, \lambda^{\beta-1} \exp(-\lambda^2) \int_0^X dx_1 \exp\left(-\lambda^2 \frac{x_1^2}{\ell^2}\right) \tag{3.86}$$

$$= \frac{2}{\Gamma\left(\frac{\beta}{2}\right)} \int_0^\infty d\lambda\, \lambda^{\beta-1} \exp(-\lambda^2) \frac{\sqrt{\pi}}{2} \frac{\ell}{\lambda} \mathrm{erf}\left(\frac{\lambda X}{\ell}\right)$$

$$= \frac{2}{\Gamma\left(\frac{\beta}{2}\right)} \int_0^\infty d\lambda\, \lambda^{\beta-1} \exp(-\lambda^2) \frac{\sqrt{\pi}}{2} \frac{\ell}{\lambda} \mathrm{erf}\left(\frac{\lambda \bar{u} t}{\ell}\right)$$

$$= \frac{\ell\sqrt{\pi}}{\Gamma\left(\frac{\beta}{2}\right)} \int_0^\infty d\lambda\, \lambda^{\beta-1} \exp(-\lambda^2) \mathrm{erf}\left(\frac{1}{\sqrt{2}} \frac{t}{\hat{\tau}_u}\right).$$

The adapted advective and dispersive timescales according to /ATT 99/ read

$$\hat{\tau}_u = \frac{\ell_1}{\bar{u}\sqrt{2}\,\lambda} = \frac{\hat{L}_1}{\bar{u}} \tag{3.87}$$

$$\hat{\tau}_D^{(1)} = \frac{\ell_1^2}{D_L 2\,\lambda^2} = \frac{\hat{L}_1^2}{D_L} \quad \text{respectively} \quad \hat{\tau}_D^{(i)} = \frac{\ell_i^2}{D_T 2\,\lambda^2} = \frac{\hat{L}_i^2}{D_T}, \quad \text{for } i = 2, \dots, d \tag{3.88}$$

$$\hat{\epsilon}_i = \frac{\hat{\tau}_u}{\hat{\tau}_D^{(i)}} = \frac{D_{ii}}{\bar{u}} \frac{\hat{L}_1}{\hat{L}_i} \frac{1}{\hat{L}_i} = \frac{1}{Pe}, \quad \text{for } i = 2, \dots, d. \tag{3.89}$$

The physical interpretation of these characteristic timescales is: Within the advective timescale τ_u the solute is transported advectively over the distance of one longitudinal disorder correlation length. During the dispersive scale $\hat{\tau}_D^{(i)}$ the solute spreads – induced by the local dispersion D – over a distance of the corresponding correlation length. In fractal media characterised by infinite correlation lengths, the flowpaths of the solute particles are very long due to the tiny fissures which build up a branched network of connected pathways. Accordingly, the travel times of the solute particles are also very long. The ratio $\hat{\epsilon}_i$ between the two timescales defines the inverse Peclet number as given in (3.89). For a realistic aquifer situation, the two timescales are expected to be well separated meaning $\hat{\tau}_D \gg \hat{\tau}_u$ according to /GEL 83/. In other words, the dispersive timescale is much larger than the advective one resulting in a small in-

verse Peclet number $\frac{1}{\mathrm{Pe}} \ll 1$. In porous media, this is the case e. g. in situations with a small local dispersion $\mathrm{D} \approx 0.01 \frac{\mathrm{m^2}}{\mathrm{d}}$. Since the focus of this study is on groundwater aquifers, the usual scale is m² / d. The local dispersion D represents the physical mechanism that causes the solute to spread and is given in (3.49).

By inserting (3.80) and rescaling the time integrations by τ_u and the k_j-integrations by the correlation lengths $\widehat{L}_i = \ell_i/(\sqrt{2}\,\lambda)$, the expressions for the dispersion coefficients (3.83) and (3.84) can be rewritten in the form accoding to /DEN 00a/:

$$\delta^{uu}\{\widehat{D}_{ii}^{ens}\}(t) = \frac{2}{\Gamma\left(\frac{\beta}{2}\right)} \int_0^\infty d\lambda\, \lambda^{\beta-1} \exp(-\lambda^2) \left\{\bar{u}\, \widehat{L}_1 \widehat{M}_i^- \left(\frac{t}{\widehat{\tau}_u}, 0, 0\right)\right\}, \tag{3.90}$$

$$\delta^{uu}\{\widehat{D}_{ii}^{eff}\}(t) = \delta^{uu}\{\widehat{D}_{ii}^{ens}\}(t)$$

$$- \frac{2}{\Gamma\left(\frac{\beta}{2}\right)} \int_0^\infty d\lambda\, \lambda^{\beta-1} \exp(-\lambda^2) \left\{\bar{u}\, \widehat{L}_1 \widehat{M}_i^+ \left(\frac{t}{\widehat{\tau}_u}, \widehat{b}_1 ..., \widehat{b}_d\right)\right\} \tag{3.91}$$

with the auxiliary functions $\widehat{M}_i^\pm$ according to /DEN 00a/ in a d-dimensional system:

$$\widehat{M}_i^\pm \left(\frac{t}{\widehat{\tau}_u}, \widehat{b}_1 ..., \widehat{b}_d\right)$$

$$= \left(\prod_{i=1}^d \frac{1}{\widehat{L}_i}\right) \int_{\mathbf{k}} \int_0^T dt \exp\left(-\sum_{i=1}^d k_i^2 \,\widehat{b}_i\right)$$

$$\cdot \exp\left(\sum_{i=1}^d \widehat{\epsilon}_i k_i^2 t - i k_1 t\right) \left(\delta_{1i} - \frac{k_1 k_i}{\mathbf{k}^2}\right)^2 \widehat{\widetilde{C}}^{ff}(\mathbf{k}) \tag{3.92}$$

with $\widehat{\widetilde{C}}^{ff}(\mathbf{k})$ defined in (3.85), $\widehat{\epsilon}_i$ in (3.89) and

$$\widehat{b}_i = \frac{2t}{\widehat{\tau}_D^{(i)}}, \qquad \text{for} \qquad i = 1, ..., d. \tag{3.93}$$

3.6   Results for transport coefficients in fractal porous media

The results are presented for the simplified case of a model with isotropic disorder correlation functions ($\widehat{L}_1 = \widehat{L}_2 = \cdots = \widehat{L}_d \equiv \widehat{L}$) and an isotropic dispersion tensor ($D_L = D_T \equiv D$). In this case, the complicated perturbation theory expressions for the disper-

sion coefficients can be evaluated explicitly with a computer algebra software like MAPLE as demonstrated by /DEN 00a/. The integrations are performed using the formulae given by /ABS 84/ and /GRA 07/. The influence on the dispersion coefficients due to variations in the different physical variables was also studied. Since in groundwater aquifers which are considered in this study, the typical groundwater velocity is in metre per day, the results are presented in this units and all the expressions are evaluated with a mean groundwater velocity of $\bar{u} = 1\frac{m}{d}$.

Nearly all geologic formations at the regional scale consist of horizontal dimensions which are much larger than the aquifer thickness. For a realistic description, they should be modelled by an anisotropic model containing infinite correlation lengths of the heterogeneities in the horizontal direction, but finite ones in the vertical direction. Situations which correspond to the simplified isotropic model – which is presented in this study – can be found in three-dimensional geologic formations in deep layers where the considered horizons may have thicknesses up to several hectometers as discussed e. g. in /BRU 06/. These layers are of utmost interest e. g. in modelling storage investigations in deep formations.

In the following, the results for the transport coefficients in fractal porous media are presented in which single fractures are neglected. Such a situation can be modelled with a continuum approach using an equidistant grid. The coefficients are evaluated for both the ensemble and effective coefficients according to /ATT 99/ and /DEN 00a/ and both quantities are distinguished between the longitudinal and the transverse component. The situation with embedded large fractures is presented in chapter 1.

3.6.1 General explicit expressions for the dispersion coefficients

Combing (3.90) to (3.92) with (3.57), the explicit expressions for the dispersion coefficients in fractal porous media can be derived:

$$\delta^{uu}\{\widehat{\mathcal{D}}_{ii}^{ens}\}(t) = \frac{2}{\Gamma\left(\frac{\beta}{2}\right)} \int_0^\infty d\lambda \ \lambda^{\beta-1} \exp(-\lambda^2)\{\bar{u} \ \widehat{L}_1 \widehat{\mathcal{M}}_i^-(\widehat{T}, 0, 0)\} \tag{3.94}$$

$$\begin{aligned}
\delta^{uu}\{\widehat{\mathcal{D}}_{ii}^{eff}\}(t) \\
&= \delta^{uu}\{\widehat{\mathcal{D}}_{ii}^{ens}\}(t) \\
&\quad - \frac{2}{\Gamma\left(\frac{\beta}{2}\right)} \int_0^\infty d\lambda \ \lambda^{\beta-1} \exp(-\lambda^2)\{\bar{u} \ \widehat{L}_1 \widehat{\mathcal{M}}_i^+(\widehat{T}, \widehat{b}, \widehat{b})\}
\end{aligned} \tag{3.95}$$

with

$$\widehat{T} = \frac{t}{\widehat{\tau}_u} = \frac{t \, \bar{u} \, \sqrt{2} \, \lambda}{\ell} = \frac{t \, \bar{u}}{\widehat{L}}; \qquad \widehat{b} = \frac{4 \, t \, \lambda^2 \, D}{L^2} = \frac{2 \, t}{\widehat{\tau}_D}. \tag{3.96}$$

In the ensemble quantities, the parameter $\widehat{b}$ vanishes. In order to obtain the explicit expressions for the effective coefficients in fractal media, the same method as used by /DEN 00a/, /DEN 00b/ and /DEN 02/ for the dispersion coefficients in media with finite correlation lengths is applied, that means a contribution owing to the dispersive timescale is subtracted from the corresponding ensemble quantities. The auxiliary functions in a three-dimensional system in isotropic fractal media are defined as:

$$\begin{aligned}
\widehat{\mathcal{M}}_1^\pm(\widehat{T}, \widehat{b}, \widehat{b}) = \mp\sigma_{ff}^2 &\sqrt{\frac{\pi}{2}} \frac{1}{(1 + 2\widehat{b})^2} \Bigg\{ \mathrm{erf}\left(g(\mp\widehat{T})\right) \\
&+ \frac{1}{\sqrt{\pi}} \exp\left(-g^2(\mp\widehat{T})\right) \left[\frac{1}{g(\mp\widehat{T})} + \frac{4\widehat{\varphi}^2 w(\widehat{T})}{g^2(\mp\widehat{T})} - \frac{3}{2g^3(\mp\widehat{T})}\right] \\
&+ \mathrm{erf}\left(g(\mp\widehat{T})\right) \left[\frac{4\widehat{\varphi}^2 w(\widehat{T})}{g(\mp\widehat{T})} + \frac{8\widehat{\varphi}^4 w(\widehat{T})}{g(\mp\widehat{T})} - \frac{1}{g^2(\mp\widehat{T})} - \frac{2\widehat{\varphi}^2 w(\widehat{T})}{g^3(\mp\widehat{T})}\right. \\
&+ \left.\frac{3}{4g^4(\mp\widehat{T})}\right] - 8\widehat{\varphi}^4 \exp\left(\frac{1}{2\widehat{\varphi}^2}\right) \left[\mathrm{erfc}\left(\frac{1}{\sqrt{2}\widehat{\varphi}}\right) - \mathrm{erfc}\left(w(\widehat{T})\right)\right] \\
&- \frac{4\sqrt{8}}{3\sqrt{\pi}} \widehat{\varphi} - \frac{4\sqrt{8}}{\sqrt{\pi}} \widehat{\varphi}^3 \Bigg\}
\end{aligned} \tag{3.97}$$

$$\widehat{\mathcal{M}}_2^{\pm}(\hat{T}, \hat{b}, \hat{b}) = \widehat{\mathcal{M}}_3^{\pm}(\hat{T}, \hat{b}, \hat{b}) \tag{3.98}$$

$$= \mp \sigma_{ff}^2 \sqrt{\frac{\pi}{8}} \frac{1}{(1 + 2\hat{b})^2} \left\{ \frac{1}{2\sqrt{\pi}} \exp\left(-g^2(\mp\hat{T})\right) \right.$$

$$\cdot \left[-\frac{8\hat{\varphi}^2 w(\hat{T})}{g^2(\mp\hat{T})} + \frac{3}{g^3(\mp\hat{T})} \right]$$

$$+ \operatorname{erf}\left(g(\mp\hat{T})\right) \left[-\frac{2\hat{\varphi}^2 w(\hat{T})}{g(\mp\hat{T})} - \frac{8\hat{\varphi}^4 w(\hat{T})}{g(\mp\hat{T})} + \frac{1}{2g^2(\mp\hat{T})} \right.$$

$$\left. -\frac{2\hat{\varphi}^2 w(\hat{T})}{g^3(\mp\hat{T})} - \frac{3}{4g^4(\mp\hat{T})} \right]$$

$$- (8\hat{\varphi}^4 - 2\hat{\varphi}^2) \exp\left(\frac{1}{2\hat{\varphi}^2}\right) \left[\operatorname{erfc}\left(w(\hat{T})\right) - \operatorname{erfc}\left(\frac{1}{\sqrt{2}\hat{\varphi}}\right) \right]$$

$$\left. + \frac{\sqrt{8}}{3\sqrt{\pi}} \hat{\varphi} + \frac{4\sqrt{8}}{\sqrt{\pi}} \hat{\varphi}^3 \right\}$$

with σ_{ff}^2 denoting the variance of the log-hydraulic conductivity and

$$w(\hat{T}) = \frac{1}{\sqrt{2}} \frac{(1 + 2\hat{b})\frac{1}{\hat{\epsilon}} + \frac{t}{\hat{\tau}_u}}{\sqrt{1 + 2\hat{b} + \frac{2t}{\hat{\tau}_D}}}; \quad g(\mp\hat{T}) = \frac{1}{\sqrt{2}} \frac{\mp\frac{t}{\hat{\tau}_u}}{\sqrt{1 + 2\hat{b} + \frac{2t}{\hat{\tau}_D}}}; \quad \hat{\varphi} = \frac{\hat{\epsilon}}{\sqrt{1 + 2\hat{b}}}. \tag{3.99}$$

The advective timescale $\hat{\tau}_u$ is given in (3.87), the dispersive timescale $\hat{\tau}_D$ in (3.88), $\hat{\epsilon}$ in (3.89) and $\hat{b}$ in (3.96). In order to reproduce the results of /DEN 00a/ and /DEN 02/, two slight changes in the auxiliary functions $\widehat{\mathcal{M}}_1^+(\hat{T}, \hat{b}, \hat{b})$ and $\widehat{\mathcal{M}}_2^+(\hat{T}, \hat{b}, \hat{b})$ had to be done:

- The sign of $w(\hat{T})$ had to be changed (instead of $w(-\hat{T})$) to ensure that the erfc-terms vanish for large times $t \gg \hat{\tau}_D$ and

- The exponent in the pre-coefficient $(1 + 2\hat{b})^{-2}$ had to be set to " - 2" (instead of " - 1") to make sure that the effective quantities do not reach the asymptotic limit too early for various values of the local dispersion coefficient D.

3.6.2 The longitudinal ensemble dispersion coefficient

The explicit expression of the longitudinal ensemble dispersion coefficient reads:

$$\delta^{uu}\{\widehat{\mathcal{D}}_{11}^{ens}\}(t) = \frac{2}{\Gamma\left(\frac{\beta}{2}\right)} \int\limits_0^\infty d\lambda \; \lambda^{\beta-1} \exp(-\lambda^2)\{\bar{u} \; \widehat{L} \; \widehat{\mathcal{M}}_1^-(\widehat{T}, 0, 0)\} \tag{3.100}$$

with $\widehat{\mathcal{M}}_1^-$ as defined in (3.97).

Hypothetical situation with no local dispersion in $\delta^{uu}\{\widehat{\mathcal{D}}_{11}^{ens}\}(t)$

In the hypothetical situation with no local dispersion at all (D = 0), the value of the dispersive timescale $\hat{\tau}_D$ vanishes and thus the inverse Peclet number ($\hat{\epsilon} = 0$) because there is no physical mechanism which causes the plume to spread. In such a situation, the solute is transported only advectively within the groundwater flow and the longitudinal component of the ensemble dispersion coefficient reduces to:

$$\delta^{uu}\{\widehat{\mathcal{D}}_{11}^{ens}\}(t)|_{D=0} = \frac{2}{\Gamma\left(\frac{\beta}{2}\right)} \int\limits_0^\infty d\lambda \; \lambda^{\beta-1} \exp(-\lambda^2) \left\{ \bar{u} \; \widehat{L} \; \sigma_{ff}^2 \sqrt{\frac{\pi}{2}} \left[\left(1 - A^2 \right.\right.\right.$$
$$\left.\left.\left. + \frac{3}{4}A^4\right) \text{erf}\left(\frac{1}{A}\right) + \frac{1}{\sqrt{\pi}}\left(A - \frac{3}{2}A^3\right) \exp\left(-\frac{1}{A^2}\right) \right] \right\} \tag{3.101}$$

with A denoting a function relating to the advective time

$$A = \frac{\bar{u} \, \lambda \, t}{\ell}. \tag{3.102}$$

Situation for infinite times $t \to \infty$ in $\delta^{uu}\{\widehat{\mathcal{D}}_{11}^{ens}\}(t)$

With increasing time, the longitudinal ensemble dispersion coefficient increases as well and there is no constant long-time value as it is the case in heterogeneous media with finite correlation lengths. The divergence of the longitudinal ensemble component in fractal media can be explained with the fact that the correlation length $\widehat{L}$ given in (3.58), which tends to be infinite, is the dominating parameter in this quantity. Furthermore, the temporal behaviour of the longitudinal ensemble dispersion coefficient can be described by a power-law:

$$\delta^{uu}\{\widehat{\mathcal{D}}_{11}^{ens}\}(t) = c \cdot t^{1-\beta} \tag{3.103}$$

with an appropriately chosen constant c. This is the same result as found by /FIO 01/ with the difference that in the model applied in this study the projector defined in (3.67) is taken into account. This function ensures that the flow field is represented by an in-

compressible random Gaussian field. As shown by /DEN 03/, in such a field there is a finite probability for closed streamlines which influence the transport behaviour. In the hypothetical case with no local dispersion, the longitudinal spreading is characterised by a longitudinal dispersion coefficient which grows linearly with increasing time. If the projector is neglected, this behaviour cannot be detected because of numerical inaccuracies. In such a flow field, the investigation of transport points out the importance of an exact numerical description of the streamlines in order to properly represent the effect on the transport behaviour in advection-dominated situations /DEN 03/. In fractal media, the effect of the projector is even stronger, especially in the ensemble quantities.

3.6.3 The longitudinal effective dispersion coefficient

The explicit expression of the longitudinal effective dispersion coefficient has the form:

$$\delta^{uu}\{\widehat{\mathcal{D}}_{11}^{eff}\}(t) = \delta^{uu}\{\widehat{\mathcal{D}}_{11}^{ens}\}(t) - \frac{2}{\Gamma\left(\frac{\beta}{2}\right)} \int\limits_{0}^{\infty} d\lambda\, \lambda^{\beta-1} \exp(-\lambda^2)\{\bar{u}\,\hat{L}\,\widehat{\mathcal{M}}_1^+(\widehat{T}, \hat{b}, \hat{b})\}$$ (3.104)

with $\delta^{uu}\{\widehat{\mathcal{D}}_{11}^{ens}\}(t)$ defined in (3.100) and $\widehat{\mathcal{M}}_1^+$ in (3.97).

Hypothetical situation with no local dispersion in $\delta^{uu}\{\widehat{\mathcal{D}}_{11}^{eff}\}(t)$

In the hypothetical situation with no local dispersion (D = 0 and hence $\hat{\epsilon}$ = 0), the longitudinal effective dispersion coefficient vanishes, because there is no physical mechanism which causes the spreading of the solute. This is the same result as in media with finite correlation lengths. It can be seen that the local dispersion is the dominant factor of the effective quantities. It is contained in the quantity $\hat{b}$ given in (3.96) which occurs in each of the terms $w(\widehat{T})$, $g(-\widehat{T})$ and $\hat{\varphi}$ defined in (3.99).

Results for the limiting case of small but finite inverse Peclet numbers $\hat{\epsilon} \ll 1$

The longitudinal effective dispersion coefficient has the following form containing only first-order contributions for $t \gg \hat{\tau}_u$ and a small inverse Peclet number $\hat{\epsilon} = D/\bar{u}\,\hat{L} \ll 1$

$$
\begin{aligned}
\delta^{uu}\{\widehat{\mathcal{D}}_{11}^{\text{eff}}\}(t) &= \frac{2}{\Gamma\left(\frac{\beta}{2}\right)} \int_0^\infty d\lambda\, \lambda^{\beta-1} \exp(-\lambda^2) \left\{ \bar{u}\,\hat{L}\,\sigma_{ff}^2 \sqrt{\frac{\pi}{2}} \left[1 - \frac{1}{\left(1 + \frac{8tD\lambda^2}{L^2}\right)^2} \right] \right\} \\
&= \frac{2}{\Gamma\left(\frac{\beta}{2}\right)} \int_0^\infty d\lambda\, \lambda^{\beta-1} \exp(-\lambda^2) \left\{ \bar{u}\,\hat{L}\,\sigma_{ff}^2 \sqrt{\frac{\pi}{2}} \left[1 - \frac{1}{(1 + 2\hat{b})^2} \right] \right\}
\end{aligned}
\tag{3.105}
$$

Equation (3.104) is a proof for the change of the exponent in the pre-coefficient of the effective expressions as described after (3.99).

Situation for infinite times $t \to \infty$ in $\boldsymbol{\delta^{uu}\{\widehat{\mathcal{D}}_{11}^{\text{eff}}\}(t)}$

For infinite times the longitudinal effective dispersion coefficient increases as well. The coefficient is characterised by the power-law:

$$
\delta^{uu}\{\widehat{\mathcal{D}}_{11}^{\text{eff}}\}(t) = c \cdot t^{\frac{1-\beta}{2}}
\tag{3.106}
$$

with an appropriately chosen constant pre-coefficient c. This result is the same as found by /FIO 01/.

3.6.4 Temporal behaviour of the longitudinal components D_{11}

Fig. 3.7 shows the temporal behaviour of the longitudinal ensemble and effective dispersion coefficient given in (3.100) and (3.104) for different degrees of fractality and a local dispersion D = 0.01 m² / d. It is emphasized, that the scale of the ordinate in media with a high degree of fractality (Fig. 3.7 a) is two orders of magnitude larger than in weakly fractal media (Fig. 3.7 b). It is visible, that the dispersion values are larger for high degrees of fractality. Furthermore, the ensemble coefficient is larger than the effective at any value of β at all times, this implies that the longitudinal ensemble dispersion overestimates the true dispersion. Therefore, the longitudinal effective quantity should be applied in order to give a more realistic description of the transport situation.

A closer look at the effective longitudinal dispersion coefficient (Fig. 3.8) indicates that the quantities are larger in media with a high degree of fractality (Fig. 3.8 a) than in weakly fractal media (Fig. 3.8 b) and increase with a higher degree of fractality.

a) $\widehat{\mathcal{D}}_{11}$ for $0 < \beta < 1$ b) $\widehat{\mathcal{D}}_{11}$ for $1 < \beta < 2$
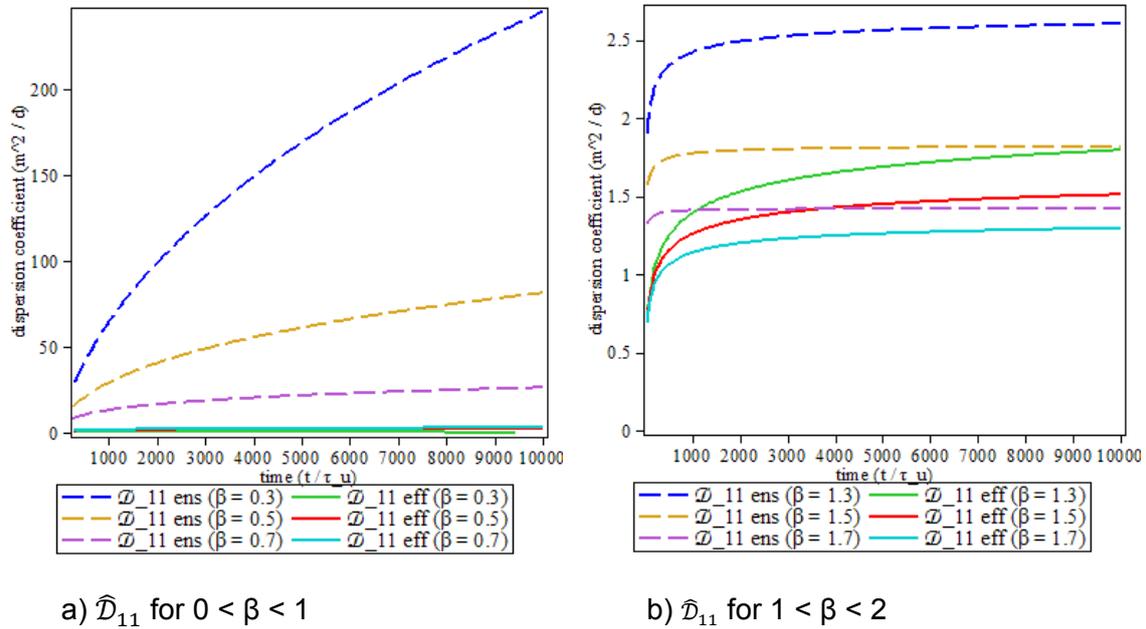
Fig. 3.7   The longitudinal ensemble and effective dispersion coefficients in fractal media

In media with a finite correlation length, the ensemble and effective quantities reach the same asymptotic limit for infinite times as shown in Fig. 3.11 a and found /DEN 00a/ and /DEN 02/. However, such an ergodic situation cannot be found in fractal media because the quantities are characterised by different power-laws $\delta^{uu}\{\widehat{\mathcal{D}}_{11}^{ens}\}(t) = c \cdot t^{1-\beta}$ and $\delta^{uu}\{\widehat{\mathcal{D}}_{11}^{eff}\}(t) = c \cdot t^{\frac{1-\beta}{2}}$, a result already found by /FIO 01/.. This implies, that both quantities indeed describe two fundamentally different properties.
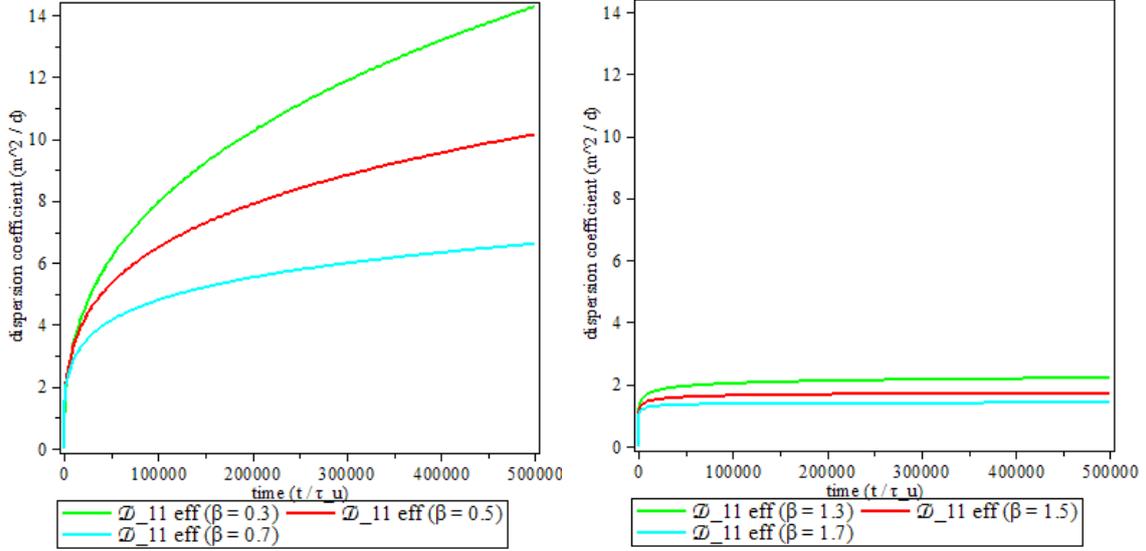
a) $\widehat{\mathcal{D}}_{11}^{eff}$ for $0 < \beta < 1$ b) $\widehat{\mathcal{D}}_{11}^{eff}$ for $1 < \beta < 2$

Fig. 3.8   The longitudinal effective dispersion coefficient in fractal media

3.6.5   The transverse ensemble dispersion coefficient

The transverse ensemble dispersion coefficient in fractal media reads

$$\delta^{uu}\{\widehat{\mathcal{D}}_{22}^{ens}\}(t) = \frac{2}{\Gamma\left(\frac{\beta}{2}\right)} \int_0^\infty d\lambda \ \lambda^{\beta-1} \exp(-\lambda^2)\{\bar{u} \ \hat{L} \ \widehat{\mathcal{M}}_2^-(\widehat{T}, 0, 0)\} \tag{3.107}$$

with $\widehat{\mathcal{M}}_2^-$ as defined in (3.98).

Hypothetical situation with no local dispersion in $\delta^{uu}\{\widehat{\mathcal{D}}_{22}^{ens}\}(t)$

In the hypothetical situation with no local dispersion (D = 0 and $\hat{\epsilon} = 0$), the transverse ensemble quantity reduces to the following expression with A as defined in (3.101):

$$\delta^{uu}\{\widehat{\mathcal{D}}_{22}^{ens}\}(t)|_{D=0} = \frac{2}{\Gamma\left(\frac{\beta}{2}\right)} \int_0^\infty d\lambda \ \lambda^{\beta-1} \exp(-\lambda^2)\left\{\bar{u} \ \hat{L} \ \sigma_{ff}^2 \sqrt{\frac{\pi}{8}} \right. \tag{3.108}$$

$$\left. \cdot \left[\frac{1}{2\sqrt{\pi}} \exp\left(-\frac{1}{A^2}\right) \cdot 3A^3 + erf\left(\frac{1}{A}\right)\left(A^2 - \frac{3}{4}A^4\right)\right]\right\}.$$

54

Situation for infinite times $t \to \infty$ in $\delta^{uu}\{\widehat{\mathcal{D}}_{22}^{ens}\}(t)$

With increasing time, the transverse ensemble dispersion coefficient reaches a constant long-time value defined as:

$$\lim_{t \to \infty} \delta^{uu}\{\widehat{\mathcal{D}}_{22}^{ens}\}(t) = \frac{2}{\Gamma\left(\frac{\beta}{2}\right)} \int_0^\infty d\lambda \; \lambda^{\beta-1} \exp(-\lambda^2) \left\{ \overline{u} \; \widehat{L} \; \sigma_{ff}^2 \sqrt{\frac{\pi}{2}} \right. \tag{3.109}$$

$$\cdot \left[\frac{2}{3\sqrt{\pi}} B - 2\,B^2 + \frac{16}{\sqrt{\pi}} B^3 - 16\,B^4 \right.$$

$$\left. \left. + \exp\left(\frac{1}{4B^2}\right) \operatorname{erfc}\left(\frac{1}{2B}\right) \left(16B^4 - 2B^2\right) \right] \right\} d\lambda$$

with B defining a function related to the dispersive time

$$B = \frac{D\,\lambda}{\ell\,\overline{u}}. \tag{3.110}$$

3.6.6   The transverse effective dispersion coefficient

The expression of the transverse effective dispersion coefficient has the form:

$$\delta^{uu}\{\widehat{\mathcal{D}}_{22}^{eff}\}(t) = \delta^{uu}\{\widehat{\mathcal{D}}_{22}^{ens}\}(t) - \frac{2}{\Gamma\left(\frac{\beta}{2}\right)} \int_0^\infty d\lambda \; \lambda^{\beta-1} \exp(-\lambda^2) \{ \overline{u} \; \widehat{L} \; \widehat{\mathcal{M}}_2^+(\widehat{T}, \widehat{b}, \widehat{b}) \} \tag{3.111}$$

with $\delta^{uu}\{\widehat{\mathcal{D}}_{22}^{ens}\}(t)$ defined in (3.107) and $\widehat{\mathcal{M}}_2^+$ in (3.98).

Hypothetical situation with no local dispersion in $\delta^{uu}\{\widehat{\mathcal{D}}_{22}^{eff}\}(t)$

The transverse effective quantity shows the characteristic vanishing temporal behaviour in the hypothetical situation with no local dispersion ($D = 0$ and $\hat{\epsilon} = 0$). This result is enforced by the vanishing parameter $\widehat{b}$ given in (3.96) that occurs in the terms $w(\widehat{T})$, $g(-\widehat{T})$ and $\widehat{\varphi}$ defined in (3.99).

Situation for infinite times $t \to \infty$ in $\delta^{uu}\{\widehat{\mathcal{D}}_{22}^{eff}\}(t)$

With increasing time, the transverse effective dispersion reaches a constant long-time value which depends on the local dispersion D. It is the same value as for the ensem-

ble quantity given in (3.108) implying that the transverse dispersion coefficients in fractal media show an ergodic behaviour:

$$\delta^{uu}\{\widehat{D}_{22}^{\infty}\}(t) \equiv \lim_{t\to\infty} \delta^{uu}\{\widehat{D}_{22}^{ens}\}(t) = \lim_{t\to\infty} \delta^{uu}\{\widehat{D}_{22}^{eff}\}(t) \ . \tag{3.112}$$

3.6.7 Temporal behaviour of the transverse components D_{22}

In the transverse ensemble component, the not divergent flow field is the dominating factor. Therefore, there is a peak for small times, whereas for large times the dispersion drops down to a certain constant long-time value which depends on the local dispersion. This is the same finding as for media with finite correlation lengths (/DEN 02/, Fig. 3.10 b), but on a much larger timescale. The transverse effective dispersion coefficient slightly increases with time and reaches for infinite times the same constant long-time value as the transverse ensemble component. This finding is given in (3.111).

Fig. 3.8 shows the temporal evolutions of the transverse ensemble and effective coefficients in fractal media for small (Fig. 3.8 a) and large (Fig. 3.8 b) values of β and D = 0.01 m² / d. The difference between the transverse components vanishes for large times and the two quantities reach the same constant long-time value. It is reached at much larger times in more fractal media denoted by a small β. Both components show an ergodic behaviour. This temporal behaviour is similar to that of the transverse component (Fig. 3.10 b) in media with finite correlation lengths /DEN 02/, but again with a remarkable difference in the timescales. In fractal media, the constant long-time value is reached at a timescale that is several orders of magnitude larger. This implies, that the natural attenuation of a solute cloud in a highly fractured medium is delayed due to more complex and branched pathways of the solute particles. The plume remains much longer in the considered medium than in media with finite correlation lengths.

a) $\widehat{\mathcal{D}}_{22}$ for $0 < \beta < 1$

b) $\widehat{\mathcal{D}}_{22}$ for $1 < \beta < 2$
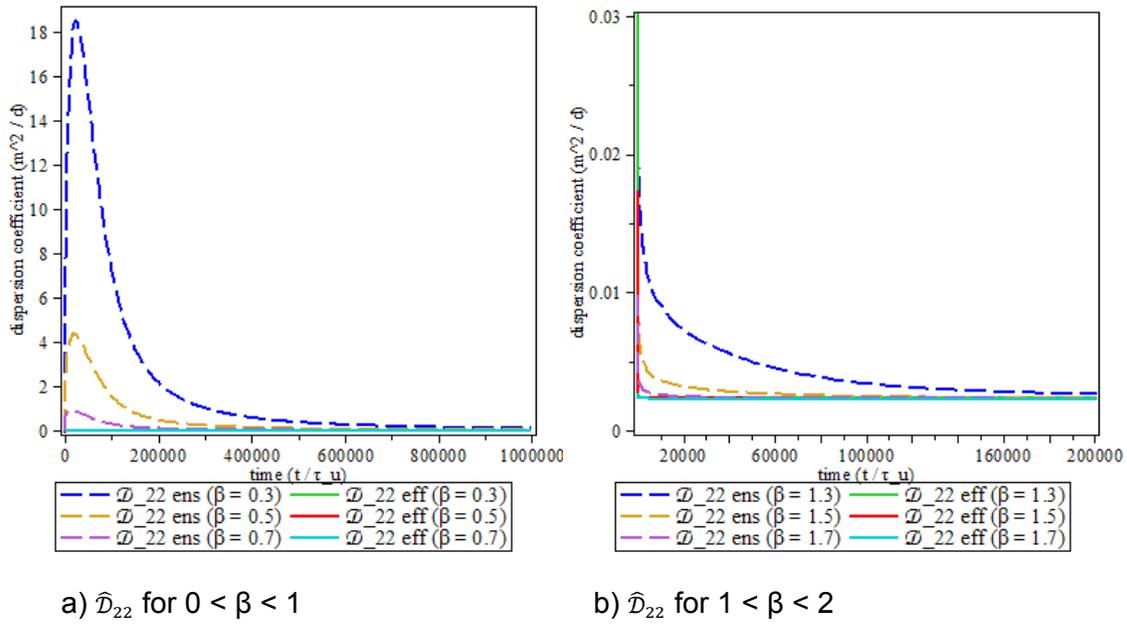
Fig. 3.9 The asymptotic behaviour of the transverse components $\widehat{\mathcal{D}}_{22}$ in fractal media

a) $\widehat{\mathcal{D}}_{22}^{\mathrm{eff}}$ for $0 < \beta < 1$

b) $\widehat{\mathcal{D}}_{22}^{\mathrm{eff}}$ for $1 < \beta < 2$
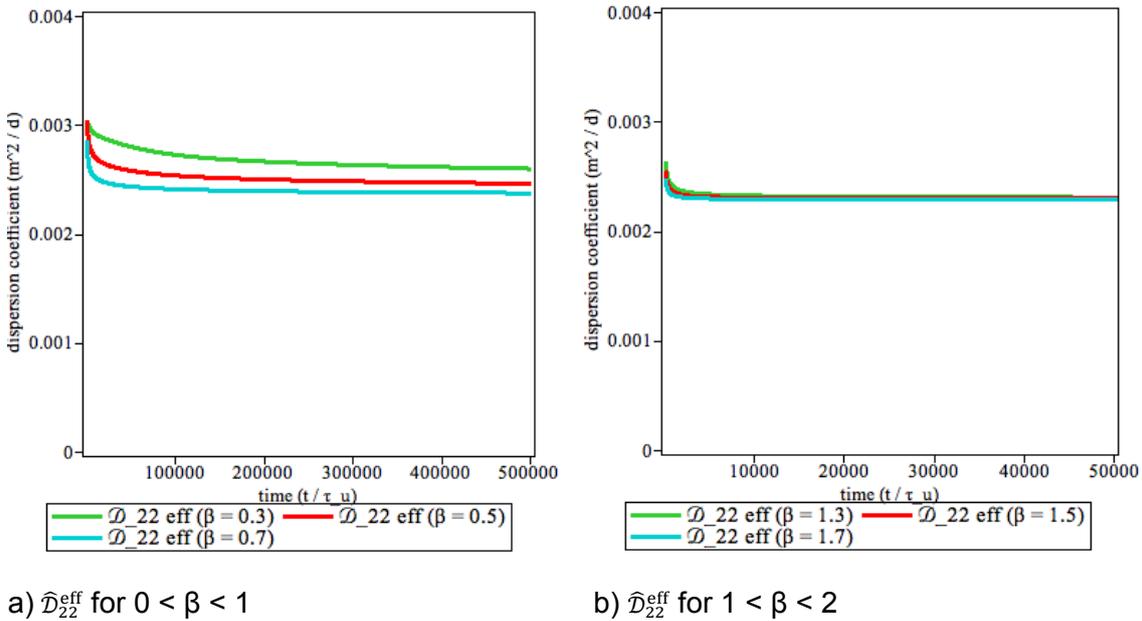
Fig. 3.10 The transverse effective dispersion coefficient in fractal media

Influence of the degree of fractality β

Fig. 3.10 shows, that the transverse effective dispersion values are higher in more fractal media (Fig. 3.10 a) than in media with a weak fractal structure (Fig. 3.10 b). In both media types the effective transverse dispersion first increases and than reaches a con-

57

stant long-time value. This value depends on the degree of fractality and is larger in highly fractal media (small β) and it is reached at a later point of time (Fig. 3.10 a).

The peak in the transverse component is also observed in media with finite correlation lengths (Fig. 3.10 b), although it persists for much smaller time periods in the advective time regime /DEN 02/. A closer view at the peak in the two types of media indicates, that in fractal media the height of the peak is a few orders of magnitude larger than in media with finite correlation lengths and it is reached at times that are also several orders of magnitude larger. This behaviour can be explained with the fact that the sudden scattering of the solute particles is larger and remains longer in media without scale separation. This fact becomes more evident in media with a high degree of fractality.

a) D_{11} for various D   b) D_{22} for various D
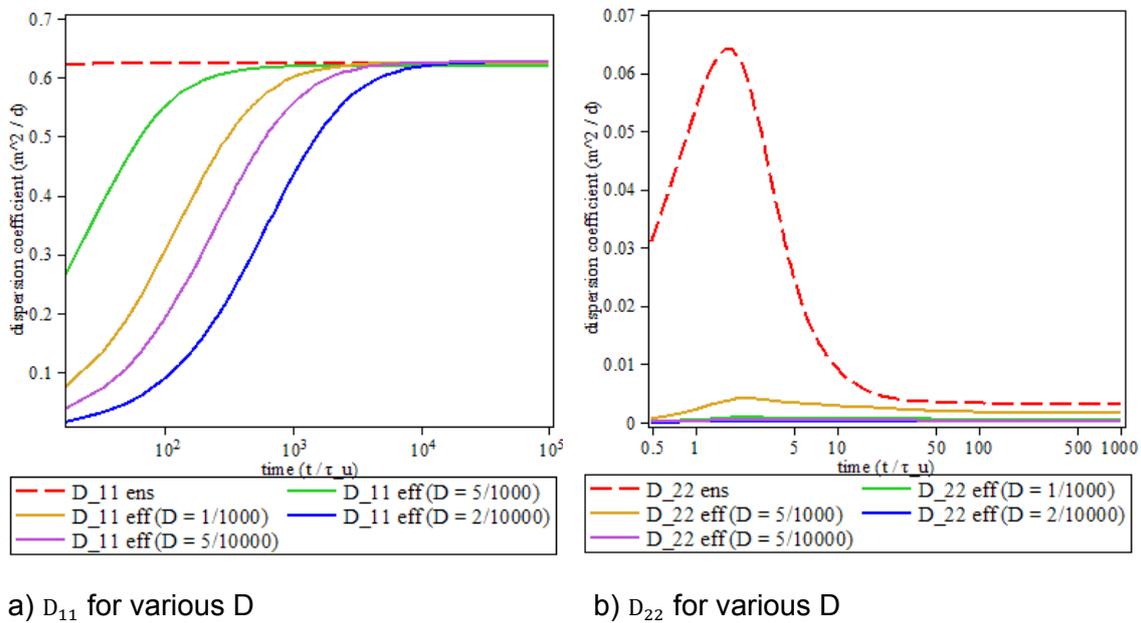
Fig. 3.11   Constant long-time value for the dispersion coefficients in situations with finite correlation lengths found by /DEN 00a/and /DEN 02/

Behaviour for infinite times

The constant long-time value is given in (3.108) and depends on the degree of fractality β: The smaller β, the larger is the value and the later it is reached (Fig. 3.8 and Fig. 3.10). A closer view at the timescale indicates that the transverse ensemble quantity in fractal media reaches the constant long-time value at times that are several orders of magnitude larger than in media with finite correlation lengths and the value itself is larger in fractal media. This clearly demonstrates that the flowpaths in fractal media are much longer and accordingly the spatial and temporal varibilities are much higher.

Influence of the local dispersion D on the effective quantities

Fig. 3.12 shows the influence of the local dispersion coefficient D on the effective dispersion quantities. As mentioned in section 3.6.1, the local dispersion coefficient D strongly influences the effective quantities and in the hypothetical situations with no local dispersion at all there is no physical mechanism which causes the plume to spread. In such situations the effective dispersion coefficient reduces to zero, whereas the ensemble quantities show a non-trivial behaviour even in this hypothetical dispersion-free case where the solute plume is only transported advectively. Although the dispersion values are much higher in the longitudinal component (Fig. 3.12a) is much larger than in the transverse one (Fig. 3.12 b), it is visible, that in both components a higher D causes larger dispersion values, because the effect that causes the spreading of the solute is stronger.

a) The longitudinal component b)   b) The transverse component
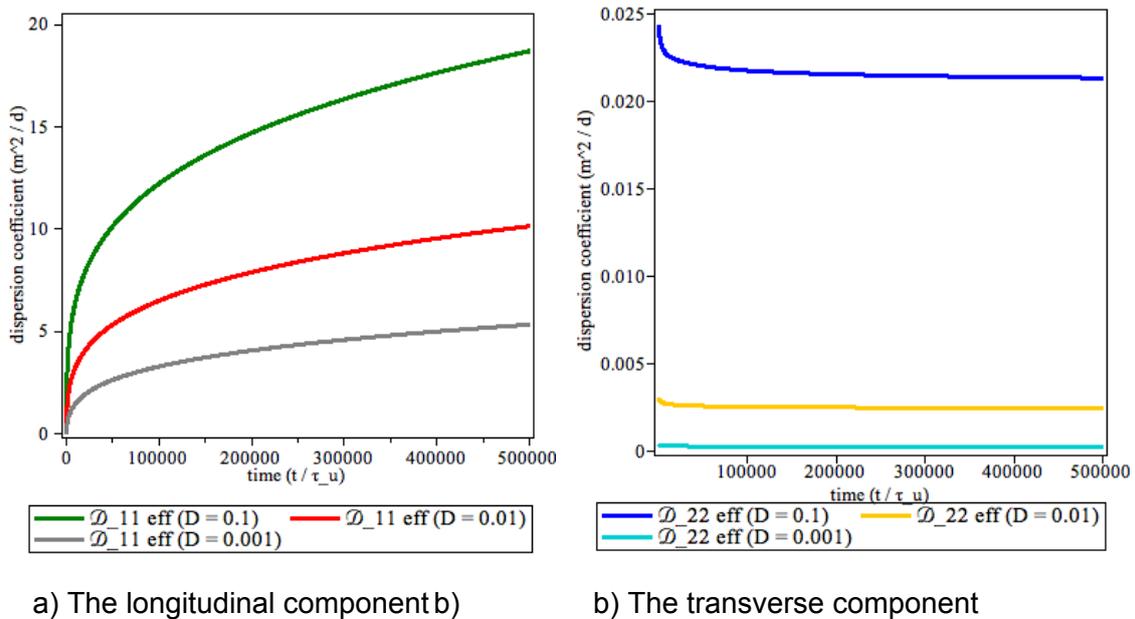
Fig. 3.12   The effective dispersion coefficients in fractal media for $\beta = 0.5$ and various D

3.7   Summary

For an appropriate representation of the natural heterogeneity of fractured aquifers, the proposition of /NEU 95/ is followed that there is a growing evidence to describe the log hydraulic conductivity field of such media with self-affine properties. The scale effects cause the longitudinal dispersion component to increase with growing travel distance

as the solute samples more and more heterogeneities. The temporal behaviour of the longitudinal component in fractal media is in contrast to media with finite correlation lengths: The latter are characterised by an ergodic situation and the ensemble and effective quantities reach the same constant long-time value for infinite times. In fractal media, the longitudinal dispersion quantities do not reach a constant limit because the infinite correlation length $\hat{L}$ dominates. Furthermore, the ensemble and effective quantities are different for all times. They are characterised by different power-laws given in (3.102) and (3.105) implying a non-ergodic temporal behaviour. This result agrees with /FIO 01/ and shows that the quantities describe two fundamentally different properties.

A comparison of the power-laws describing the two quantities shows that the ensemble longitudinal component overestimates the dispersion values remarkably. Therefore, for realistic situations the effective quantity should be applied which describes the temporal behaviour of the longitudinal dispersion more exactly. In the model of the present study, a projector $p_i(\mathbf{k})$ defined in (3.67) is taken into account to ensure the incompressibility of the flow field /DEN 02/. The consideration of this projector allows the derivation of explicit expressions of the transverse coefficients in fractal media as well.

The behaviour of the transverse dispersion coefficients is similar to that in media with finite correlation lengths which was shown in e. g. /DAG 88/, /KIT 88/, /MUS 11a/ or /MUS 11b/ to first increase and then reduce with increasing travel distance. This fact is forced by the absence of divergence in the flow field and could imply a degradation of the contaminant. However, a remarkable difference between the temporal behaviour in the transverse dispersion coefficients in both media with finite and infinite correlation lengths is the much larger timescale in the latter. This fact is forced by more branched and much longer pathways of the solute particles caused by the tiny fissures that remove any preferential scales. It was shown that the timescale increases with the degree of fractality. In other words, the smaller the value of the exponent β the longer are the flow pathways of the solute particles due to very tiny fissures. This corresponds to a high tortuosity and a much longer retention period of the contaminants in fractal media.

4 Numerical solver for the meso-scale reference model

4.1 Higher Order Finite Volume Schemes

Thermohaline flow is described by three conservation equations: the flow equation, expressing the conservation of the fluid-phase as a whole, the equation for the transport of salt, formulating the balance of mass of the brine, and the heat transport equation, which represents the balance of energy. Here, to simplify matters only the first two equations are regarded, given by /FEI 99/:

$$\frac{\partial}{\partial t}\left(\phi \rho_f\right) + \nabla\left(\boldsymbol{q}\,\rho_f\right) = s_f, \tag{4.1}$$

$$\frac{\partial}{\partial t}\left(\phi \rho_f \chi_s\right) + \nabla\left(\boldsymbol{q}\,\rho_f \chi_s - \boldsymbol{D}_s \rho_f \nabla \chi_s\right) = s_s, \tag{4.2}$$

where

$$\boldsymbol{q} = -\frac{K}{\mu}\,\left(\nabla p - \rho_f \boldsymbol{g}\right) \tag{4.3}$$

is the Darcy velocity. An important aspect of these equations is the flux balance that becomes more obvious when the equations are written in integral form:

$$\frac{\partial}{\partial t}\int_B \phi \rho_f\, dV + \int_{\partial B} \boldsymbol{q}\,\rho_f\, dS = \int_B s_f\, dV \tag{4.4}$$

$$\frac{\partial}{\partial t}\int_B \phi \rho_f \chi_s\, dV + \int_{\partial B} \boldsymbol{q}\,\rho_f \chi_s - \boldsymbol{D}_s \rho_f \nabla \chi_s\, dS = \int_B s_s\, dV. \tag{4.5}$$

Here, the integration volume B is an arbitrary subset of the considered domain Ω and is usually called control volume. Each integral equation expresses the fact that changes of quantities in the control volume are due to fluxes over the boundary or sinks/sources within the control volume.

Since the conservation property of these equations arise from the underlying basic physical properties, a discretization scheme should ideally reflect these properties in the numerical scheme. In order to guarantee the discrete conservation property, a finite

volume scheme is used in d³f /FRO 96a/. A generalization of this type of discretization scheme has been implemented for the equations of d³f.

4.1.1 Definition of a Finite Volume Scheme of Higher Order

The generalization of the vertex-centered finite volume scheme has been proposed in /VOG 10/. It can be applied to conservation equations that are of the form:

$$\frac{\partial}{\partial t} \int_B c \, dV + \int_{\partial B} \boldsymbol{F}(c) \, dS = \int_B f \, dV, \tag{4.6}$$

where c is some unknown solution, $\boldsymbol{F}$ is a flux function and f is some source term.

In order to solve such type of equation numerically by a vertex-centered finite volume technique, two choices have to be made: The Ansatz space for the unknown solution has to be chosen, and the set of discrete control volume B, where the conservation law is fulfilled numerically, must be specified.

The usual choice for the Ansatz functions in d³f is a set of linear trial functions, i. e. the unknown solution is represented by linear functions on each element of the mesh discretizing the domain. This approach requires only degrees of freedom that are located in the vertices of the mesh, see Fig. 4.1 (left) for an example. The generalization to higher orders can be achieved by using a polynomial representation for the unknown solution on each element that uses functions of order greater than one. Lagrange finite elements can be used for this purpose and result in degrees of freedom on vertices, edges, faces and volumes in order to ensure the continuity of the solution. A visualization of the degrees of freedom for quadratic Ansatz functions is given in Fig. 4.1 (right).
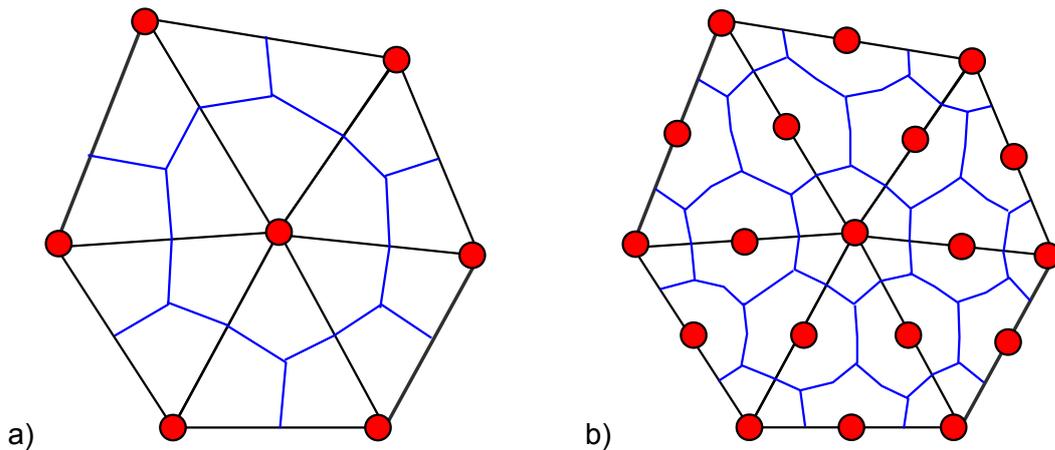
Fig. 4.1   A finite-element mesh (black lines) with the degrees of freedom (red dots)
for linear Ansatz functions (a) and quadratic Ansatz functions (b)

The blue lines show the discrete control volumes constructed by the barycentric method.

For the set of control volumes several possibilities exist. In the software d^3f the bary-
centric control volumes are used /FRO 96b/. These are constructed by taking the con-
vex hull of the following points: a vertex of the mesh, all barycenters of adjacent edges
and faces of the vertex and all barycenters of the adjacent elements. An example of
such a control volume is shown in Fig. 4.1 (left). The generalization of this construction
is related to the chosen Ansatz space. The idea is to construct one control volume for
each degree of freedom. This ensures that the resulting linear system remains quadrat-
ic. The procedure to construct such control volumes is as follows: For a given element
of the mesh, subdivide the element virtually into smaller elements of the same type,
such that the finer partition corresponds to a distribution of degrees of freedom equiva-
lent to the linear case, i. e. all virtual subelements carry exclusively degrees of freedom
in their vertices. Now, the same barycentric construction procedure as used for the lin-
ear case can be applied to the virtually refined elements to produce control volumes re-
lated to the subelements. Fig. 4.2 visualizes this procedure for a triangle with quadratic
(left) and cubic (right) Ansatz spaces. The result of such a refinement is demonstrated
in Fig. 4.1 (right).
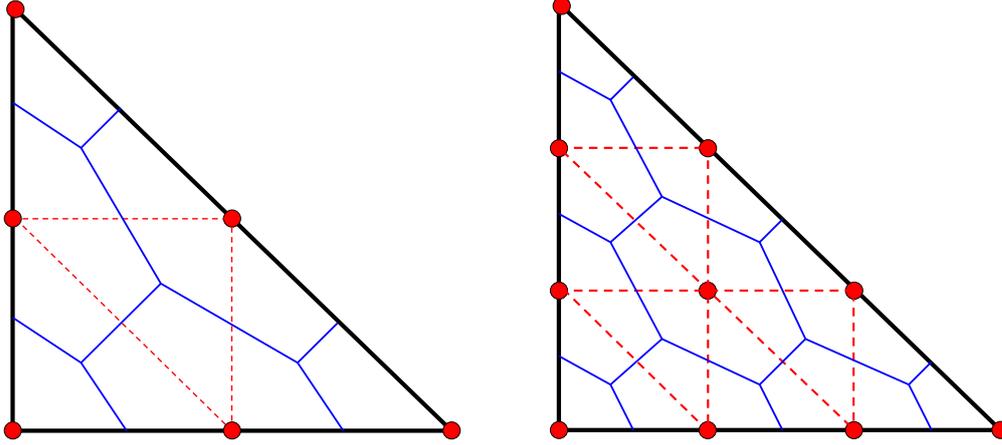
Fig. 4.2   A single triangle (black lines) is virtually subdivided into smaller triangles (red lines) such that the subtriangles have the same structure as linear elements

Applying the barycentric construction for linear control volumes results in control volumes as indicated by the blue lines.

4.1.2   Application to the equation for density driven flow

The finite volume scheme with Ansatz functions of higher order can be used to discretize the equation modeling the density driven flow.

Let $\{\Phi_i(\boldsymbol{x})\}_{i=1,...,N}$ be the set of Ansatz functions that are necessary to form a basis of the piecewise polynomial spaces described above, where N is the total number of degrees of freedom. For both unknown solutions χ_s, p the same Ansatz space, formed by these functions, is used. Thus, numerical solutions are searched that represent the unknown brine mass fraction by

$$\chi_s(\boldsymbol{x}, t) = \sum_{i=1}^{N} \chi_{s_i}(t)\,\Phi_i(\boldsymbol{x}) \tag{4.7}$$

and the unknown pressure by

$$p(\boldsymbol{x}, t) = \sum_{i=1}^{N} p_i(t)\Phi_i(\boldsymbol{x}) \tag{4.8}$$

Now, let $\{B_i\}_{i=1,...,N}$ be the set of control volumes that are constructed based on the generalized barycentric control volume approach described above. The discretized form of the equations (4.4), (4.5) is given by:

$$\frac{\partial}{\partial t} \int_{B_i} \phi \rho_f \, dV + \int_{\partial B_i} \boldsymbol{q} \, \rho_f \, dS = \int_{B_i} s_f \, dV, \quad \text{for all } i = 1, ..., N, \tag{4.9}$$

$$\frac{\partial}{\partial t} \int_{B_i} \phi \rho_f \chi_s \, dV + \int_{\partial B_i} \boldsymbol{q} \, \rho_f \chi_s - \boldsymbol{D}_s \rho_f \nabla \chi_s \, dS = \int_{B_i} s_s \, dV, \quad \text{for all } i = 1, ..., N. \tag{4.10}$$

Here, by χ_s, p the finite dimensional representations from (4.7), (4.8) are used.

4.1.3 Numerical test example

In order to test the implementation using higher order Ansatz functions the scheme is applied to the Henry problem /HEN 64/.

Tab. 4.1 Measurements of the approximation rate for different orders of Ansatz spaces used to discretize the density driven flow equations

FVp (p=1,2,3) denotes the order of Ansatz function, N the number of degrees of freedom, δ the difference between the computed solution and the reference solution.

FV1			FV2			FV3		
N	δ	rate	N	δ	rate	N	δ	rate
15	3,23e0	---	45	2,58e0	---	91	1,93e0	---
45	3,08e0	0,07	153	2,15e0	0,27	325	1,43e0	0,43
153	2,62e0	0,23	561	1,52e0	0,50	1225	7,79e-1	0,88
561	2,05e0	0,35	2145	7,93e-1	0,94	4753	2,96e-1	1,40
2145	1,27e0	0,69	8385	3,18e-1	1,31	18721	7,64e-2	1,96
8385	6,85e-1	0,88	33153	1,01e-1	1,65	74 305	1,30e-2	2,56
33153	3,29e-1	1,06	131 841	2,67e-2	1,92			
131 841	1,56e-1	1,07						

The quality of the solutions, computed using different orders of Ansatz spaces, is compared using a reference solution. This is a numerical solution of the problem at time step t = 120 s, that is computed on a very fine grid and using very small time steps

such that this solution is expected to be close to the true solution. The difference between the reference solution χ_s^{ref} and some coarser approximation χ_s is computed in H^1-norm, i. e. by

$$\delta := \left(\int_{\Omega} \left| \chi_s - \chi_s^{ref} \right|^2 + \left| \nabla \chi_s - \nabla \chi_s^{ref} \right|^2 dV \right)^{1/2} \tag{4.11}$$

The results for the linear, quadratic and cubic Ansatz spaces are shown in Tab. 4.1. A visualization of the decrease of the approximation difference is shown in Fig. 4.3.
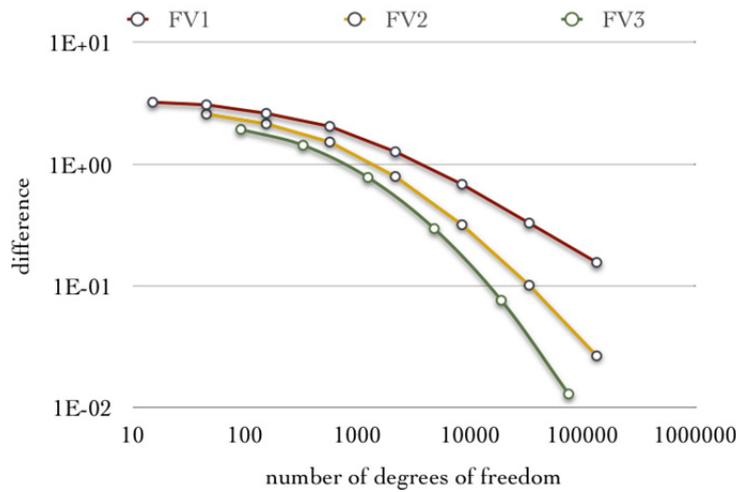
Fig. 4.3   Difference to a reference solution of the Henry problem for the first three orders of Ansatz spaces measures in H^1-norm

4.2   Filtering algebraic multigrid solver

The linear systems generated by the described discretization technique tend to be rather large in real world problems and can normally not be solved using exact solvers (e. g., LU-decomposition) or simple iterative solvers (e. g., Jacobi/Gauss-Seidel solvers). More powerful solvers have been created for such cases. Two-grid solvers are used to reduce the error on different length scales: A so-called *smoother* is used to reduce high-frequency parts of the error. The remaining error is then solved by looking at the problem on a coarser grid. For this, the two-grid solver needs transfer operators: a restriction operator which restricts vectors from the fine grid to the coarse grid, and a prolongation operator, which prolongates vectors from the coarse grid to the fine grid. Finally, a direct solver is used to calculate the solution on the coarse grid. Choosing re-

cursively two-grid methods as coarse solvers results in multi-grid solvers. The advantage of multigrid-solvers is that they regard multiple related problems with vastly differing complexity instead of only regarding one large problem. Different multigrid solvers exist, most prominently are the group of geometric multigid methods and of algebraic multigrid methods (cf. /HAC 85/, /RUG 87/). While geometric multigrid methods build grid hierarchies through repeated refinement, starting from a coarse problem, algebraic multigrid methods start from the fine problem and calculate the coarse grid and the transfer operators algebraically. The Filtering Algebraic Multigrid method, which will be described in the following, is a variant of an algebraic multigrid method. The key ideas can be summarized as follows (cf. /WAG 00/, /HEP 12/):

On each level of a given hierarchy, a smoothing operator is applied, with the goal to reduce high frequencies of the error. Components of the error, which aren't reduced by the application of a smoother are then subject to the coarse grid correction. Note that we regard those components as algebraically smooth. The coarse grid correction involves restriction of the defect from a fine grid to a coarser grid through the so called restriction operator R and a prolongation operator P, which projects corrections from coarser grids to finer grids. Furthermore, the coarse grid operator A_H, which represents the fine operator on the coarse grid, is calculated by the *Galerkin product $A_H = RAP$.* Note that the notation is for the two-grid algorithm, since the generalization to the multigrid-algorithm is trivial.

Algebraic multigrid is an iterative algorithm for solving linear equations systems of the form $Ax = b$. The approximation x is corrected by the two-grid-operator T by

$$x^{i+1} = Sx^i - A_H^{-1}R(ASx^i - b) = Tx^i + c \tag{4.12}$$

where c = $PA_H^{-1}Rb$ and $T = (I - PA_H^{-1}RA)S$, which means: smooth, calculate new defect, restrict to coarse grid, solve on coarse grid, prolongate to fine grid and add correction. Since for the error it holds $e^{i+1} = A^{-1}b - x^{i+1} = Te^i$, every algebraic multigrid method tries to minimize $\|T\|$ in some norm. FAMG uses a special approximation of $\|T\|$:

$$\|T\|_A \leq max_{e \neq 0} \| D^{\frac{1}{2}}(1 - PR^{inj})SD^{-\frac{1}{2}}D^{\frac{1}{2}}A^{-\frac{1}{2}}e \| / \|e\| \tag{4.13}$$

with D diagonal of A. The minimization can be separated if all vectors t for which $\frac{\|D^{1/2}t\|}{\|A^{1/2}t\|}$ is not small are interpolated exactly onto the coarse grid: $\left(I - PR^{inj}\right)t = 0$. These are exactly the vectors which are algebraically smooth, so they are not efficiently reducible for smoothers. They are also called zero-energy modes. In the FAMG algorithm, a representative subset of so-called test vectors t has to be chosen to capture all the zero-energy-modes. Then the minimization (with the restriction above) can be done by $\|D^{1/2}\left(I - PR^{inj}\right)SD^{1/2}\|_F$.

For the sake of illustration, only the symmetric case will be regarded in the following, i. e., $A = A^T$, which leads to $R^T = P$. Note that there are extensions to FAMG for non-symmetric matrices, systems of equations and multiple testvectors (cf. /NAE 10/, /NÄG 12/)

4.2.1   Global and local minimization

In the following $R = R^{inj}$ is used, which is sufficient as shown in /WAG 00/. This leads to the following minimization problem:

$$\min_P \|(I - PR)S\|_{D^{-1}},$$
$$s.t.\,(I - PR)St = 0 \tag{4.14}$$

$\|\cdot\|_{D^{-1}}$ is the induced operator norm of the vector norm $\|x\|_{D^{-1}} = \sqrt{\langle D^{-1}x, x\rangle}$.

In order to express this locally, it is assumed that a fine node i (a node which only exists on the fine grid) is interpolated by coarse nodes (nodes which also exist in the coarse grid), which are neighbours of i in the adjacency graph of the matrix A. Given a partitioning of all nodes in coarse (C) and fine (F) and a vector $q_i = i$-th row of $(I - PR)$, problem (4.14) can be rewritten as a sum over local and independent minimization problems:

$$\sum_{i\in} \min_{q_i} |a_{ii}| \|S'^T q_i\|^2_{D^{-1}}$$
$$s.t.\,\langle q_i, S't\rangle = 0\;\forall i \in F \tag{4.15}$$

This leads to the following algorithm:

1. For all nodes i

    a. get the (local) representation of the testvector t_i

    b. Calculate for all neighbour pairs $n \neq m \in N_i$

$$F_{i,nm} = \min_{q_{i,nm}} a_{ii} \left\| S'^T q_{i,nm} \right\|_{D^{-1}}^2$$
$$s.t. \langle q_{i,nm}, S't \rangle = 0$$

(4.16)

    c. if $\theta F_{i,nm} \leq \min_{a \neq b \in N^i} F_{i,ab}$ and $F_{i,nm} \leq \delta, \delta < 1$ then

       save the pair (n, m) in PN^i and their quality value $F_{i,nm}$.

Afterwards, a set of possible parent nodes PN^i is assigned to every node i.

4.2.2 Smoother

The construction of the interpolation operator focuses on the interpolation of smooth vectors only. For this, a special smoothing operator S' is used. S' consists of one Jacobi-step $S_{jac} = I - \omega D^{-1} A$, followed by a Jacobi-step updating only fine nodes (F-smoothing):

$$S_{jac,F} = I - \sum_{i \in F} e_i e_i^T D^{-1} A$$

(4.17)

resulting in

$$S' = S_{jac,F} S_{jac}.$$

(4.18)

4.2.3 Coarsening Algorithm

During the coarsening algorithm, nodes are classified as fine and coarse nodes. Fine nodes on a grid level l are nodes, which are not contained in the grid level $l + 1$. On the contrary, coarse nodes of level l are contained in level $l + 1$, too. Prolongation and restriction thus have to be constructed in a way that fine nodes are interpolated by neighbouring coarse nodes. The quality of this interpolation is crucial to the successful application of the solver.

The FAMG method chooses fine- and coarse nodes by minimizing the number of coarse nodes while still maintaining a good interpolation for fine nodes. A rating for each node is calculated by

$$R_i = \min_{M \in PN^i \setminus F} |M| - |M \cap C| + F_{i,nm}/\delta \tag{4.19}$$

Note, that $F_{i,nm}/\delta < 1$, so that reducing the number of coarse nodes has higher priority. Since a node can only be either classified as coarse or fine, the advantage of calculating multiple possible parent pairs in section 4.2.1 becomes apparent: it results in greater flexibility when it comes to performing the actual classification.

The reasoning above results in the following coarsening algorithm:

1. calculate ratings R_i for all nodes
2. while interpolateable nodes are left:
   a. get unclassified interpolateable node i with lowest rating
   b. get best available parent nodes n, m for i, regarding $F_{i,nm}$
   c. set i fine
   d. set parent nodes n, m coarse
   e. for all neighbours $j \in N_i$
      i. remove all parent pairs in PN_j which contain i
         (i can't be coarse anymore)
      ii. update rating R_j

4.3   Parallelization

Parallel computers are required to solve problems which are too large to be solved on serial computers. Regarding domains of fractured rock, which possibly feature tunnels or interwinding layers of different soil types, it is clear that geometries which represent such domains often consist of a huge amount of elements. To allow for justifiable solving times, such domains are distributed amongst multiple processes on parallel computers. Assembling and solving are then performed on those distributed domains. Of course, special concepts, algorithms and data structures are required to parallelize those tasks and to efficiently perform the required synchronization between different processes.

All parallelization efforts regarding domain distribution and parallel solving in UG4 are based on the pcl-library ("**P**arallel **C**ommunication **L**ayer"), which has been developed as a part of the UG4 library (cf. /REI 12a/ /VOG 12/). Note that the structures introduced in the following have originally been introduced in those articles.

4.3.1 The Parallel Communication Layer

The parallelization layer has been designed to be usable by all the different modules in UG4, e. g., the grid and algebra libraries, while adding a minimal overhead to the required parallel communication. Based on some general concepts, a C++ template library has been implemented, which can be used to define paths of parallel communication. An overview over those concepts is given in the following (cf. /REI 12a/).

4.3.1.1 Interface

An interface I_{AB} on a process A stores objects which are related to objects on a process B in a determined order. At the same time there has to be an interface I_{BA} on process B with $|I_{AB}| = |I_{BA}|$. The order of the objects in the interfaces is crucial, since during communication data is exchanged between the i-th object in interface I_{AB} and the i-th object in interface I_{BA}.

The dependency on the order of objects in the interfaces has several advantages. No global id has to be exchanged along with communicated data during communications, since data can be associated with objects in interfaces based on the index of a data entry in a communicated data block. This approach is highly efficient, since it reduces communication load and avoids lookups in id-tables. Of course this means that processes have to assure that objects which are inserted into interfaces are inserted at the correct locations. This, however, can be done in a process local way without additional communication and is thus preferable regarding scalability and overall parallel performance. It should be noted that global ids can still be efficiently generated at any time only requiring a single communication step between direct process neighbours.

4.3.1.2 Layouts

On a process A several interfaces $I_{AB}, I_{AC}, \dots$ can be grouped together in a layout L. Layouts can be used to group all interfaces on a process that are used in a special context, e. g. 'master' and 'slave' interfaces. An arbitrary number of layouts may exist, making it possible to group interfaces not only by their 'master' and 'slave' properties, but also by the level in which associated objects lie in a multigrid hierarchy (both algebraic and geometric multigrid hierarchies). This allows for the construction of algorithms and solvers, like smoothers or exact solvers, which only operate on a given level of a hierarchy. This again is crucial to guarantee good scalability in multigrid methods.

In Fig. 4.4 a schematic construction of interfaces and layouts is shown for some distributed objects.
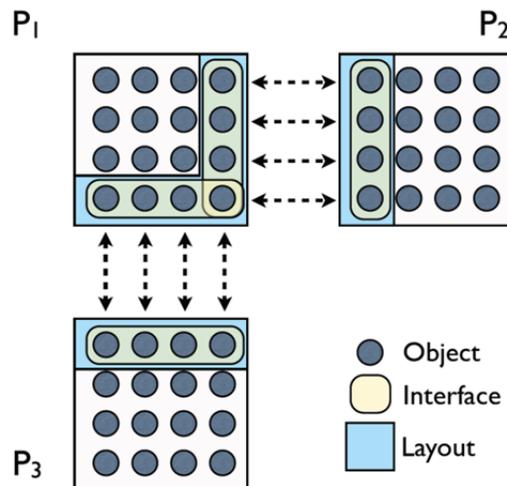
Fig. 4.4   Example of interfaces and layouts on three processes for a set of objects

4.3.1.3 Interface Communicator

The interface communicator performs the actual communication between distributed objects. Data is thereby scheduled for separate interfaces or for whole layouts. Data can not only be scheduled for multiple interfaces, it is also possible to schedule multiple data sources for one interface for a single communication step. For this, the interface communicator features send and receive methods. Data is not transferred to other processes until the user calls the communicate method. During this method data is collected using communication policies (detailed below), which pack the data into binary

buffers, which are then transferred to the processes associated with the interfaces. When the buffers arrive at the target processes, the interface communicator uses communication policies again to extract the data. Communication is performed using asynchronous communication. The required buffers for asynchronous communication are maintained by the interface communicator and are reused between successive communication calls. This is especially useful for iterative solvers, since a similar communication pattern is executed in each iteration. Buffer reuse thus minimizes overhead related to memory allocations.

4.3.1.4   Communication Policy

Through the concept of **communication policies** it is possible to adjust the data collection and extraction process to the structures and data types used in a concrete application or library. Data is written and read from binary streams which are supplied by an interface communicator. Those streams are later directly used as buffers during communication, which means that data is only copied into a buffer once and can then be communicated with data from other elements in one block, which is highly efficient on current platforms. Instances of specialized communication policies are passed to an interface communicator in calls to its send and receive methods, together with the interfaces or layouts on which data shall be collected and extracted using the policy.

4.3.1.5   Process Communicator

This communicator is used to perform communication between processes, in contrast to individual distributed objects. It contains methods to broadcast data, to gather and scatter data, to send and receive raw data, to perform reduce and allreduce operations, and more. Process communicators are associated with a group of processes to which the communication is restricted. One can think of a process communicator as a slightly enhanced wrapper to MPI methods using MPI communicators in order to restrict communication to a given set of processes.

They can, e. g., be used to distribute grids and matrices between processes or to check whether all processes reached a given accuracy during application of an iterative solver.

4.3.1.6 Implementation details

The concepts of the **parallel communication layer (pcl)** have been implemented using the C++ programming language. Users may adjust the provided structures to arbitrary object- and container-types through the use of template parameters and type traits. The library has been constructed in a way that even allows users to write custom interface- and layout-structures from scratch, as long as they adhere to the basic concepts. The provided interface and layout implementations should, however, be sufficient for most applications.

The clear interfaces defined by the pcl allow for an implementation of the actual communication code, which is hidden from the user. It is therefore possible to completely replace the message passing library used in the background. The current implementation uses MPI (cf. /GRO 99/), which is broadly supported by a great majority of current cluster and HPC systems.

It should be noted, that no special object type has been defined above. Indeed, a special object type is not required, since the pcl-structures are designed to support any type with which a user may want to identify his distributed objects. The object type is specified through template arguments to the interface and layout classes of the pcl. Two examples from the simulation framework UG4 are given to illustrate this:

- UG4's grid manager stores pointers to the grid objects (vertices, edges, faces and volumes) in the interfaces. During communication, communication policies can thus directly access values associated with grid objects simply by using the pointer supplied by the interface. No redirection through handles or lookup tables is required. More details on how distributed domains are handled can be found in section 4.3.2.
- UG4's algebra library stores algebraic indices in the interfaces. Parallel matrix and vector operations can then be implemented with low runtime overhead, since the indices stored in those interfaces can be used during communication to simply index into associated matrices and vectors.

4.3.2 Distributed domains

The UG4 grid manager supports adaptive unstructured hybrid hierarchical grids in 1, 2 and 3 dimensions. In a parallel environment, a grid is normally loaded on one process (the root process) and then distributed to associated processes. To establish a connec-

tion between distributed grid parts, the grid manager creates pcl-interfaces and pcl-layouts during distribution. Those interfaces and layouts can then be used to identify object copies of distributed objects and to communicate data, e. g., refinement marks during adaptive refinement.

Two major types of interfaces are thereby used: horizontal and vertical interfaces. While horizontal interfaces are used to connect grid parts on each level, vertical interfaces are used to establish a connection between parents and children in a grid hierarchy, which reside on different processes. Both horizontal and vertical interfaces are furthermore subdivided into master and slave interfaces. This is important to allow for clear communication paths and simplifies the synchronization of distributed data tremendously.
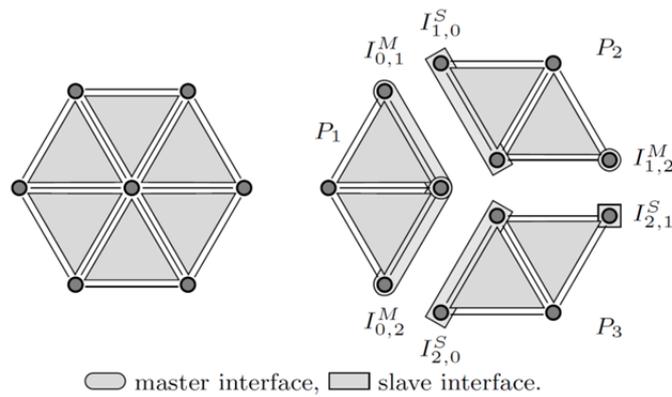
Fig. 4.5 Horizontal vertex interfaces on a given grid level

> Three master interfaces and associated slave interfaces are depicted. Note that a specific copy of a grid object can lie in multiple master interfaces but at most in one slave interface /REI 12a/.

In Fig. 4.5 the horizontal interfaces created during the distribution of a single grid level are depicted. The breakdown into slave and master interfaces can be seen here. It should be noted that the grid manager constructs a low dimensional overlap only. In Fig. 4.6 horizontal and vertical interfaces are depicted for a 1d example.
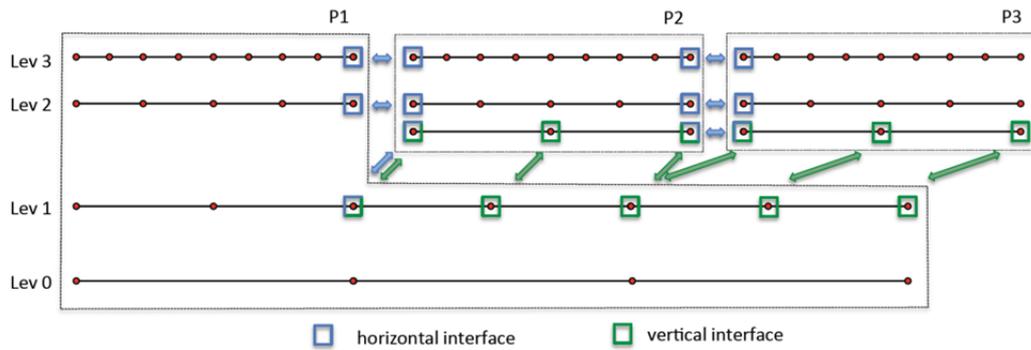
Fig. 4.6 Schematic overview of the parallel multigrid setup for a 1d example

Horizontal interfaces are used to establish connections between distributed objects on one level, whereas vertical interfaces are used to establish connections between different levels (from /REI 12a/).

The UG4 grid manager, whose grids are used during discretization, supports adaptive and anisotropic refinement and coarsening, both for serial and parallel environments. The adaption process can be driven by an error estimator or by an adaption criterion during simulation. Horizontal interfaces are thereby used to communicate involved refinement marks and are dynamically adjusted to the adapted grids. Parallel adaptive refinement is fully supported for hybrid grids consisting of triangles, quadrilaterals, tetrahedrons, hexahedrons, prisms and pyramids. This allows for the construction of thin anisotropic layers to represent fractures. The featured adaptive refinement can hereby be used to improve the element quality of anisotropic elements during the first refinement steps.

4.3.3 Parallel algebra setup

Since requirements on the algebraic structures are different from those related to adaptive grid hierarchies, the implementation of algebra structures in UG4 is independent from the grid structures. Still the structure and content of finite element (FE) and finite volume (FV) matrices is tightly connected to the content of associated grids, since degrees of freedom for the algebra are normally associated with grid elements. The parallelization of distributed matrix and vector classes is thus connected to distributed grids, too. As mentioned above, pcl-interfaces are used for the parallel algebra, too. Instead of grid objects, indices are stored in the pcl-interfaces for the algebra. Those algebra interfaces are constructed from the existing grid interfaces. For each element of a grid interface, the indices of associated degrees of freedom are pushed to associated alge-

bra interfaces, resulting in matching orderings of associated algebra interfaces, even if the interfaces are built by each process separately.

Values associated distributed degrees of freedom can be stored in a distributed vector in a couple of ways. The following storage types are used in UG4:

- **consistent**: all copies store the true value,
- **additive**: the sum of stored values over all copies gives the true value,
- **unique**: the master stores the true value and slave copies have zero value.

One should note that the unique storage type is a special case of the additive storage type. Each distributed vector keeps track of its internal storage type. Methods to transform one state into the other are supplied by UG4. They are implemented using the constructed pcl-interfaces and layouts.

The storage type of a distributed matrix allows for even more states. Some examples are given in the following:

- **additive**: the sum over all matrix-couplings between two indices on all processes is the true coupling.
- **additive-diagonal-consistent**: same as additive, but self-couplings of indices are stored as true values on each process,
- **process-local-consistent**: each process stores the true coupling values between all indices that have a copy on the process.

4.3.4 A parallel geometric multigrid solver on hierarchically distributed grids

In /REI 12a/ scaling studies of a highly scalable multigrid solver on hierarchically distributed grids, based on the parallelization schemes introduced above, are presented. Those studies demonstrate that the introduced structures of the parallel communication layer, together with the grid and algebra parallelization which are built on top, are perfectly suitable for high performance computing on large HPC systems (> 100 000 processes). The basic ideas and the most important results are presented below.

The parallel version of the geometric multigrid solver in UG4 is usually applied on grids which are distributed in a tree-like structure: The coarse grid is typically contained on

one or on a few processes only. Several refinement steps are performed before the new top-level is then distributed to more processes. Further refinement steps are then performed on all those processes until the new top level is distributed to even more processes. The result is a hierarchically distributed multigrid which successively spans over all available processes. The highest levels of the grid hierarchy are distributed over all available processes, whereas lower levels only span over a subset of available processes. This makes perfectly sense, since the highest workload concentrates on the upper levels of the grid hierarchy.

For the application of the smoothing operator, horizontal interfaces are used on each level separately. During restriction and prolongation, vertical interfaces are employed to transfer data from higher to lower levels and vice versa.

The highly encouraging results of the weak scaling studies for benchmarks performed on the 2d and 3d Laplace problem given in equation (4.20) on the JuGene system at Jülich supercomputing center (JSC, FZ Jülich) using up to 262 144 processes (from 294 912 available processes) are presented in Tab. 4.2.

$$-\Delta u = f \qquad \text{on } [0,1]^d \tag{4.20}$$

Tab. 4.2   Weak scaling of Laplace 2d problem on JuGene

PE: Number of processing entities, T_s: time for solving, $T_{a+s}, E_{a+s}, S_{a+s}$: time, efficiency, and speedup for assembly and solving. S_{ideal}: ideal speedup.

PE	grid levels	DoF	$T_s(s)$	$T_{a+s}(s)$	E_{a+s} (s)	S_{a+s}	S_{ideal}
4	6	263 169	2.608	5.064	-	-	-
16	7	1 050 625	2.653	5.102	99.2	4.0	4
64	8	4 198 401	2.694	5.136	98.6	15.8	16
256	9	16 785 409	2.752	5.175	97.8	62.6	64
1 024	10	67 125 249	2.800	5.216	97.1	249	256

PE	grid levels	DoF	$T_s(s)$	$T_{a+s}(s)$	E_{a+s} (s)	S_{a+s}	S_{ideal}
4 096	11	268 468 225	2.854	5.294	95.7	980	1 024
16 384	12	1 073 807 361	2.934	5.360	94.5	3 870	4 096
65 536	13	4 295 098 369	3.023	5.452	92.9	15 217	16 384
262 144	14	17 180 131 329	3.162	5.585	90.7	59 424	65 536

The results show a very good scaling behaviour of the solver for the 2d and 3d case. The assembling time even stays constant. The given ideal speedup is hypothetical only for the given problem, since it only considers the increase of process numbers but completely ignores required communication. Still the results closely approach this hypothetical perfect scaling behaviour and are a clear indicator for the high efficiency of the proposed parallelization approach.

Tab. 4.3   Weak scaling of Laplace 3d problem on JuGene

PE: Number of processing entities, T_s: time for solving, $T_{a+s}, E_{a+s}, S_{a+s}$: time, efficiency, and speedup for assembly and solving. S_{ideal}: ideal speedup.

PE	grid levels	DoF	$T_s(s)$	$T_{a+s}(s)$	E_{a+s} (%)	S_{a+s}	S_{ideal}
1	4	35 937	2.516	6.967	-	-	-
8	5	274 625	2.657	7.368	94.6	7.6	8
64	6	2 146 689	2.835	7.540	92.4	59.1	64
512	7	16 974 593	2.935	7.626	91.4	468	512
4 096	8	135 005 697	2.956	7.676	90.8	3 718	4 096
32 768	9	1 076 890 625	3.116	7.829	89.0	29 161	32 768
262 144	10	8 602 523 649	3.073	7.786	89.5	234 575	262 144

4.3.5   Parallelization of the FAMG solver

The parallelization of the FAMG solver (cf., /HEP 12/) is based on the parallel algebra structures detailed in section 4.3.3. However, in addition to the low dimensional overlap constructed by the grid manager during domain distribution, the FAMG solver additionally requires a broader overlap of degrees of freedom. This is required, since the values of a matrix A have to be known in the direct neighbourhood N_i^1 of a node i and in the neighbourhood of neighbours N_i^2 of i (cf., section 4.2.3), resulting in a required overlap of 2 of the matrix A.

4.3.5.1   Parallel coarsening

To ensure a consistent coarsening the coarsening process has to be parallelized, too. To avoid unintentional interference between neighboured processes, a graph colouring algorithm is used on the neighbourhood graph of processes. Using this graph colouring, one can assert that no two processes which could set the same nodes to coarse or fine are performing coarsening at the same time. The parallel coarsening is described by the following algorithm:

1. Calculate a graph colouring so that no two cores which could set the same node coarse or fine have the same colour
2. Receive coarsening data from cores with lower colour
3. Perform the serial coarsening algorithm described in section 4.2.3
4. Send coarsening data to cores with higher colour

Combining the serial coarsening approach with those parallel extensions, one receives the algorithm to construct the prolongation/restriction operators for the parallel FAMG method:

1. Calculate a 2-overlap of the matrix A
2. Gather all possible parent nodes (cf., section 4.2.1)
3. Perform parallel coarsening as described above
4. Send and receive local prolongation operators on border nodes
5. Calculate $R = P^T, A_H = RAP$

4.3.5.2 Agglomeration

For a good parallel performance it is important that the computational part of a parallel algorithm outweighs the time spent with communications. Since the coarsening algorithms of the FAMG method successively decreases the problem size, eventually a point is reached where the problem size on a given core is so small that communication times dominate over computation times. To avoid this bottleneck small matrices on several processes are gathered on one process and united to a larger matrix, thus increasing the problem size on one process while removing other processes from the FAMG-computations on coarse levels entirely.

As soon the number of unknowns on a single process falls below a given constant N_{min} on the current level, the following information will be gathered on the root process:

* The number of unknowns on each process
* The process-ids with which each process is connected to via interfaces together with the size of those interfaces

This information is used in an agglomeration algorithm on the root process, which calculates a heuristic graph partitioning so that:

* All participating cores have more than $N_{desired}$ unknowns.
* The number of participating cores is maximized.
* The maximal size of all interfaces between two cores is minimized.

After the agglomeration procedure some processes will be idle on the current level and on levels below. This, however, is preferable to a scenario where all processes are involved with a generally low work load. This can also be seen in the results of geometric multigrid methods on hierarchically distributed grids (see section 4.3.4. Note, that the agglomeration approach for parallel algebraic multigrid methods and the hierarchical distribution approach for parallel geometric multigrid methods share the same idea of a tree-like problem distribution on the given processes, using more processes for the upper levels of a given problem hierarchy.

4.3.5.3   Benchmarks

Benchmarks have been performed to prove the viability of the proposed approach (originally published in /HEP 12/). The 2d Laplace equation (equation (4.20)) has been solved on the triangulated unit square using FAMG as preconditioner for the CG method. The calculations have been performed on the Cray XE6 system "Hermit" at the HLRS Stuttgart. Tab. 4.4 shows the weak scaling for a series of initial grid refinement levels, Tab. 4.5 shows the numbers of participating cores for associated agglomeration numbers $N_{min} = N_{desired} = 1000$ for each run.

Tab. 4.4   Weak scaling of the 2d Laplace problem on Hermit using FAMG

T_{total}: total application run time, T_{setup}: time for FAMG setup, T_{solve}: time for CG solver using FAMG multigrid as preconditioner, N_{iter}: number of CG iterations.

PE	grid levels	DoF	T_{total} (s)	T_{setup} (s)	AMG levels	$T_{solve}(s)$	N_{iter}	$\dfrac{T_{solve}}{N_{iter}}$
4	8	263 169	6.87	3.47	9	1.20	9	0.13
16	9	1 050 625	9.92	4.17	11	2.26	11	0.21
64	10	4 198 401	12.11	4.92	13	2.40	11	0.22
256	11	16 785 409	14.02	5.92	15	2.78	12	0.23
1 024	12	67 125 249	16.60	6.95	18	3.37	14	0.24
4 096	13	268 468 225	20.39	8.53	20	3.90	15	0.26

While an increase in total processing time can be observed with growing problem size and process numbers, the increase stays in reasonable bounds. Reasons for the increased setup and solution times may be found in the fact that the coarsening rate of the standard FAMG method is only 50 % per level, resulting in a larger number of required levels to reach the same coarse-grid to fine-grid node ratio as geometric multigrid. Furthermore the number of iterations does not stay constant with increasing process numbers. However, the time per iteration is bounded and even remains constant if the increase in operator complexity is considered as well.

Tab. 4.5   Number of participating processes for parallel FAMG

AMG level	PEs 4, used PE	PEs 16, used PE	PEs 64, used PE	PEs 256, used PE	PEs 1024, used PE	PEs 4096, used PE
0-7	4	16	64	256	1 024	4 096
8	2	8	30	120	479	1 883
9	1	4	15	62	249	1 044
10		2	8	31	124	533
11		1	4	16	72	291
12			2	8	44	188
13			1	4	24	110
14				3	13	61
15				1	7	37
16					3	17
17					2	11
18					1	5
19						2
20						1

5 Concepts and criteria for multi-scale adaptivity

5.1 Motivation

In multi-grid codes, the mesh size influences the transport parameters – namely the ensemble and effective dispersion coefficients. Therefore, grid-size dependent parameters are needed for a realistic description. But according to the grid size there is an artificial mixing effect which distorts the ensemble quantities in a significant manner as shown in chapter 3 and results in a remarkable difference between the ensemble and effective quantities for small distances or a finite time regime.

The aim of this chapter is, to improve the results for the dispersion values which should capture the true dispersion more exactly. With the upscaling method of coarse graining, this artificial mixing effect can be quantified.

A criterion for the multi-scale adaptivity would be, that for short time regimes – corresponding to short distances of the solute from the source of injection – the ensemble quantity would be the same as the much more exact effective one. Thus, the main criteria for the multi-scale adaptivity is the distance to the fracture: Near the fracture a fine
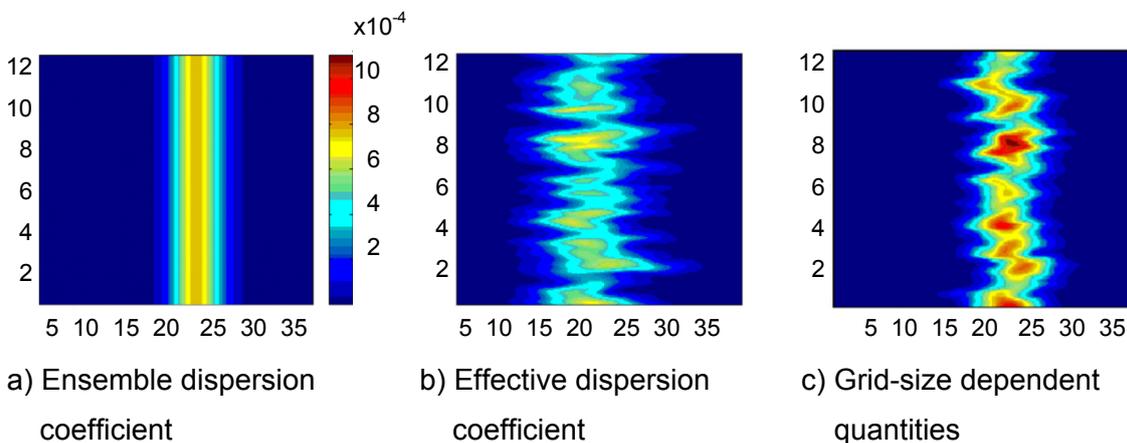

a) Ensemble dispersion   b) Effective dispersion   c) Grid-size dependent
   coefficient   coefficient   quantities

Fig. 5.1   Effect of the filtering method coarse graining

grid should be used, whereas in the far field a coarser grid should be applied (e. g. /HEN 00/, /NOE 00/, /GRA 01/). In this chapter, a criterion for the multi-scale adaptivity is developed by defining the spatial filter in dependence of the grid size. For that purpose, the model described in section (3.3) is now extended to scales which do not de-

pend on the grid size that means that single fractures are embedded in the fractured porous medium.

5.2 Introduction

To capture observed phenomena accurately, one has to discretize numerical models by grid cells of smaller size than the scale of heterogeneity. The computational effort to solve field scale problems is very demanding and it is common to diminish the computational resolution by choosing coarser grids. Variability is lost in this case and one has the problem how to model the impact of unresolved velocity fluctuations upon transport. Standard upscaling procedures such as homogenization and stochastic modelling compensate unresolved effects by introduction of macro-dispersive fluxes. Both methods average out all heterogeneities resulting in a total loss of spatial variability in the flow and transport parameters (Fig. 5.1 a and Fig. 5.1 b). The challenge now is to find an approach which averages out only the real or physical mixing (Fig. 5.1 c).

In doing this, one usually has to make a compromise between computational efficiency and the preciseness/correctness of the model solution. However, numerical grid cells of size much larger than the heterogeneity scale might be not desired nor might yield reliable results with respect to the required preciseness of the results. Practical problems might be dominated by additional scales not much larger than the heterogeneity scale.

A classical example is given by solute transport in a dipole flow field where the additional length scale is set by the dipole size respectively the curvature of the larger scale dipole flow. In this case, the numerical model has to resolve the curvature of the larger scale flow. Smoothing out all variability in the flow by ensemble average gives only reliable results for the single realization if the ensemble average may be substituted by spatial averaging because of the ergodicity assumption. By construction, the spatial average is performed over volumes containing many correlation lengths. Thus, the total loss of variability and numerical computation on grid cells which are small enough to resolve the large scale flow field leads to inconsistent results. /DUR 96/ and /DUR 97/ neglected subgrid effects. /CHR 96/ and /BAR 97/ used an a priori estimate of the global flow field to compute upscaled fluxes. /EFE 00/ presented a methodology that models subgrid effects without requiring a priori estimates. The method has some elements in common with the large eddy simulation (coarse graining) method described by /BEC 96a/ and /BEC 96b/. However, /EFE 00/ apply a non-uniform coarsening

through the domain (see /DUR 96/ and /DUR 97/). The drawback of their results is an empirical function that appears in the results for coarse grained dispersivities which has to be estimated by numerical runs of the model. /RUB 99/ applied coarse graining to solute transport and stated explicit results for block-scale macrodispersivity values.

A solute plume is represented by the concentration field c($\mathbf{x}$, t). In heterogeneous media, the mixing coefficients depend implicitly on the spatial distribution of the heterogeneities, $D_{ij} = D_{ij}(c)$, via this concentration. In the stochastic approach, the large-scale plume is characterized by the ensemble dispersion coefficient D_{ij}^{ens} (t) as defined in (3.78) and denotes the average over the ensemble of aquifer realizations representing the dispersion characteristics of the whole aquifer, whereas the effective dispersion coefficient D_{ij}^{eff} (t) as defined in (3.77) describes the experimentally observable dispersion. The two quantities are identical only for infinite times in media with finite correlation lengths of the heterogeneities (/MET 99/, section 3.6.4; Fig. 3.10 a and Fig. 3.10 b). In general, the experimentally observable dispersion, which is a property related to one given aquifer, is represented by the effective quantity D_{ij}^{eff} (t). Thus, deriving real block-scale mixing coefficients needs coarse graining of effective mixing coefficients instead of ensemble quantities if the interest is on finite time regimes and small distances of the solute transport.

The aim is, to improve standard upscaling procedures by introducing a method that is capable to transfer a heterogeneous model not only on very large scales but also to intermediate scales. Standard upscaling methods are also called asymptotic methods whereas the method of coarse graining accounts for pre-asymptotic effects as well. In particular, the support volume does not always correspond to a representative volume of the heterogeneous medium.

In the groundwater literature, spatial filters have long been used to conceptually represent measurement processes /BAV 84/, /CUS 84/, /CUS 86/. The specific application of spatial filter concepts that has received the most attention is the measurement of hydraulic conductivity on different scales /ALA 89/, /BEC 94/, /BE2 96/, /DES 92/, /DES 94a/, /DEU 94/, /HAR 92/, /OLI 90/, /TID 99a/, /TID 99b/, /VEL 70/. These works contain a variety of approaches to determine measurement filters. In this study the focus is on one particular method which is referred to coarse graining.

5.3 The method of coarse graining

The idea of coarse graining is to average local functions over volumes of intermediate sizes in order to obtain functions on coarser resolution scales. The coarse scale can be e g. the resolution scale of a measurement or the discretisation scale of a numerical simulation. In other words, it is searched for a compromise between the computational effort and the numerical accuracy.

5.3.1 Definition of the filter

According to /ATT 04a/, in the following the coarse scale is assumed to be characterised by a typical length ξ and the concept of the coarse graining procedure is demonstrated on a locally fluctuating function $f(\mathbf{x})$. Fluctuations of $f(\mathbf{x})$ are smoothed out over a typical volume ξ^d around the location $\mathbf{x}$ by the following averaging procedure

$$\langle f(\mathbf{x}) \rangle_\xi \equiv \frac{1}{\xi^d} \int_{-\frac{\xi}{2}}^{\frac{\xi}{2}} d^d\,\mathbf{y}\, f(\mathbf{x} + \mathbf{y})\,. \tag{5.1}$$

$\langle f(\mathbf{x}) \rangle_\xi$ is the coarse part of the function $f(\mathbf{x})$ and $d^d\mathbf{y}$ is the infinitesimal d-dimensional volume element. Using the Fourier transform, for the smoothed function follows:

$$\langle f(\mathbf{x}) \rangle_\xi = \frac{1}{\xi^d} \int_{-\frac{\xi}{2}}^{\frac{\xi}{2}} d^d\, y\, f(\mathbf{x} + \mathbf{y}) = \frac{1}{\xi^d} \int_{-\frac{\xi}{2}}^{\frac{\xi}{2}} d^d\, y \int d^d\,\mathbf{k}\, \exp\!\big(-i\mathbf{k}\,(\mathbf{x}+\mathbf{y})\big)\, f(\mathbf{k}) \tag{5.2}$$

$$= \int d^d\,\mathbf{k}\, \exp(-i\mathbf{k}\cdot\mathbf{x}) \prod_i \frac{\sin(k_j\xi)}{k_i\xi} f(\mathbf{k})\,.$$

k_i is the component of the Fourier vector $\mathbf{k}$ in the i-th spatial direction. That means, the coarser function is characterised by a Fourier transform which differs from the Fourier transform of the original function by multiplication with the functions $\prod_i \frac{\sin(k_i\xi)}{k_i\xi}$.

The impact of these functions is illustrated in Fig. 5.2. For simplicity, a single function $\frac{\sin(k\,\xi)}{k\,\xi}$ is plotted against the Fourier variable $\mathbf{k}$ for different smoothing parameters ξ. At

k = 0, the function is equal to 1, independent of ξ. For increasing **k**-values, it decreases and starts to oscillate around 0.
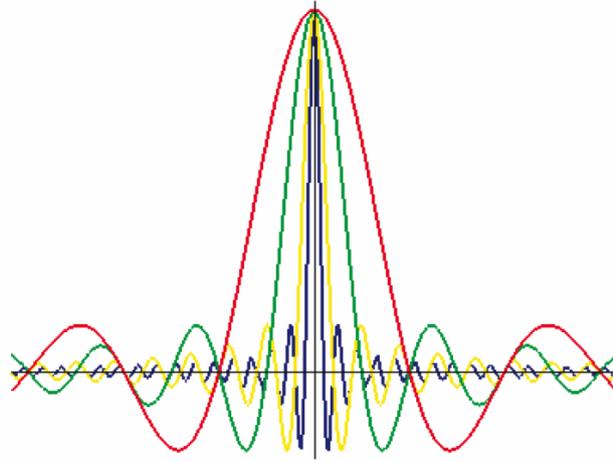

Fig. 5.2 Fourier-transformed filter functions for various scales ξ /ATT 04a/

The behaviour of the functions for different values of ξ is shortly discussed: For ξ → 0, they are equivalent to one,

$$\frac{\sin(\mathbf{k}\,\xi)}{\mathbf{k}\,\xi}\bigg|_{\xi=0} = 1 . \tag{5.3}$$

This implies that no coarse graining is performed: In this case, the function is still locally resolved:

$$\langle f(\mathbf{x})\rangle_{\xi=0} = f(\mathbf{x}). \tag{5.4}$$

In the limit of ξ → ∞, the sine function converges towards the Dirac' Delta distributions:

$$\frac{\sin(\mathbf{k}\,\xi)}{\mathbf{k}\,\xi}\bigg|_{\xi=\infty} = \lim_{\xi\to\infty}\left(\frac{1}{\xi}\right)\delta(\mathbf{k}) \tag{5.5}$$

and $\langle f(\mathbf{x})\rangle_{\xi=0}$ approaches its total volume average:

$$\begin{aligned}
\langle f(\mathbf{x})\rangle_{\xi} &= \int d^d\,\mathbf{k}\,\exp(-i\mathbf{k}\cdot\mathbf{x})\left(\frac{1}{\xi}\right)^d \delta^d(\mathbf{k})\,f(\mathbf{k}) \\
&= \left(\frac{1}{\xi}\right)^d f(\mathbf{k}=0) \\
&= \left(\frac{1}{\xi}\right)^d \int d^d\,\mathbf{x}\,f(\mathbf{x}) .
\end{aligned} \tag{5.6}$$

For finite values of ξ, the shape of the functions are the narrower, the larger are the values for ξ. Small **k**-values contribute to the integral, whereas large **k**-values are suppressed by the fast oscillations of the sine-functions. In other words, the sine-functions act as filter functions for **k**-values: The larger ξ, the wider is the spectrum of **k**-values that are filtered out (Fig. 5.2).

In summary it can be said, that the coarse graining process transforms the function $f(\mathbf{x})$ into Fourier space, filters out all **k**-values larger than a certain cut-off value ξ^{-1} and transforms the function back to real space:

$$\langle f(\mathbf{x}) \rangle_\xi \cong \int d^d \mathbf{k} \exp(-i\mathbf{k} \cdot \mathbf{x}) \, f(\mathbf{k})|_{k < 1/\xi} \equiv \int d^d \mathbf{k} \exp(-i\mathbf{k} \cdot \mathbf{x}) \, f(\mathbf{k}_-) \, . \tag{5.7}$$

For further mathematical manipulation, the sine functions are replaced by a Gaussian filter which is a simpler type of filter functions. The complementary filter function is given by

$$1 - \exp\left(-\frac{(\mathbf{k}\,\xi)^2}{8}\right) . \tag{5.8}$$

The width of the Gaussian filter is chosen in a way that its Fourier back transform has a similar shape as the sharp cut-off function defined in the original spatial filter.

5.3.2 Applications to the log-hydraulic conductivity field

In the following, the filter is applied in order to smooth a spatially variable function and to determine the statistical properties of the smoothed function. Assuming a statistically stationary function $f(\mathbf{x})$ and applying a spatial filter will not change the mean value since it is constant in space due to stationarity:

$$\overline{\langle f(\mathbf{x}) \rangle_\xi} = \frac{1}{\xi^d} \int_{-\frac{\xi}{2}}^{-\frac{\xi}{2}} d^d\mathbf{y} \, f(\mathbf{x} + \mathbf{y}) = \frac{1}{\xi^d} \int_{-\frac{\xi}{2}}^{-\frac{\xi}{2}} d^d\mathbf{y} \, \overline{f(\mathbf{x} + \mathbf{y})} = \overline{f} . \tag{5.9}$$

More interesting is the evaluation of the correlation function of the smoothed function. The function is decomposed into the mean value and a deviation from this value:

$$f(\mathbf{x}) = \overline{f} + \tilde{f}(\mathbf{x}) . \tag{5.10}$$

90

Then, the smoothed correlation function has the form

$$C^{\langle ff \rangle}(\mathbf{x} - \mathbf{x}') = \overline{\langle \tilde{f}(\mathbf{x}) \rangle_\xi \langle \tilde{f}(\mathbf{x}') \rangle_\xi} = \int d^d\mathbf{k} \exp\big(i\mathbf{k}(\mathbf{x} - \mathbf{x}')\big) \, \tilde{C}^{\langle ff \rangle}(\mathbf{k}_-) \,. \tag{5.11}$$

The integral of the right-hand side in (5.11) follows by using stationarity in the Fourier space:

$$\int d^d\mathbf{k} \exp\big(i\mathbf{k}(\mathbf{x} - \mathbf{x}')\big) \tilde{C}^{\langle ff \rangle}(\mathbf{k}_-) = \tilde{C}^{\langle ff \rangle}(\mathbf{k}, \mathbf{k}') \, \delta^d(\mathbf{k} + \mathbf{k}') = \tilde{C}^{\langle ff \rangle}(\mathbf{k}, -\mathbf{k}) \tag{5.12}$$

$$\equiv \tilde{C}^{\langle ff \rangle}(\mathbf{k}) \,.$$

Hereafter, the filter is applied to situations with a finite correlation length of heterogeneities and afterwards to cases with infinite ones in order to detect how the stochastic properties are changing.

5.3.2.1 Situations with finite correlation lengths

In porous media with finite correlation lengths, a Gaussian shaped function with isotropic correlation lengths $\ell = \ell_1 = \ell_2 = \ell_3 < \infty$) is inserted to the explicit form of the correlation function:

$$C^{\langle ff \rangle}(\mathbf{x}) = \sigma_{ff}^2 \exp\left(-\frac{\mathbf{x}^2}{2\,\ell^2}\right). \tag{5.13}$$

Then, the Fourier-transformed correlation function is given by

$$\tilde{C}^{\langle ff \rangle}(\mathbf{k}) = \sigma_{ff}^2 \, (2\pi\,\ell^2)^{d/2} \exp\left(-\frac{\mathbf{k}^2\ell^2}{2}\right). \tag{5.14}$$

The new correlation length $\ell_{(f)}$ can be derived by inserting this correlation function into the integral (5.11) and performing the integration:

$$C^{\langle ff \rangle}(\mathbf{x} - \mathbf{x}') = \int d^d\mathbf{k} \exp\big(i\mathbf{k}(\mathbf{x} - \mathbf{x}')\big)\tilde{C}^{\langle ff \rangle}(\mathbf{k}_-) \tag{5.15}$$

$$= \int d^d\mathbf{k} \exp\big(i\mathbf{k}(\mathbf{x} - \mathbf{x}')\big) \sigma_{ff}^2 \, (2\pi\,\ell^2)^{\frac{d}{2}} \exp\left(-\frac{\mathbf{k}^2\ell^2}{2} - \frac{\mathbf{k}^2\xi^2}{8}\right)$$

$$= \sigma_{ff}^2 \left(\frac{\ell^2}{\ell^2 + \frac{\xi^2}{4}}\right)^{d/2} \exp\left(-\frac{(\mathbf{x} - \mathbf{x}')^2}{2\left(\ell^2 + \frac{\xi^2}{4}\right)}\right).$$

The result implies, that the correlation length and the variance of the smoothed function are changed:

$$\ell_{\langle f\rangle} = \sqrt{\ell^2 + \frac{\xi^2}{4}} \tag{5.16}$$

$$\sigma^2_{\langle ff\rangle} = \sigma^2_{ff}\left(\frac{\ell^2}{\ell^2 + \frac{\xi^2}{4}}\right)^{d/2} = \sigma^2_{ff}\left(\frac{\ell^2}{\ell^2_{\langle f\rangle}}\right)^{d/2}. \tag{5.17}$$

The new correlation length is larger than that one in the unfiltered situation, $\ell_{\langle f\rangle} > l$, and obviously, it cannot be smaller than the new resolution scale ξ. The new variance is smaller than that one in the unfiltered case, $\sigma^2_{\langle ff\rangle} < \sigma^2_{ff}$. With growing ratio ξ / ℓ, the variance decreases. In particular, the decrease depends of the spatial dimension. In higher spatial dimension, it decreases faster than in lower dimensions. The decrease in higher dimensions may occur faster because for smaller ratios ξ / ℓ the average is already performed over larger volumes. $\xi / \ell >> 1$ implies, that the function is smoothed over many correlation lengths. Therefore, the function appears after smoothing almost homogeneous and the variance goes to zero. In contrast, for $\xi / \ell << 1$ the function is smoothed within one correlation length, meaning that almost all spatial variability is still resolved and it holds $\sigma^2_{\langle ff\rangle}/\sigma^2_{ff} \approx 1$.

These results can be generalised to smoothing functions with anisotropic correlation lengths ℓ_i and anisotropic Gaussian filter functions ξ_i:

$$C^{\langle ff\rangle}(\mathbf{x}-\mathbf{x}') = \sigma^2_{ff}\prod_{i=1}^{d}\left(\frac{\ell_i^2}{\ell_i^2 + \frac{\xi_i^2}{4}}\right)^{d/2}\prod_{i=1}^{d}\exp\left(-\frac{(x_i - x_i')^2}{2\left(\ell_i^2 + \frac{\xi_i^2}{4}\right)}\right). \tag{5.18}$$

5.3.2.2   Situations with infinite correlation lengths

In fractal porous media with infinite correlation lengths, the correlation function can be expressed as a superposition of Gaussian f as described in (3.57):

$$\hat{C}^{ff}(\mathbf{x}) = \frac{2}{\Gamma\left(\frac{\beta}{2}\right)}\int_0^{\infty} d\lambda\, \lambda^{\beta-1}\exp(-\lambda^2)\left\{\sigma^2_{ff}\exp\left(-\frac{1}{2}\frac{\sum_{j=1}^{d}x_j'^2}{\hat{L}^2}\right)\right\}. \tag{5.19}$$

with the correlation length scale $\hat{L}$ as defined in (3.58). Accordingly, the Fourier transformed correlation function has the form:

$$\widetilde{C}^{ff}(\mathbf{k}) = \frac{2}{\Gamma\left(\frac{\beta}{2}\right)} \int_0^\infty d\lambda\ \lambda^{\beta-1} \exp(-\lambda^2) \left\{ \sigma_{ff}^2 \left(2\pi\ \widehat{L}^2\right)^{d/2} \exp\left(-\frac{\mathbf{k}^2\widehat{L}^2}{2}\right)\right\}. \tag{5.20}$$

To obtain the adapted correlation length $\widehat{L}_{\langle f\rangle}$ for fractal media, the correlation function (5.19) has to be inserted into the integral (5.11) and the integration over the Fourier transformed variable $\mathbf{k}$ has to be performed:

$$\tag{5.21}$$

$$\widehat{C}^{\langle ff\rangle}(\mathbf{x}-\mathbf{x}') = \frac{2}{\Gamma\left(\frac{\beta}{2}\right)} \int_0^\infty d\lambda\ \lambda^{\beta-1} \exp(-\lambda^2) \int d^d\mathbf{k} \exp\big(i\mathbf{k}(\mathbf{x}-\mathbf{x}')\big)\widetilde{C}^{\langle ff\rangle}(\mathbf{k})$$

$$= \frac{2}{\Gamma\left(\frac{\beta}{2}\right)} \int_0^\infty d\lambda\ \lambda^{\beta-1} \exp(-\lambda^2) \int d^d\mathbf{k} \exp\big(i\mathbf{k}(\mathbf{x}$$

$$-\mathbf{x}')\big)\left\{\sigma_{ff}^2(2\pi\ \widehat{L}^2)^{\frac{d}{2}} \exp\left(-\frac{\mathbf{k}^2\widehat{L}^2}{2} - \frac{\mathbf{k}^2\xi^2}{8}\right)\right\}$$

$$= \frac{2}{\Gamma\left(\frac{\beta}{2}\right)} \int_0^\infty d\lambda\ \lambda^{\beta-1} \exp(-\lambda^2) \left\{\sigma_{ff}^2\left(\frac{\widehat{L}^2}{\widehat{L}^2+\frac{\xi^2}{4}}\right)^{\frac{d}{2}} \exp\left(-\frac{(\mathbf{x}-\mathbf{x}')^2}{2\left(\widehat{L}^2+\frac{\xi^2}{4}\right)}\right)\right\}$$

The new correlation length and the variance of the smoothed function in fractal porous media with infinite correlation lengths have the form:

$$\widehat{L}_{\langle f\rangle} = \sqrt{\widehat{L}^2 + \frac{\xi^2}{4}} = \sqrt{1 + \frac{\xi^2\lambda^2}{2\ell^2}} \tag{5.22}$$

$$\widehat{\sigma}_{\langle ff\rangle}^2 = \sigma_{ff}^2 \left(\frac{\widehat{L}^2}{\widehat{L}^2+\frac{\xi^2}{4}}\right)^{d/2} = \sigma_{ff}^2 \left(\frac{\widehat{L}^2}{\widehat{L}_{\langle f\rangle}^2}\right)^{d/2}. \tag{5.23}$$

Due to numerical problems, in this study the pre-coefficient related to grid-size dependent quantities in fractal porous media has to be written in the form:

$$\widehat{\sigma}_{\langle ff\rangle}^2 = \sigma_{ff}^2 \left(\frac{\widehat{L}^2}{\widehat{L}_{\langle f\rangle}^2}\right)^{d/2} = \sigma_{ff}^2 \left(\frac{\frac{\ell}{\sqrt{2}\lambda}}{\left[\sqrt{1+\frac{\xi^2\lambda^2}{2\ \ell^2}}\right]^3}\right) = \sigma_{ff}^2 \left(\frac{\widehat{L}}{\widehat{L}_{\langle f\rangle}^3}\right). \tag{5.24}$$

Although $\hat{L}$ tends to be infinite, the new correlation length $\hat{L}_{\langle f \rangle}$ is even larger, $\hat{L}_{\langle f \rangle} > \hat{L}$, due to the spatial filter width $\xi > 0$. The adapted variance $\hat{\sigma}^2_{\langle ff \rangle}$ is smaller than the "old" variance σ^2_{ff}.

According to situations in porous media with finite correlation lengths, the generalised result for smoothing functions with anisotropic correlation lengths in fractal media, $\hat{L}_i = \ell_i / (\sqrt{2}\lambda)$, i = 1, …, d and anisotropic filter functions ξ_j has the form:

$$\hat{C}^{\langle ff \rangle}_{ij}(\mathbf{x} - \mathbf{x}') \tag{5.25}$$

$$= \frac{2}{\Gamma\left(\frac{\beta}{2}\right)} \int_0^\infty d\lambda\, \lambda^{\beta-1} \exp(-\lambda^2) \left\{ \sigma^2_{ff} \prod_{i=1}^{d} \left(\frac{\hat{L}_i^2}{\hat{L}_i^2 + \frac{\xi_j^2}{4}} \right)^{\frac{d}{2}} \prod_{j=1}^{d} \exp\left(-\frac{(x_j - x_j')^2}{2\left(\hat{L}_j^2 + \frac{\xi_i^2}{4}\right)} \right) \right\}.$$

5.3.3   Grid-size dependent transport equations

In the previous sections, the statistical properties of a filtered random function f(**x**) were investigated. The grid-size dependent correlation length and the variance were explicitly evaluated using a Gaussian filter function. In this case, the calculations were straight forward because the filter could be applied directly to the function f(**x**).

The situation becomes more complicated if the scope is at filtering a differential equation with heterogeneous coefficients such as porosity or hydraulic conductivity. In this case, the solution of the probability density equation (PDE) depends in a complicated manner on coefficients and filtering the medium's properties independently of the PDE yields incorrect results. Making use of the Green's function formalism implies, that filtering the solution of a differential equation is equivalent to filtering the Green's function or the inverse differential operator /ATT 04a/. Nevertheless, the general procedure remains the same and can be summarised in three steps:

1. transformation of the differential equation into the Fourier space,
2. filtering out larger Fourier modes and
3. taking the Fourier back transform which gives the desired filtered differential equation and thus the filtered function.

Hereafter, the different steps of the coarse graining method, which was originally developed for large Eddy-simulations in fluid mechanics, are summarised according to /ATT 04a/. A detailed description of the coarse graining method can be found e. g. in /MCC 90/.

Step 1: Fourier transformation of the PDE equation

The Fourier transformation of the PDE reads

$$Z(\mathbf{k}, \mathbf{k}') \, \tilde{c}(\mathbf{k}', t) = S^0(\mathbf{k}) \, \tilde{c}(\mathbf{k}', t) + R(\mathbf{k}, \mathbf{k}') \, \tilde{c}(\mathbf{k}', t') = -\tilde{\rho}(\mathbf{k}) \,. \qquad (5.26)$$

S^0 indicates an operator with constant coefficients and $R(\mathbf{k}, \mathbf{k}')$ is the residual operator given in (3.65). Following Einstein's rule, the summation goes over the same indices. The Fourier-transformed operators are defined on the continuum, thus the summation is replaced by an integration over the Fourier variable. Using the Green's function formalism, the solution can be written as

$$\tilde{c}(\mathbf{k}, t) = -G^0(\mathbf{k}) \tilde{\rho}(\mathbf{k}) - G^0(\mathbf{k}) \, R(\mathbf{k}, \mathbf{k}') \, \tilde{c}(\mathbf{k}', t') \,. \qquad (5.27)$$

$G^0(\mathbf{k})$ is the inverse or Green's function of the PDE with constant coefficients. It is assumed, that the inverse operator $Z^{-1}(\mathbf{k}, \mathbf{k}')$ also exists. It is defined by

$$Z^{-1}(\mathbf{k}, \mathbf{k}'') \, Z(\mathbf{k}'', \mathbf{k}') \equiv \delta \, (\mathbf{k}, \mathbf{k}') \,. \qquad (5.28)$$

$Z^{-1}(\mathbf{k}, \mathbf{k}')$ is related to the Fourier-transformed Green's function of the full PDE by

$$Z^{-1}(\mathbf{k}, \mathbf{k}') \equiv G(\mathbf{k}, -\mathbf{k}') \,. \qquad (5.29)$$

In this context, it is emphasized, that in the Green's function a minus sign arises: The Green's function in real space is the solution of the full head equation assuming delta functions $\delta(\mathbf{x} - \mathbf{x}')$ as source terms. By transforming the governing equation into Fourier space, $\delta(\mathbf{k} - \mathbf{k}')$ follows as source term differing from the right-hand side of (5.28) by a minus sign.

Step 2: Performance of the filtering procedure

Applying the filtering procedure to the solution, provides the following set of equations

$$\tilde{c}(\mathbf{k}_-, t) = -G^0(\mathbf{k}_-)\tilde{p}(\mathbf{k}_-) - G^0(\mathbf{k}_-)R'(\mathbf{k}_-, \mathbf{k}') \, \tilde{c}(\mathbf{k}', t') \tag{5.30}$$
$$= -G^0(k_-)\tilde{p}(\mathbf{k}_-) - G^0(k_-)R'(\mathbf{k}_-, \mathbf{k}'_+) \, \tilde{c}(\mathbf{k}'_+, t')$$
$$- G^0(\mathbf{k}_-)R'(\mathbf{k}_-, \mathbf{k}'_-) \, \tilde{c}(\mathbf{k}'_-, t') \,,$$

$$\tilde{c}(\mathbf{k}_+, t) = -G^0(\mathbf{k}_+)\tilde{p}(\mathbf{k}_+) - G^0(\mathbf{k}_+)R'(\mathbf{k}_+, \mathbf{k}') \, \tilde{c}(\mathbf{k}', t') \tag{5.31}$$
$$= -G^0(\mathbf{k}_+)\tilde{p}(\mathbf{k}_+) - G^0(\mathbf{k}_+)R'(\mathbf{k}_+, \mathbf{k}'_+) \, \tilde{c}(\mathbf{k}'_+, t')$$
$$- G^0(\mathbf{k}_+)R'(\mathbf{k}_+, \mathbf{k}'_-) \, \tilde{c}(\mathbf{k}'_-, t') \,.$$

Due to the filter, the inner integration variables **k'**, **k''** and **k'''** are restricted to large- respectively small-wave numbers. The arguments of the functions and the operators are also defined on the restricted wave number spectra. Both equations are coupled because the heads on the right-hand side still depend on long- and on short wave-number contributions. As pointed out above, the main interest is on $\tilde{c}(\mathbf{k}_-, t)$ because its Fourier back transform is the grid-size dependent head distribution which is desired to determine. To that end, the solution for $\tilde{c}(\mathbf{k}_+, t)$ is inserted into the equation for $\tilde{c}(\mathbf{k}_-, t)$.

Step 3: Decoupling

The implicit set of equations (5.30) and (5.31) is solved by making use of the inverse operator as introduced in step 1 but with restricted wave spectra:

$$\tilde{c}(\mathbf{k}_-, t) = -Z^{-1}(\mathbf{k}_-, \mathbf{k}'_-)\tilde{p}(\mathbf{k}_-) - Z^{-1}(\mathbf{k}_-, \mathbf{k}'_-)R\,(\mathbf{k}'_-, \mathbf{k}''_+) \, \tilde{c}(\mathbf{k}''_+, t'') \,, \tag{5.32}$$

$$\tilde{c}(\mathbf{k}_+, t) = -Z^{-1}(\mathbf{k}_+, \mathbf{k}'_+)\tilde{p}(\mathbf{k}_+) - Z^{-1}(\mathbf{k}_+, \mathbf{k}'_+)R\,(\mathbf{k}'_+, \mathbf{k}''_-) \, \tilde{c}(\mathbf{k}''_-, t'') \,. \tag{5.33}$$

For the remaining step, $\tilde{c}(\mathbf{k}_+, t)$ has to be inserted into (5.32):

$$\tilde{c}(\mathbf{k}_-, t) = -Z^{-1}(\mathbf{k}_-, \mathbf{k}'_-)\tilde{p}(\mathbf{k}_-) \tag{5.34}$$
$$+ Z^{-1}(\mathbf{k}_-, \mathbf{k}'_-)R\,(\mathbf{k}'_-, \mathbf{k}''_+)[Z^{-1}(\mathbf{k}''_+, \mathbf{k}'''_+)\tilde{p}(\mathbf{k}'''_+)$$
$$- Z^{-1}(\mathbf{k}''_+, \mathbf{k}'''_+)R\,(\mathbf{k}'''_+, \mathbf{k}''''_-) \, \tilde{c}(\mathbf{k}''''_-, t'')] \,.$$

Step 4: Mean field approximation and localisation approximation

Equation (5.34) is rewritten into

$$Z(\mathbf{k}_-, \mathbf{k}'_-)\, \tilde{c}(\mathbf{k}'_-, t') = -\tilde{\rho}(\mathbf{k}_-) + R(\mathbf{k}_-, \mathbf{k}'_+) \tag{5.35}$$

$$\cdot\, [Z^{-1}(\mathbf{k}'_+, \mathbf{k}''_+)\tilde{\rho}(\mathbf{k}''_+) + Z^{-1}(\mathbf{k}'_+, \mathbf{k}''_+)R\,(\mathbf{k}''_+, \mathbf{k}'''_-)\, \tilde{c}(\mathbf{k}'''_-, t''')]\,.$$

Expression (5.35) looks already like the desired filtered head equation. The left-hand side of the equation is equivalent to (5.26) with all Fourier variables restricted to small-wave numbers. The large-wave fluctuations show their impact by means of the second and third terms on the right hand side. For further mathematical treatment, the long-wave fluctuations are approximated by their ensemble mean values (mean field approximation) and, hence, the second term on the right-hand side vanishes. This can be seen by expanding Z^{-1} in a perturbation series and performing the ensemble average term by term: The statistical translation invariance of the hydraulic conductivity field requires that **k + k'' = 0** with **k** > 1 / ξ and **k''** < 1 / ξ which cannot be fulfilled simultaneously and the terms have to vanish.

The third term on the right-hand side does not vanish and can be understood as a scale-dependent effective operator which is induced by small-scale heterogeneities varying on typical length scales smaller than ξ.

Step 5: Fourier back transformation

In real space, expression (5.35) reads after localisation

$$Z\langle c(\mathbf{x}, t)\rangle_\xi - \langle R' Z^{-1}\, R'\rangle\langle c(\mathbf{x}', t')\rangle_\xi = -\langle\rho\rangle_\xi\,. \tag{5.36}$$

Applying these results to the transport situation, then for the filtered concentration $\tilde{c}(\mathbf{k}_-, t)$ follows:

$$\frac{\partial}{\partial t}\tilde{c}(\mathbf{k}_-, t) + Z(\mathbf{k}_-, \mathbf{k}'_-)\, \tilde{c}(\mathbf{k}'_-, t') = -\tilde{\rho}(\mathbf{k}_-)\delta(t) \tag{5.37}$$

$$+ R'(\mathbf{k}_-, \mathbf{k}'_+)Z^{-1}(\mathbf{k}'_+, \mathbf{k}''_+)\tilde{c}(\mathbf{k}''_+, t'')$$
$$+ R'(\mathbf{k}_-, \mathbf{k}'_+)\, Z^{-1}(\mathbf{k}'_+, \mathbf{k}''_+)R'(\mathbf{k}''_+, \mathbf{k}'''_-)\tilde{c}(\mathbf{k}'''_-, t)\,.$$

In real space, the grid-size dependent transport equation then reads after substituting the scale-dependent dispersion tensor

$$\frac{\partial}{\partial t}\langle c(\mathbf{x}, t)\rangle_\xi + \nabla\big(\langle\mathbf{u}\rangle_\xi - D(t, \xi)\nabla\big)\langle c(\mathbf{x}, t)\rangle_\xi = 0\,. \tag{5.38}$$

5.3.4 Grid-size dependent dispersion coefficients

From the definitions of the centre-of-mass velocity and the dispersion coefficients in one single realisation as given by equations (3.69) and (3.70), these general grid-size dependent transport coefficients follow:

$$u_i^{CG}(t, \xi) = \frac{d}{dt} \left(-i\,\partial_{k_i}\right) \overline{\{\ln \tilde{c}(\mathbf{k}_-, t)\}}|_{\mathbf{k}_-} = 0 \tag{5.39}$$

∂_{k_i} denotes the partial derivative with respect to the $\mathbf{k}$-component in the i-th direction. The grid-size dependent quantities then have the form:

$$u_i^{eff,CG}(t, \xi) = \frac{d}{dt}\left(-i\,\partial_{k_i}\right) \overline{\{\ln \tilde{c}(\mathbf{k}_-, t)\}}|_{\mathbf{k}_-} = 0 \,, \tag{5.40}$$

$$D_{ij}^{eff,CG}(t, \xi) = \frac{1}{2}\frac{d}{dt}\left(-i\,\partial_{k_i}\right)\left(-i\,\partial_{k_j}\right) \overline{\{\ln \tilde{c}(\mathbf{k}_-, t)\}}|_{\mathbf{k}_-} = 0 \,, \tag{5.41}$$

$$D_{ij}^{ens,CG}(t, \xi) = \frac{1}{2}\frac{d}{dt}\left(-i\,\partial_{k_i}\right)\left(-i\,\partial_{k_j}\right) \ln\overline{\{\tilde{c}(\mathbf{k}_-, t)\}}|_{\mathbf{k}_-} = 0 \,. \tag{5.42}$$

Following the steps sketched in the previous sections, the following integral expressions for the contributions to the grid-size dependent dispersion coefficients in porous fractal media with finite correlation lengths can be derived:

$$\delta^{uu}\{D_{ij}^{ens,CG}\}(t, \xi) \tag{5.43}$$

$$= \bar{u}^2 \int\limits_{k'>\Lambda} \int\limits_{-\infty}^{\infty} dt'\, \tilde{c}_0(-\mathbf{k}', t-t')p_i(\mathbf{k}')\ p_j(\mathbf{k}')\ \tilde{C}^{\langle ff\rangle}(\mathbf{k}_-) \,,$$

$$\delta^{uu}\{D_{ij}^{eff,CG}\}(t, \xi) = \delta^{uu}\{D_{ij}^{ens,CG}\}(t, \xi) \tag{5.44}$$

$$-\bar{u}^2 \int\limits_{k'>\Lambda} \int\limits_{-\infty}^{\infty} dt'\, \tilde{c}_0(-\mathbf{k}', t-t')p_i(\mathbf{k}')\ p_j(\mathbf{k}')\ \tilde{C}^{\langle ff\rangle}(\mathbf{k}_-)\tilde{c}_0(-\mathbf{k}', t') \,.$$

These quantities are determined by the non-dimensional auto-correlation function $\tilde{C}^{\langle ff\rangle}(\mathbf{k}_-)$ of the velocity fluctuations.

5.4 Results for grid-size dependent transport parameters

In this part, the results for the temporal behaviour of the grid-size dependent ensemble and effective dispersion coefficients are presented in the simple case of a completely

three-dimensional isotropic model with only one single disorder correlation length $\ell_h = \ell_v = \ell$ respectively $\hat{L}_h = \hat{L}_v \equiv \widehat{L}$, an isotropic local dispersion tensor, $D_L = D_T \equiv D$, and an isotropic filter width ξ. This case corresponds to natural geological formations in deep layers which may have thicknesses up to a few hundred metres (e. g. /BRU 06/).
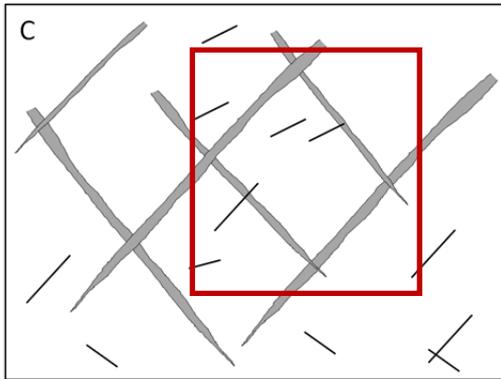
a) Situation in heterogeneous porous media with finite correlation lengths; graph modified after /KRO 91/
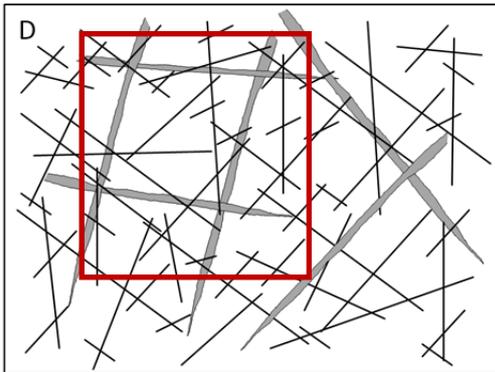
b) Situation in fractal porous media with infinite correlation lengths; graph modified after /KRO 91/
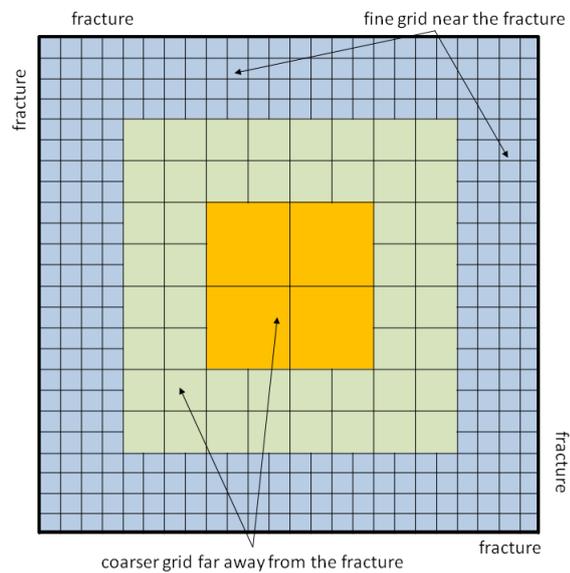
c) A grid should be used with different mesh sizes according to the distance of the fracture

Fig. 5.3 In order to model fissures and large fractures (red box in Fig. a and b), a fine grid should be used at the interface between fractures and fissures and a coarser grid elsewhere (Fig. c)

In the following, the heterogeneous background medium consists of embedded single large fractures (Fig. 5.3 a and Fig. 5.3 b) as it was shown in regions C and D in Fig. 3.1. In order to model such a situation, a fine grid should be used at the interface between the fractures and the surrounding background medium and a coarser grid at

larger distances to the fracture in order to reduce the computational effort as shown in Fig. 5.3 c and discussed e. g. by /HEN 00/, /NOE 00/ or /GRA 01/.

In this study, first the results for finite correlation lengths of the heterogeneities are presented (shown in Fig. 5.3 a) and afterwards for infinite ones (Fig. 5.3 b). In the graphs, the grid-size dependent quantities are marked by the label **CG** and quantities related to fractal porous media are indicated by a hat $\widehat{}$. Since the focus of this study is on fractal media, the results of the grid-size dependent quantities in media with finite correlation lengths are briefly presented and their explicit expressions are given in Appendix B.

5.4.1   Grid-size dependent coefficients with finite correlation lengths

The problem is characterised by four different timescales

$$\tau_u = \frac{\ell}{\bar{u}} < \tau_{u,\xi} = \tau_u \sqrt{1 + \frac{\xi^2}{4\ell^2}} = \tau_u\, \ell_{\langle f \rangle} \tag{5.45}$$

$$\tau_D = \frac{\ell^2}{D} < \tau_{D,\xi} = \tau_D \left(1 + \frac{\xi^2}{4\ell^2} \right) = \tau_D\, \ell_{\langle f \rangle}^2 \tag{5.46}$$

and a second inverse Peclet number ϵ_ξ defined as

$$\epsilon = \frac{\tau_u}{\tau_D} > \epsilon_\xi = \frac{\tau_{u,\xi}}{\tau_{D,\xi}} = \frac{\epsilon}{\sqrt{1 + \frac{\xi^2}{4\ell^2}}} = \frac{\epsilon}{\ell_{\langle f \rangle}} \tag{5.47}$$

The explicit expressions for the grid-size dispersion quantities in a 3-dimensional isotropic system have the form:

$$\delta^{uu}\{D_{ii}^{ens}(t,\xi)\} = \delta^{uu}\{D_{ii}^{ens}(t)\} - \left(\frac{\ell^2}{\ell_{\langle f \rangle}^2} \right)^{d/2} \bar{u}\, \ell_{\langle f \rangle}\, M_i^{CG,-}\left(T_\xi, 0, 0 \right) \tag{5.48}$$

$$\delta^{uu}\{D_{ii}^{eff}(t,\xi)\} = \delta^{uu}\{D_{ii}^{ens}(t,\xi)\} - \left(\frac{\ell^2}{\ell_{\langle f \rangle}^2} \right)^{d/2} \bar{u}\, \ell_{\langle f \rangle}\, M_i^{CG,+}\left(T_\xi, b_\xi, b_\xi \right) \tag{5.49}$$

with the dispersion coefficients in the unfiltered situation $\delta^{uu}\{D_{ii}(t)\}$ derived by /DEN 00a/ and given in the Appendix A and the auxiliary functions $M_i^{CG,\pm}$ due to the coarse graining method defined in (13.16) and (13.17) in the Appendix B. To obtain the grid-size dependent effective quantities, a contribution containing the parameter b_ξ has

to be subtracted from the corresponding ensemble coefficients. Hence, the grid-size dependent effective coefficients consist of four parts: two for the grid-size dependent ensemble expression and two more for the grid-size dependent effective contribution.

5.4.1.1 Temporal behaviour of the grid-size dependent coefficients with finite correlation lengths

The most remarkable new feature is an asymptotic value determined by the ratio between the width of the filter and the correlation length. In a realistic aquifer situation, the advective and the dispersive timescales are well separated and one expects $\epsilon_\xi < \epsilon \ll 1$ /GEL 83/. The presentation and discussion of the results is therefore limited to this regime. All relevant features characteristic for the various time regimes are found also in the case of a small inverse Peclet number.

The plume evolves after instantaneous solute injection at time t = 0. For times smaller than the advective timescales it has travelled advectively over distances shorter than the correlation length. The behaviour in the given aquifer still depends sensitively on the particular microscopic structure of this aquifer, so in this time regime the ensemble averaged quantities obviously have a very restricted formal meaning only. In the following discussion the focus is on the more relevant time regime $t \gg \tau_u$.

5.4.1.2 Asymptotic behaviour of the plume

For zero coarse graining, both dispersion coefficients are zero: All velocity fluctuations are modelled explicitly and, thus, no subscale part of the model exists which has to account for unresolved velocity fluctuations. With increasing filter, the asymptotic value is still below the value for the macro dispersion coefficient calculated by Homogenization or alternativly by stochastic modelling but approaches the large scale value in the limit of $\xi \gg \ell$. In this limit, coarse graining is performed over large volumes. Large scale resolution and small scale heterogeneity are well separated and coarse graining compared to homogenization respectively stochastic modelling gives the same results. For large times, the effective and ensemble dispersion coefficients become identical (13.11). If small-scale mixing is present, the width of the filter should be chosen according to the spreading of the plume in transverse direction:

$$\xi \sim \sqrt{16\, D_T\, t}\ . \tag{5.50}$$

101

In an isotropic model, as it is considered in this study, where there is only one dispersion tensor $D_L = D_T \equiv D$, the correct physical filter width is influenced by the local dispersion coefficient D.

Fig. 5.4 shows the longitudinal component for both ensemble and effective dispersion coefficients for different filter widths of ξ. The grid-size dependent ensemble quantities are indicated by dotted curves, whereas the scale-dependent effective coefficients are denoted by dashed-dotted ones. All the values are normalised with the macroscopic value $D_{11}^* = \delta^{uu}\{D_{11}\} / \delta^{uu}\{D_{11}^{macro}\}$.

Fig. 5.4 a shows the quantities without coarse graining and the scale-dependent coefficients for different ratios $\xi = a / \ell$. It is visible that for large filter widths the asymptotical limit is reached more exactly. If the correct physical filter width as given in (5.50) is inserted, both quantities show a more exact temporal behaviour because the increasing of the dispersion in the intermediate time regime $\tau_u \ll t \ll \tau_D$ starts later and the constant long-time value is reached later as well.
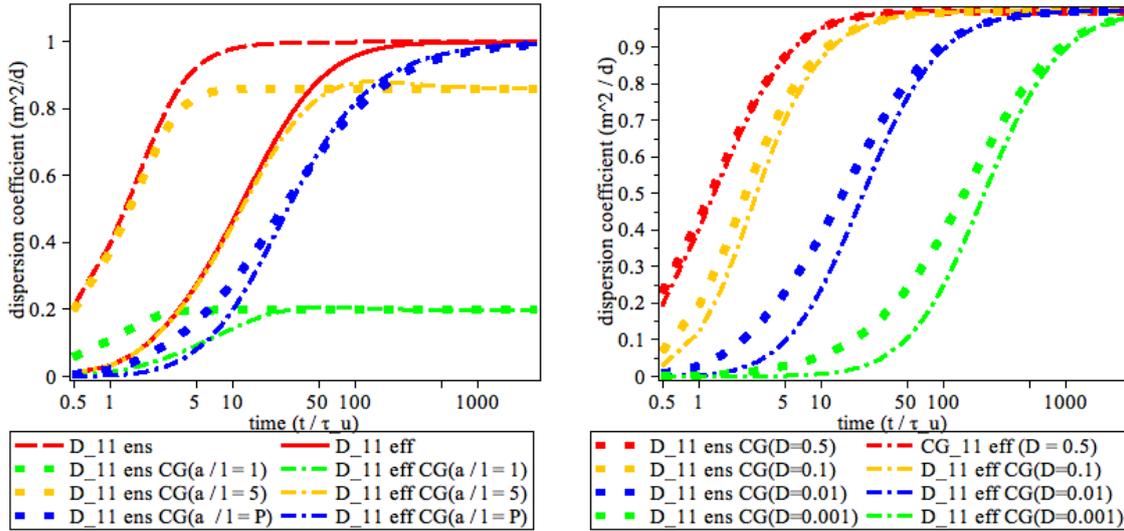
a) $D_{11}^{CG}(t, \xi)$ for D=0.01 m² / d and different ratios $\xi = a / l$

b) $D_{11}^{CG}(t, \xi)$ for various local dispersion coefficients D

Fig. 5.4 The longitudinal dispersion coefficients for different values of the filter width ξ.

All the values are normalized with $\mathbf{D_{11}^* = \delta^{uu}\{D_{11}\} / \delta^{uu}\{D_{11}^{macro}\}}$.

A closer view on the temporal behaviour of the grid-size dependent quantities using the correct physical filter width for different values of the local dispersion coefficient D is shown in Fig. 5.4 b. The effect of this parameter causes a later start of the increasing dispersion the smaller the local dispersivity is and the later the asymptotical limit is reached. For large inverse Peclet numbers $\epsilon_\xi < 1$ which do not refer to realistic aquifer situations according to /GEL 83/ the true dispersion is overestimated significantly. The difference between the ensemble and effective quantities becomes remarkable in the intermediate time regime $\tau_u \ll t \ll \tau_D$ and vanishes with increasing time.

Fig. 5.5 shows the transverse component for both ensemble and effective dispersion coefficients for various values of the filter width ξ. The ensemble quantities are again indicated by dotted curves whereas the effective coefficients are shown by dashed-dotted ones. All the values are normalized with the macroscopic value $D_{22}^* = \delta^{uu}\{D_{22}\} / \delta^{uu}\{D_{22}^{macro}\}$ as given in /DEN 00a/. Fig. 5.5 a shows the quantities without the coarse graining procedure as well as the grid-size dependent coefficients for different filter widths.
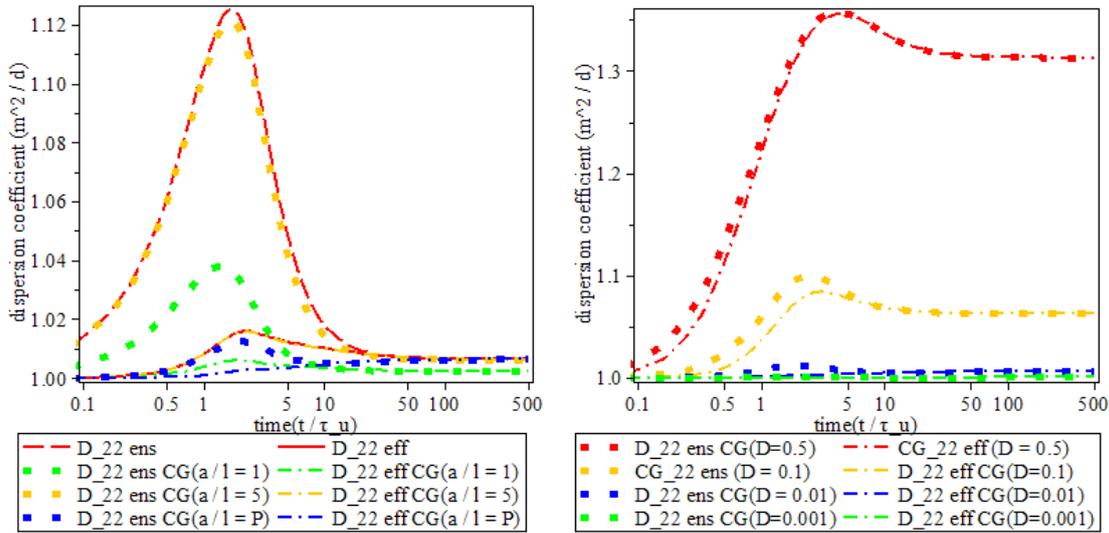
a) $D_{22}^{CG}(t, \xi)$ for D = 0.01 m² / d and different ratios $\xi = a / l$

b) $D_{22}^{CG}(t, \xi)$ for various local dispersion coefficients D

Fig. 5.5   The transverse dispersion coefficients for different values of the filter width ξ.

All the values are normalized by $D_{22}^* = \delta^{uu}\{D_{22}\} / \delta^{uu}\{D_{22}^{macro}\}$.

The ensemble dispersion approaches its long time value on timescales larger than $t \gg \tau_u$. /RUB 99/ used an exponential correlation function for the log conductivity field whereas in this study a Gaussian shaped function is used. The exponential variogram renders the results more complicated. However, the dependence of the dispersion coefficients on the ratio ξ / ℓ is comparable. Similar as in the previous section, the ensemble dispersion coefficient displays artificial mixing effects due to the spatial filter.

The effect of the coarse graining in the transverse component is similar to that one of the longitudinal component: For large filter widths the asymptotical limit is reached more exactly and for large inverse Peclet numbers – which are not common in realistic aquifer situations – the dispersion is overestimated significantly as shown in Fig. 5.5 b.

Fig. 5.4 and Fig. 5.5 show clearly that the results for the temporal behaviour of the dispersion coefficients can be improved with the coarse graining method since the effect of this method resolves only the true mixing due to the filter width. In situations with a finite correlation length of the heterogeneities this effect is important especially for small travel times of the particles because the difference between the dispersion coefficients and the coarse grained quantities vanishes with increasing time and the asymptotic limit of the quantities with and without coarse graining are the same (Fig. 5.4).

5.4.2 Grid-size dependent coefficients with infinite correlation lengths

In fractal media, the transport situation is characterised by the following four different timescales:

$$\hat{\tau}_u = \frac{\ell}{\sqrt{2}\,\lambda\,\bar{u}} = \frac{\hat{L}}{\bar{u}} < \hat{\tau}_{u,\xi} = \hat{\tau}_u \sqrt{\hat{L}^2 + \frac{\xi^2}{4}} = \hat{\tau}_u\,\hat{L}_{\langle f \rangle} \tag{5.51}$$

$$\hat{\tau}_D = \frac{\ell^2}{2\,\lambda^2 D} = \frac{\hat{L}^2}{D} < \hat{\tau}_{D,\xi} = \hat{\tau}_D \left(\hat{L}^2 + \frac{\xi^2}{4} \right) = \hat{\tau}_D\,\hat{L}_{\langle f \rangle}^2 \tag{5.52}$$

$$\hat{\epsilon}_\xi = \frac{\hat{\tau}_{u,\xi}}{\hat{\tau}_{D,\xi}} = \frac{\hat{\epsilon}}{\hat{L}_{\langle f \rangle}} \tag{5.53}$$

with the new correlation length $\hat{L}_{\langle f \rangle}$ defined in (5.22). For not getting confused with the quantities in media with finite correlation lengths, the quantities in fractal media are denoted in the following with a hat $\hat{}$ and a $\mathcal{D}$. The explicit expressions for the grid-size dependent dispersion coefficients in fractal media have the form:

104

$$\delta^{uu}\{\widehat{\mathcal{D}}_{ii}^{ens}(t,\xi)\} = \delta^{uu}\{\widehat{\mathcal{D}}_{ii}^{ens}(t)\} \tag{5.54}$$

$$- \frac{2}{\Gamma\left(\frac{\beta}{2}\right)} \int_0^\infty d\lambda\ \lambda^{\beta-1} \exp(-\lambda^2) \left(\frac{\widehat{L}}{\widehat{L}_{\langle f\rangle}^3}\right)\ \{\bar{u}\ \widehat{L}_{\langle f\rangle}\ \widehat{\mathcal{M}}_i^{CG,-}(\widehat{T}_\xi,0,0)\},$$

$$\delta^{uu}\{\widehat{\mathcal{D}}_{ii}^{eff}(t,\xi)\} = \delta^{uu}\{\widehat{\mathcal{D}}_{ii}^{ens}(t,\xi)\} \tag{5.55}$$

$$- \left[\begin{array}{c} \frac{2}{\Gamma\left(\frac{\beta}{2}\right)} \int_0^\infty d\lambda\ \lambda^{\beta-1} \exp(-\lambda^2)\left\{\bar{u}\ \widehat{L}\ \widehat{\mathcal{M}}_i^+(\widehat{T},\widehat{b},\widehat{b})\right\} \\ - \frac{2}{\Gamma\left(\frac{\beta}{2}\right)} \int_0^\infty d\lambda\ \lambda^{\beta-1} \exp(-\lambda^2)\left(\frac{\widehat{L}}{\widehat{L}_{\langle f\rangle}^3}\right)\ \left\{\bar{u}\ \widehat{L}_{\langle f\rangle}\ \widehat{\mathcal{M}}_i^{CG,+}(\widehat{T}_\xi,\widehat{b}_\xi,\widehat{b}_\xi)\right\} \end{array} \right].$$

with

$$\widehat{T}_\xi = \frac{t}{\widehat{\tau}_{u,\xi}} = \frac{t}{\widehat{\tau}_u\ \widehat{L}_{\langle f\rangle}}\ ; \qquad \widehat{b}_\xi = \frac{2t}{\widehat{\tau}_{D,\xi}} = \frac{2t}{\widehat{\tau}_D\ \widehat{L}_{\langle f\rangle}^2}\ . \tag{5.56}$$

$\widehat{L}_{\langle f\rangle}$ denotes the new correlation length given in (5.22) and ξ the filter width. As mentioned after expression (5.49), the effective coefficients consist of four parts and due to numerical problems, the pre-coefficient related to grid-size dependent quantities in fractal porous media has to be written in the form as given in (5.24). The auxiliary functions in a 3-dimensional isotropic system are given by:

$$\widehat{\mathcal{M}}_1^{CG,\pm}(\widehat{T}_\xi,\widehat{b}_\xi,\widehat{b}_\xi) \tag{5.57}$$

$$= (\mp\sigma_{ff}^2)\sqrt{\frac{\pi}{2}}\frac{1}{(1+2\widehat{b}_\xi)^2}\left\{\mathrm{erf}\left(g(\mp\widehat{T}_\xi)\right)\right.$$

$$+ \frac{1}{\sqrt{\pi}}\exp\left(-g^2(\mp\widehat{T}_\xi)\right)\left[\frac{1}{g(\mp\widehat{T}_\xi)} + \frac{4\widehat{\varphi}_\xi^2 w(\widehat{T}_\xi)}{g^2(\mp\widehat{T}_\xi)} - \frac{3}{2g^3(\mp\widehat{T}_\xi)}\right]$$

$$+ \mathrm{erf}\left(g(\mp\widehat{T}_\xi)\right)\left[\frac{4\widehat{\varphi}_\xi^2 w(\widehat{T}_\xi)}{g(\mp\widehat{T}_\xi)} + \frac{8\widehat{\varphi}_\xi^4 w(\widehat{T}_\xi)}{g(\mp\widehat{T}_\xi)} - \frac{1}{g^2(\mp\widehat{T}_\xi)}\right.$$

$$\left. - \frac{2\widehat{\varphi}_\xi^2 w(\widehat{T}_\xi)}{g^3(\mp\widehat{T}_\xi)} + \frac{3}{4g^4(\mp\widehat{T}_\xi)}\right]$$

$$- 8\widehat{\varphi}_\xi^4 \exp\left(\frac{1}{2\widehat{\varphi}^2}\right)\left[\mathrm{erfc}\left(\frac{1}{\sqrt{2}\widehat{\varphi}_\xi}\right) - \mathrm{erfc}\left(w(\widehat{T}_\xi)\right)\right]$$

$$\left. - \frac{4\sqrt{8}}{3\sqrt{\pi}}\widehat{\varphi}_\xi - \frac{4\sqrt{8}}{\sqrt{\pi}}\widehat{\varphi}_\xi^3\right\}$$

$$\widehat{\mathcal{M}}_2^{CG,\pm}(\widehat{T}_\xi, \widehat{b}_\xi, \widehat{b}_\xi) = \widehat{\mathcal{M}}_3^{CG,\pm}(\widehat{T}_\xi, \widehat{b}_\xi, \widehat{b}_\xi) \tag{5.58}$$

$$
\begin{aligned}
= (\mp\sigma_{ff}^2)\sqrt{\frac{\pi}{8}}\,\frac{1}{(1+2\widehat{b}_\xi)^2}\Bigg\{ &\frac{1}{2\sqrt{\pi}}\exp\left(-g^2(\mp\widehat{T}_\xi)\right)\left[-\frac{8\widehat{\varphi}_\xi^2 w(\widehat{T}_\xi)}{g^2(\mp\widehat{T}_\xi)}+\frac{3}{g^3(\mp\widehat{T}_\xi)}\right] \\
&+ \mathrm{erf}\left(g(\mp\widehat{T}_\xi)\right)\left[-\frac{2\widehat{\varphi}_\xi^2 w(\widehat{T}_\xi)}{g(\mp\widehat{T}_\xi)}-\frac{8\widehat{\varphi}_\xi^4 w(\widehat{T}_\xi)}{g(\mp\widehat{T}_\xi)}+\frac{1}{2g^2(\mp\widehat{T}_\xi)}\right. \\
&\quad\left.-\frac{2\widehat{\varphi}_\xi^2 w(\widehat{T}_\xi)}{g^3(\mp\widehat{T}_\xi)}-\frac{3}{4g^4(\mp\widehat{T}_\xi)}\right] \\
&-(8\widehat{\varphi}_\xi^4 - 2\widehat{\varphi}_\xi^2)\exp\left(\frac{1}{2\widehat{\varphi}_\xi^2}\right)\left[\mathrm{erfc}\left(w(\widehat{T}_\xi)\right)-\mathrm{erfc}\left(\frac{1}{\sqrt{2}\widehat{\varphi}_\xi^2}\right)\right] \\
&+\frac{\sqrt{8}}{3\sqrt{\pi}}\widehat{\varphi}_\xi + \frac{4\sqrt{8}}{\sqrt{\pi}}\widehat{\varphi}_\xi^3\Bigg\}.
\end{aligned}
$$

σ_{ff}^2 denotes the variance of the log-hydraulic conductivity and

$$\widehat{\varphi}_\xi = \frac{\dfrac{\widehat{\tau}_{u,\xi}}{\widehat{\tau}_{D,\xi}}}{\sqrt{1+2\widehat{b}_\xi}} = \frac{\widehat{\epsilon}_\xi}{\sqrt{1+2\widehat{b}_\xi}} \tag{5.59}$$

$$w(\widehat{T}_\xi) = \frac{1}{\sqrt{2}}\frac{(1+2\widehat{b}_\xi)\dfrac{1}{\widehat{\epsilon}_\xi}+\dfrac{t}{\widehat{\tau}_{u,\xi}}}{\sqrt{(1+2\widehat{b}_\xi)+\dfrac{2t}{\widehat{\tau}_{D,\xi}}}}\;;\qquad g(\mp\widehat{T}_\xi) = \frac{1}{\sqrt{2}}\frac{\mp\dfrac{t}{\widehat{\tau}_{u,\xi}}}{\sqrt{(1+2\widehat{b}_\xi)+\dfrac{2t}{\widehat{\tau}_{D,\xi}}}}\;. \tag{5.60}$$

5.4.3 Temporal behaviour of the grid-size dependent coefficients in fractal media with infinite correlation lengths

In the following, the filter is applied to the situation in fractal porous media with finite correlation lengths.

5.4.3.1 Grid-size dependent longitudinal ensemble dispersion coefficient

The explicit expression of the longitudinal ensemble dispersion coefficient in situations with small local dispersion coefficients D has the form:

$$\delta^{uu}\{\widehat{\mathcal{D}}_{11}^{ens,CG}(t,\xi)\} = \delta^{uu}\{\widehat{\mathcal{D}}_{11}^{ens}(t)\} \tag{5.61}$$

$$- \frac{2}{\Gamma\left(\frac{\beta}{2}\right)}\int_0^\infty d\lambda\ \lambda^{\beta-1}\exp(-\lambda^2)\left(\frac{\widehat{L}}{\widehat{L}_{\langle f\rangle}^3}\right)\ \{\bar{u}\ \widehat{L}_{\langle f\rangle}\ \widehat{\mathcal{M}}_1^{CG,-}(\widehat{T}_\xi,0,0)\}$$

with $\delta^{uu}\{\widehat{\mathcal{D}}_{11}^{ens}\}(t)$ given in (3.100) and $\widehat{\mathcal{M}}_1^{CG,-}$ in (5.57).

Situations with infinite Peclet numbers for $\delta^{uu}\{\widehat{\mathcal{D}}_{11}^{ens,CG}\}(t,\xi)$

In situations with infinite Peclet numbers, the expression of the longitudinal ensemble dispersion coefficient reduces to the time-independent expression:

$$\delta^{uu}\{\widehat{\mathcal{D}}_{11}^{ens,CG}\}(\xi)$$

$$= \frac{2}{\Gamma\left(\frac{\beta}{2}\right)}\int_0^\infty d\lambda\ \lambda^{\beta-1}\exp(-\lambda^2)\left\{\bar{u}\ \widehat{L}\ \sigma_{ff}^2\sqrt{\frac{\pi}{2}}\cdot\left(1-\frac{1}{\left(1+\frac{\xi^2\lambda^2}{2\,l^2}\right)^{\frac{d-1}{2}}}\right)\right\} \tag{5.62}$$

If small-scale mixing is present and the filter width is chosen according to the spreading of the plume in transverse direction $\xi\sim\sqrt{16\,D_T\,t}$, the results for effective mixing without coarse graining are recovered:

$$\delta^{uu}\{\widehat{\mathcal{D}}_{11}^{ens,CG}\}(\xi=\sqrt{16\,D_T\,t})$$

$$= \frac{2}{\Gamma\left(\frac{\beta}{2}\right)}\int_0^\infty \lambda^{\beta-1}\exp(-\lambda^2)\left\{\bar{u}\ \widehat{L}\ \sigma_{ff}^2\sqrt{\frac{\pi}{2}}\left(1-\frac{1}{\left(1+\frac{D_T\,t}{\widehat{L}^2}\right)^{\frac{d-1}{2}}}\right)\right\}d\lambda \tag{5.63}$$

$$= \delta^{uu}\{\widehat{\mathcal{D}}_{11}^{eff}\}(t)$$

This implies that – by adapting the width of the filter to the physical spreading of the plume – artificial mixing effects can be avoided in the situation for infinite correlation lengths $\widehat{L}$ as well. Therefore, the filter width of $\xi\sim\sqrt{16\,D_T\,t}$ defines the criterion for the multi-scale adaptivity.

5.4.3.2   Grid-size dependent longitudinal effective coefficient

The explicit expression of the scale-dependent longitudinal effective dispersion coefficient for small local dispersion coefficients D has the form:

$$\delta^{uu}\{\widehat{\mathcal{D}}_{11}^{\text{eff}}(t,\xi)\} = \delta^{uu}\{\widehat{\mathcal{D}}_{11}^{\text{ens}}(t,\xi)\} \tag{5.64}$$

$$-\left[\frac{2}{\Gamma\left(\frac{\beta}{2}\right)} \int_0^\infty d\lambda\ \lambda^{\beta-1} \exp(-\lambda^2) \left\{ \bar{u}\ \widehat{L}\ \widehat{\mathcal{M}}_1^+(\widehat{T},\widehat{b},\widehat{b}) \right\} \\ - \frac{2}{\Gamma\left(\frac{\beta}{2}\right)} \int_0^\infty d\lambda\ \lambda^{\beta-1} \exp(-\lambda^2) \left(\frac{\widehat{L}}{\widehat{L}_{\langle f\rangle}^3}\right) \left\{ \bar{u}\ \widehat{L}_{\langle f\rangle}\ \widehat{\mathcal{M}}_1^{\text{CG},+}(\widehat{T}_\xi,\widehat{b}_\xi,\widehat{b}_\xi) \right\} \right]$$

with $\delta^{uu}\{\widehat{\mathcal{D}}_{11}^{\text{ens,CG}}(t,\xi)\}$ defined in (5.61), $\widehat{\mathcal{M}}_1^+$ in (3.98) and $\widehat{\mathcal{M}}_1^{\text{CG},+}$ in (5.57).

Situations with infinite Peclet numbers for $\delta^{uu}\{\widehat{D}_{11}^{\text{eff,CG}}(t,\xi)\}$

For times $t \gg \widehat{\tau}_{u,\xi} > 1$ it is:

$$\delta^{uu}\{\widehat{D}_{11}^{\text{eff,CG}}\}(t,\xi) = \delta^{uu}\{\widehat{D}_{11}^{\text{ens,CG}}\}(t,\xi) \tag{5.65}$$

$$- \frac{2}{\Gamma\left(\frac{\beta}{2}\right)} \int_0^\infty d\lambda\ \lambda^{\beta-1} \exp(-\lambda^2) \bar{u}\ \widehat{L}\ \sigma_{ff}^2 \sqrt{\frac{\pi}{2}} \left[\frac{1}{\left(1+4\frac{t}{\widehat{\tau}_D}\right)^{\frac{d-1}{2}}} - \frac{1}{\left(1+\frac{\xi^2\lambda^2}{2\ l^2}+4\frac{t}{\widehat{\tau}_D}\right)^{\frac{d-1}{2}}} \right]$$

with $\delta^{uu}\{\widehat{D}_{11}^{\text{ens,CG}}(t,\xi)\}$ defined in   (5.63).

Fig. 5.6 shows the effect of the coarse graining method on the longitudinal dispersion coefficients in fractal porous media for $\beta = 0.5$. In Fig. 5.6 a, the grid-size dependent dispersion coefficients are shown for a filter width $\xi = a$, where a does not depend on the local dispersion tensor or the time, but the green curves in this figure denote the correct physical filter width $\xi = \sqrt{16\,D_T\,t}$. The unfiltered effective dispersion coefficient is shown by the red curve. It is visible, that the larger the filter width $\xi = a$ – which corresponds to a smaller cut-off effect – the larger are the dispersion values and with increasing time, the grid-size dependent longitudinal dispersion coefficients show an ergodic behaviour because they reach the same constant long-time value. The larger the filter width is, the larger is this constant value and the later it is reached. This result is

similar to that one found for the longitudinal component in media with finite correlation lengths (section 5.4.1), but the timescale is much larger in fractal media.
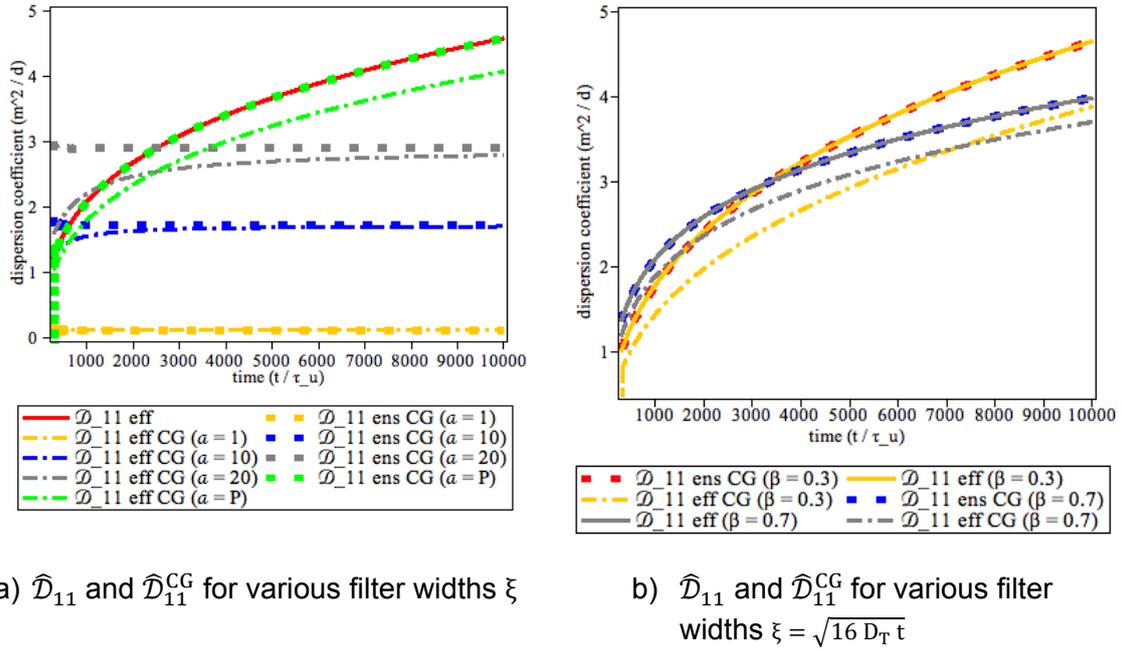
a) $\hat{\mathcal{D}}_{11}$ and $\hat{\mathcal{D}}_{11}^{CG}$ for various filter widths ξ

b) $\hat{\mathcal{D}}_{11}$ and $\hat{\mathcal{D}}_{11}^{CG}$ for various filter widths $\xi = \sqrt{16\,D_T\,t}$

Fig. 5.6   The grid-size dependent longitudinal dispersion coefficients for different values of the filter width ξ and a fractality of $\beta = 0.5$

If the correct physical filter width $\xi = \sqrt{16\,D_T\,t}$ is applied – indicated by the green curves – the grid-size dependent coefficients will not reach a constant long-time value, but they increase with growing time. In this case, the grid-size dependent ensemble dispersion coefficient is identical to the effective coefficient without the coarse graining procedure. This implies, that in fractal media the overestimation of the dispersion values in the ensemble longitudinal component can be remarkably reduces by applying the coarse graining method and the much more exact effective dispersion values can be recovered. Furthermore, if the correct physical filter width $\xi = \sqrt{16\,D_T\,t}$ is applied to the effective coefficient, the effect of the coarse graining procedure will remain visible at all times.

Fig. 5.6 b shows the effect of the coarse graining method on the longitudinal dispersion coefficients for various degrees of fractality β. In more fractal media denoted by a smaller value of β, the dispersion values and the corresponding grid-size dependent quantities are smaller for short travel times corresponding to short distances to the fracture and with increasing time and distances they are getting larger than in less fractal

media. Furthermore, it is again visible that the grid-size dependent ensemble quantity recovers the values of the corresponding unfiltered effective coefficient and that the effect of the coarse graining method on the effective coefficients remains visible at all times.

The effect of the spatial filtering is important especially for small distances corresponding to finite times. This implies, that the distance to the fracture is important: Near the fracture (small distances) a fine grid should be applied, whereas in the far field a coarser grid should be used (Fig. 5.3) e. g. /HEN 00, /NOE 00/, /GRA 01/.

5.4.3.3   Grid-size dependent transverse ensemble coefficient

The explicit grid-size dependent transverse ensemble dispersion coefficient reads:

$$
\delta^{uu}\{\widehat{\mathcal{D}}_{22}^{ens,CG}(t,\xi)\} = \delta^{uu}\{\widehat{\mathcal{D}}_{22}^{ens}(t)\}
$$

(5.66)

$$
- \frac{2}{\Gamma\left(\frac{\beta}{2}\right)} \int\limits_0^\infty d\lambda\ \lambda^{\beta-1} \exp(-\lambda^2) \left(\frac{\widehat{L}}{\widehat{L}_{\langle f\rangle}^3}\right)\ \{\bar{u}\ \widehat{L}_{\langle f\rangle}\ \widehat{\mathcal{M}}_2^{CG,-}(\widehat{T}_\xi,0,0)\}
$$

with $\delta^{uu}\{\widehat{D}_{22}^{ens}\}(t)$ defined in (3.107) and $\widehat{\mathcal{M}}_2^{CG,-}$ in (5.58).

5.4.3.4   Grid-size dependent transverse effective coefficient

The explicit expression of the grid-size dependent transverse effective dispersion coefficient has the form:

$$
\delta^{uu}\{\widehat{\mathcal{D}}_{22}^{eff}(t,\xi)\}\ =\ \delta^{uu}\{\widehat{\mathcal{D}}_{22}^{ens}(t,\xi)\}
$$

(5.67)

$$
- \left[
\begin{array}{l}
\dfrac{2}{\Gamma\left(\frac{\beta}{2}\right)} \int\limits_0^\infty d\lambda\ \lambda^{\beta-1} \exp(-\lambda^2) \left\{\bar{u}\ \widehat{L}\ \widehat{\mathcal{M}}_2^{+}(\widehat{T},\widehat{b},\widehat{b})\right\} \\[3mm]
- \dfrac{2}{\Gamma\left(\frac{\beta}{2}\right)} \int\limits_0^\infty d\lambda\ \lambda^{\beta-1} \exp(-\lambda^2) \left(\dfrac{\widehat{L}}{\widehat{L}_{\langle f\rangle}^3}\right)\ \left\{\bar{u}\ \widehat{L}_{\langle f\rangle}\ \widehat{\mathcal{M}}_2^{CG,+}(\widehat{T}_\xi,\widehat{b}_\xi,\widehat{b}_\xi)\right\}
\end{array}
\right]
$$

with $\delta^{uu}\{\widehat{D}_{22}^{ens,CG}(t,\xi)\}$ defined in (5.66), $\widehat{\mathcal{M}}_2^{+}$ in (3.98) and $\widehat{\mathcal{M}}_2^{CG,+}$ in (5.58).

Fig. 5.7 shows the effect of the coarse graining procedure on the transverse dispersion component in fractal media for various degrees of fractality and different values of the filter width $\xi = \sqrt{16\,D_T\,t}$. Fig. 5.7 a shows the effect for a local dispersion tensor D = 0.01 m² / d and various degrees of fractality β. In more fractal media indicated by a smaller value of β, the dispersion values and the corresponding grid-size dependent quantities are larger. Furthermore, it is visible that the effect of the coarse graining procedure reduces the overestimation in the transverse ensemble coefficients and recovers the values of the unfiltered transverse effective quantity.
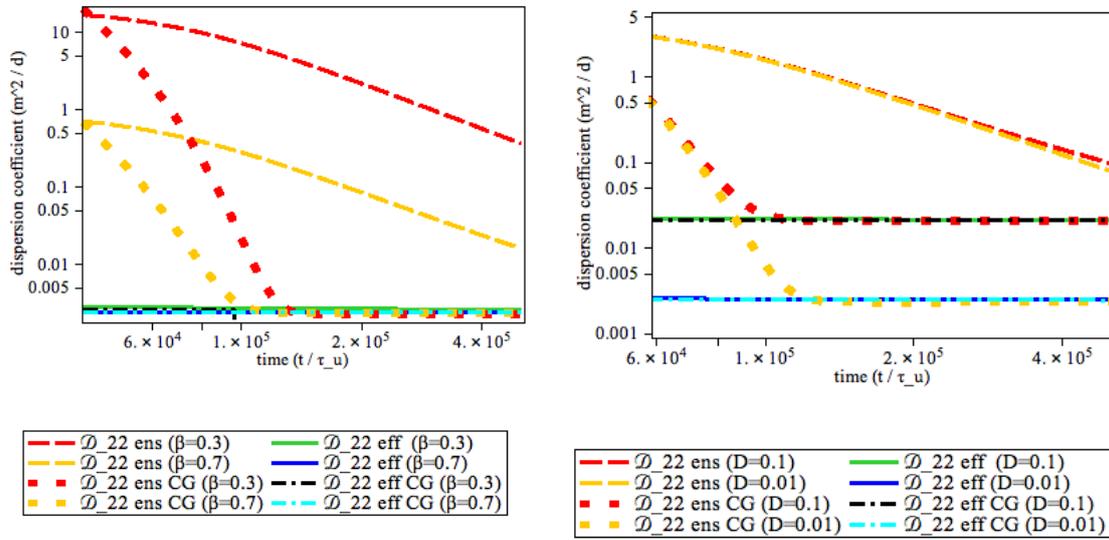
a) $\widehat{\mathcal{D}}_{22}$ and $\widehat{\mathcal{D}}_{22}^{CG}$ for D = 0.01 m² / d and various degrees of fractality β

b) $\widehat{\mathcal{D}}_{22}$ and $\widehat{\mathcal{D}}_{22}^{CG}$ for β = 0.5 and various filter widths $\xi = \sqrt{16\,D_T\,t}$

Fig. 5.7 The grid-size dependent transverse dispersion coefficients in fractal media for various degrees of fractality β and different values of the filter width ξ

This effect becomes more visible in Fig. 5.7 b where the grid-size dependent transverse coefficients are shown for various values of the correct physical filter $\xi = \sqrt{16\,D_T\,t}$. The dispersion quantities and their corresponding grid-size dependent coefficients are larger for high values of D. The grid-size dependent ensemble and the effective quantities seem to be the same and hence, the transverse quantities seem to show an ergodic behaviour. The effect of the coarse graining procedure on the transverse effective coefficient and the influence of a filter width of $\xi = a$, which does not depend on the time and the local dispersion tensor D on the transverse quantities is only marginal.

5.5 Comparison between finite and infinite correlations lengths

In the following, the results of the coarse graining method in media with finite and infinite correlation lengths of the heterogeneities are compared in order to emphasize the differences between the two types of media. Quantities without coarse graining are denoted by solid and dashed curves, whereas grid-size dependent quantities are indicated by dotted and dashed-dotted ones.
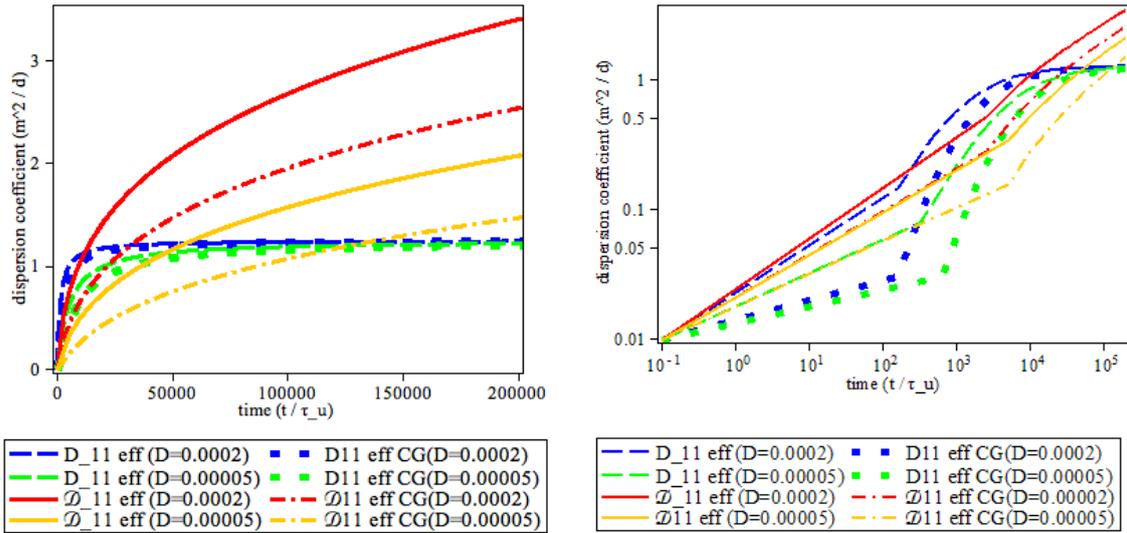
a) Effective longitudinal coefficients

b) Log-log-plot of the effective longitudinal coefficients

Fig. 5.8 Longitudinal effective coefficients in media with finite and infinite correlation lengths without and with the coarse graining procedure for $\xi = \sqrt{16\,D_T\,t}$

Fig. 5.8 shows the effective longitudinal dispersion quantities for both media with finite and infinite correlation lengths of the heterogeneities without and with coarse graining for local dispersivities of D = 2 x 10^{-4} m² / d and D = 5 x 10^{-5} m² / d. Quantities related to finite correlations lengths are denoted by D_ii, whereas quantities related to infinite correlation lengths are indicated by the script symbol $\mathcal{D}$_ii. The different line types indicate various values of the local dispersion tensor D.

It is clearly visible, that the dispersion coefficients in media with finite correlation lengths reach the same constant long-time value for both quantities with and without the coarse graining procedure (Fig. 5.8 a). On the other hand, the dispersion coefficients in fractal media do not reach a constant value. Furthermore, the quantities with-

out and with the spatial filtering procedure are always different. This fact is visible in particular in the log-log-plot (Fig. 5.8 b) by the same gradient of the curves.

In the transverse component of the dispersion coefficients the temporal behaviour of the quantities without and with coarse graining in the two media types is similar: Both the quantities without and with the spatial filtering reach the same constant long-time value – but with the difference of the much longer timescale in fractal media. Therefore, the influence of the coarse graining method on the transverse dispersion coefficients vanishes for large times in both media with finite and infinite correlation lengths.

5.6   Summary

The results for grid-size dependent ensemble and effective mixing coefficients for both media with finite and infinite correlation lengths of the heterogeneities as well as the longitudinal and transverse dispersion component were presented (Tab. 5.1).

In multi-grid codes the mesh size influences the dispersion coefficients. Therefore, grid-size dependent transport coefficients are needed for a realistic description of the situation, but according to the grid size there is an artificial mixing effect which distorts the real mixing. With the upscaling method of coarse graining this artificial mixing effect can be quantified. This spatial filtering method allows the determination of the true mixing according to the grid size.

Closed results are stated for weakly heterogeneous media, avoiding empirical functions as needed in /EFE 00/. It could be shown, that the coarse graining method reduces the artificial mixing effect in the ensemble quantities –in particular in the longitudinal dispersion component – which is responsible for a remarkable overestimation of those quantities. The coarse graining method filters out the fluctuations in the effective dispersion quantities as well. In media with finite correlation lengths, this effect is visible especially for small distances to the fracture, whereas this difference vanishes with growing distance and the same constant long-time value is reached by both the effective quantities without and with the spatial filtering procedure.

On the other hand, in fractal media the coarse graining method reduces the artificial mixing effect especially in the ensemble longitudinal quantity. If a filter width of $\xi = a$ – which does not depend on the time or the local dispersion tensor – is applied to the

longitudinal quantities, a small value of the filter width will result in a large cut-off effect and the corresponding grid-size dependent quantities will be small and reach the same constant long-time value. The larger the filter width, the smaller is the cut-off effect and the larger is the long-time value.

However, if the correct physical filter width $\xi \sim \sqrt{16\,D_T\,t}$ is applied to the longitudinal dispersion coefficients in fractal porous media, the corresponding grid-size dependent ensemble quantity recovers the values of the unfiltered effective coefficient, which reflects the dispersion more exactly. In the effective longitudinal quantity itself, the effect of this filter width persists at all times. Therefore, the coarse graining method indeed improves the dispersion quantities defining the true physical mixing.

In the transverse component in both media types with finite and infinite correlation lengths, the effect of the coarse graining method is not as significant as in the longitudinal component because it persists only for small times. With increasing time, both quantities without and with the coarse graining procedure reach the same constant long-time value and show an ergodic behaviour. In media with finite correlation lengths, this constant value is reached much earlier than in fractal media.

Tab. 5.1 Overview of the results for the temporal behaviour of the dispersion coefficients without and with the coarse graining procedure

	Heterogeneous porous media				Fractal porous media			
	longitudinal: D_{11}		transverse: D_{22}		longitudinal: $\widehat{D}_{11}$		transverse: $\widehat{D}_{22}$	
	$D_{11}^{ens}(t)$	$D_{11}^{eff}(t)$	$D_{22}^{ens}(t)$	$D_{22}^{eff}(t)$	$\widehat{D}_{11}^{ens}(t)$	$\widehat{D}_{11}^{eff}(t)$	$\widehat{D}_{22}^{ens}(t)$	$\widehat{D}_{22}^{eff}(t)$
without coarse graining	ergodic		ergodic		$\sim c\,t^{1-\beta}$	$\sim c\,t^{\frac{1-\beta}{2}}$	ergodic	
	/DEN 00a/, /DEN 00b/, /DEN 02/				/FIO 01/			
with coarse graining	$D_{11}^{ens,CG}(t,\xi)$	$D_{11}^{eff,CG}(t,\xi)$	$D_{22}^{ens,CG}(t,\xi)$	$D_{22}^{eff,CG}(t,\xi)$	$\widehat{D}_{11}^{ens,CG}(t,\xi)$	$\widehat{D}_{11}^{eff,CG}(t,\xi)$	$\widehat{D}_{22}^{ens,CG}(t,\xi)$	$\widehat{D}_{22}^{eff,CG}(t,\xi)$
$\xi \sim a$	ergodic		ergodic		ergodic		ergodic	
$\xi \sim \dfrac{}{\sqrt{16 D_T t}}$	ergodic		ergodic		$\sim c\,t^{\frac{1-\beta}{2}}$	$\sim s\,t^{\frac{1-\beta}{2}}$	ergodic)	
	/DUR 96/ /DUR 97/ /RUB 99/ /EFE 00/		/DUR 96/ /DUR 97/ /RUB 99/ /EFE 00/		/DUR 96/ /DUR 97/ /RUB 99/ /EFE 00/			

6   Adaptive numerical multi-scale solver

6.1   Introduction

Simulation of groundwater flow and solute transport in fractured porous media is currently one of the most active research fields and is of great practical importance cf. e. g. /NEU 05/, /BEA 93/, /MUR 79/, /MAL 97/, /SHI 98/, /GRA 05/, /GRA 09/, /SHA 09/. Fractures influence flow and transport processes essentially. Especially, the often high conductivity in the fractures leads to their representation as preferential fast pathways for contaminant transport. Because of their long and thin geometry, fractures are difficult to handle numerically: On the one hand, computational grids covering the whole domain where hydrology is simulated usually cannot resolve the thickness of fractures. On the other hand, the simulations on finer grids resolving the fractures even in smaller domains encounter specific difficulties with numerical solvers that demonstrate poor performance in this case.

In order to deal with these issues, fractures are often considered as objects of reduced dimensionality (surfaces in three dimensions), and the field equations are averaged along the fracture width cf., for example, /ANG 09/, /BAS 00b/, /MAR 06/, /SOR 01/. This is motivated by the thickness of the fractures, which is usually negligible in comparison with the size of the whole domain, the fact that the complicated geometry of fracture networks reduces essentially the efficiency of numerical methods and the geological data that usually do not contain enough geometrical information for the exact representation of the fractures as thin layers.

In order to analyze the quality of the results of a $(d-1)$-dimensional approach, two different representations of a fracture are considered. In the first one, the fractures have the same geometric dimension as the embedding bulk medium and are thus said to be d-dimensional, with $d = 2$ in 2d and $d = 3$ in 3d. In the second representation, the fractures are considered as $(d-1)$-dimensional manifolds, and we use the averaged model introduced in /GRI 12a/, /GRI 10/, /GRI 13/, /REI 12b/, /STI 12/. The first approach is well-established, more general, but computationally more expensive and practically applicable only for very simple geometries of the domain and the fractures. The second approach, instead, requires some working hypotheses but is computationally essentially cheaper. The second approach was verified by numerical computations

115

and comparison with the well-established d-dimensional approach. It could be shown that the results obtained by the two methods are in good agreement with each other for sufficiently small fracture widths cf. /GRI 12a/, /GRI 10/, /GRI 13/, /REI 12b/, /STI 12/. Though, for increasing fracture width, phenomena, e. g. vortices, are observed inside the fractures that are not reproduced by the $(d-1)$-dimensional model.

Therefore, the aim is to define a criterion indicating the validity of the $(d-1)$-dimensional approach. Furthermore, a dimension-adaptive strategy is introduced that is able to simulate the flow in the fracture sufficiently exact, including specific phenomena as the appearance of vortices, while keeping the computational cost sufficiently small. The resulting dimension-adaptive methods and the computation of the criterion were included in the software package d^{3}f.

6.2 Model equations

In this model, a fracture $\mathcal{F}$ is a region occupied by a porous medium whose permeability is bigger than the permeability of the medium $\mathcal{M}$ in which it is embedded. It is assumed that the same flow and transport processes occur both in the fracture and in the embedding medium. The regions $\mathcal{F}$ and $\mathcal{M}$ interact through exchange processes. To be consistent with the macroscopic continuum description, the partial differential equations governing density-driven flow are obtained by means of the balance laws of mass, momentum, and energy, and the Second Principle of Thermodynamics. These laws have to be written for each constituent of the fluid-phase (i. e. water and brine), and for the solid-phase. However, suitable hypotheses allow for a considerable reduction of the number of equations to be solved. It is assumed that the fracture and the surrounding porous medium satisfy the following requirements:

a) they are subject to a uniform temperature field;
b) pore-scale mass exchange processes between the fluid- and the solid-phase are absent everywhere in Ω;
c) the solid-phase is undeformable and at rest;
d) inertial terms are negligible in the balance laws of momentum; and
e) the porosities of the medium and the fracture are constant but, in general, different from each other.

In order to model the interaction between $\mathcal{F}$ and $\mathcal{M}$, it is necessary to provide a description of the interface separating the fracture from the embedding medium. For simplicity, this interface is assumed to be ideal. This means that mass and momentum are transferred from the fractures to the medium (and vice versa) without undergoing further processes at the interfaces.

6.2.1 The d-dimensional model

According to these simplifying hypotheses, the problem of fluid flow and brine transport in a fractured porous medium is macroscopically governed by the laws of mass balance of the brine and the fluid-phase as a whole. These equations must be written for both the porous medium and the fracture. By renaming the mass fraction of the brine by ω, these equations read

$$\partial_t(\phi_\alpha \rho_\alpha) + \nabla \cdot (\rho_\alpha \mathbf{q}_\alpha) = \rho_{\alpha,S} S_\alpha, \tag{6.1}$$

$$\partial_t(\phi_\alpha \rho_\alpha \omega_\alpha) + \nabla \cdot (\rho_\alpha \omega_\alpha \mathbf{q}_\alpha + \mathbf{J}_\alpha) = \omega_{\alpha,S} \rho_{\alpha,S} S_\alpha, \tag{6.2}$$

The index $\alpha \in \{f, m\}$ specifies whether a physical quantity is defined in the fracture, $\mathcal{F}$, or in the surrounding porous medium, $\mathcal{M} := \Omega \setminus \mathcal{F}$. The quantities ϕ_α, ρ_α, and $\mathbf{q}_\alpha$ are the fluid-phase volume fraction (porosity), mass density, and specific discharge, while ω_α and $\mathbf{J}_\alpha$ are the mass fraction and mass flux of the brine, respectively. In the right-hand side, S_α denotes the power of the source/sink, $\omega_{\alpha,S}$ is the mass fraction of the brine in the source (for a sink, $\omega_{\alpha,S} = \omega_\alpha$), $\rho_{\alpha,S} := \rho_\alpha(\omega_{\alpha,S})$.

Under the assumption of negligible inertial terms, the momentum balance laws of the brine and the fluid-phase as a whole enable to express $\mathbf{q}_\alpha$ and $\mathbf{J}_\alpha$ in terms of the quantities ϕ_α, ρ_α, ω_α (already present in (6.1) – (6.2)), and the pressure, p_α. If the validity of Darcy's and Fick's laws is assumed for the problem at hand, then $\mathbf{q}_\alpha$ and $\mathbf{J}_\alpha$ are given by

$$\mathbf{q}_\alpha = -\frac{\mathbf{K}_\alpha}{\mu}(\nabla p_\alpha - \rho_\alpha \mathbf{g}), \tag{6.3}$$

$$\mathbf{J}_\alpha = -\rho_\alpha \mathbf{D}_\alpha \nabla \omega_\alpha. \tag{6.4}$$

where $\mathbf{K}_\alpha$, μ, $\mathbf{g}$, and $\mathbf{D}_\alpha$ are the permeability tensor, fluid viscosity, gravity acceleration vector, and diffusion-dispersion tensor, respectively. Equations (6.3) – (6.4) can be obtained through the exploitation of the dissipation inequality for both $\mathcal{F}$ and $\mathcal{M}$ cf. /BEA 90/, /BEN 00/, /DEG 54/.

In general, the tensor $\mathbf{D}_\alpha$ [$\mathrm{m}^2\ \mathrm{s}^{-1}$] describes diffusion and mechanical dispersion, i. e.

$$\mathbf{D}_\alpha := \mathbf{D}_\alpha^d + \mathbf{D}_\alpha^{md} \tag{6.5}$$

The diffusion tensor, $\mathbf{D}_\alpha^d$, accounts for tortuosity, and is therefore defined by $\mathbf{D}_\alpha^d := D^d \mathbf{T}_\alpha$, where D^d is the scalar molecular diffusivity, and $\mathbf{T}_\alpha$ is the tortuosity tensor. In the following, only the case of isotropic tortuosity (i. e. $\mathbf{T}_\alpha = T_\alpha \mathbb{I}$) is considered. Furthermore, by postulating isotropic dispersivity, the tensor of mechanical dispersion, $\mathbf{D}_\alpha^{md}$, is transversely isotropic, and admits the expression given by Scheidegger /SCH 74/, i. e.

$$\mathbf{D}_\alpha^{md} := a_\alpha^t |\mathbf{q}_\alpha| \mathbb{I} + (a_\alpha^\ell - a_\alpha^t) \frac{\mathbf{q}_\alpha \otimes \mathbf{q}_\alpha}{|\mathbf{q}_\alpha|} \tag{6.6}$$

where a_α^t and a_α^ℓ are the transversal and longitudinal dispersivity lengths, respectively, and the symmetry axis which generates the transverse isotropy is given by the direction of flow, $\mathbf{q}_\alpha$, or, equivalently, by the second-order symmetric tensor $\mathbf{q}_\alpha \otimes \mathbf{q}_\alpha$ /BEA 90/.

In order to close the mathematical problem, a constitutive law for the mass density of the fluid-phase, ρ_α, is supplied. Following Oldenburg and Pruess /OLD 98/, perfect mixing of water and brine is hypothesized, which gives

$$\rho_\alpha = \rho_\alpha(\omega_\alpha) := \frac{\rho^{pW} \rho^{pB}}{\rho^{pB} - (\rho^{pB} - \rho^{pW})\omega_\alpha} \tag{6.7}$$

where the mass densities of "pure water", ρ^{pW}, and "pure brine", ρ^{pB}, are given constants. Since the mass density $\rho_\alpha(\omega_\alpha)$ varies in response to the mass fraction, the resulting non-potential flow cf. /BEA 72/ is said to be density-driven.

Requiring the validity of Darcy's law (6.3) in the fracture may be a strong assumption. Indeed, since the fluid is expected to flow faster in the fracture than in the surrounding medium, the Forchheimer's correction term cf. /DIE 05/ may become necessary for a more precise description of the flow in the fracture. Therefore, the Forchheimer equation is introduced:

$$(1 + A_\alpha q_\alpha)\boldsymbol{q}_\alpha = \boldsymbol{q}_{\alpha D} \qquad \text{with} \qquad \boldsymbol{q}_{\alpha D} = -\frac{\mathbf{K}_\alpha}{\mu}(\nabla p_\alpha - \rho_\alpha \mathbf{g}) \qquad (6.8)$$

with the Euclidean norm $q_\alpha := \sqrt{\boldsymbol{q}_\alpha \cdot \boldsymbol{q}_\alpha}$ and the Forchheimer coefficient A_α. For a detailed derivation of this equation see /GRI 13/. The non-dimensional quantity

$$F_\alpha := A_\alpha q_\alpha \qquad (6.9)$$

is said to be the Forchheimer "number". Physically, F_α represents the ratio of liquid-solid interaction to viscous resistance /ZEN 06/.

The norm of the specific discharge, q_α, can be expressed as a function of the norm $q_{\alpha D}$. Indeed, by taking the norm on both sides of (6.8), one finds the expression

$$(1 + A_\alpha q_\alpha)q_\alpha = q_{\alpha D}, \qquad \Rightarrow \qquad A_\alpha (q_\alpha)^2 + q_\alpha - q_{\alpha D} = 0. \qquad (6.10)$$

The physically meaningful solution to (6.10) reads

$$q_\alpha = \frac{-1 + \sqrt{1 + 4 A_\alpha q_{\alpha D}}}{2 A_\alpha} \qquad (6.11)$$

Substituting this result into (6.8), the formula

$$\boldsymbol{q}_\alpha = f(A_\alpha, q_{\alpha D})\boldsymbol{q}_{\alpha D} \qquad \text{with} \qquad \boldsymbol{q}_{\alpha D} = -\frac{\mathbf{K}_\alpha}{\mu}(\nabla p_\alpha - \rho_\alpha \mathbf{g}) \qquad (6.12)$$

with $f(A_\alpha, q_{\alpha D}) = \frac{2}{1 + \sqrt{1 + 4 A_\alpha q_{\alpha D}}}$ can be obtained. Equation (6.12) can be used with the equation system (6.1) – (6.4) replacing (6.3). Since equation (6.12) with $A_\alpha = 0$ yields $\boldsymbol{q}_\alpha = \boldsymbol{q}_{\alpha D}$, equation (6.12) is more general than equation (6.3), including Darcy and Forchheimer flow, and will, therefore, be considered in the following.

The assumption of Fick-type diffusion (equation (6.4)) may be questionable too, when big values of brine mass fraction are involved, though, for simplicity this is not further discussed here.

In order to close the system of equations for fracture and medium, balance laws at the fracture-medium interface need to be introduced. The mass balance at the fracture-medium interface is given by the continuity of the normal components of the mass fluxes of both the fluid-phase as a whole and the brine on $\partial \mathcal{F}$:

$$q_f \cdot n = q_m \cdot n \qquad\qquad \text{on } \partial\mathcal{F}, \qquad\qquad (6.13)$$

$$J_f \cdot n = J_m \cdot n \qquad\qquad \text{on } \partial\mathcal{F}, \qquad\qquad (6.14)$$

with n being the outer unit normal vector on $\partial\mathcal{F}$.

The balance of momentum, under the hypotheses of macroscopically inviscid fluid and negligible advective contributions, implies that both p_α and ω_α are continuous across the interface /HAS 89a/, i. e.

$$p_f = p_m \qquad \text{and} \qquad \omega_f = \omega_m \qquad \text{on } \partial\mathcal{F} \qquad\qquad (6.15)$$

6.2.2 The $(d-1)$-dimensional model

In order to get the equations for the $(d-1)$-dimensional fracture representation (with geometric shape as shown in Fig. 6.1, equations (6.1), (6.2), (6.4) and (6.12) with $\alpha = f$ are averaged. Then the fracture $\mathcal{F}$ is ideally replaced by its mean plane $\mathcal{S}$. Accordingly the band-shaped lateral boundary $\mathcal{B}$ degenerates to the closed line $\widehat{\mathcal{B}} = \mathcal{B} \cap \mathcal{S}$, which coincides with the contour of $\mathcal{S}$. By $\hat{\mathcal{S}}^{(1)}$ and $\hat{\mathcal{S}}^{(2)}$ the two sides of $\mathcal{S}$ are denoted that are geometrically indistinguishable from $\mathcal{S}$, but separate the fracture from the medium.
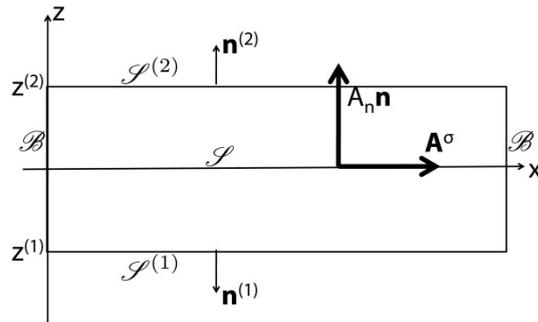
Fig. 6.1   Scheme of a planar *d*-dimensional fracture in the averaging process

The average is performed along the thickness of the fracture according to the averaging method introduced in /BEA 72/, /BEA 77/, /BEA 79/, /BEA 90/. To simplify the averaging process, first a change of variables reducing the number of fluctuations featuring in the averaged form of (6.1), (6.2), (6.4) and (6.12) is performed by using the defini-

tions of brine concentration, c_α, instead of mass fraction, $\omega_\alpha := \frac{c_\alpha}{\rho_\alpha}$. For a detailed discussion on this topic cf. /GRI 10/, /GRI 12a/, /STI 12/, /REI 12b/. After the averaging process the change is performed backwards for the new variable $\bar{c}_f \equiv \langle c_f \rangle$, denoting the average of the concentration in the fracture, to $\widehat{\omega}_f := \frac{\bar{c}_f}{\bar{\rho}_f}$, where $\widehat{\omega}_f$ is then refered to as "equivalent" mass fraction in the fracture and

$$\bar{\rho}_f \equiv \rho\big(\widehat{\omega}_f\big) = \frac{\rho^{pW}\rho^{pB}}{\rho^{pB}+(\rho^{pW}-\rho^{pB})\widehat{\omega}_f}.$$

A detailed derivation of the averaging process can be found in /GRI 12a/, /GRI 10/, /GRI 13/, /REI 12b/, /STI 12/. After some simplifications the following system of equations in $\widehat{\omega}_f$ is derived cf. /REI 12b/, /GRI 13/:

$$\partial_t(\phi_f \epsilon \rho(\widehat{\omega}_f)) + \nabla^\sigma \cdot \big(\epsilon\rho(\widehat{\omega}_f)\langle \mathbf{q}_f^\sigma \rangle\big) + \sum_k \widehat{Q}_{fn}^{(k)} = \epsilon\rho\big(\widehat{\omega}_{f,S}\big)\bar{S}_f, \tag{6.16}$$

$$\partial_t(\phi_f \epsilon \rho(\widehat{\omega}_f)\widehat{\omega}_f) + \nabla^\sigma \cdot \big(\epsilon\rho\big(\widehat{\omega}_f\big)\widehat{\omega}_f\langle \mathbf{q}_f^\sigma \rangle + \epsilon\langle \mathbf{J}_f^\sigma \rangle\big) + \sum_k \widehat{P}_{fn}^{(k)} \tag{6.17}$$

$$= \epsilon\rho\big(\widehat{\omega}_{f,S}\big)\widehat{\omega}_{f,S}\bar{S}_f,$$

where $k = 1,2$ and $\bar{S}_f := \langle S_f \rangle$ does not depend on the unknown functions and is considered to be given.

The fluxes $\langle \mathbf{q}_f^\sigma \rangle$ and $\langle \mathbf{J}_f^\sigma \rangle$ are defined by

$$\langle \mathbf{q}_f^\sigma \rangle = f\big(A_f, \widehat{q}_{fD}\big)\langle \mathbf{q}_{fD}^\sigma \rangle \qquad \text{with} \qquad \langle \mathbf{q}_{fD}^\sigma \rangle = -\frac{K_f}{\mu}\big[\nabla^\sigma \bar{p}_f - \rho\big(\widehat{\omega}_f\big)\mathbf{g}^\sigma\big], \tag{6.18}$$

$$\langle \mathbf{J}_f^\sigma \rangle = -\rho\big(\widehat{\omega}_f\big)\widehat{\mathbf{D}}_f \nabla^\sigma \widehat{\omega}_f, \tag{6.19}$$

where $\widehat{\mathbf{D}}_f := D_f \mathbf{I} + \widehat{\mathbf{D}}_f^{md}$ with the $(d-1) \times (d-1)$-tensor $\widehat{\mathbf{D}}_f^{md}$:

$$\widehat{\mathbf{D}}_f^{md} := a_f^t |\mathbf{q}_f^\sigma|\mathbb{I} + (a_f^\ell - a_f^t)\frac{\mathbf{q}_f^\sigma \otimes \mathbf{q}_f^\sigma}{|\mathbf{q}_f^\sigma|}. \tag{6.20}$$

The fluxes $\widehat{Q}_{fn}^{(k)}$ and $\widehat{P}_{fn}^{(k)}$ that are defined on the interface $\widehat{S}^{(k)}$ and express the rate at which mass leaves or enters the fracture at this interface are defined by

$$\widehat{Q}_{fn}^{(k)} = \rho\left(\widehat{\omega}_m^{(k)}\right)\widehat{q}_{fn}^{(k)}, \tag{6.21}$$

$$\hat{P}_{fn}^{(k)} = \rho\left(\widehat{\omega}_m^{(k)}\right) \omega_{upwind}^{(k)} \hat{q}_{fn}^{(k)} + \hat{J}_{fn}^{(k)}, \tag{6.22}$$

where $\omega_{upwind}^{(k)} = \widehat{\omega}_m^{(k)}$ if $\hat{q}_{fn}^{(k)} < 0$, and $\omega_{upwind}^{(k)} = \widehat{\omega}_f$ if $\hat{q}_{fn}^{(k)} \geq 0$, and

$$\hat{J}_{fn}^{(k)} = -\rho\left(\widehat{\omega}_m^{(k)}\right) D_f \frac{\widehat{\omega}_m^{(k)} - \widehat{\omega}_f}{\epsilon/2}, \tag{6.23}$$

$$\hat{q}_{fn}^{(k)} = f\left(A_f, \hat{q}_{fD}^{(k)}\right) \hat{q}_{fDn}^{(k)}, \tag{6.24}$$

$$\hat{q}_{fDn}^{(k)} = -\frac{K_f}{\mu} \left[\frac{\hat{p}_m^{(k)} - \bar{p}_f}{\epsilon/2} - \left(\rho\left(\widehat{\omega}_m^{(k)}\right) - \rho(\widehat{\omega}_f)\right) \mathbf{g} \cdot \mathbf{n}^{(k)} \right]. \tag{6.25}$$

Since (6.16) – (6.17) describe density-driven flow and brine diffusion by means of the averaged quantities $\langle \mathbf{q}_f^\sigma \rangle$ and $\langle \mathbf{J}_f^\sigma \rangle$, which are defined on the mean plane of the fracture, $\mathcal{S}$, we say that they provide an $(d-1)$-dimensional representation of the phenomena taking place in the fracture. Equations (6.16) – (6.17) in the unknowns $\widehat{\omega}_f$ and $\bar{p}_f$ are thus defined on $\mathcal{S}$ (not in $\mathcal{F}$), and have to be coupled to the set of equations for the mass fraction and the pressure defined in $\widehat{\mathcal{M}} := \Omega \setminus \mathcal{S}$, not in $\mathcal{M}$. We denote these new unknowns by $\widehat{\omega}_m \colon \widehat{\mathcal{M}} \to \mathbb{R}$ and $\hat{p}_m \colon \widehat{\mathcal{M}} \to \mathbb{R}$. They approximate the original unknown functions $\omega_m \colon \mathcal{M} \to \mathbb{R}$ and $p_m \colon \mathcal{M} \to \mathbb{R}$ defined in the smaller domain $\mathcal{M} \subset \widehat{\mathcal{M}}$. For $\widehat{\omega}_m$ and $\hat{p}_m$, we formulate equations analogous to (6.1) – (6.2):

$$\partial_t(\phi_m \rho(\widehat{\omega}_m)) + \nabla \cdot (\rho(\widehat{\omega}_m)\widehat{\mathbf{q}}_m) = \rho_{m,S} S_m, \tag{6.26}$$

$$\partial_t(\phi_m \rho(\widehat{\omega}_m)\widehat{\omega}_m) + \nabla \cdot \left(\rho(\widehat{\omega}_m)\widehat{\omega}_m \widehat{\mathbf{q}}_m + \hat{\mathbf{J}}_m\right) = \widehat{\omega}_{m,S} \rho(\widehat{\omega}_{m,S}) S_m, \tag{6.27}$$

Where

$$\widehat{\mathbf{q}}_m = f(A_m, \hat{q}_{mD})\widehat{\mathbf{q}}_{mD} \qquad \text{with} \qquad \widehat{\mathbf{q}}_{mD} = -\frac{K_m}{\mu}(\nabla \hat{p}_m - \rho(\widehat{\omega}_m)\mathbf{g}), \tag{6.28}$$

$$\hat{\mathbf{J}}_m = -\rho(\widehat{\omega}_m)\mathbf{D}_m \nabla \widehat{\omega}_m. \tag{6.29}$$

In order to close the system of equations, balance laws at the fracture-medium interface need to be introduced similar to equations (6.13) – (6.15). Since the values taken

by mass fraction and pressure on $\mathcal{S}^{(1)}$, $\mathcal{S}^{(2)}$ and in $\mathcal{F}$ may generally be different from one another in the d-dimensional model, and the $(d-1)$-dimensional model has to be able to reproduce this contingency, we require that at each point of $\mathcal{S}$ there exist three values of mass fraction and three values of pressure, i. e. we allow for the inequalities

$$\widehat{\omega}_m^{(1)} \neq \widehat{\omega}_f \neq \widehat{\omega}_m^{(2)}, \qquad \widehat{p}_m^{(1)} \neq \bar{p}_f \neq \widehat{p}_m^{(2)}, \qquad \text{on } \mathcal{S} \qquad (6.30)$$

where, in accordance with (6.15), $\widehat{\omega}_m^{(k)}$ and $\widehat{p}_m^{(k)}$ are interpreted as the values of mass fraction and pressure that the fracture and the enclosing medium have in common at $\widehat{\mathcal{S}}^{(k)}$ ($k=1,2$). So, the surface $\mathcal{S}$ behaves as a discontinuity surface in the $(d-1)$-dimensional model.

The continuity conditions at the fracture-medium interface $\mathcal{S}^{(k)}$ read

$$\widehat{Q}_{fn}^{(k)} = \widehat{Q}_{mn}^{(k)}, \quad \text{and} \quad \widehat{P}_{fn}^{(k)} = \widehat{P}_{mn}^{(k)}, \qquad \text{on } \mathcal{S}^{(k)} \text{ with } k = 1,2. \qquad (6.31)$$

with $\widehat{Q}_{mn}^{(k)} = \rho\left(\widehat{\omega}_m^{(k)}\right)\widehat{q}_{mn}^{(k)}$ and $\widehat{P}_{mn}^{(k)} = \rho\left(\widehat{\omega}_m^{(k)}\right)\widehat{\omega}_m^{(k)}\widehat{q}_{mn}^{(k)} + \widehat{J}_{mn}^{(k)}$.

The conditions on the tangential fields $\langle\mathbf{q}_f^\sigma\rangle$ and $\langle\mathbf{J}_f^\sigma\rangle$ are replaced by the simpler ones stating that $\widehat{\mathcal{B}}$ is impervious, i. e.

$$\boldsymbol{q}_f^\sigma \cdot \boldsymbol{\tau} = \boldsymbol{q}_m^\sigma \cdot \boldsymbol{\tau} = 0, \qquad \text{and} \quad \boldsymbol{J}_f^\sigma \cdot \boldsymbol{\tau} = \boldsymbol{J}_m^\sigma \cdot \boldsymbol{\tau} = 0, \qquad \text{on } \widehat{\mathcal{B}}, \qquad (6.32)$$

with $\boldsymbol{\tau}$ being the unit normal vector on $\widehat{\mathcal{B}}$. Note that equations (6.16) – (6.17) obtained by adopting Bear's method /BEA 79/, are similar to those determined by Hassanizadeh and Gray /HAS 89b/, which are based on the averaging procedure put forward by Gray /GRA 82/, /GRA 83/.

6.3 Numerical methods

In this section the numerical methods are discussed that are used to solve the equation systems introduced in section 6.2. The basic operations that are needed for modelling fractured media are implemented in the UG framework cf. /BAS 94/, /LAN 05/, where all the basic numerics are placed. Application-specific parts were implemented in d³f cf. /FEI 99/, and /SCH 12/ for the fracture specific implementation.

6.3.1   Computational grid

The computational grid is generated using the general purpose meshing software ProMesh cf. /REI 13/, further described in section 12.5. Here only some basic demands on the grid are stated that are necessary for the discretisation.

For both, the d- and the $(d-1)$-dimensional model, a regular conform grid needs to be generated that covers the whole domain Ω. Within this grid, the fracture interfaces are corresponding to edges in 2d (or surfaces in 3d) of the grid. The width of the fracture should be resolved by exactly two layers of elements that may be degenerated. Those elements are needed in order to get the three degrees of freedom in the fracture that are necessary for the $(d-1)$-dimensional discretisation. For the d-dimensional model, the coarse grid has to be of the same structure as the coarse grid for the $(d-1)$-dimensional model, meaning that the fracture is also resolved by exactly two layers of elements, only the fracture width is geometrically resolved and not replaced by zero. The reason for the same structure is the possibility to use a dimension-adaptive method as described in section 6.5.1.

6.3.2   Discretisation

The $(d-1)$-dimensional model, i. e. the coupled system (6.16) – (6.17) and (6.26) – (6.27), has different dimensionalities and separate unknown functions defined in the same domain. This feature is important for the discretization, which is a finite-volume method, also known as the control volume /KAR 95/ or finite volume element methods /CAI 90/. Application of this method to density driven flow according to Darcy's law in domains with fractures was presented in /GRI 10/, /REI 12b/, /SCH 12/. Here, a similar method is desribed cf. /GRI 13/, though, an essential difference is that the tangential part of the velocity in fractures depends not only on the degrees of freedom associated with the inner part of the fractures. Furthermore, the Forchheimer correction introduces much stronger nonlinearity in the discretised system than the Darcy law. In this section we recall the discretisation from /GRI 13/.

6.3.2.1   Discretization grids and degrees of freedom

The following notation is used. The time interval is covered by a grid $\{t^n : n \geq 0\}$ with $0 = t^0 < \cdots < t^n < \cdots;\ \tau^n := t^n - t^{n-1}$. It is assumed that Ω is polygonal, and the

$(d-1)$ -dimensional network of fractures $\mathcal{S} \subset \Omega$ is piecewise planar. The domain Ω is covered by a conformal triangulation $\mathbf{T}_\Omega$ that consists of triangles and quadrilaterals if $d = 2$ and tetrahedra, prisms and hexahedra if $d = 3$. It is supposed that for every element $e \in \mathbf{T}_\Omega$, $e \cap \mathcal{S}$ is either empty or consists only of corners, *whole* sides and *whole* edges of e. Thus, $\mathcal{S}$ is covered by the $(d-1)$-dimensional triangulation $\mathbf{T}_\mathcal{S} := \{e \cap \mathcal{S} : e \in \mathbf{T}_\Omega, e \cap \mathcal{S} \text{ is a side of } e\}$. To simplify the notation, it is assumed that every $e \in \mathbf{T}_\Omega$ has at most one side on $\mathcal{S}$ and at most one on $\partial\Omega$. Similarly, $e \in \mathbf{T}_\mathcal{S}$ may not have more than one side on $\widehat{\mathcal{B}}$. The generalization is straightforward.

Denote by Ω_h the set of all grid points, i. e. corners of the elements of $\mathbf{T}_\Omega$. Let $\mathcal{S}_h := \Omega_h \cap \mathcal{S}$. For the approximation of the discontinuities on $\mathcal{S}$, grid functions that may have several values at every $x \in \mathcal{S}_h$ are considered. To define them properly, a special enumeration of the grid points is introduced so that several indices correspond to the same x. Degrees of freedom are uniquely assigned to these indices and not directly to geometric positions.

To this end, for every $x \in \Omega_h$, consider a ball $B(x) = \{y : |y - x|_2 < \frac{1}{2}\operatorname{dist}(x, \mathbf{T}_\Omega)\}$, where $\operatorname{dist}(x, \mathbf{T}_\Omega)$ is the minimum distance between x and those sides and edges of elements $e \in \mathbf{T}_\Omega$ which do not contain x. Fractures $\mathcal{S}$ cut these balls into disjoint open subsets (cf. Fig. 6.2). Denote these subsets of $B(x)$ for all $x \in \Omega_h$ by $B_1, \dots, B_N$, where $N \geq |\Omega_h|$ is the total number of them. The closure of every B_i contains only one $x \in \Omega_h$, that is denoted by x_i. Under this enumeration, there may be $x_i = x_j \in \mathcal{S}_h$ for $i \neq j$. For simple straight fractures, points $x \in \mathcal{S} \setminus \widehat{\mathcal{B}}$ have two different indices, and the intersection points of the fractures have even more ones. For $x \in \Omega_h \setminus \mathcal{S}_h$ or $x \in \mathcal{S}_h \cap \widehat{\mathcal{B}}$, $\mathcal{S}$ does not split $B(x)$, so $\mathcal{S}$ cuts $B(x)$ into one part. For $e \in \mathbf{T}_\Omega$, denote $\Lambda^e := \{i : 1 \leq i \leq N, x_i \in e, B_i \cap e \neq \emptyset\}$. These are indices of corners of e regarding the orientation of e with respect to the fractures.
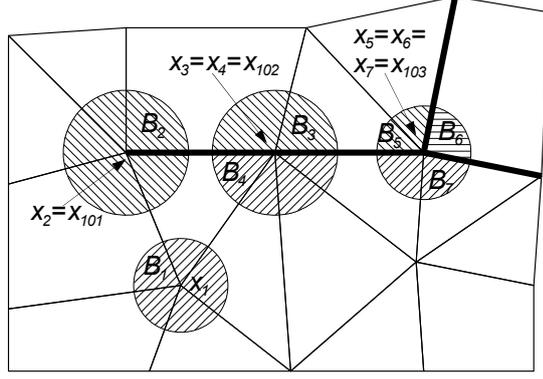
Fig. 6.2 Enumeration of the grid nodes in a piece of a grid with $N = 100$. The thick lines denote the fracture

To represent the numerical solution of (6.26) – (6.27), for time t^n and index $1 \le i \le N$ the degrees of freedom are denoted by $\hat{\omega}_{mi}^n$ and $\hat{p}_{mi}^n$. For each i, $\hat{\omega}_m(t,x)$ and $\hat{p}_m(t,x)$ in the solution of (6.26) – (6.27) are continuous in B_i. In the numerical solution, $\hat{\omega}_{mi}^n$ and $\hat{p}_{mi}^n$ approximate the limits

$$\hat{\omega}_{mi}^n \approx \lim_{x \to x_i, x \in B_i} \hat{\omega}_m(t^n, x), \qquad \hat{p}_{mi}^n \approx \lim_{x \to x_i, x \in B_i} \hat{p}_m(t^n, x). \tag{6.33}$$

Piecewise linear functions $\hat{\omega}_{mh}^n, \hat{p}_{mh}^n : \Omega \to \mathbb{R}$ are defined by the linear interpolation of the values $\hat{\omega}_{mi}^n$ and $\hat{p}_{mi}^n$ for $i \in \Lambda^e$ in every $e \in \mathbf{T}_\Omega$. These functions may be discontinuous only at $\mathcal{S}$.

In the fractures, grid functions $\hat{\omega}_{fh}^n$ and $\bar{p}_{fh}^n$ approximating $\hat{\omega}_f$ and $\bar{p}_f$ at time t^n independently on $\hat{\omega}_{mh}^n$ and $\hat{p}_{mh}^n$ are introduced. Let $N_f := |\mathcal{S}_h|$. Additionally to the enumeration above, indices $N+1, \dots, N+N_f$ are assigned to all the points from $\mathcal{S}_h$, so that $\mathcal{S}_h = \{x_{N+1}, \dots, x_{N+N_f}\}$. Then $\hat{\omega}_{fh}^n, \bar{p}_{fh}^n : \mathcal{S} \to \mathbb{R}$ are continuous piecewise linear functions with nodal values $\hat{\omega}_{fi}^n$ and $\bar{p}_{fi}^n$ at $x_i \in \mathcal{S}_h$. For $e \in \mathbf{T}_\mathcal{S}$, let $\Lambda^e := \{i : N < i \le N + N_f, x_i \in e\}$.

Furthermore, let $\Lambda_i^e := \Lambda^e \setminus \{i\}$, if $i \in \Lambda^e$, and $\Lambda_i^e := \emptyset$ otherwise. Then $\Lambda_i := \bigcup_{e \in \mathbf{T}_\Omega} \Lambda_i^e$ is the set of all the indices of neighbouring grid points of x_i. For $1 \le i \le N$, $\Lambda_i \subset \{1, \dots, N\}$, whereas for $i > N$, $\Lambda_i \subset \{N+1, \dots, N+N_f\}$. Besides this, for $i \le N$, let $\hat{\Lambda}_i := \{j : N < j \le N + N_f, x_i = x_j\}$ and, for $i > N$, let $\hat{\Lambda}_i := \{j : 1 \le j < N, x_i = x_j\}$. Sets $\hat{\Lambda}_i$ represent the relations between the "fracture DOF (degree of freedom) indices" and the "bulk medium DOF indices" of points $x_i \in \mathcal{S}_h$. Note that for $i \le N$, $|\hat{\Lambda}_i| \le 1$.

6.3.2.2   The finite-volume scheme

With each i, $1 \leq i \leq N$, a computation cell ("control volume") is associated by constructing a conformal dual mesh of finite volumes $V_i \subset \mathbb{R}^d$ using the so-called barycenter based control volumes. Then V_i is defined as a union of V_i^e for all $e \in \mathbf{T}_\Omega$ such that $i \in \Lambda^e$. To get V_i^e, the element e is cut by the segments of the straight lines, connecting the barycenter of this element with the centers of its sides (for $d = 2$), or by the segments of the plains spanning the barycenter of the element, the centers of the edges and the barycenters of the sides (for $d = 3$). Then V_i^e is the part of e containing x_i. The segments are denoted by γ_{ij}^e, i. e. $\gamma_{ij}^e := e \cap \partial V_i \cap \partial V_j$ for $j \leq N$. Besides, $\gamma_{ij}^e := e \cap \partial V_i \cap \mathcal{S}$ with $j \in \hat{\Lambda}_i$ and $\gamma_{i0}^e := e \cap \partial V_i \cap \partial \Omega$. Then

$$\partial V_i = \bigcup_{e:i \in \Lambda^e} \bigcup_{j \in \Lambda_i^e \cup \hat{\Lambda}_i \cup \{0\}} \gamma_{ij}^e. \tag{6.34}$$

By $\mathbf{n}_{ij}^e$ the unit normal vector to γ_{ij}^e pointing out of V_i, i. e. $\mathbf{n}_{ji}^e = -\mathbf{n}_{ij}^e$, is denoted. Normals $\mathbf{n}^{(1)}$ and $\mathbf{n}^{(2)}$ are constant on γ_{ij}^e. One of them is $\mathbf{n}_{ij}^e$, the other one $\left(-\mathbf{n}_{ij}^e\right)$.

Control volumes V_i are used in the discretization of (6.26) – (6.27). For every i, $1 \leq i \leq N$, if x_i does not lie on the Dirichlet boundary, (6.26) – (6.27) are integrated over V_i. After the application of the divergence theorem, one gets:

$$\phi_m \int_{V_i} \partial_t \rho(\hat{\omega}_{mh}) \, dx + \sum_{e,j} \int_{\gamma_{ij}^e} \rho(\hat{\omega}_{mh}) \hat{\mathbf{q}}_m \cdot \mathbf{n}_{ij}^e \, ds = \int_{V_i} \rho(\hat{\omega}_{mh,S}) S_m \, dx, \tag{6.35}$$

$$\phi_m \int_{V_i} \partial_t (\rho(\hat{\omega}_{mh}) \hat{\omega}_{mh}) \, dx + \sum_{e,j} \int_{\gamma_{ij}^e} \left(\hat{\omega}_{mh}^n \rho(\hat{\omega}_{mh}^n) \hat{\mathbf{q}}_m + \hat{\mathbf{J}}_m\right) \cdot \mathbf{n}_{ij}^e \, ds$$

$$= \int_{V_i} \hat{\omega}_{mh,S} \rho(\hat{\omega}_{mh,S}) S_m \, dx, \tag{6.36}$$

where the summation runs over all $e \in \mathbf{T}_\Omega$, such that $i \in \Lambda^e$, and $j \in \Lambda_i^e \cup \hat{\Lambda}_i \cup \{0\}$. For the approximation of the time derivative the backward Euler scheme is used:

$$\int_{V_i} \partial_t \rho(\hat{\omega}_{mh}) \, dx = |V_i| [\rho(\hat{\omega}_{mh}^n) - \rho(\hat{\omega}_{mh}^{n-1})] / \tau^n, \tag{6.37}$$

$$\int_{V_i} \partial_t(\rho(\widehat{\omega}_{mh})\widehat{\omega}_{mh})\, dx = |V_i| \big[\rho(\widehat{\omega}_{mh}^n)\widehat{\omega}_{mh}^n - \rho(\widehat{\omega}_{mh}^{n-1})\widehat{\omega}_{mh}^{n-1}\big]/\tau^n, \tag{6.38}$$

The summands (6.35)-(6.36) corresponding to the indices $i \in \Lambda_i^e \cup \{0\}$ depend only on $\widehat{\omega}_{mh}^n$ and $\widehat{p}_{mh}^n$. For them, the approximation from /FRO 98b/ is used, except that the Darcy velocity at the integration points is replaced by the Forchhheimer velocity according to (6.12). In particular, the so-called consistent velocity cf. /FRO 98a/, /FRO 96a/ is used for $\widehat{\mathbf{q}}_{mD}(\widehat{\omega}_{mh}^n, \widehat{p}_{mh}^n)$ (and therefore for $\widehat{\mathbf{q}}_m = F(A_m, \widehat{\mathbf{q}}_{mD})\widehat{\mathbf{q}}_{mD}$). An upwind method is applied for the discretization of the convection term $\widehat{\omega}_{mh}^n\rho(\widehat{\omega}_{mh}^n)\widehat{\mathbf{q}}_m$.

The summand with $j \in \hat{\Lambda}_i$ in (6.35) – (6.36) requires a special treatment. Let e be such an element that $i \in \Lambda^e$ and $\gamma_{ij}^e \neq \emptyset$. Let $k \in \{1,2\}$ be such that $\mathbf{n}_{ij}^e = -\mathbf{n}^{(k)}$. Then (6.31) and the following approximations are used:

$$\int_{\gamma_{ij}^e} \rho(\widehat{\omega}_{mh}^n)\widehat{\mathbf{q}}_m \cdot \mathbf{n}_{ij}^e ds = \int_{\gamma_{ij}^e} \widehat{Q}_{fn}^{(k)} ds \approx |\gamma_{ij}^e|\widehat{Q}_{fn}^{(k)}(\widehat{p}_{mi}^n, \bar{p}_{fj}^n; \widehat{\omega}_{mi}^n, \widehat{\omega}_{fj}^n), \tag{6.39}$$

$$\int_{\gamma_{ij}^e} (\widehat{\omega}_{mh}^n\rho(\widehat{\omega}_{mh}^n)\widehat{\mathbf{q}}_m + \mathbf{J}_m) \cdot \mathbf{n}_{ij}^e ds = \int_{\gamma_{ij}^e} \widehat{P}_{fn}^{(k)} ds \approx |\gamma_{ij}^e|\widehat{P}_{fn}^{(k)}(\widehat{p}_{mi}^n, \bar{p}_{fj}^n; \widehat{\omega}_{mi}^n, \widehat{\omega}_{fj}^n). \tag{6.40}$$

These approximations are algebraic functions of $\widehat{\omega}_{mh}^n$, $\widehat{p}_{mh}^n$, $\widehat{\omega}_{fh}^n$ and $\bar{p}_{fh}^n$.

For the discretization of (6.16) – (6.17), $(d-1)$-dimensional computation cells are constructed in $\mathcal{S}$: With every $i > N$, the $(d-1)$-dimensional control volume $S_i := \bigcup_{j\in\hat{\Lambda}_i} \bigcup_{e\in\mathbf{T}_\Omega:j\in\Lambda^e} \gamma_{ij}^e$ is associated. At the intersections of the fractures, S_i may lie in several intersecting planes. For $e \in \mathbf{T}_S$, boundary segments σ_{ij}^e of S_i analogously to γ_{ij}^e are introduced: For $i, j > N$, $\sigma_{ij}^e := e \cap \partial S_i \cap \partial S_j$. Besides this, σ_{i0}^e is the intersection of $e \cap \partial S_i$ with the edge of the fracture. For every σ_{ij}^e, $\mathbf{n}_{ij}^e$ is the unit normal vector that lies in the plane of e and points out of S_i. Note that S_i are barycenter based control volumes, too. Integration of (6.16) – (6.17) over S_i and performing some algebraic transformations yields:

$$\sum_{k=1,2} \left[\frac{\varphi_f \epsilon}{2} \int_{S_i} \partial_t \rho(\widehat{\omega}_{fh}) \, dx + \frac{\epsilon}{2} \sum_{e,j} \int_{\sigma_{ij}^e} \rho(\widehat{\omega}_{fh}^n) f\left(A_f, \widehat{q}_{fD}^{(k)}\right) \langle \widehat{\mathbf{q}}_{fD}^{\sigma} \rangle \cdot \mathbf{n}_{ij}^e \, dl \right.$$

$$\left. + \int_{S_i} \widehat{Q}_{fn}^{(k)} \, ds \right] = \epsilon \int_{S_i} \rho(\widehat{\omega}_{fh,S}) \bar{S}_f \, ds, \tag{6.41}$$

$$\sum_{k=1,2} \left[\frac{\varphi_f \epsilon}{2} \int_{S_i} \partial_t \left(\rho(\widehat{\omega}_{fh}) \widehat{\omega}_{fh}\right) dx \right.$$

$$+ \frac{\epsilon}{2} \sum_{e,j} \int_{\sigma_{ij}^e} \left(\widehat{\omega}_{fh} \rho(\widehat{\omega}_{fh}) f\left(A_f, \widehat{q}_{fD}^{(k)}\right) \langle \widehat{\mathbf{q}}_{fD}^{\sigma} \rangle + \langle \mathbf{J}_f^{\sigma} \rangle \right) \cdot \mathbf{n}_{ij}^e \, dl$$

$$\left. + \int_{S_i} \widehat{P}_{fn}^{(k)} \, ds \right] = \epsilon \int_{S_i} \rho(\widehat{\omega}_{fh,S}) \widehat{\omega}_{fh,S} \bar{S}_f \, ds, \tag{6.42}$$

where the summation runs over all $e \in \mathbf{T}_S$, such that $i \in \Lambda_i^e$, and $j \in \Lambda_i^e \cup \widehat{\Lambda}_i \cup \{0\}$. For the time derivatives in (6.41) – (6.42) the backward Euler scheme is used analogously as in (6.37) – (6.38).

As σ_{ij}^e are segments of straight lines (for $d = 3$) or points (for $d = 2$), the integrals over them in (6.41)-(6.42) are discretized using the method from /FRO 98b/ formulated in $(d-1)$ dimensions for $\widehat{\omega}_{fh}^n$ and $\bar{p}_{fh}^n$. The only modification is that the velocity is multiplied by $f(A_f, \widehat{q}_{fD}^{(k)})$. For the convection term in (6.42), a $(d-1)$-dimensional version of the upwind method for the discretization of (6.36) is applied. For $\langle \widehat{\mathbf{q}}_{fD}^{\sigma} \rangle$, the consistent velocity from /FRO 96b/ is used. Furthermore, the approximations of these integrals require the values of $f(A_f, \widehat{q}_{fD}^{(k)})$ at the integration points located at the centers of σ_{ij}^e. They are approximated using $f(A_f, \widehat{q}_{fD}^{(k)}) \approx f(A_f, \tilde{q}_{fD}^{(k)})$ with $\tilde{q}_{fD}^{(k)} := \sqrt{\langle \widehat{\mathbf{q}}_{fD}^{\sigma} \rangle \cdot \langle \widehat{\mathbf{q}}_{fD}^{\sigma} \rangle + \left(\widehat{q}_{fDn,i}^{(k)} + \widehat{q}_{fDn,j}^{(k)} \right)^2 /4}$, where $\widehat{q}_{fDn,i}^{(k)}$ and $\widehat{q}_{fDn,j}^{(k)}$ are values of $\widehat{q}_{fDn}^{(k)}$ according to (6.25) at x_i and x_j, resp..

To approximate the integrals of $\hat{Q}_{fn}^{(k)}$ and $\hat{P}_{fn}^{(k)}$ (cf. (6.21) – (6.22)) in (6.41) – (6.42), the fact that $S_i := \bigcup_{j \in \widehat{\Lambda}_i} \bigcup_{e:j \in \Lambda^e, \mathbf{n}_{ij}^e = -\mathbf{n}^{(k)}} \gamma_{ij}^e$ is used where γ_{ij}^e are disjoint planar sets:

$$\int\limits_{S_i} \hat{Q}_{fn}^{(k)} ds \approx \sum_{j \in \widehat{\Lambda}_i} \sum_{e:j \in \Lambda^e, \mathbf{n}_{ij}^e = -\mathbf{n}^{(k)}} |\gamma_{ji}^e|\, \hat{Q}_{fn}^{(k)}(\hat{p}_{mj}^n, \bar{p}_{fi}^n; \widehat{\omega}_{mj}^n, \widehat{\omega}_{fi}^n), \tag{6.43}$$

$$\int\limits_{S_i} \hat{P}_{fn}^{(k)} ds \approx \sum_{j \in \widehat{\Lambda}_i} \sum_{e:j \in \Lambda^e, \mathbf{n}_{ij}^e = -\mathbf{n}^{(k)}} |\gamma_{ji}^e|\, \hat{P}_{fn}^{(k)}(\hat{p}_{mj}^n, \bar{p}_{fi}^n; \widehat{\omega}_{mj}^n, \widehat{\omega}_{fi}^n). \tag{6.44}$$

The contribution of (6.43) – (6.44) to (6.41) – (6.42) is exactly the same as the contribution of the terms (6.39) – (6.40) to (6.35) – (6.36) so that the entire discretization is conservative w.r.t. the mass of the total fluid phase and mass of the salt.

Note that the exact evaluation of $\hat{Q}_{fn}^{(k)}$ and $\hat{P}_{fn}^{(k)}$ in (6.39) – (6.40) and (6.43) – (6.44) is not possible because of $\nabla^\sigma \bar{p}_f$ in $\langle \widehat{\mathbf{q}}_{fD}^\sigma \rangle$ (cf. (6.21), (6.22), (6.24)): At grid nodes, $\bar{p}_{fh}^n$ is not differentiable. For this, we approximate $\langle \widehat{\mathbf{q}}_{fD}^\sigma \rangle$ in the integrands over $S_i \cap e$ by the arithmetical average of $\langle \widehat{\mathbf{q}}_{fD}^\sigma \rangle$ at the integration points of σ_{ij}^e for $j \in \Lambda_i^e$.

Conditions (6.32) at $\widehat{\mathcal{B}}$ are natural boundary conditions for the finite-volume discretization. They introduce no additional terms in (6.35) – (6.36) and (6.41) – (6.42). Further boundary conditions should be used for $\widehat{\omega}_f$ and $\bar{p}_f$ at $\mathcal{S} \cap \partial\Omega$.

Using the introduced approximations of the integrals in (6.35) – (6.36) for all V_i and in (6.41)-(6.42) for all S_i, a sparse system of $N + N_f$ nonlinear algebraic equations is obtained.

Technically, the assembling of this nonlinear system can be implemented as a cycle over only the elements of $\mathbf{T}_\Omega$. When assembling the contribution of, say, triangle (x_1, x_2, x_4) in Fig. 6.2, not only the local matrices for (6.35) – (6.36) are computed, but also a part of the local matrix for (6.41) – (6.42) for the segment $[x_{101}, x_{102}]$ for only one k such that $\mathbf{n}^{(k)}$ is the inner normal for the triangle. As soon as the contribution of the element on the opposite side of the fracture is assembled, the terms with the second k are added to the local matrix of $[x_{101}, x_{102}]$. Thus distinguishing between the sides of the fractures is avoided.

For the d-dimensional model, i. e. equations (6.1) – (6.2), the same finite-volume discretisation as for (6.26) – (6.27) is used.

6.3.3 Numerical solution

In programs d³f and r³t, implicit time discretisations are used. This means, the discretisation of the model in space and time leads to a large sparse system of algebraic equations in every time step. Computation of the stationary flow with d³f requires the solution of a large sparse non-linear system of algebraic equations, too. In r³t, further methods like operator splitting, can be used for the reaction terms.

In the simulations, these non-linear systems are solved by the Newton method. To make use of the sparsity of the linear systems in the iterations of the nonlinear solver, they are solved by the BiCGStab method with the geometric multigrid preconditioning cf. /BAR 09/. In the multigrid cycle, the ILU$_\beta$-smoothers and the Gaussian elimination as the coarse grid solver are used. This multigrid preconditioner proved to be very efficient in the case of not too complicated geometries such that the coarse grid is not extremely detailed. The matrices in the grid hierarchy are not computed by the Galerkin formula but assembled as the Jacobians of the discretized nonlinear systems for each grid.

However, for the d-dimensional fracture representation the geometric anisotropy of the fractures may lead to convergence problems in the linear solver. To overcome this problem a multigrid method using a dimension-transfer is introduced in section 6.5.1.

6.4 Comparison of d- and $(d-1)$-dimensional approaches

In this section results of the d- and the $(d-1)$-dimensional approaches are compared in order to see, whether the use of the $(d-1)$-dimensional model is adequate or a full resolution of the fracture is necessary.

6.4.1 Benchmark problems

A modified version of the classic seawater intrusion problem by Henry /HEN 64/ is considered where the domain, a rectangle 2×1 m^2, features a fracture (cf. Fig. 6.3a). For

the test problem in 3d the geometry is extended to a three-dimensional one, a hexahedron $2 \times 2 \times 1$ m^3 (cf. Fig. 6.3b).
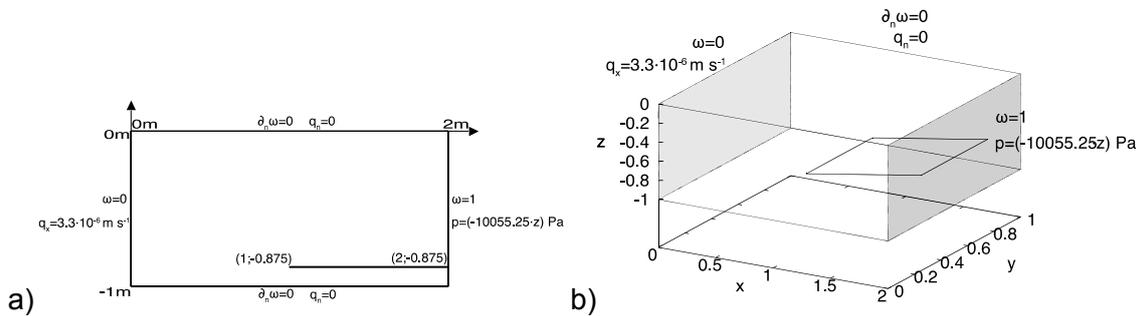
Fig. 6.3   Geometry and boundary conditions for the modified Henry problem featuring a fracture. a) 2d case, b) 3d case

At the top ($z = 0$) and the bottom ($z = -1$ m) (and in 3d at the front ($y = 0$) and the backside ($y = 1$ m)), zero-flux boundary conditions for both the flow and the transport equations are imposed. At the inland side ($x = 0$), $\omega_m = 0$ (fresh water) and a constant flux ($q = -3.3 \cdot 10^{-5}$ m $\cdot$ s^{-1}, cf. /SIM 04/) is prescribed. At the sea side ($x = 2$ m), $\omega_m = \widehat{\omega}_f = 1$ and hydrostatic pressure is imposed. The parameters used for computations are listed in Tab. 6.1.

Tab. 6.1   Parameters for the Henry problem

Symbol	Quantity	Value
D_m	Diffusion coefficient in the medium	$6.6 \cdot 10^{-6}$ m^2 s^{-1}
D_f	Diffusion coefficient in the fracture	$13.2 \cdot 10^{-6}$ m^2 s^{-1}
g	Gravity	9.81 m s^{-2}
K_m	Permeability of the medium	$1.019368 \cdot 10^{-9}$ m^2
K_f	Permeability of the fracture	$1.019368 \cdot 10^{-6}$ m^2
ϕ_m	Porosity of the medium	0.35
ϕ_f	Porosity of the fracture	0.7
μ	Viscosity	10^{-3} kg m^{-1} s^{-1}
ρ^{pW}	Density of water	10^3 kg m^{-3}
ρ^{pB}	Density of brine	$1.025 \cdot 10^3$ kg m^{-3}
$a_\alpha^t, a_\alpha^\ell$	Dispersivity lengths	0
A_α	Forchheimer coefficient	0

Simulations were performed on a grid with about $6 \cdot 10^4$ grid nodes in 2d and $6 \cdot 10^6$ degrees of freedom in 3d. The timestep was chosen $\tau^n = 15$ sec. In the d-dimensional representation, fracture width was resolved by 8 layers of elements inside the fracture.

More details and results of these fractured Henry problem and also of other test problems can be found in /GRI 12a/, /GRI 10/, /GRI 13/, /REI 12b/, /STI 12/.

6.4.2   Comparison results

In order to compare the two approaches for modelling flow in fractured porous media, simulations with both the d- and the $(d-1)$-dimensional fracture representation are performed. The results are then compared by computing in both simulations the value of mass fraction and pressure at a given point in the fracture, and the values of the jump of mass fraction and pressure at the two sides of the fracture.

In the $(d-1)$-dimensional simulation, equations (6.16) – (6.17) in the fracture are considered which provide averaged values for the mass fraction and the pressure. In order to get from the d-dimensional simulation, where equations (6.1) – (6.2) are solved, values that are comparable to those of the $(d-1)$-dimensional simulation, an average along the fracture width is performed. At fixed points in the fracture mass fraction and pressure are compared for varying time. The results for the pressure and the jump of the pressure of the two simulations agree quite acceptable and are, therefore, not shown here.

a)   b)
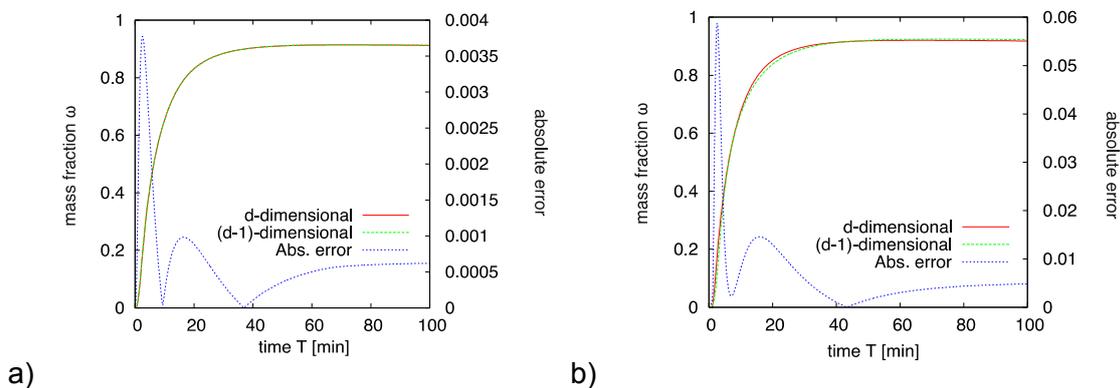
Fig. 6.4   Comparisons of d- and $(d-1)$-dimensional simulations of the 2d problem at x = 1.5 m: mass fraction in the fracture and its absolute error for a fracture of width (a) ϵ = 0.003 m and (b) ϵ = 0.024 m

In Fig. 6.4 the mass fraction in the fracture for the two-dimensional Henry problem (cf. Fig. 6.3a) is compared using geometries with different fracture widths. It can be noticed that the results of the two approaches agree with each other until the fracture width exceeds a certain value. When the fracture width is bigger than this value, the fracture becomes too thick for the averaging procedure to give acceptable results. However, below this value, the results obtained by the two approaches seem to be in good agreement. Indeed, it can be observed that for a thin fracture (cf. Fig. 6.4a) the absolute error is small, whereas for a thicker fracture (cf. Fig. 6.4b) the error made is increased. Especially in the beginning ($t < 5\,\mathrm{min}$) a relative error of over 30% is made.

As the $(d-1)$-dimensional model yields not only averaged values inside the fracture, but also values at the interfaces between fracture and medium, allowing to approximate a vertical gradient, it is worthwhile to compare these values as well.

a)   b)
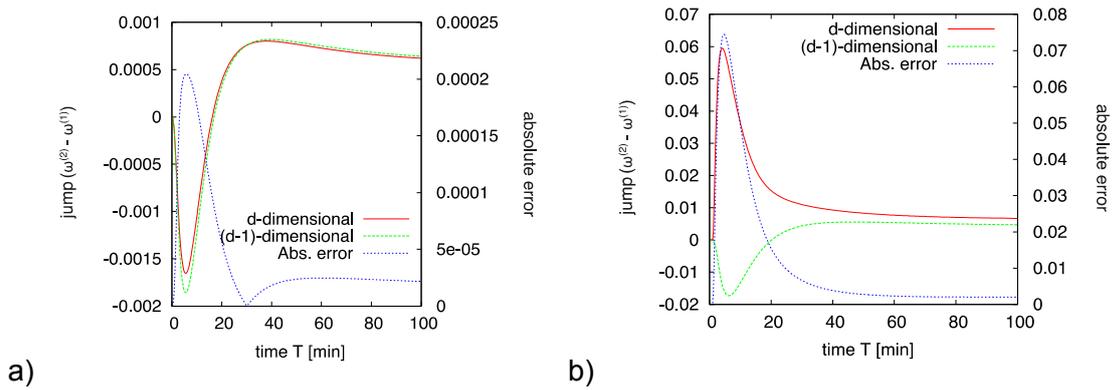
Fig. 6.5   Comparisons of d- and $(d$-$1)$-dimensional simulations of the 2d problem at $x = 1.5$ m: jump of mass fraction in the fracture and its absolute error for a fracture of width (a) $\epsilon = 0.003$ m and (b) $\epsilon = 0.024$ m

In Fig. 6.5 the comparison of the jump of the mass fractions at upper and lower interfaces of fracture and medium $(\omega_m^{(2)} - \omega_m^{(1)})$ is shown. It can be noticed that even for the fracture of width $\epsilon = 0.003\,\mathrm{m}$ where the comparison of the averaged mass fraction showed barely no difference between $(d-1)$- and d-dimensional simulation results, an relative error of about 10% is made in the beginning ($t < 10\,\mathrm{min}$). By further decreasing the fracture width to, e. g., $\epsilon = 0.001\,\mathrm{m}$, also this error decreases. This implies that, the jump of the mass fraction is even more sensitive on fracture width than the average. For the fracture of width $\epsilon = 0.024\,\mathrm{m}$ the result of the jump comparison is obviously really bad (cf. Fig. 6.5b). A change of signs between d- and $(d-1)$-dimensional simula-

134

tions can be observed: The jump in the d-dimensional simulation is positive, meaning that the mass fraction at the lower interface is bigger than the mass fraction at the upper interface, whereas the $(d-1)$-dimensional simulation indicates this the other way around. So here not only the error is big, but a different result is generated. This may be explained by an observation made considering the thick fracture of width $\epsilon = 0.024$ m.
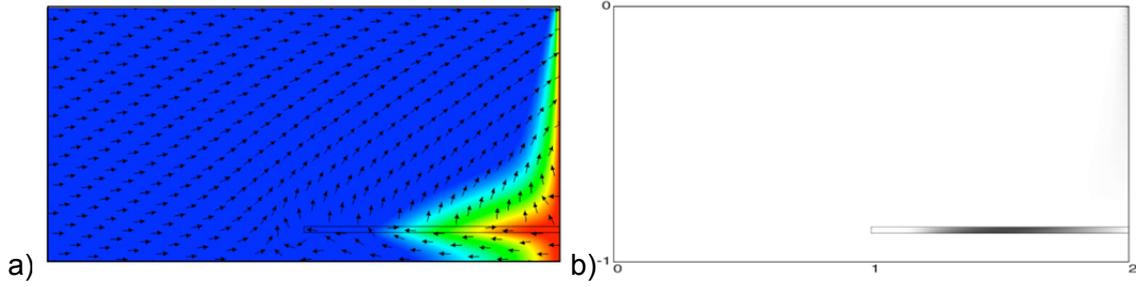
Fig. 6.6 d-dimensional simulation results for the 2d problem with a fracture of width ϵ = 0.024 m. a) concentration profile and velocity directions, b) vorticity

For increasing fracture width it can be noticed (cf. Fig. 6.6a) that there are also phenomena taking place inside the fractures. It can be observed that the velocity inside the fracture is turning around, i. e. a vortex is generated. Such phenomena cannot be reproduced by the $(d-1)$-dimensional simulation. For a fracture of width $\epsilon = 0.024$ m the major effect is given by the production of vortices in the fracture. This result is assumed to follow from the fact that the fracture is thick enough to develop the density contrast necessary for the rotation of velocity. Therefore, the vorticity defined by

$$\boldsymbol{\zeta}_\alpha := \nabla \times \mathbf{q}_\alpha \tag{6.45}$$

is considered. Under the assumptions of uniform viscosity, and isotropic and piecewise constant permeability, using equation (6.3)

$$\boldsymbol{\zeta}_\alpha = \mu^{-1}\mathbf{K}_\alpha(\nabla\rho_\alpha \times \boldsymbol{g}) = \mu^{-1}\mathbf{K}_\alpha\rho'(\nabla c_\alpha \times \boldsymbol{g}) \tag{6.46}$$

with $\rho' = \frac{(\rho^{pB}-\rho^{pW})}{\rho^{pB}}$ can be obtained. It can be noticed that the absolute value of vorticity is maximal when the gradient of the brine concentration is orthogonal to the gravity acceleration vector or, in other words, when $\boldsymbol{g}$ is tangent to the isolines of the concentration. In Fig. 6.6b it can be observed that the vorticity reaches comparably high values inside the fracture. When the fracture is thick enough, the brine finds sufficient

space to distribute itself along the fracture width. This means that, for a given cross section of the fracture, the brine concentration deviates appreciably from its mean value (cf. Fig. 6.6a). Consequently, vorticity varies as a function of height along the fracture width. This is accompanied by a nonuniform distribution of the specific discharge in the fracture, as in Fig. 6.6a an inversion of the tangential component of $\boldsymbol{q}_f$ can be observed.

As the rotation of the velocity, i. e. the vorticity, is a three-dimensional phenomenon, increasing the fracture width in three dimensions can lead to even bigger differences between d- and $(d-1)$-dimensional simulation results.

a)   b)
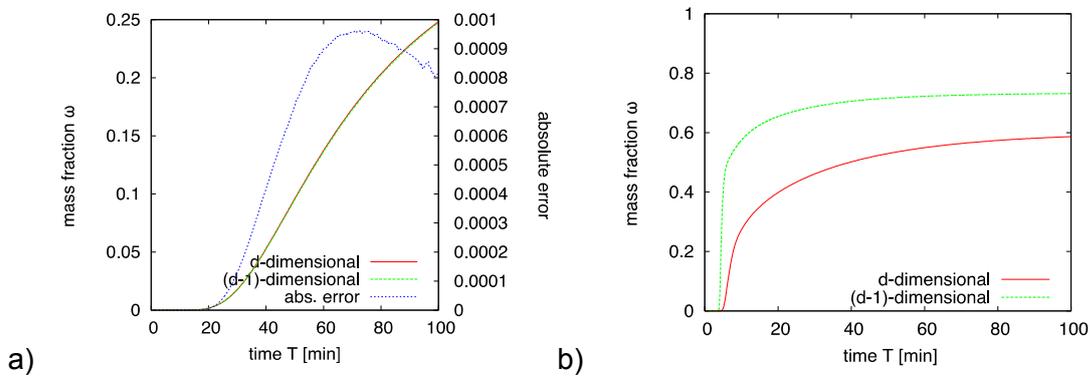
Fig. 6.7   Comparisons of d- and $(d$-$1)$-dimensional simulations of the 3d problem

At (x, y, z) = (1.125, 0.5, -0.675) m: mass fraction in the fracture and its absolute error for a fracture of width (a) $\epsilon = 0.003$ m and (b) $\epsilon = 0.024$ m.

In Fig. 6.7 the comparison of the concentration for the three-dimensional Henry problem is shown (cf. Fig. 6.3b) and a very good consistency for the fracture of width $\epsilon = 0.003\,\mathrm{m}$ can be observed. As expected, the results for the fracture of width $\epsilon = 0.024\,\mathrm{m}$ of d- and $(d-1)$-dimensional simulations differ enormously and the absolute error (not shown) is even a lot higher than in the two-dimensional case.

Comparisons of pressure and of jumps are not shown here because of space restrictions, but for the fracture of width $\epsilon = 0.003\,\mathrm{m}$ they can be found in /REI 12b/.

6.5 Dimension-adaptive methods

Both, d- and $(d-1)$-dimensional approaches for modelling flow in fractured porous media are very common. As shown in section 6.4, there are certain cases where the $(d-1)$-dimensional model fails to give reliable results and, therefore, the usage of a d-dimensional model is necessary. On the other hand, the application of a d-dimensional model requires high resolution and, therefore, leads to high storage demands and computational cost. Also, due to the geometric anisotropy and the jumps of the coefficients, introduced by the thin subdomains representing the fractures, the convergence rate of the multigrid solver may deteriorate.

In this section two new approaches are introduced. The first one is a dimension-adaptive multigrid method that improves the convergence of the multigrid solver for the d-dimensional fracture representation. The second approach is based on the idea to use the d-dimensional approach only if the $(d-1)$-dimensional model is not valid, i. e. the results from the $(d-1)$-dimensional model differ essentially from those of the d-dimensional model. Therefore, a criterion is introduced indicating the validity of the $(d-1)$-dimensional approach.

6.5.1 Dimension-adaptive multigrid method

In order to overcome possible convergence problems of the linear solver, that are due to geometric anisotropies in the d-dimensional model, a multigrid method featuring a dimension transfer is introduced: The fractures are fully resolved on the fine grids, and, therefore, the obtained solution corresponds to the solution of the d-dimensional model. Though, on coarser grids of the grid hierarchy, where the geometric anisotropy is more evident, the fracture is considered to be $(d-1)$-dimensional. This leads to an improved convergence of the linear solver.

We consider a grid hierarchy Ω_l ($l \in \{0, \dots, L\}$) that is constructed from a coarse grid Ω_0 (generated as described in section 12 with the properties stated in section 6.3.1) by regular, conform and anisotropic refinement. On the finest level Ω_L all n fractures $\mathcal{F}_i$ ($i = 1, \dots, n$) are d-dimensional. On every other grid Ω_l ($l \in \{0, \dots, L-1\}$) the aspect ratio is calculated for all fracture elements. If it is smaller than the reference value, `DEGENERATED_SIZE`, the element is considered to be $(d-1)$-dimensional. If only one element in a fracture on the grid Ω_l is marked as $(d-1)$-dimensional, then all elements

137

in this fracture on the grid Ω_l are marked as $(d-1)$-dimensional as well. Allowing different dimensionalities of a fracture on one grid level would require further assumptions and considerations, which are not discussed here.

If the fracture is not treated as $(d-1)$-dimensional, i. e. all elements are marked as d-dimensional, the fracture is d-dimensional and not treated in a special way. It is obvious that if a fracture is $(d-1)$-dimensional on the grid Ω_ℓ with $0 \leq \ell < L$, then the fracture is $(d-1)$-dimensional on all grids Ω_l with $l \leq \ell$. The finest grid, where a fracture $\mathcal{F}_i$ is $(d-1)$-dimensional, defines $L_{DEG}(\mathcal{F}_i) := \max\{l: \mathcal{F}_i$ is $(d-1) - $ dimensional on $\Omega_l\}$. Note that it is essential that $L_{DEG}(\mathcal{F}_i) < L$ for all fractures $\mathcal{F}_i$ in order to obtain the same solution as by using the d-dimensional approach. Furthermore, on the grids Ω_l $(l \in \{0, \dots, L_{DEG}(\mathcal{F}_i) - 1\})$ only anisotropic refinement has to be applied in the fracture $\mathcal{F}_i$.

On levels Ω_l $(l \in \{0, \dots, L_{DEG}(\mathcal{F}_i)\})$ the $(d-1)$-dimensional discretisation (section 6.3.2) is performed according to equations (6.16) – (6.17) in the fracture $\mathcal{F}_i$ and equations (6.26) – (6.27) in the medium. On levels Ω_l $(l \in \{L_{DEG}(\mathcal{F}_i) + 1, \dots, L\})$ the d-dimensional discretisation (section 6.3.2) is performed according to equations (6.1) – (6.2) in the fracture $\mathcal{F}_i$ as well as in the medium. Between the levels $L_{DEG}(\mathcal{F}_i)$ and $L_{DEG}(\mathcal{F}_i) + 1$ a dimension-transfer is performed in the fracture $\mathcal{F}_i$ by a special choice for the restriction and the prolongation.

This approach improves the convergence of the multigrid solver in comparison to solving equations (6.1) – (6.2) in the fracture on the whole grid hierarchy Ω_l $(l \in \{0, \dots, L\})$, but the obtained solution is the same because the fracture is d-dimensional on the fine grid.

6.5.2   Dimension-adaptive computation

The dimension-adaptive multigrid method, described in section 6.5.1, is suitable for keeping the computational grids relatively coarse while still resolving the fractures d-dimensional. Though, the computational grids containing d-dimensional resolved fractures still contain a lot more vertices (esp. in 3 dimensions) than those using a $(d-1)$-dimensional fracture representation resulting in larger storage demands and longer computational times. Moreover, the construction of these grids is often more difficult

and complex. Hence, in order to keep the numerical cost small, $(d-1)$-dimensional fracture representations should be used as often as possible.

On the one hand the comparisons in section 6.4 showed that for really thin fractures the $(d-1)$-dimensional approach yields reasonable results. Furthermore, it is obvious that if, e. g., saltwater has not (yet) approached the fracture, a full resolution of the fracture is not necessary. On the other hand the comparisons for thicker fractures show that the $(d-1)$-dimensional model is not always able to yield correct results.

Therefore, the idea is to construct a dimension-adaptive approach that is able to switch at run-time depending on the actual flow conditions and fracture properties between d- and $(d-1)$-dimensional fracture representations.

In order to establish this approach, the following features are needed:

a) Two computational grids (d- and $(d-1)$-dimensional)
b) Transfer operators that transfer the solution (the unknowns) between the grids
c) A condition, when to perform this switch

In order to simplify the transfer operator, only grids where the fracture ends with triangles in the d- as well as the $(d-1)$-dimensional representation are allowed. The multigrid structures can be switched using the functionality already implemented in UG.

The transfer operators are constructed, such that they keep the solution in the medium $\mathcal{M}$ by copying the values of the solution if the two grids are identical in $\mathcal{M}$, or else, by interpolating them. The solution in the fracture $\mathcal{F}$ needs more consideration. Comparing d- and $(d-1)$-dimensional grids, it can be observed that the geometric position of the grid nodes at the interface between fracture and medium is shifted. This is due to the fact that in the d-dimensional grid in contrast to the $(d-1)$-dimensional grid the fracture width ϵ is actually present (and resolved). During the transfer, this shift has to be taken into account in the hydrostatic part of the pressure p, by adjusting p with $\pm \rho g_z \Delta z$, where Δz corresponds to the shift in z-direction and g_z is the z-component of the gravity acceleration vector $\boldsymbol{g}$.

In order to simplify the notation, we assume in the following that Ω contains only one fracture $\mathcal{F}$. Let $\Omega_l^{(d-1)}$ ($l \in \{0, ..., L\}$) be the grid hierarchy featuring the $(d-1)$-

dimensional fracture and Ω_l^d ($l \in \{0, ..., L\}$) the grid hierarchy featuring the d-dimensional fracture. Let $V_l^{(d-1)}$ and V_l^d be the vector spaces defined on $\Omega_l^{(d-1)}$ and Ω_l^d.

The operator $\mathcal{L}_d^{(d-1)} : V_l^d \to V_l^{(d-1)}$ ($l \in \{0, ..., L\}$) maps from the d-dimensional grid to the $(d-1)$-dimensional grid. The values of the solution at the interfaces between fracture and medium are copied, as they are the same in the $(d-1)$-dimensional model. Hereby, the pressure is corrected with the hydrostatic part given by the shift, as explained above. The averaged value inside the fracture, needed for the $(d-1)$-dimensional model, is determined by calculating the average along the fracture width by numerical integration.

The other transfer operator $\mathcal{L}_{(d-1)}^d : V_l^{(d-1)} \to V_l^d$ ($l \in \{0, ..., L\}$) maps from the $(d-1)$-dimensional grid to the d-dimensional grid. In the $(d-1)$-dimensional model only the values of the solution at the interfaces between fracture and medium and an averaged solution inside the fracture are known. Therefore, on every line parallel to $\boldsymbol{n}$ that contains vertices in $\mathcal{F}$ a quadratic polynom is considered, fulfilling the following conditions: The values of the solution at the interfaces (where the pressure is corrected with the hydrostatic part given by the shift) are the same as well as the averaged solution. This quadratic polynom is then used to calculate the values of the solution inside the fracture on all vertices on the line parallel to $\boldsymbol{n}$. The choice of this quadratic polynom mostly yields suitable results. Only in some special cases, e. g., when vortices are involved, the calculated values are different compared to the actual values.

The construction of the transfer operators implies that using them one after another starting at the d-dimensional grid, $\mathcal{L}_d^{(d-1)} \mathcal{L}_{(d-1)}^d$, preserves the values for average and interface values, but yields different concentration and pressure profiles, as the values inside the fracture may differ due to $\mathcal{L}_{(d-1)}^d$. However, using them one after another starting at the $(d-1)$-dimensional grid preserves all values: $\mathcal{L}_d^{(d-1)} \mathcal{L}_{(d-1)}^d = \mathbb{I}$.

After defining the transfer operators, the criterion for the validity of the $(d-1)$-dimensional approach needs to be defined. The comparisons in section 6.4.2 indicate the following as influencing factors:

a) Width of the fracture: The fracture width is an essential condition for the validity of the averaging process. Moreover, for increasing fracture width there might appear processes inside the fracture (e. g. vortices) that cannot be resolved by the $(d-1)$-dimensional model.

b) Angle of the fracture to gravitation: The appearance of vortices is related to the angle of concentration gradient and gravity. Due to the high permeability in the fracture, the concentration gradient is often high along the fracture. Therefore, the appearance of vortices is more likely in horizontal than in vertical fractures.

c) Permeability in the fracture: Increasing the permeability leads to higher velocities and, therefore, a higher chance for a phenomenon to appear in the fracture. Increasing the ratio of permeabilities between fracture and medium leads to a higher discontinuity at the interface in result of which, e. g., vortices can appear.

d) Current flow conditions: If the concentration at the fracture is very small, the $(d-1)$-dimensional model is sufficient to describe all necessary phenomena. It is obvious that only a fast flow can generate vortices.

Considering these factors, the following criterion was empirically established:

$$\theta := \epsilon \, \frac{K_f}{K_m} \max_{\mathcal{F}} \{\zeta_f\} \frac{\partial_x \omega}{\partial_z \omega} \tag{6.47}$$

with the vorticity ζ_f as defined in (6.45). Now, the value of this criterion indicates, whether to use the d- or the $(d-1)$-dimensional model. Therefore, two threshold values are introduced

$$\theta > \theta_0 \qquad\qquad d\text{-dimensional} \tag{6.48}$$

$$\theta < \theta_1 \qquad\qquad (d-1)\text{-dimensional} \tag{6.49}$$

Thereby, $\theta_0 \neq \theta_1$ and an overlapping zone is left between θ_0 and θ_1 to avoid a switch back and forth between the two models if the criterion is near the threshold.

The established criterion may not be the final criterion, as until now its significance was only tested on a few benchmark problems. It is part of the current work to further analyse this criterion and to assure its significance by testing it on various different test cases. Section 6.5.3 shows that the criterion works well for the considered Henry problem. Note that, the criterion in (6.47) has the physical unit of a velocity. It is also part of the current work to understand the meaning of this and to modify the criterion in a way such that it is dimensionless.

6.5.3   Numerical Experiments

Numerical experiments using the dimension-adaptive method introduced in section 6.5.2 are shown considering the Henry problem described in section 6.4.1 with a different domain, where the fracture is not attached to the right boundary (cf. Fig. 6.9a).

In Fig. 6.8 the results obtained by the three different approaches, d- and $(d-1)$-dimensional fracture representations and dimension-adaptive approach, are shown. Thereby, the d-dimensional simulation result is considered to be the correct reference solution. The absolute errors made by the $(d-1)$-dimensional as well as by the dimension-adaptive simulation in comparison to the d-dimensional simulation are shown. It can be observed that using the dimension-adaptive approach, the error can be kept small.
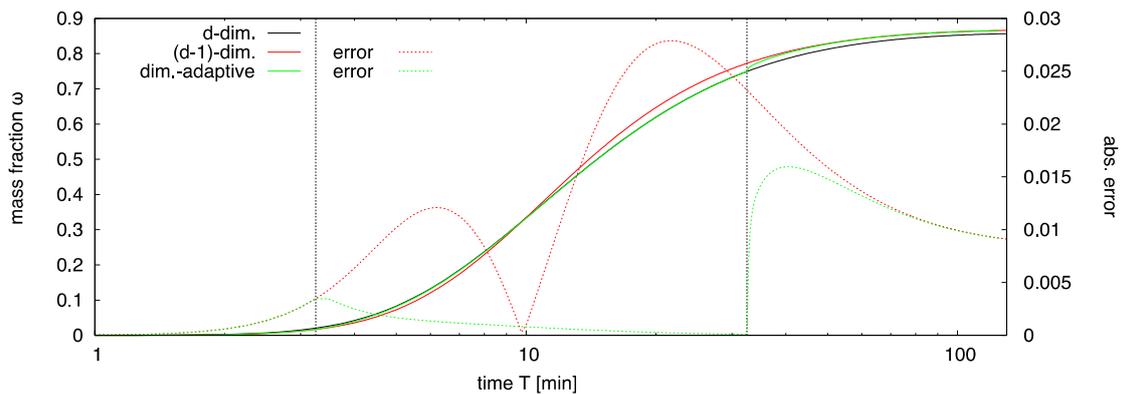
Fig. 6.8   Comparisons of d-, $(d-1)$-dimensional and dimension-adaptive simulations of the 2d problem at x = 1.5 m: mass fraction in the fracture and its absolute error for a fracture of width ϵ = 0.024 m (cf. Fig. 6.9a)

In the beginning, when the incoming saltwater has not reached the fracture, the error made by the $(d-1)$-dimensional model is small and the dimension-adaptive approach uses the $(d-1)$-dimensional fracture representation (cf. Fig. 6.8). Then, the saltwater intrudes the fracture, a vortex is built and at $T = 3.25\,\mathrm{min}$ the criterion indicates to switch to the d-dimensional fracture representation. As it can be seen, the error decreases and is going to zero instead of increasing as it is the case for the $(d-1)$-dimensional model. Later, at $T = 32.5\,\mathrm{min}$, when the fracture is filled with saltwater and the solution approximates the stationary state, the criterion indicates that a switch back to the $(d-1)$-dimensional model is possible. In result, the error increases a bit, but the

142

relative error stays below 2 % (cf. Fig. 6.9 (right)). So, with this approach the error can be kept small over the whole computation time, while the full resolution of the fracture with more storage demands is only used for some part of the time.
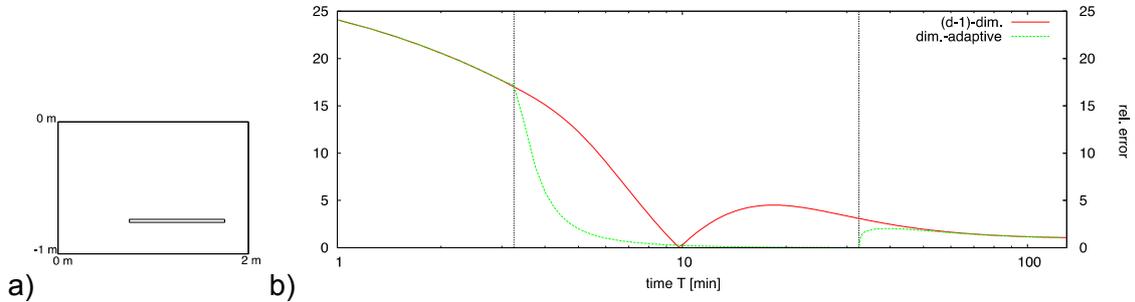
Fig. 6.9   a) Geometry, b) Comparisons of d-, $(d$-$1)$-dimensional and dimension-adaptive simulations of the 2d problem at x = 1.5 m: relative error

Also for the jump of the mass fraction (not shown), the error can be reduced significantly using the dimension-adaptive method instead of using the $(d-1)$-dimensional method.

For the 3d case, the dimension-adaptive switch is not implemented, but the behaviour of the criterion can be observed. For the examples considered in 6.4 it was observed (cf. Fig. 6.7) that for a fracture of width $\epsilon = 0.003$ m the $(d-1)$-dimensional model yields really good results, whereas for a fracture of width $\epsilon = 0.024$ m the $(d-1)$-dimensional model is not able to model the right behaviour of the flow. Computation of the criterion shows that in this example for the fracture of width $\epsilon = 0.003$ m the criterion stays well below the threshold and approves so the use of the $(d-1)$-dimensional model. However, for a fracture of width $\epsilon = 0.024$ m the value of the criterion lies above the threshold over the whole time, meaning that in this case the d-dimensional approach should be used solely. This is consistent with the results from section 6.4.
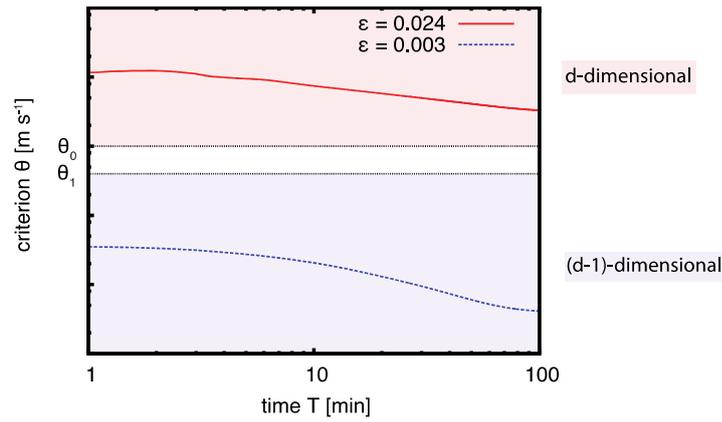
Fig. 6.10   Criterion θ for the 3d Henry problem (cf. Fig. 6.3b) with fractures of different width.

6.6   Discussion

In this chapter a d- and a $(d-1)$-dimensional approach for modeling fractured porous media were discussed. The $(d-1)$-dimensional approach has in favour less computational cost and less problems with the numerical solver. Though, in section 6.4.2 it was shown that it can not cover all phenomena that might happen inside the fracture and that its validity should be seriously questioned. In order to deal with this, a dimension-adaptive multigrid method improving the convergence of the numerical solver for the d-dimensional case was introduced in section 6.5.1. Furthermore, a criterion indicating the validity of the $(d-1)$-dimensional approach was introduced (cf. section 6.5.2). This criterion can be computed while run-time and allows, e. g., to use a dimension-adaptive approach that switches between d- and $(d-1)$-dimensional fracture representations depending on actual flow-conditions and fracture properties. The results of this approach in section 6.5.3 show that the error made with the $(d-1)$-dimensional model can be kept small, while also keeping the numerical cost small.

7 Development of simple models for the fast computation of flow and transport through fractured rocks

7.1 Introduction

The prediction of large-scale transport of solutes through fractured rock is essential for risk assessment of long term disposal of waste. The choice of a model concept for the description of fractured rocks strongly depends on the scale of the problem, the geological characteristics of the area of investigation and the purpose of the simulation.

Generally, fractured rocks can be considered to consist of a hierarchy of connected flow paths. The largest and highly connected fractures conduct the main part of the flow. This highly connected system is embedded in a system of smaller-scale fractures and fissures that form a background system or the rock matrix with a much smaller hydraulic conductivity.

Transport of nuclides takes places in the large-scale fracture system but also in the heterogeneous background system. However, transport mechanisms differ in both systems. Nuclide transport is due to advection and dispersion. The transport in the large fractures is mostly dominated by advective transport. Dispersion along the large fractures is often neglected. In contrast, solute transport in the heterogeneous background system is due to diffusion or dispersion and eventually due to advection. The advective movement in the rock matrix is small compared to the advection of plume in the large-scale fracture system and is therefore often neglected. Mass exchange between the fracture system and the rock matrix is governed by a diffusive flux across the matrix/fracture boundary.

In detailed models, the connected network of large-scale fractures is modelled explicitly. The position and distribution of fractures is known or generated statistically by a fracture network generator. Modelling in detail also the background or smaller-scale fracture network is often computationally not feasible. In this case, the background system can be replaced by a heterogeneous continuum if statistical properties like fracture length distribution, fracture orientation, fracture density and transmissivity distribution are known. The latter approach has been investigated by /REE 08a/ who introduced a fracture continuum approach using MODFLOW. Their findings allow to make use of

scaling results derived and presented in the previous chapters 3 and 5 of this report and to assign effective medium's properties (e. g. effective dispersion coefficients) to the background material. Nevertheless, the computational burden is large if transport through the large-scale fracture system and the effective rock matrix is modelled in high spatial resolution.

The aim of this work package is the development of a faster computational method for risk assessment of nuclide transport through fractured rocks. To this end, the complexity of models needs to be reduced further and compromises with respect to accuracy have to be made.

The simplest and computationally fastest models are effective 1-D-models in which not only the rock matrix but also large scale fracture system is replaced by an effective medium with effective properties. In addition, the two effective media might interact with each other via a linear exchange.

Before the effective 1d-model is stated, it is desired to emphasize that also the target variable of model may influence the model type: If a fast model for giving conservative estimates of the first arrival time of nuclides is desired to be built, it is needed to characterise the transport behaviour of nuclides in an ensemble of realisations in order to account for centre-of-mass fluctuations from realisation to realisation. From that follows that the ensemble spread needs to be considered in the effective model. In contrast, if peak concentrations of radioactive nuclides reaching specific locations in the subsurface are aimed to be given, it is needed to account for the effective dispersion coefficient in the effective model since the ensemble dispersion overestimates the physical mixing due to heterogeneities and conservative estimates of peak concentrations would be too small.

To this end, it will be distinguished in the following between the effective 1d-model for estimating first arrival times and the effective 1d-model for estimating peak concentrations. The main difference of the two models will be that the first model will build on the ensemble mixing, whereas the latter will rely on the effective mixing behaviour of the plume.

In order to establish the effective transport model, it is needed to specify the advective movement of the plume which is determined by the mean groundwater flow through the fractured system, the spreading behaviour of the plume within the large-scale fracture

system and the interaction of the plume with the background material or the rock matrix.

7.2   Effective transport properties

Replacing the large-scale fracture system by an effective medium implies that the fracture system is not resolved in detail but that the main impact of the heterogeneous system on the solute transport behaviour is captured by an effective description. The suggestion is to replace the transport through the large-scale fracture system by an one-dimensional transport description that correctly models the centre-of-mass movement of the plume through the medium and the spreading of the plume due to the heterogeneity of the fracture system.

/REE 08a/, /REE 08b/ investigated particle transport in various fracture networks that differ in fracture length distribution, fracture density and transmissivity distribution. They could demonstrate that depending on their characteristics, multi-Gaussian or so-called operator-stable solute distributions evolve.

Multi-Gaussian distributions are completely described by their first two centralised spatial moments – the centre-of-mass and the width of the plume. In particular, the second centralised spatial moment or the width of the plume grows linearly with time if the spreading is normal-diffusive or dispersive. To this end, the spread or variance of the plume grows proportional to the square root of time and multi-Gaussian distributions can be modelled by conventional advection-dispersion equations (ADEs) with constant dispersion coefficients.

In contrast, operator-stable distributions show a different behaviour. For instance, the spatial moments of multi-Gaussian and operator-stable distributions scale very differently. Operator-stable distributions show a super-diffusive spreading of the plume. In other words, the variance also grows according to a power-law of time but with an exponent that is larger than 0.5. The exponent can be linked to the fracture networks characteristics. As /REE 08a/, /REE 08b/ found, the main influence on the effective transport behaviour stems from the fracture length distribution that is given for fractures above a certain lower cutoff size L by

$$P(L > \ell) = \omega \, \ell^{-a} \ . \tag{7.1}$$

where the probability of a fracture of length ℓ is dependent on ω, a constant that depends on the minimum fracture length and a power-law exponent a that ranges between 1 and 3 /DAV 93/. For $1.0 < a < 1.9$, the effective transport behaviour is governed by anomalous dispersion. For $1.9 < a < 2.2$, multi-Gaussian or operator-stable distributions may evolve depending on high or low fracture densities. For larger values of the exponent a, multi-Gaussian distributions evolve.

/REN 99/ proposed that fracture length exponent values for natural fracture networks are in the range $1.4 < a < 2.2$. This suggests that a super-Fickian model of transport such as the fractional advection-dispersion equation (FADE) may be applicable to more field sites than the conventional ADE, which has shown poor performance for sparsely fractured domains dominated by long fractures.

The next step is to relate the fracture length exponent a with the ensemble spread $\sigma_{11}^{2,\mathrm{ens}}(t)$ of the solute plume. /REE 08b/ empirically estimated the ensemble spreading as

$$\sigma_{11}^{2,\mathrm{ens}}(t) \propto t^{2/a} \tag{7.2}$$

which implies an anomalous super-dispersive movement for $a < 2.0$.

With this result, the power-law fracture length distribution can be also related to heterogeneous continuum conductivity fields that show a power-law covariance function

$$\hat{C}_{\ln(K)}(\mathbf{x}) = \sigma_{\mathrm{uu}}^2\, z^{-\beta}, \quad 0 \le \beta \le 1 \tag{7.3}$$

with

$$\tag{7.4}$$

$$z = \left(1 + \frac{\sum_{i=1}^{d} x_i^2}{\ell^2} \right)^{1/2}.$$

For comparing the results for the ensemble dispersion coefficients as presented in chapter 3 with the results of /REE 08b/, the longitudinal ensemble dispersion coefficient has to be integrated over time in order to get the ensemble spreading. It can be concluded that

$$\frac{2}{a} = 2 - \beta \tag{7.5}$$

or

$$\beta = 2 - \frac{2}{a}; \qquad a = \frac{2}{2 - \beta} \ .$$

(7.6)

To this end, for the first time fracture network properties like the length distribution are linked with the statistical property of a continuous heterogeneous medium. In this context, the large-scale discrete fracture network can be replaced by a continuous heterogeneous medium and all results of effective transport coefficients can be used as presented in chapters 3 and 5.

The background small-scale fracture system can be also represented by statistically distributed small-scale fractures. The difference between the fractured background system and the large-scale fracture system is that the background system is dominated by shorter finite length fractures. To this end, a multi-Gaussian plume behaviour is much more likely in the background system than in the large-scale fracture system. The simplest approach is to neglect advection and longitudinal dispersion in the background system and only accounts for mixing transverse to the large-scale fractures. Since it is known /ATT 04b/ that transverse mixing is almost not impacted by heterogeneous conductivity distributions, it might be sufficient to approximate the transverse mixing by its local value. If the dispersive or diffusive movement in the rock matrix is not resolved at all, the interaction with the rock matrix can be replaced by a second porosity and a simple linear exchange between these two porosities.

7.3 Simple effective 1d-transport models

In this context, relatively simple effective 1d-transport equation models can be stated:

a) The simple 1d-model that estimates the first arrival time distributions follows as

$$\frac{\partial c_F}{\partial t} + \frac{\partial (u\, c_F)}{\partial x} - \left(\sigma_{11}^{2,\mathrm{ens}}(t) \right)^{\frac{1}{2-\beta}} \left(\frac{\partial}{\partial x} \right)^{\frac{2}{2-\beta}} c_F = -\alpha\, (c_F - k\, c_B) \ .$$

(7.7)

with

$$\frac{\partial c_B}{\partial t} = +\alpha\, (c_F - k\, c_B) \ .$$

(7.8)

The coefficient $\sigma_{11}^{2,\text{ens}}(t)$ can be calculated from the results presented in chapters 3 and 5. For $\beta = 2$, the transport equation reduces to the standard Advection-Dispersion-Equation (ADE). For $\beta < 2$, an anomalous transport behaviour with a fractional ADE results.

b) The simple 1d-model that should be used for estimating peak concentrations is given by

$$\frac{\partial c_F}{\partial t} + \frac{\partial (u\,c_F)}{\partial x} - \left(\sigma_{11}^{2,\text{eff}}(t)\right)^{\frac{2}{3-\beta}} \left(\frac{\partial}{\partial x}\right)^{\frac{4}{3-\beta}} c_F = -\alpha\,(c_F - k\,c_B)\ . \tag{7.9}$$

with

$$\frac{\partial c_B}{\partial t} = +\alpha\,(c_F - k\,c_B)\ . \tag{7.10}$$

The coefficient $\sigma_{11}^{2,\text{eff}}(t)$ can be taken again from chapters 3 and 5.

7.4   Analytical solution for the simple effective 1d-models

The use of analytical solutions for solute transport predictions provides advantages over numerical simulations as less intensive field characterisation is needed to produce screening-level predictions. In general, for operator-stable plumes eigenvectors correspond to principal fracture set orientations, power-law fracture length exponent values provide a good estimate for values of a. This result implies that first cut transport approximations for the leading plume edge in fractured media can be constructed from fracture network statistics and the analytical results presented in chapters 3 and 5.

In order to give explicit solutions, initial and boundary conditions still need to be specified. It will be presented here the explicit solution of a plume of nuclides being released from a source in such a way that a fixed nuclide concentration is kept at one boundary of the computational domain. For simplicity, this boundary is set to x = 0. The second boundary is set to infinity. At time t = 0, no nuclides are within the computational domain.

For the standard ADE or Gaussian transport, the analytical solution can be taken from textbooks like /HAE 92/ (page 446, formula 6.133). The solution for case 7.3 a) reads

$$c_F(x,t) = \frac{c_0 x}{\sqrt{4\,\pi\,D_{11}^{ens}}} \int_0^t dt' \, \frac{1}{\sqrt{t^3}} \, \exp\left(-\frac{(x - ut')^2}{4D_{11}^{ens}\,t'}\right) J\big(kt', \alpha k(t - t')\big), \tag{7.11}$$

whereas the solution for case 7.3 b) reads

$$c_F(x,t) = \frac{c_0 x}{\sqrt{4\,\pi\,D_{11}^{eff}}} \int_0^t dt' \, \frac{1}{\sqrt{t^3}} \, \exp\left(-\frac{(x - ut')^2}{4D_{11}^{eff}\,t'}\right) J\big(kt', \alpha k(t - t')\big). \tag{7.12}$$

The function J(a,b) denotes in both formulae the Goldstein function. In case of a fractional transport equation (FADE), the above stated solution can be extended to the fractional case making use of the fact that the exponential function under the integral states the nuclide distribution after a point-like release of nuclides without any interaction with the rock matrix following the standard ADE – denoted by g(x,t) in the following:

$$c_F(x,t) = \frac{c_0 x}{\sqrt{4\,\pi\,D_{11}^{eff}}} \int_0^t dt' \, \frac{1}{\sqrt{t^3}} \, g(x,t) \, J\big(kt', \alpha k(t - t')\big). \tag{7.13}$$

The nuclide distribution after a point-like release but following the FADE, reads

$$g(x,t) = \int dq \, \exp(iqx) \, \exp\left(-iuqt - \sigma_{11}^2(t)\right) |q|^2, \tag{7.14}$$

where q denotes the transformed variable into the Fourier space. Note, that an explicit solution for g(x,t) cannot be stated in case of a FADE. Nevertheless, the integral representation (7.14) can be inserted into (7.13) and the nuclide concentration can be evaluated numerically.

8 Algorithms and tools for inverse modelling and parameter estimation

8.1 Introduction

In density-driven flow problems, as well as in many other mathematical problems, some model parameters, for example permeabilities and porosities, are used. Their values have to be determined before a simulation can be started. Usually, these parameters can be taken from measurements. But in many cases the measurements are not sufficient or data does not exist for all hydrogeological units of the model domain. A calibration becomes necessary.

In this case inverse modelling can be applied to estimate the undetermined parameters. In this chapter the implementation of a parameter estimation method within the d³f framework is presented. Furthermore, a short user manual is provided and the application of the method to two d³f problems is investigated.

8.2 Problem definition

Given observations by means of an experimental data set, one typical task is to find model-parameters which adequately describe the data. To make this more specific, the following notation is introduced:

- $\vec{y} \in Y \subset \mathbb{R}^n$ is a vector of observations,
- $\vec{\theta} \in P \subset \mathbb{R}^p$ is a vector of model parameters,
- $\vec{f}: \mathbb{R}^p \to \mathbb{R}^n$ is the output function of the model. $\vec{f}$ deterministically maps model parameters to the space of observations.

Evaluating the function $\vec{f}$ may be an expensive operation with respect to computational time. In the context of this work it is, e. g., running a simulation with high spatial resolution for many time steps. It is required that the number of observations is larger or equal to the number of model parameters, i. e., $n \geq p$.

Let the function $\vec{r} := \vec{f}(\theta) - \vec{y}$ denote the residual between simulated and observed data. The goal is to find a set of parameters, which describes the experimental data adequately. Mathematically, this can be described as follows:

Find $\vec{\theta} \in P$ such that the parameter estimation function ϕ defined by

$$\phi(\vec{\theta}) := \frac{1}{2}\left\|\vec{r}(\vec{\theta})\right\|^2 \rightarrow min \tag{8.1}$$

is minimal.

For the remainder of this work, the norm in this objective is the Euclidean norm of $\mathbb{R}^n$. This simplifies the presentation. One should bear in mind, however, that there is some freedom in the choice of the norm. In some cases, e. g., when standard deviations of the residuals are available, a weighted norm may be more appropriate.

8.3 Gauß-Newton-Method

One standard strategy for the solution of Eq. (8.1) is a Gauß-Newton solver cf. /NOC 06/ and /BAT 88/. Starting from some initial guess $\vec{\theta}^{(0)}$, this method iteratively seeks to find an update

$$\vec{\theta}_{k+1} \leftarrow \vec{\theta}_k + \Delta\vec{\theta}_k \tag{8.2}$$

such that the parameter estimation function ϕ decreases from step to step, i. e., $\phi(\vec{\theta}_{k+1}) < \phi(\vec{\theta}_k)$.

Assuming that $\vec{f}$ and thus also $\vec{r}$ is differentiable the following linearization is obtained

$$\vec{r}(\vec{\theta}_{k+1}) \approx \vec{r}(\vec{\theta}_k) + J_k\ (\vec{\theta}_{k+1} - \vec{\theta}_k) \tag{8.3}$$

Here, $J_k := D\vec{f}(\vec{\theta}_k) = D\vec{r}(\vec{\theta}_k)$ denotes the Jacobian of $\vec{r}$ and $\vec{f}$ for the current parameters $\vec{\theta}_k$ respectively. Note that the step length satisfies $\Delta\vec{\theta}_k := (\vec{\theta}_{k+1} - \vec{\theta}_k)$.

Replacing $\vec{r}$ in eq. (8.1) by the linearization in eq. (8.3), an alternative minimization problem is obtained: Find $\Delta \vec{\theta}$, such that

$$\frac{1}{2} \left\| \vec{r}_k + J_k \, \Delta \vec{\theta}_k \right\|^2 \to min. \tag{8.4}$$

Here $\vec{r}(\vec{\theta}_k)$ has been replaced by $\vec{r}_k$. The benefit of this formulation is that it is equivalent to the linear problem

$$J_k^T J_k \, \Delta \vec{\theta}_k = -J_k^T \vec{r}_k. \tag{8.5}$$

Assuming that $J_k \in \mathbb{R}^{n \times p}$ has full rank, which means that the derivatives of $\vec{r}_k$ w.r.t. $\vec{\theta}$ are linearly independent and thus $J_k^T J_k > 0$ is symmetric positive definite. However, this problem may be ill-conditioned. In the current implementation a QR-decomposition of J_k is used to avoid problems. As for any other Newton-type method, a special strategy is required for increasing the convergence radius. In this work a standard line-search strategy has been implemented.

That is, the update step is replaced by

$$\vec{\theta}_{k+1} \leftarrow \vec{\theta}_k + \lambda_k \Delta \vec{\theta}_k \tag{8.6}$$

and λ_k is selected form the discrete set such that

$$\phi^2 \left(\vec{\theta}_k + \lambda_k \Delta \vec{\theta}_k \right) = \min_{\lambda \in L} \phi^2 \left(\vec{\theta}_k + \lambda \Delta \vec{\theta}_k \right) \tag{8.7}$$

and $L = \{2^{-n} : n = 0, \dots K\}$. In the experiments presented below, $K = 8$ turned out to be efficient.

The computation of the derivatives merits some additional comments:

1) It is not assumed that J is available explicitly. Instead it is determined implicitly by numerical differentiation. The derivatives are approximated by

$$\frac{\partial \vec{r}}{\partial \vec{\theta}_j} \approx \frac{\vec{r}(\vec{\theta}_k + \delta_j \vec{e}_j) - \vec{r}(\vec{\theta}_k - \delta_j \vec{e}_j)}{2\delta_j} \tag{8.8}$$

This formula is of second order w.r.t $\delta_j > 0$.

155

2) This is quite expensive, since $2p$ evaluations of $\vec{r}$ must be performed. However, this is an inherently parallel task. The same holds true for the previously mentioned line-search strategy in eq. (8.6).

It is important to note, that the Gauß-Newton algorithm does not only yield estimates of the parameters, but also their sensitivity by virtue of eq. (8.5). Using some decent standard assumptions this allows to estimate the (co-)variance and the correlation of the estimated parameters.

8.4   Implementation and Parallelization

The main steps of the implementation of the Quasi-Newton method described in section 8.3 are depicted in Fig. 8.1. A description in detail and a user manual for parameter estimation can be found in 13D.
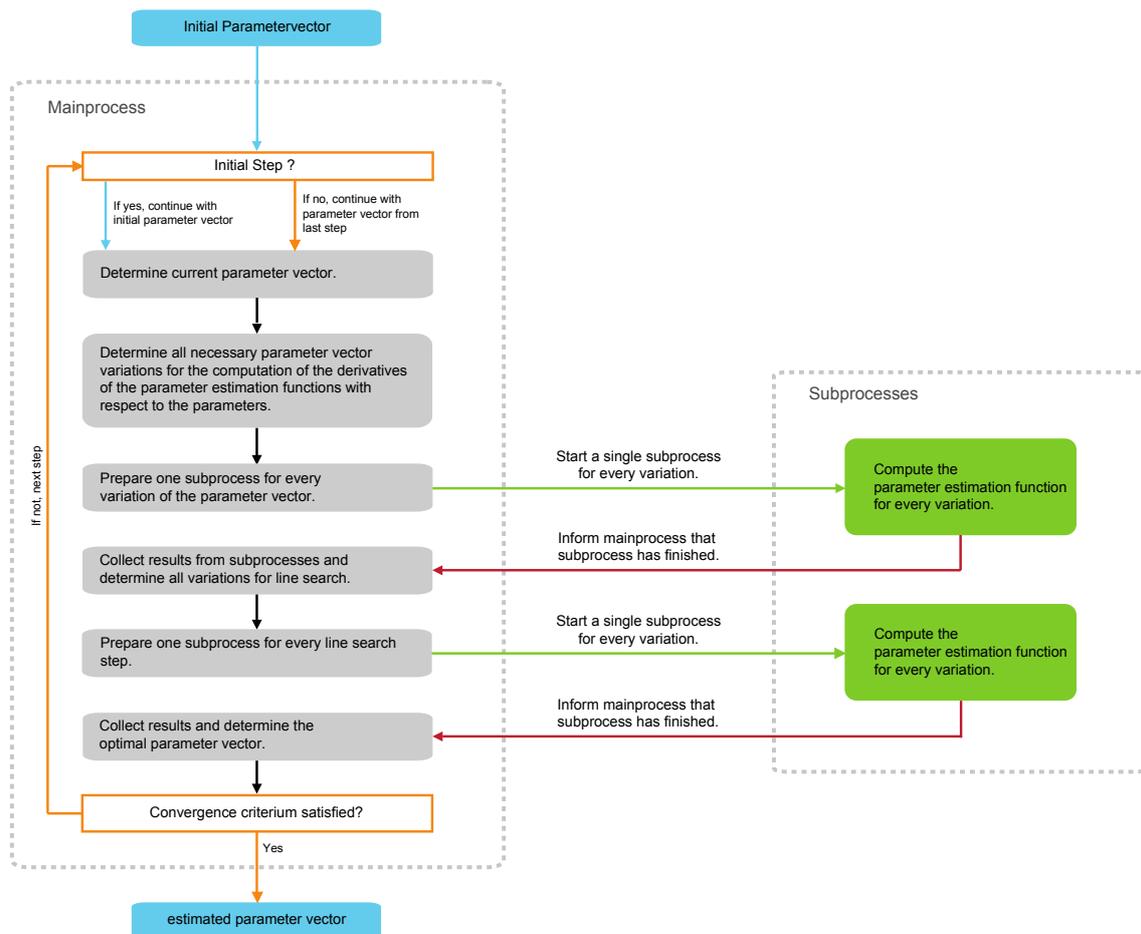
Fig. 8.1   Most important steps of the parameter estimation algorithm implemented in d^{3}f (figure taken from /MUH 12/)

8.5　　　Numerical Experiments

In this section the presented method for parameter estimation is applied to two different density driven flow problems. Section 8.5.1 covers the Gorleben example (gorleben_left_fit) and Section 8.5.2 covers the Saltdome example (saltdome_fit) from d³f. In both cases the permeability parameter K is estimated from a given set of datapoints for the mass fraction. These examples can be used to create all necessary files needed by the parameter estimation method for other d³f problems.

The underlying equations for density driven flow in the subdomain α read:

$$\partial_t(\phi_\alpha \rho_\alpha \omega_\alpha) + \nabla \cdot (\rho_\alpha \omega_\alpha \mathbf{q}_\alpha - \rho_\alpha \mathbf{D}_\alpha \nabla \omega_\alpha) = 0 \tag{8.9}$$

$$\partial_t(\phi_\alpha \rho_\alpha) + \nabla \cdot (\rho_\alpha \mathbf{q}_\alpha) = 0 \tag{8.10}$$

$$\mathbf{q}_\alpha = -\mu_\alpha^{-1} \mathbf{K}_\alpha (\nabla p_\alpha - \rho_\alpha \mathbf{g}) \tag{8.11}$$

$$\rho_\alpha = (1 - \omega_\alpha)\rho^{pW} + \omega_\alpha \rho^{pB} \tag{8.12}$$

$$\mu_\alpha := \mu_0 \cdot \mu_c^*(\omega_\alpha) \tag{8.13}$$

$$\mu_c^*(\omega_\alpha) := 1 + 1.85 \cdot \omega_\alpha \cdot \omega_{\alpha,abs} - 4.1 \cdot (\omega_\alpha \cdot \omega_{\alpha,abs})^2 + 44.5 \\ \cdot (\omega_\alpha \cdot \omega_{\alpha,abs})^3 \tag{8.14}$$

$$\mathbf{D}_\alpha := \mathbf{D}_\alpha^d + \mathbf{D}_\alpha^{md} \tag{8.15}$$

$$\mathbf{D}_\alpha^{md} := a_\alpha^t |\mathbf{q}_\alpha| \mathbf{I} + (a_\alpha^\ell - a_\alpha^t) \frac{\mathbf{q}_\alpha \otimes \mathbf{q}_\alpha}{|\mathbf{q}_\alpha|} \tag{8.16}$$

A nomenclature can be found in Appendix 13A.

8.5.1　　　Example Gorleben

The geometry and boundary conditions are depicted in Fig. 8.2, initial values for mass fraction can be found in Tab. 8.1 and the parameters used in the computation are shown in Tab. 8.2. The a priori given datapoints for the mass fraction are shown in Tab. 8.3. The parameter estimation method is then applied to two different test cases. These cases have a different initial value for the permeability K. Results are shown in Tab. 8.4 and Tab. 8.5.

It is shown that in both cases the parameter estimation method works sufficiently well. After a total of seven Newton-steps the value for the parameter estimation function is reduced by a factor of about 10^{-8} in the first case and 10^{-12} in the second case. The permeability parameter K is estimated up to an error of 6 % in the first case and <1 % in the second case.
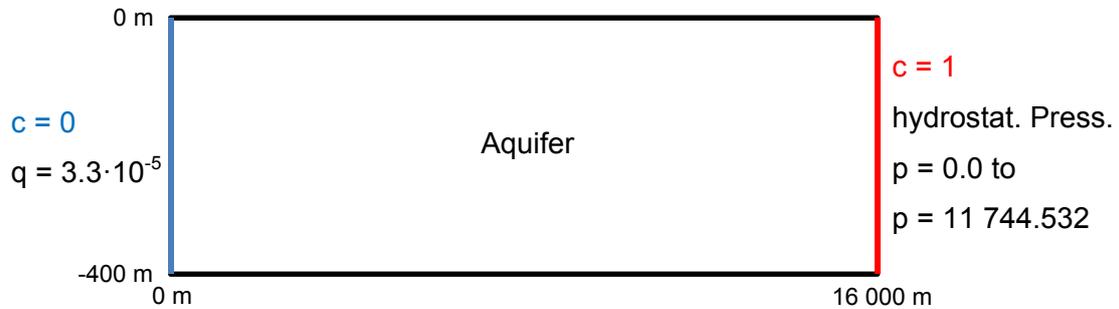
Fig. 8.2   Domain and boundary conditions for the example "Gorleben"

If boundary conditions are not specified then Neumann zero boundary conditions are used

Tab. 8.1   Initial conditions for the example "Gorleben"

Condition	Value
$\forall(x, y)$	$\omega = 0$

Tab. 8.2   Parameters for the example "Gorleben"

Symbol	Value in subdomain "Aquifer"
$\mathbf{g}$	$(0, -9.81 \text{ m s}^{-2})$
$\mathbf{D}^d$	$1.00 \cdot 10^{-9} \text{ m}^2 \text{ s} \cdot \mathbf{I}$
K	$1.00 \cdot 10^{-8} \text{ m}^2 \cdot \mathbf{I}$
ϕ	0.2
μ_0	$1.99 \cdot 10^{-3} \text{ kg m}^{-1} \text{ s}^{-1}$
ω_{abs}	0.26
ρ^{pW}	998.2 kg m^{-3}
ρ^{pB}	1197.2 kg m^{-3}
$[a^t, a^\ell]$	[10 m, 100 m]

Tab. 8.3 Data for the UG3 numproc "l2_param_est"

Time	Coordinates	Value
$1.0 \cdot 10^7$	$(8332, -221)$	$\omega = 0.0732404$
$1.1 \cdot 10^7$	$(8332, -221)$	$\omega = 0.0835534$
$1.2 \cdot 10^7$	$(8332, -221)$	$\omega = 0.0927142$
$1.3 \cdot 10^7$	$(8332, -221)$	$\omega = 0.1009130$
$1.4 \cdot 10^7$	$(8332, -221)$	$\omega = 0.1083080$
$1.5 \cdot 10^7$	$(8332, -221)$	$\omega = 0.1211720$

Tab. 8.4 Numerical Test 1

Newton Step	L2-Error	Value for K
0	$5.5 \cdot 10^{-4}$	$5.00 \cdot 10^{-9}$ m$^2 \cdot$ **I**
1	$2.0 \cdot 10^{-5}$	$7.61 \cdot 10^{-9}$ m$^2 \cdot$ **I**
2	$1.7 \cdot 10^{-5}$	$8.59 \cdot 10^{-9}$ m$^2 \cdot$ **I**
3	$1.3 \cdot 10^{-7}$	$9.22 \cdot 10^{-9}$ m$^2 \cdot$ **I**
4	$9.1 \cdot 10^{-9}$	$9.58 \cdot 10^{-9}$ m$^2 \cdot$ **I**
5	$6.1 \cdot 10^{-10}$	$9.78 \cdot 10^{-9}$ m$^2 \cdot$ **I**
6	$4.0 \cdot 10^{-11}$	$9.89 \cdot 10^{-9}$ m$^2 \cdot$ **I**
7	$2.5 \cdot 10^{-12}$	$9.94 \cdot 10^{-9}$ m$^2 \cdot$ **I**

Tab. 8.5 Numerical Test 2

Newton Step	L2-Error	Value for K
0	$1.6 \cdot 10^{-3}$	$2.00 \cdot 10^{-8}$ m$^2 \cdot$ **I**
1	$4.6 \cdot 10^{-5}$	$1.35 \cdot 10^{-8}$ m$^2 \cdot$ **I**
2	$2.2 \cdot 10^{-6}$	$1.16 \cdot 10^{-8}$ m$^2 \cdot$ **I**
3	$1.5 \cdot 10^{-7}$	$1.09 \cdot 10^{-8}$ m$^2 \cdot$ **I**
4	$1.0 \cdot 10^{-8}$	$1.04 \cdot 10^{-8}$ m$^2 \cdot$ **I**
5	$6.5 \cdot 10^{-10}$	$1.02 \cdot 10^{-8}$ m$^2 \cdot$ **I**
6	$3.8 \cdot 10^{-11}$	$1.01 \cdot 10^{-8}$ m$^2 \cdot$ **I**
7	$2.4 \cdot 10^{-12}$	$1.00 \cdot 10^{-8}$ m$^2 \cdot$ **I**

8.5.2 Example Saltdome

In contrast to the gorleben example, where the domain is build from one layer only, a total of three different layers are used in the saltdome example (Q-Sand, Clay, and T-Sand). This leads to three permeability parameters, which need to be estimated by the parameter estimation method.

The domain and boundary conditions are depicted in Fig. 8.3, initial conditions for the mass fractions are shown in Tab. 8.6, and the parameters used in the computation can be found in

Tab. 8.7. As expected, with these additional datapoints the parameters converge to the correct values. After a total of seven newton steps the parameter estimation function is reduced by a factor of 10^{-9}. The permeability parameter for the subdomain Q-Sand is estimated up to an error of 2 %, the permeability parameters for the subdomains T-Sand and Clay are estimated up to an error of 1 %.

The saltdome example shows, that datapoints should be chosen depending on the computational domain and the number of parameters to be estimated.
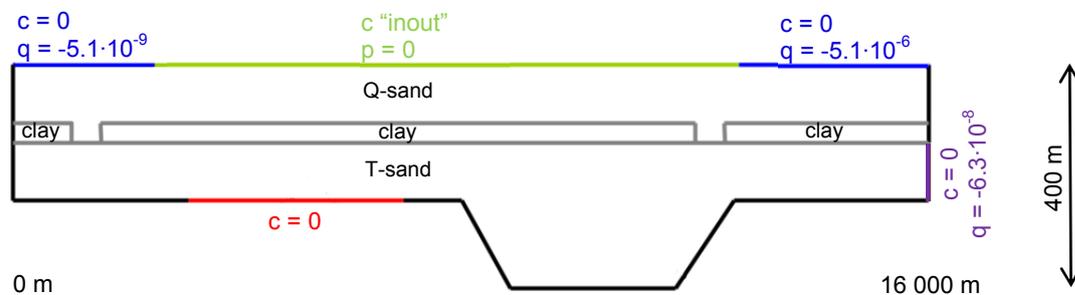
Fig. 8.3 Domain and boundary conditions for the example "Saltdome"

If boundary conditions are not specified then Neumann zero boundary conditions are used.

Tab. 8.6 Initial conditions for the example "Saltdome"

Condition	Value
$y < 300$	$\omega = 1$
$y \leq y \leq 330$	$\omega = 1 - (y - 300)/30$
$330 < y$	$\omega = 0$

Tab. 8.7 Parameters for the example "Saltdome"

Symbol	Value in subdomain "Clay"	Value in subdomain "Q-Sand"	Value in subdomain "T-Sand"
$\mathbf{g}$	$(0, -9.81 \text{ m s}^{-2})$	$(0, -9.81 \text{ m s}^{-2})$	$(0, -9.81 \text{ m s}^{-2})$
$\mathbf{D}^d$	$1.00 \cdot 10^{-9} \text{ m}^2 \text{ s} \cdot \mathbf{I}$	$1.00 \cdot 10^{-9} \text{ m}^2 \text{ s} \cdot \mathbf{I}$	$1.00 \cdot 10^{-9} \text{ m}^2 \text{ s} \cdot \mathbf{I}$
$\mathbf{K}$	$1 \cdot 10^{-13} \text{ m}^2 \cdot \mathbf{I}$	$5 \cdot 10^{-10} \text{ m}^2$	$1 \cdot 10^{-10} \text{ m}^2$
ϕ	0.05	0.2	0.2
μ_0	$1.99 \cdot 10^{-3} \text{ kg m}^{-1} \text{ s}^{-1}$	$1.99 \cdot 10^{-3} \text{ kg m}^{-1} \text{ s}^{-1}$	$1.99 \cdot 10^{-3} \text{ kg m}^{-1} \text{ s}^{-1}$
ω_{abs}	0.26	0.26	0.26
ρ^{pW}	998.2 kg m^{-3}	998.2 kg m^{-3}	998.2 kg m^{-3}
ρ^{pB}	1197.2 kg m^{-3}	1197.2 kg m^{-3}	1197.2 kg m^{-3}
$[a^t, a^\ell]$	[1 m, 10 m]	[1 m, 10 m]	[1 m, 10 m]

Tab. 8.8 Data for the UG3 numproc "l2_param_est" (Numerical Test 1)

Time	Coordinates	Value
$1.0 \cdot 10^9$	(13000,200)	$\omega = 0.868481$
$1.1 \cdot 10^9$	(13000,200)	$\omega = 0.858477$
$1.2 \cdot 10^9$	(13000,200)	$\omega = 0.847902$
$1.3 \cdot 10^9$	(13000,200)	$\omega = 0.837481$
$1.4 \cdot 10^9$	(13000,200)	$\omega = 0.827644$
$1.6 \cdot 10^9$	(13000,200)	$\omega = 0.807919$
$1.7 \cdot 10^9$	(13000,200)	$\omega = 0.798205$
$1.8 \cdot 10^9$	(8000,200)	$\omega = 0.852578$
$1.9 \cdot 10^9$	(8000,200)	$\omega = 0.843073$
$2.0 \cdot 10^9$	(8000,200)	$\omega = 0.833789$
$2.1 \cdot 10^9$	(8000,200)	$\omega = 0.824735$
$2.2 \cdot 10^9$	(8000,200)	$\omega = 0.815915$

Tab. 8.9   Numerical Test 1

New-ton Step	L2-Error	Value for K "Q-Sand"	Value for K "T-Sand"	Value for K "Clay"
0	$3.8 \cdot 10^{-3}$	$7.00 \cdot 10^{-10}$ m$^2 \cdot \mathbf{I}$	$2.00 \cdot 10^{-10}$ m$^2 \cdot \mathbf{I}$	$3.00 \cdot 10^{-13}$ m$^2 \cdot \mathbf{I}$
1	$8.8 \cdot 10^{-6}$	$1.45 \cdot 10^{-10}$ m$^2 \cdot \mathbf{I}$	$1.13 \cdot 10^{-10}$ m$^2 \cdot \mathbf{I}$	$4.43 \cdot 10^{-13}$ m$^2 \cdot \mathbf{I}$
2	$5.1 \cdot 10^{-8}$	$1.36 \cdot 10^{-10}$ m$^2 \cdot \mathbf{I}$	$9.94 \cdot 10^{-11}$ m$^2 \cdot \mathbf{I}$	$3.60 \cdot 10^{-13}$ m$^2 \cdot \mathbf{I}$
3	$5.2 \cdot 10^{-9}$	$1.36 \cdot 10^{-10}$ m$^2 \cdot \mathbf{I}$	$8.91 \cdot 10^{-11}$ m$^2 \cdot \mathbf{I}$	$4.92 \cdot 10^{-13}$ m$^2 \cdot \mathbf{I}$
4	$3.5 \cdot 10^{-10}$	$1.36 \cdot 10^{-10}$ m$^2 \cdot \mathbf{I}$	$8.48 \cdot 10^{-11}$ m$^2 \cdot \mathbf{I}$	$6.39 \cdot 10^{-13}$ m$^2 \cdot \mathbf{I}$
5	$1.0 \cdot 10^{-11}$	$1.38 \cdot 10^{-10}$ m$^2 \cdot \mathbf{I}$	$8.52 \cdot 10^{-11}$ m$^2 \cdot \mathbf{I}$	$6.79 \cdot 10^{-13}$ m$^2 \cdot \mathbf{I}$
6	$8.7 \cdot 10^{-12}$	$1.38 \cdot 10^{-10}$ m$^2 \cdot \mathbf{I}$	$8.48 \cdot 10^{-11}$ m$^2 \cdot \mathbf{I}$	$6.94 \cdot 10^{-13}$ m$^2 \cdot \mathbf{I}$
7	$8.4 \cdot 10^{-12}$	$1.38 \cdot 10^{-10}$ m$^2 \cdot \mathbf{I}$	$8.46 \cdot 10^{-11}$ m$^2 \cdot \mathbf{I}$	$7.03 \cdot 10^{-13}$ m$^2 \cdot \mathbf{I}$

Tab. 8.10   Data for the UG3 numproc "l2_param_est" (Numerical Test 2)

Time	Coordinates	Value
$1.00 \cdot 10^9$	(15000,200)	$\omega = 0.710631$
$1.05 \cdot 10^9$	(8000,275)	$\omega = 0.701684$
$1.10 \cdot 10^9$	(15000,200)	$\omega = 0.697345$
$1.15 \cdot 10^9$	(8000,275)	$\omega = 0.679212$
$1.20 \cdot 10^9$	(15000,200)	$\omega = 0.684607$
$1.25 \cdot 10^9$	(8000,275)	$\omega = 0.657997$
$1.30 \cdot 10^9$	(15000,200)	$\omega = 0.672264$
$1.35 \cdot 10^9$	(8000,275)	$\omega = 0.638124$
$1.40 \cdot 10^9$	(15000,200)	$\omega = 0.660415$
$1.45 \cdot 10^9$	(8000,275)	$\omega = 0.619393$
$1.60 \cdot 10^9$	(15000,200)	$\omega = 0.637511$
$1.65 \cdot 10^9$	(8000,275)	$\omega = 0.585251$
$1.70 \cdot 10^9$	(15000,200)	$\omega = 0.626399$
$1.75 \cdot 10^9$	(15000,350)	$\omega = 0.055336$
$1.80 \cdot 10^9$	(15000,350)	$\omega = 0.054888$
$1.85 \cdot 10^9$	(500,350)	$\omega = 0.202641$
$1.90 \cdot 10^9$	(500,200)	$\omega = 0.913014$
$1.95 \cdot 10^9$	(500,350)	$\omega = 0.193654$
$2.00 \cdot 10^9$	(8000,350)	$\omega = 0.159648$

Time	Coordinates	Value
$2.05 \cdot 10^9$	(8000,350)	$\omega = 0.156330$
$2.10 \cdot 10^9$	(8000,350)	$\omega = 0.153129$
$2.15 \cdot 10^9$	(8000,350)	$\omega = 0.15004$
$2.20 \cdot 10^9$	(8000,200)	$\omega = 0.815915$

Tab. 8.11 Numerical Test 2

Newton Step	L2-Error	Value for K "Q-Sand"	Value for K "T-Sand"	Value for K "Clay"
0	$8.4 \cdot 10^{-3}$	$7.00 \cdot 10^{-10}$ m$^2 \cdot$ **I**	$2.00 \cdot 10^{-10}$ m$^2 \cdot$ **I**	$3.00 \cdot 10^{-13}$ m$^2 \cdot$ **I**
1	$2.7 \cdot 10^{-4}$	$2.07 \cdot 10^{-10}$ m$^2 \cdot$ **I**	$1.46 \cdot 10^{-10}$ m$^2 \cdot$ **I**	$2.04 \cdot 10^{-13}$ m$^2 \cdot$ **I**
2	$7.5 \cdot 10^{-7}$	$1.87 \cdot 10^{-10}$ m$^2 \cdot$ **I**	$1.07 \cdot 10^{-10}$ m$^2 \cdot$ **I**	$2.05 \cdot 10^{-13}$ m$^2 \cdot$ **I**
3	$2.7 \cdot 10^{-7}$	$2.45 \cdot 10^{-10}$ m$^2 \cdot$ **I**	$1.09 \cdot 10^{-10}$ m$^2 \cdot$ **I**	$1.31 \cdot 10^{-13}$ m$^2 \cdot$ **I**
4	$1.7 \cdot 10^{-7}$	$2.80 \cdot 10^{-10}$ m$^2 \cdot$ **I**	$1.09 \cdot 10^{-10}$ m$^2 \cdot$ **I**	$1.19 \cdot 10^{-13}$ m$^2 \cdot$ **I**
5	$6.2 \cdot 10^{-8}$	$3.72 \cdot 10^{-10}$ m$^2 \cdot$ **I**	$1.06 \cdot 10^{-10}$ m$^2 \cdot$ **I**	$1.04 \cdot 10^{-13}$ m$^2 \cdot$ **I**
6	$1.7 \cdot 10^{-9}$	$4.76 \cdot 10^{-10}$ m$^2 \cdot$ **I**	$1.03 \cdot 10^{-10}$ m$^2 \cdot$ **I**	$1.01 \cdot 10^{-13}$ m$^2 \cdot$ **I**
7	$6.1 \cdot 10^{-12}$	$4.91 \cdot 10^{-10}$ m$^2 \cdot$ **I**	$1.01 \cdot 10^{-10}$ m$^2 \cdot$ **I**	$1.01 \cdot 10^{-13}$ m$^2 \cdot$ **I**

8.6 Conclusions

This chapter describes the parameter estimation method, which has been implemented and submitted to the d³f repository within the A-Dur project. In Appendix D a user manual can be found describing all necessary details about the parameter estimation method. Furthermore, the functionality of the parameter estimation method is investigated by two examples. It is shown that the method works sufficiently well, as long as the parameter estimation problem is not ill-conditioned. This is not the case if sufficient data points are provided.

9 Fast predictions by random-walk methods

9.1 Introduction

In the simulation of solute transport in porous media, the advection-dispersion equation /BEA 79/ is usually adopted as governing equation, which can be solved by standard finite difference methods (FDM) and finite element methods (FEM). These methods may suffer from the numerical dispersion or artificial oscillations unless a high grid resolution and small time steps are applied. An alternative is the particle tracking method which does not have the Peclet constraint, thus is applicable especially for the advection-dominated problems.

The basic idea of particle tracking is that a finite number of particles represent the distribution of a solute mass. Each particle carries a certain concentration or a certain fraction of the total mass and moves in the porous media according to the velocity field and dispersive process. The concentration distribution of the system is converted from particle clouds by spatial discretization and counting of particles in the cell. The particle tracking method does not solve the transport equation directly; instead, it uses the flow velocities obtained from the solution of the flow equation to advect the particles, and adds some additional displacement to simulate dispersion.

The benchmarks presented in this section are organized in such a way that they can be classified by both dimension and application field.

Tab. 9.1   RWPT benchmarks organization

	Classification by dimension		
Field	1d	2d	3d
Porous Media	ADuR5-1		ADuR5-2
Pore Scale		ADuR13-1	ADuR13-2

9.2   Theory

The classical advection-dispersion equation of a conservative solute in porous media can be written as /BEA 79/

$$\frac{\partial C}{\partial t} = -\nabla(VC) + \nabla(\mathbf{D}\nabla C) \tag{9.1}$$

where C is the concentration (ML^{-3}), V is the pore velocity vector (ML^{-1}), and $\mathbf{D}$ is the hydrodynamic dispersion tensor (L^2T^{-1}), t is time (T^2) and ∇ is the differential operator.

The random walk particle tracking (RWPT) method is issued from stochastic physics. The stochastic differential equation is /ITO 51/

$$\mathbf{x}(t_i) = \mathbf{x}(t_{i-1}) + \mathbf{v}(\mathbf{x}(t_{i-1}))\Delta t + Z\sqrt{2\mathbf{D}(\mathbf{x}(t_{i-1}))\Delta t} \tag{9.2}$$

where $\mathbf{x}$ is the coordinates of the particle location, Δt is the time step, and Z is a random number whose mean is zero and variance is unity.

It has been shown that this equation is equivalent to an equation that is slightly different from the advection-dispersion eq. (9.1). To be equivalent to eq. (9.1), the modified velocity /KIN 86/ is expressed as

$$V_i^* = V_i + \sum_{j=1}^{3} \frac{\partial D_{ij}}{\partial x_j} \tag{9.3}$$

with dispersion tensor /BEA 79/

$$D_{ij} = \alpha_T |V|\delta_{ij} + (\alpha_L - \alpha_T)\frac{V_i V_j}{|V|} + D_{ii}^d \tag{9.4}$$

where δ_{ij} is the Kronecker symbol, α_L is the longitudinal dispersion length, α_T is the transverse dispersion length, D_{ij}^d is the tensor of molecular diffusion coefficient, and V_i is the component of the mean pore velocity in the ith direction.

The equivalent stochastic differential equation to eq. (9.1) in three-dimensional problems can be written as (cf. /TOM 90/, /LAB 96/, /KIN 88/)

$$
\begin{aligned}
x_{t+\Delta t} &= x_t + \left(V_x(x_t, y_t, z_t, t) + \frac{\partial D_{xx}}{\partial x} + \frac{\partial D_{xy}}{\partial y} + \frac{\partial D_{xz}}{\partial z} \right) \Delta t \\
&\quad + \sqrt{2D_{xx}\Delta t}\, Z_1 + \sqrt{2D_{xy}\Delta t}\, Z_2 + \sqrt{2D_{xz}\Delta t}\, Z_3 \\
y_{t+\Delta t} &= y_t + \left(V_y(x_t, y_t, z_t, t) + \frac{\partial D_{yx}}{\partial x} + \frac{\partial D_{yy}}{\partial y} + \frac{\partial D_{yz}}{\partial z} \right) \Delta t \\
&\quad + \sqrt{2D_{yx}\Delta t}\, Z_1 + \sqrt{2D_{yy}\Delta t}\, Z_2 + \sqrt{2D_{yz}\Delta t}\, Z_3 \\
z_{t+\Delta t} &= z_t + \left(V_z(x_t, y_t, z_t, t) + \frac{\partial D_{zx}}{\partial x} + \frac{\partial D_{zy}}{\partial y} + \frac{\partial D_{zz}}{\partial z} \right) \Delta t \\
&\quad + \sqrt{2D_{zx}\Delta t}\, Z_1 + \sqrt{2D_{zy}\Delta t}\, Z_2 + \sqrt{2D_{zz}\Delta t}\, Z_3
\end{aligned}
\tag{9.5}
$$

where x, y, and z are the coordinates of the particle location, Δt is the time step, and Z_i is a random number whose mean is zero and variance is unity.

In eq. (9.5), the spatial derivatives of the dispersion coefficients are introduced from the modified velocity /KIN 86/. Together with eq. (9.4), the spatial derivatives of the dispersion coefficients can be expressed as a function of the derivatives of velocity. Note that to obtain the derivatives of velocity, velocity has to be continuous mathematically. To this end, velocity is interpolated at any location in an element from the known velocity at the element nodes.
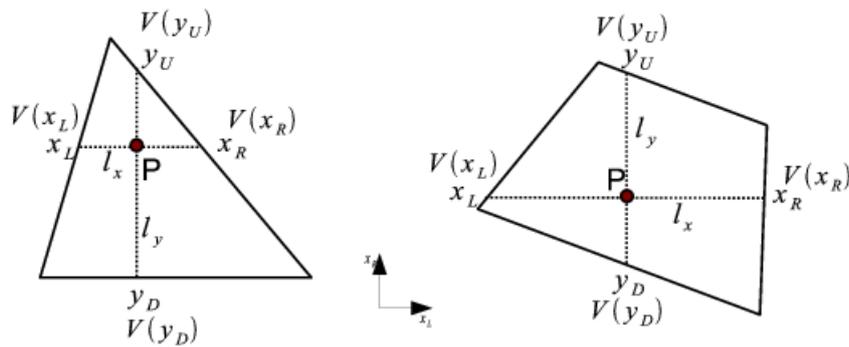
Fig. 9.1   Spatial derivatives of velocity for a particle in triangular and quadrilateral elements

Since the proposed RWPT method makes use of the FEM for velocity estimation, the derivative of velocity within each element is computed as in Fig. 9.1 and written as

167

$$\frac{\partial V_x}{\partial x} = \frac{V(x_R) - V(x_L)}{l_x}; \frac{\partial V_y}{\partial y} = \frac{V(y_U) - V(y_D)}{l_y}; \frac{\partial V_z}{\partial z} = \frac{V(z_N) - V(z_S)}{l_z}$$

(9.6)

while recognizing,

$$\frac{\partial V_x}{\partial y} = \frac{\partial V_x}{\partial z} = \frac{\partial V_y}{\partial x} = \frac{\partial V_y}{\partial z} = \frac{\partial V_z}{\partial x} = \frac{\partial V_z}{\partial y} \simeq 0$$

(9.7)

where x_L and x_R are intersection points of the element edges with a line parallel to the global x axis at which velocities are $V(x_L)$ and $V(x_R)$, y_D and y_U are intersection points of the element edges from down to up with a line parallel to the global y axis at which velocities are $V(y_D)$ and $V(y_U)$, z_S and z_N are the intersection points of the element edges from south to north with a line parallel to the global z axis at which velocities are $V(z_S)$ and $V(z_N)$, and l_x, l_y, and l_z are the length of each intersection line, respectively.

Thus, the derivatives of the dispersion coefficients are as follows /HOT 02/

$$\frac{\partial D_{xx}}{\partial x} = V_x \frac{\partial V_x}{\partial x} \left[\alpha_L \left(\frac{2}{V} - \frac{V_x^2}{V^3} \right) - \alpha_T \frac{V_y^2 + V_z^2}{V^3} \right]$$

$$\frac{\partial D_{xy}}{\partial y} = (\alpha_L - \alpha_T) \left[\frac{\partial V_y}{\partial y} \frac{V_x}{V} - \frac{V_x V_y^2}{V^3} \frac{\partial V_y}{\partial y} \right]$$

$$\frac{\partial D_{xz}}{\partial z} = (\alpha_L - \alpha_T) \left[\frac{\partial V_z}{\partial z} \frac{V_x}{V} - \frac{V_x V_z^2}{V^3} \frac{\partial V_z}{\partial z} \right]$$

$$\frac{\partial D_{yy}}{\partial y} = V_y \frac{\partial V_y}{\partial y} \left[\alpha_L \left(\frac{2}{V} - \frac{V_y^2}{V^3} \right) - \alpha_T \frac{V_x^2 + V_z^2}{V^3} \right]$$

$$\frac{\partial D_{yx}}{\partial x} = (\alpha_L - \alpha_T) \left[\frac{\partial V_x}{\partial x} \frac{V_y}{V} - \frac{V_y V_x^2}{V^3} \frac{\partial V_x}{\partial x} \right]$$

$$\frac{\partial D_{yz}}{\partial z} = (\alpha_L - \alpha_T) \left[\frac{\partial V_z}{\partial z} \frac{V_y}{V} - \frac{V_y V_z^2}{V^3} \frac{\partial V_z}{\partial z} \right]$$

(9.8)

$$\frac{\partial D_{zz}}{\partial z} = V_z \frac{\partial V_z}{\partial z} \left[\alpha_L \left(\frac{2}{V} - \frac{V_z^2}{V^3} \right) - \alpha_T \frac{V_x^2 + V_y^2}{V^3} \right]$$

$$\frac{\partial D_{zx}}{\partial x} = (\alpha_L - \alpha_T) \left[\frac{\partial V_x}{\partial x} \frac{V_z}{V} - \frac{V_z V_x^2}{V^3} \frac{\partial V_x}{\partial x} \right]$$

$$\frac{\partial D_{zy}}{\partial y} = (\alpha_L - \alpha_T) \left[\frac{\partial V_y}{\partial y} \frac{V_z}{V} - \frac{V_z V_y^2}{V^3} \frac{\partial V_y}{\partial y} \right]$$

Because velocity is not derivable at the interface of two adjacent elements in a nonuniform flow, computing dispersion coefficient derivatives by using a finite element approach would yield erroneous values /HOT 02/. To prevent these errors, a particle is coded to have information of an element index and the velocity estimation is

continuous even at the elemental boundaries in this method. Thus, the derivatives of dispersion coefficients will be computed accordingly. This is an improved approach from the work by /HOT 02/.

9.3 Random walk particle tracking (RWPT) in porous media (Benchmark ADuR5-1 and ADuR5-2)

9.3.1 One-Dimensional Benchmark (ADuR5-1)

9.3.1.1 Problem definition

A one-dimensional homogeneous aquifer is chosen to simulate a soil column experiment conducted by /HAR 00/. In the experiment, a constant flow rate was established, 2.5 pore volumes NaCl-tap water solution and 2.5 pore volumes *Cryptosporidium parvum* solution (1×10^5 oocysts per mL) were injected respectively, the outflow was continuously collected. Fig. 9.2 shows the schematic description of the experiment.
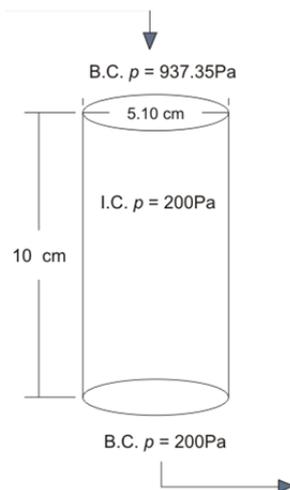
Fig. 9.2   Schematic of soil column experiment

NaCl-tap water solution is used as a tracer, which experiences only advection and dispersion. The *Cryptosporidium parvum* can be classified as a biological colloid. Colloids moving in porous media experience advection, dispersion, sorption-desorption, and filtration.

9.3.1.2   Motivation

This benchmark aims to verify the proposed RWPT method by comparing it with traditional FEM in mass transport. Furthermore, RWPT provides features to simulate complex processes such as sorption-desorption and filtration.

9.3.1.3   Analytical solution

For the one-dimensional transport including sorption-desorption and filtration through a homogeneous medium the following differential equation is applied

$$\frac{\partial C}{\partial t} + \frac{\rho_b}{n}\frac{\partial C_S}{\partial t} = v\alpha_L \frac{\partial^2 C}{\partial x^2} - v(\frac{\partial C}{\partial x} + \lambda C) \tag{9.8}$$

where C is dissolved concentration (kg·m^{-3}), C_S is sorbed concentration (kg·kg^{-1}), t is time (s), ρ_b is bulk density (kg·m^{-3}), n is porosity (-), v is velocity (m·s^{-1}), α_L is longitudinal dispersivity (m), x is distance (m), and λ is filtration coefficient (m^{-1}).

The instantaneous, linear sorption model assumes that

$$C_S = K_d C \tag{9.9}$$

where K_d is the partitioning coefficient ($m^3 \cdot kg^{-1}$). The retardation coefficient R is

$$R = 1 + \frac{\rho_b}{n}K_d \tag{9.10}$$

The dispersion coefficient in the x-direction D_{xx} ($m^2 \cdot s^{-1}$) is

$$D_{xx} = v\alpha_L \tag{9.11}$$

The analytical solution for a pulse input (inject time from 0 to τ) is /VAN 81/):

$$C = \frac{1}{2}C_0 \left[\exp\left(\frac{vx(1-\gamma)}{2D_{xx}}\right) \mathrm{erfc}\left(\frac{x - v\gamma t/R}{2\sqrt{D_{xx}t/R}}\right) \right.$$

$$\left. + \exp\left(\frac{vx(1+\gamma)}{2D_{xx}}\right) \mathrm{erfc}\left(\frac{x+v\gamma t/R}{2\sqrt{D_{xx}t/R}}\right) \right] \tag{9.12}$$

for $t \in (0, \tau)$,

$$C = \frac{1}{2}C_0 \left[\exp\left(\frac{vx(1-\gamma)}{2D_{xx}}\right) \text{erfc}\left(\frac{x - v\gamma t/R}{2\sqrt{D_{xx}t/R}}\right) \right.$$

$$+\exp\left(\frac{vx(1+\gamma)}{2D_{xx}}\right) \text{erfc}\left(\frac{x+v\gamma t/R}{2\sqrt{D_{xx}t/R}}\right)$$

$$-\exp\left(\frac{vx(1-\gamma)}{2D_{xx}}\right) \text{erfc}\left(\frac{x-v\gamma(t-\tau)/R}{2\sqrt{D_{xx}(t-\tau)/R}}\right)$$

$$\left. - \exp\left(\frac{vx(1+\gamma)}{2D_{xx}}\right) \text{erfc}\left(\frac{x+v\gamma(t-\tau)/R}{2\sqrt{D_{xx}(t-\tau)/R}}\right) \right]$$

(9.13)

for $t \in (\tau, \infty)$, where

$$\gamma = \sqrt{1 + 4v\lambda RD_{xx}/v^2}$$

(9.14)

9.3.1.4   Numerical solution

The calculation area is simplified to a line with the length of 0.1m. For the numerical model 100 elements and 101 nodes are included. Head gradient is set by giving two constant pressures at both left and right boundaries to establish a uniform velocity field with the value of 7.1 md^{-1}.

The number of pore volume (x-axis) is calculated by

$$P_V = \frac{vt}{L}$$

(9.15)

where v is the seepage velocity, L is the length of the soil column. Considering the Courant number, the time step size is set by assigning P_V to 0.01. In the simulation, 100 particles per time steps are loaded near the left boundary for 250 time steps.

The filtration process is described by using the filtration coefficient. The sorption-desorption process is described by the two-rate model from /JOH 95/. In the two-rate model, desorption is governed by two different rate coefficients

$$N/N_0 = Ae^{-k_1 t} + (1 - A)e^{-k_2 t}$$

(9.16)

where N is the number of particles remaining on the medium at time t, N_0 is the initial number of particles on the medium at the time of initial sorption, A is a weighting factor,

and k_1 and k_2 are the fast and slow sorption rate coefficient, respectively. Relevant parameters are listed in Tab. 9.2.

Tab. 9.2   Model parameters for the column experiment

Symbol	Parameter	Value	Unit
k	Permeability	$1.114476 \cdot 10^{-11}$	m^2
α_L	Longitudinal dispersivity	0.005	m
n	Porosity(tracer)	0.5	–
n	Porosity(colloid)	0.42	–
A	Weighting factor	0.9	–
k_1	Fast sorption rate coefficient	0.1	–
k_2	Slow sorption rate coefficient	0.001	–
λ	Filtration coefficient	5.2	m^{-1}

9.3.1.5   Results

The tracer experiences only advection and dispersion, which means in eq. (9.9), $C_S = 0$, $\lambda = 0$. The results of RWPT simulation for the distribution of concentration over time are compared to those of measured value from the experiment by Harter, the analytical solution, and the OGS simulation with the mass transport method. The comparison results are shown in Fig. 9.3, where the green curve is the measured value, the dashed black curve is the simulation result operated with FEM, the blue curve is the RWPT simulation result, and the red curve is the analytical solution.
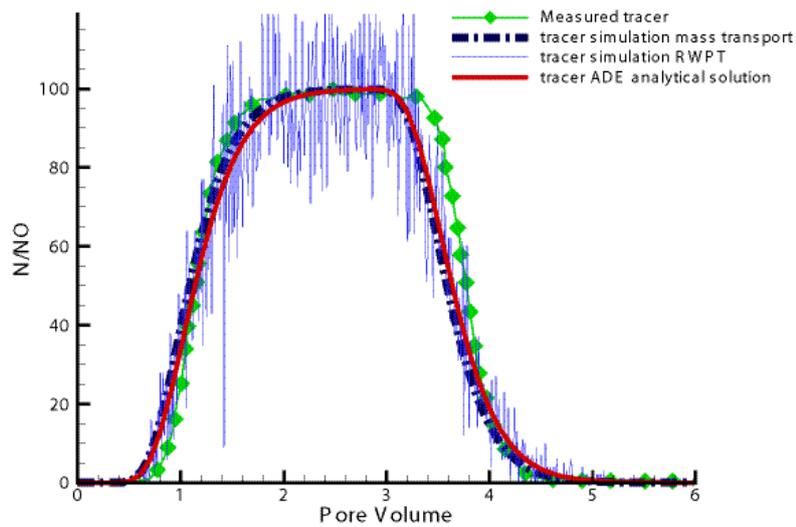
Fig. 9.3   Tracer transport with advection and dispersion

In the colloid transport simulation, the number of particles leaving the right boundary is counted each time step. The number is then converted to concentration in order to obtain the corresponding breakthrough curve over time. The comparison with the measured value from Harter's experiment is shown in Fig. 9.4, where the green curve is the measured value, and the blue curve is the RWPT simulation result. No analytical solution is available in this kind of situation.
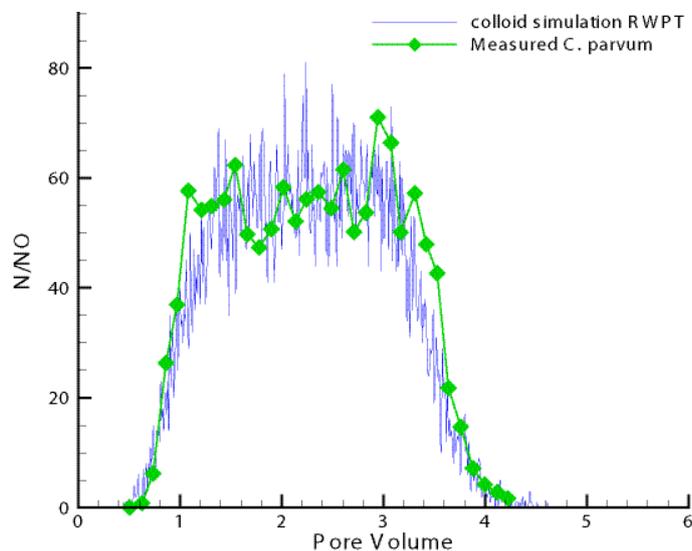
Fig. 9.4   Colloid transport with sorption-desorption and decay

9.3.2 Three-Dimensional Benchmark (ADuR5-2)

9.3.2.1 Problem definition

A three-dimensional homogeneous cube is chosen to verify advective dispersive transport. The side length of the cube model domain is 100 m. The velocity field is held constant in the diagonal direction from the bottom left to top right (Fig. 9.5).
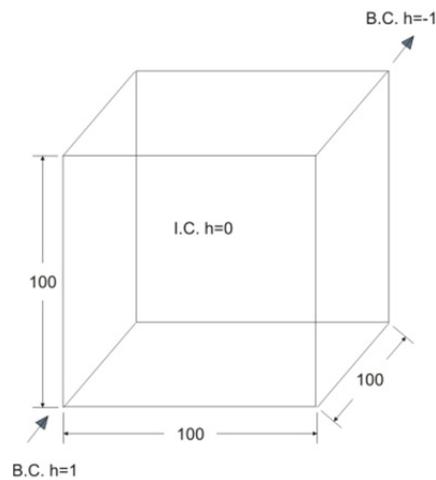
Fig. 9.5 Schematic of 3d homogeneous model

9.3.2.2 Analytical solution

The stated problem can be solved with an analytical solution provided by /OGA 61/.

$$C(x, y, z, t) = \frac{C_0 V}{8(\pi t)^{3/2} \sqrt{D_{xx} D_{yy} D_{zz}}} \exp\left[-\frac{(x - x_0)^2}{4 D_{xx} t} - \frac{(y - y_0)^2}{4 D_{yy} t} - \frac{(z - z_0)^2}{4 D_{zz} t} \right] \tag{9.17}$$

where C_0 is the initial concentration.

9.3.2.3 Numerical solution

The domain is discretized with tetrahedral elements. The same grid density is used for converting particle distributions to element concentrations. The head gradient is set by assigning two constant boundary conditions on the diagonal joint points.

The initial source load is applied to an area close to the bottom left of the domain with an initial concentration of $C_0 = 1 \ kgm^{-3}$. The material properties for this model setup are given in Tab. 9.3.

Tab. 9.3   Material properties for 3d homogeneous medium

Symbol	Parameter	Value	Unit
k	Permeability	$6.0804 \cdot 10^{-10}$	m^2
α_L	Longitudinal dispersivity	0.005	m
α_T	Transverse dispersivity	0.005	m
n	Porosity	0.2	–

9.3.2.4   Results

The advection-dispersion of the particles pulse across the cube is shown in Fig. 9.6. At the beginning, particles are assembled together as they were released from positions that are very close to each other. As the particles moving along with the flow, they disperse and form a spherical surface-shaped cloud. When the particles move to the center of the cube, the area of the spherical surface-shaped cloud reach to the maximum. After particles across the center of the cube, as the flowpaths begin to converge, the shape of the particle cloud change to a funnel-shaped curved surface. Particles move along the diagonal line have the bigger velocities and shorter pathlines so they reach to the top right corner of the cube earlier than other particles.

The number of particles that pass the top right corner of the cube is counted at every time step in order to generate the concentration breakthrough curve. The result of RWPT simulation for the distribution of concentration over time is compared to the analytical solution. The comparison results are shown in Fig. 9.7, where the blue curve is the RWPT simulation result, and the red curve is the analytical solution. The shape of the breakthrough curve is classical and similar to 1d and 2d simulations. With a relatively large number of particles the problem of fluctuations in concentration calculation can be overcome.
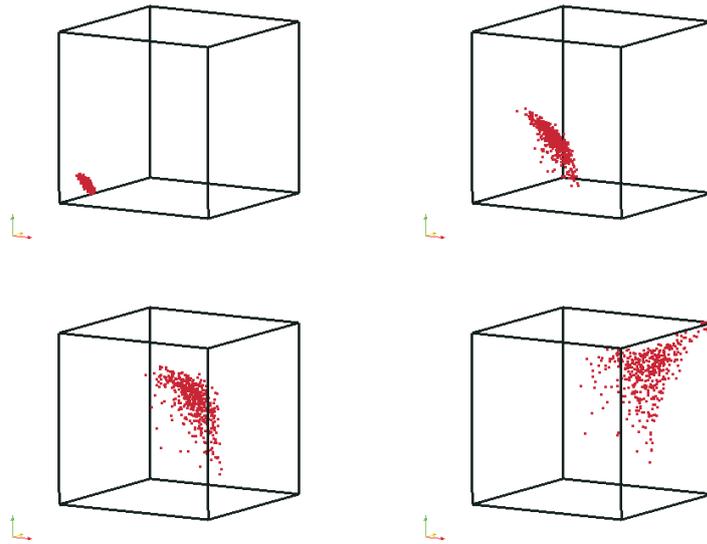
Fig. 9.6   Particle clouds in the cube
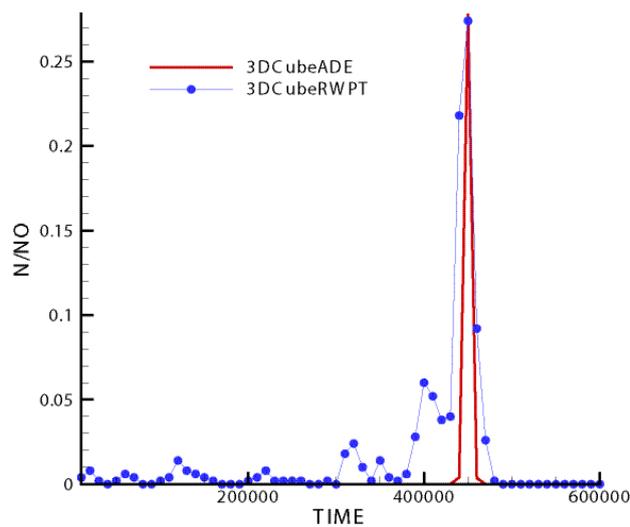
Fig. 9.7   Transport results of the 3d RWPT method compared with analytical solution

9.4   RWPT in pore scale space (Benchmark ADuR13-1 and ADuR13-2)

Physical observations and theoretical treatments of flow in porous media are usually associated with three different length scales: pore-, local-, and field-scales. Dominant processed and governing equations may vary with scales. In this benchmark, efforts are taken in order to simulate solute transport in pore scale in a simplified manner. The governing equation adopted here is the groundwater flow equation based on Darcy's law.

176

9.4.1 Two-Dimensional Pore Scale Benchmark (ADuR13-1)

9.4.1.1 Problem definition

To simulate particles moving in pore scale space, first the problem is simplified into a two-dimensional case which is a box with only one grain inside. The calculation area is a rectangular space with a circle in the middle, the void between the circle and the rectangular is the calculation domain and discretized by triangle mesh (Fig. 9.8).
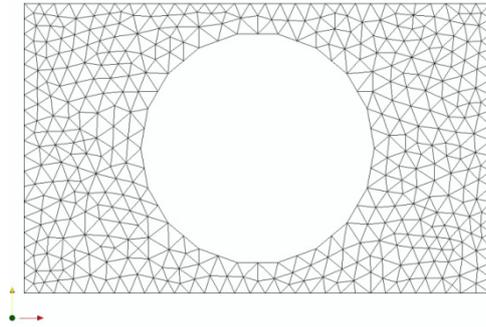
Fig. 9.8   Mesh of 2d box with one grain inside

9.4.1.2 Numerical solution

Firstly, the proposed RWPT method in this model is testified by assign constant hydraulic head to the left and right boundaries (Dirichlet boundary condition), and no-flow boundary conditions to the top and bottom boundaries. Particles are released from a line that is close to the left boundary. Relative parameters are listed in Tab. 9.4.

Tab. 9.4   Material properties for 2d pore scale model with one grain inside – advective

Symbol	Parameter	Value	Unit
k	Permeability	$1 \cdot 10^{-10}$	m^2
D	Diffusion coefficient	0.0	$m^2 s^{-1}$
n	Porosity	1.0	–

9.4.1.3　　Results

The particles are moving in the pore space according to the velocity field. Particle cloud develops over time is show in Fig. 9.9. The shape of the particle cloud is a straight line in the beginning, and then is curved a little as it getting closer to the grain. The velocities in the area surrounding the grain are very small that particles in this area are moving very slowly. When a particle hit the surface of the grain or the boundary of the box, it will be captured. Particles pass through the throats between the grain and the box are accelerated as the velocities in these throats are large. After passing through the throats, particles spread to form an arc and move on to the right side boundary. In the zone that is behind the grain no particles are observed because the flow velocity is relatively small and dispersion is not considered in this benchmark.
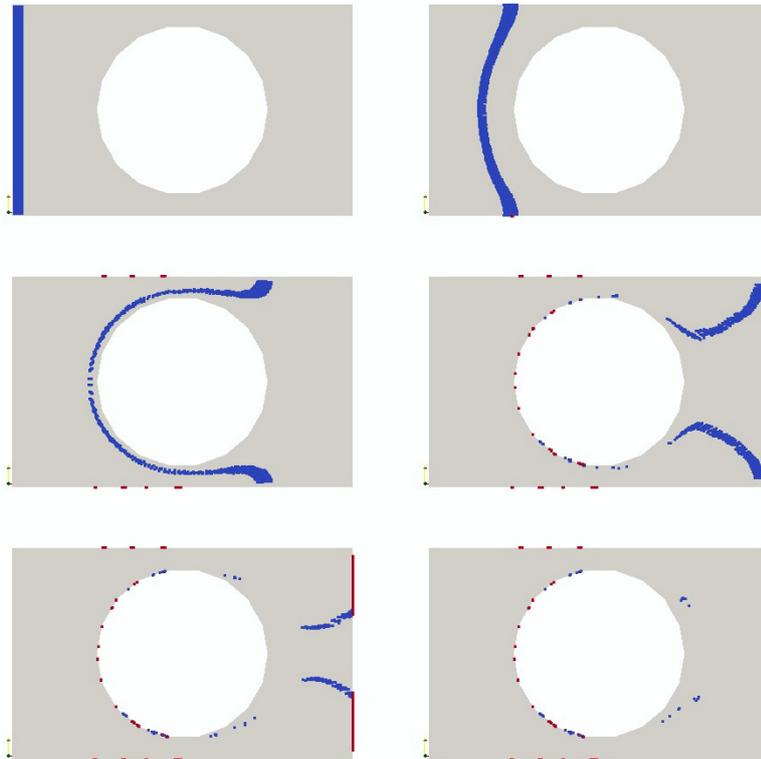
Fig. 9.9　　Particles advect in rectangular domain with one grain

9.4.1.4 Discussion 1

If there is no flow in this domain, and the molecular diffusion coefficient is increased, then the movements of the particles are dominated by the molecular diffusion process. Relative parameters are listed in Tab. 9.5.

Tab. 9.5 Material properties for 2d pore scale model with one grain inside – diffusive

Symbol	Parameter	Value	Unit
k	Permeability	$1 \cdot 10^{-10}$	m^2
D	Diffusion coefficient	$1 \cdot 10^{-8}$	$m^2 s^{-1}$
n	Porosity	1.0	–

Particles are released from a line that is close to the left boundary. As there is no flow, particles are moving randomly in the pore space. Particle cloud develops over time is show in Fig. 9.10. Some of the particles attach to the surface of the grain or the boundary of the box. The molecular diffusion coefficient is relative to temperature. This benchmark is aimed to achieve the effect that particles are moving differently when temperature changes.

9.4.1.5 Discussion 2

Next, the number of grains in the box is increased from one to six. The void between the circles and the rectangular is the calculation domain and discretized by triangle mesh (Fig. 9.11). Dirichlet boundary conditions are set by assign constant hydraulic head to the left and right boundaries. No-flow boundary conditions are set to the top and bottom boundaries. Particles are released from a line that is close to the left boundary. Relative parameters are unchanged as listed in Tab. 9.4.
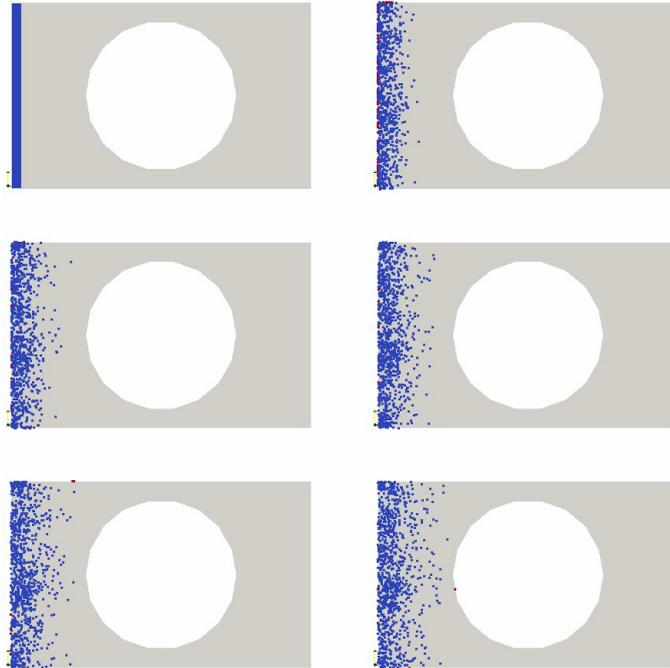
Fig. 9.10 Particles diffuse in rectangular domain with one grain
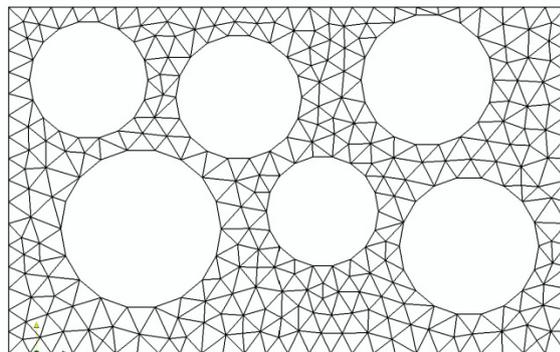
Fig. 9.11 Mesh of 2d box with several grains inside

Particle cloud develops over time is show in Fig. 9.12. Note that in this benchmark, released particles are displayed in the color of blue. When a particle hits the boundary and gets attached, it turns to red. But in the next time step, the attached particle still has the chance to detach and move again. It is clear that this benchmark is not a simple combination of six single grains, because they can affect each other. The velocity field in this case is with more complexity thus the particle cloud is complicated. But the particle cloud development obeys the same trend as in the single grain case.
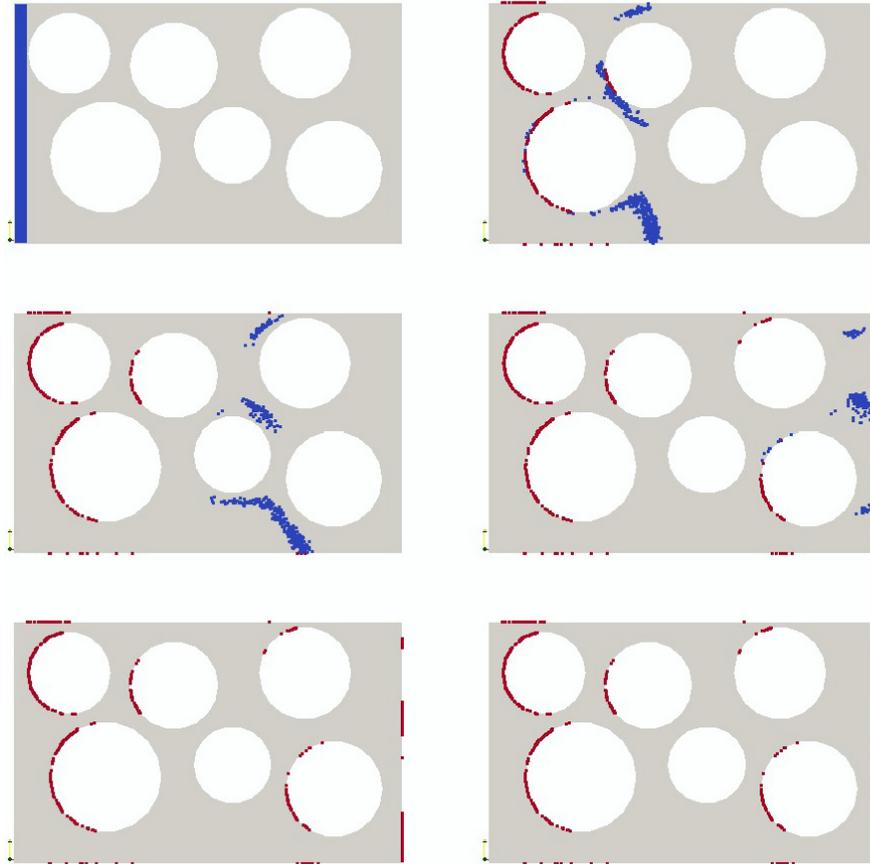
Fig. 9.12   Particles transport in rectangular domain with several grains

9.4.1.6   Discussion 3

If the grain (circle) is discretized inside (Fig. 9.13), then particles attached to the surface of the grain can go into the grain and diffuse inside. Different porosity and permeability coefficient are given to grains and the pore space. Note that the different colors here represent materials with different properties. Dirichlet boundary conditions are set by assign constant hydraulic head to the left and right boundaries. No-flow boundary conditions are set to the top and bottom boundaries. Particles are released from a line that is close to the left boundary. Relative parameters are listed in Tab. 9.6.
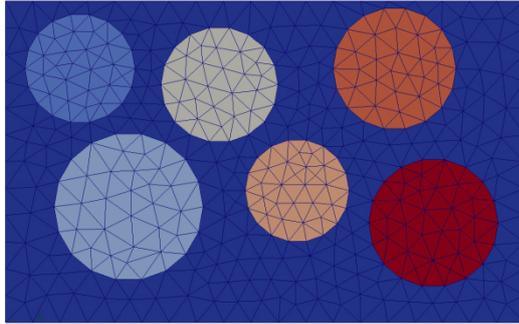
Fig. 9.13   Mesh of 2d box with meshed grains inside

Tab. 9.6   Material properties for 2d pore scale model with six meshed grains inside

Symbol	Parameter	Value	Unit
k	Permeability (pore space)	$1 \cdot 10^{-10}$	m^2
k	Permeability (grains)	$1 \cdot 10^{-12}$	m^2
D	Diffusion coefficient	$1 \cdot 10^{-15}$	$m^2 s^{-1}$
n	Porosity (pore space)	1.0	–
n	Porosity (grains)	0.1	–

Particle cloud develops over time is show in Fig. 9.14. The particles in the pore space are moving according to the velocity field. Note that there's no flow inside of the grains, only molecular diffusion. Particles that hit the surface of the grains can go into the grains and move inside. Their movements are because of molecular diffusion thus are random.
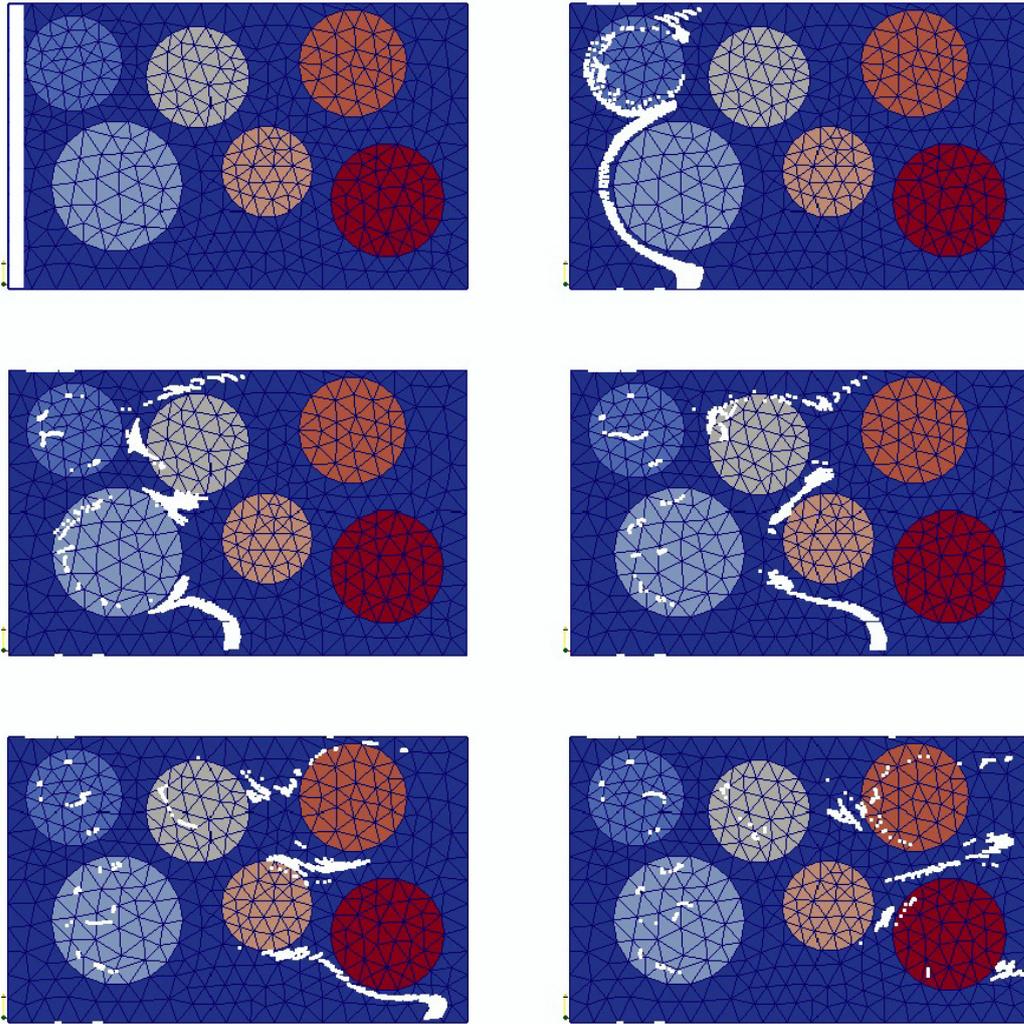
Fig. 9.14   Particles transport in rectangular domain with several meshed grains

9.4.2   Three-Dimensional Pore Scale Benchmark (ADuR13-2)

9.4.2.1   Problem definition

Similar to the 2d case study, the problem is first simplified into a three-dimensional case with only one grain in a box. The calculation area is a cube space with a sphere in the center, the void space between the sphere and the cube is the calculation domain and discretized by tetrahedral mesh (Fig. 9.15).
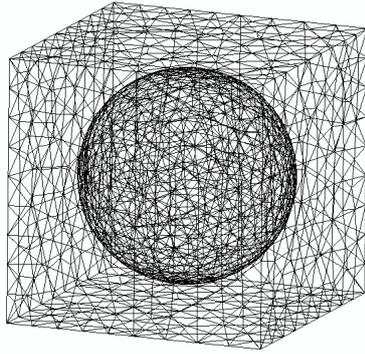
Fig. 9.15   Mesh of 3d box with one grain inside

9.4.2.2   Numerical solution

The proposed RWPT method in this model is testified by assign constant hydraulic head to the left surface and right surface boundaries (Dirichlet boundary condition), and no-flow boundary conditions to the top, bottom, front, and back surface boundaries. Particles are released from a surface that is close and parallel to the left surface boundary. Relative parameters are listed in Tab. 9.7.

Tab. 9.7   Material properties for 3d pore scale model with one grain inside

Symbol	Parameter	Value	Unit
k	Permeability	$1 \cdot 10^{-10}$	m^2
D	Diffusion coefficient	$1 \cdot 10^{-15}$	$m^2 s^{-1}$
n	Porosity	1.0	–

9.4.2.3   Results

The particles are moving in the pore space according to the velocity field. Particle cloud develops over time is show in Fig. 9.16. The shape of the particle cloud is a plain surface in the beginning, then is curved a little as it getting closer to the grain. The velocities in the area surrounding the grain is very small that particles in this area are moving very slowly. When a particle hit the surface of the grain or the box, it will be attached. In the zone that is behind the grain no particles are observed because the flow velocity is relatively small that no turbulence is happened in that zone.
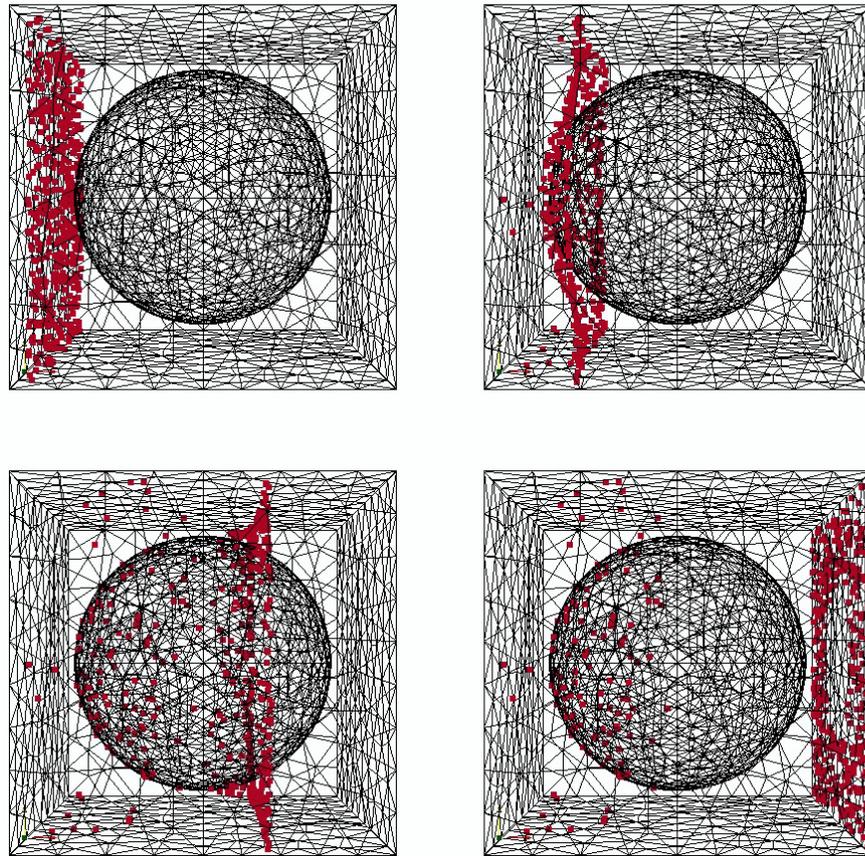
Fig. 9.16   Particles advect in cube domain with one grain

9.4.2.4   Mutiple Grains

To establish a numerical model, not only a detailed understanding of the flow behavior in the pore space is needed, an accurate and realistic characterization of the structure of the pore space is significant as well. In this work, the pore space computational mesh is generated by the utilization of CGAL and settleDyn.

To generate a mesh, first a polyhedral domain (Fig. 9.17a) is prepared, and a tetrahedral mesh of the domain is generated with CGAL. For the grains, a 3d image (Fig. 9.17b) is used, which is very flexible, can be obtained from micro-CT scans or generated manually. The structure of the grains is generated with settleDyn. Grains are represented by polyhedrons.

a) Domain outline   b) Grain image]
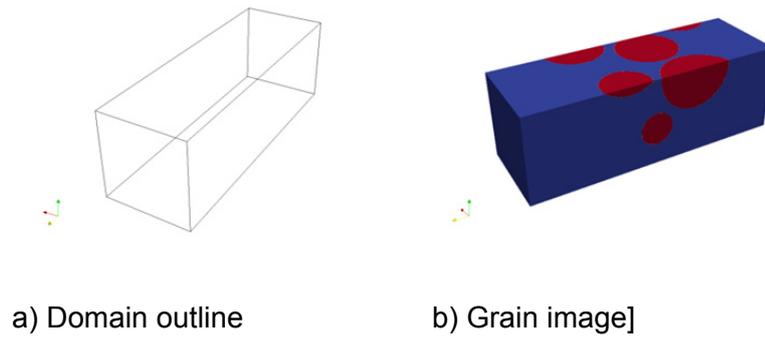
Fig. 9.17   CGAL mesh generation

Secondly, use the grain mesh to refine the domain mesh with CGAL's mesh refining algorithm. Using the Delaunay triangulation, with sub domain labels, the labeled tetrahedral mesh with embedded grains (Fig. 9.18) is generated.

Fig. 9.18   Mesh with embedded grains

In this example, the calculation domain is a rectangular parallelepiped with several grains inside (see Fig. 9.18). The grains' sizes are not uniform and grains are randomly distributed among the domain. The pore space is discretized with tetrahedral elements and the inside spaces of the grains are discretized as well.

The flow field is simplified to potential flow that on the inlet and outlet boundary, Dirichlet boundary conditions are adopted that constant hydraulic heads are set on both front and back surfaces. Other surfaces are set to be no-flow boundaries that fluid cannot pass the boundary and adjacent flow lines are parallel to the boundary surface.

The pore space is treated as a medium which is set to be homogeneous and isotropic. Fig. 9.19 shows the hydraulic head isosurfaces of the calculation domain.
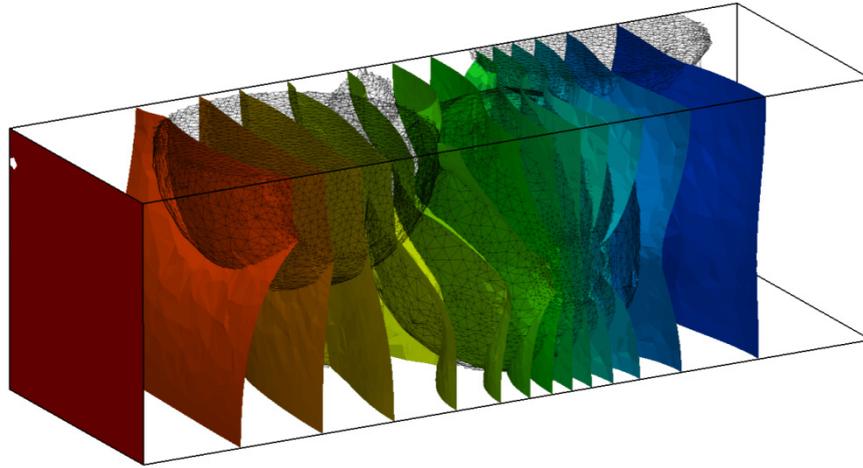
Fig. 9.19   Hydraulic head isosurfaces in domain with grains – potential flow

In the potential flow, the hydraulic head gradient has a direction that is always perpendicular to the equipotential lines. As this is an isotropic medium, the direction of fluid flow is parallel to the hydraulic head gradient, i. e., flow lines will cross the hydraulic head isosurfaces at right angles.

Particles are released to the domain from an area close to the inlet boundary for a constant time. Fig. 9.20 shows the simulation results of particles' distribution over time.

The particles are carried along by the fluid and move in the pore space. The "random walk" property allows the particles to digress from the flow line to some extent. Some of the particles enter the dead end of the pore space where the velocity is extremely low. Some hit to the surface of the grains and get captured because the velocity there is close to zero. The simulation results show the advantage of the proposed RWPT method that it is capable to describe the detailed flow properties.

a) t = 0

b) t = 50

c) t = 100

d) t = 150

e) t = 200
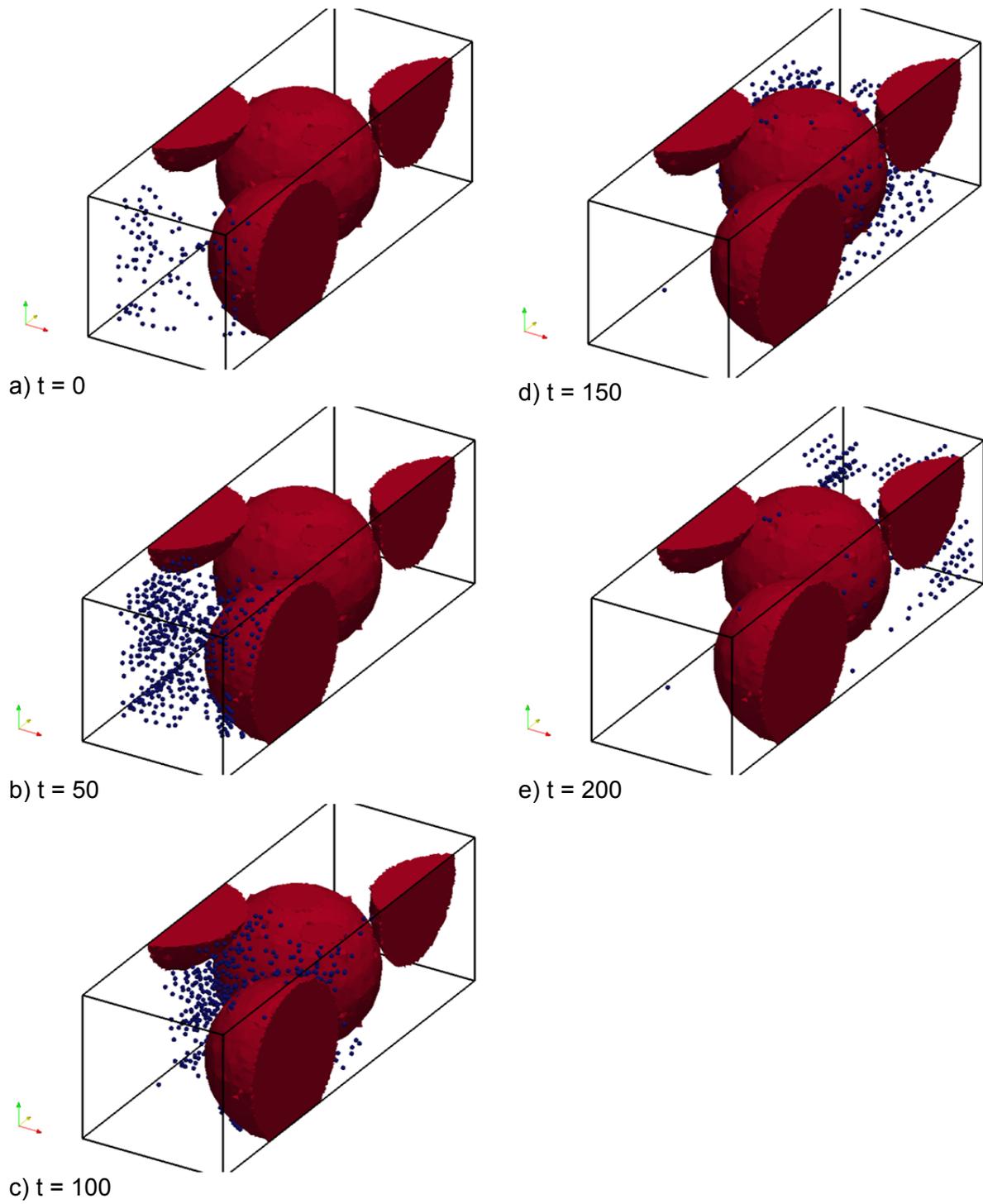
Fig. 9.20 Particle clouds in domain with embedded grains

10 Benchmarking

10.1 Introduction

10.1.1 Measurements of fracture aperture

Fractures may be defined through direct measurement or geo-statistical reproduction. In the benchmarks of this report, both methods will be utilized. Where fractures are directly measured, as in benchmark ADuR3 for instance, the methodology utilizes a laser profiler. Profiles (elevation measurements) are taken of each fracture surface, and these are manipulated numerically. Point-wise fracture aperture is the difference between the top and bottom surfaces at corresponding locations. Statistically reproduced fractures, as in ADuR2 for instance, reproduce roughness of the aperture (not each surface) to achieve a desired mean and standard deviation. The result is used directly as fracture aperture in numerical simulations.

10.1.2 Effective parameters: hydraulic vs. mechanical permeability

For a fracture represented by two parallel (planar) plates, permeability is a function of the fracture aperture by the cubic law,

$$k = \frac{b^2}{12} \qquad\qquad (10.1)$$

For a uniformly fracture rock mass, the cubic law takes form as $b^3/12\,s$, where s is fracture spacing.

The aperture, b, however, represents only the mechanical state of the fracture. In reality, observed flow rates are dependent on the hydraulic state of the fracture. In other words, fracture roughness matters. Therefore two different apertures are distinguished: the so-called "void" aperture, b_v, and the "hydraulic" aperture, b_h. The void aperture is the mean geometrically measured distance between the two fracture surfaces, including only those points that are not in contact (as the name implies, including only voids). The hydraulic aperture is a correction from this value ($b_h \leq b_v$), with one possibility known as the geometric correction /PIG 93/,

$$b_h^3 = \exp\langle\ln(k)\rangle = \exp(3\langle\ln(b_v)\rangle), \qquad (10.2)$$

where the angled brackets indicate that the mean is taken over the logarithm of the pointwise void aperture. Therefore, as an approximation to reality, the (effective) true permeability of a rough fracture is given by,

$$k = \frac{b_h^2}{12} \qquad (10.3)$$

In the following, this permeability is used to approximate behavior of the fracture and to generate an analytical solution for (qualitative) comparison to simulations within rough fractures, where permeability occurs point-wise (and mechanically) as $k_i = b_i^2/12$. Therefore, this is an *effective permeability*, and shall be used as an attempt to approximate (or provide reference to) true flow behavior in a rough fracture from a single bulk property.

10.1.3 Benchmarks organization and responsible authors

The benchmarks are organized in such a way that they can be classified by both dimension and process.

Tab. 10.1 Benchmarks organization

| Process | Classification by dimension | | | | |
	1d	1.5d	2d	2.5d	3d
H			ADuR1		
			ADuR2		
	ADuR6				
	ADuR7				
				ADuR8	
				ADuR10	
					ADuR11
			ADuR12		
HT		ADuR3			
HM			ADuR4		

The benchmarks are kindly provided by colleagues listed below.

Tab. 10.2 Benchmark authors

Benchmark name	Responsible authors
ADuR1	Joshua Taron
ADuR2	Joshua Taron
ADuR3	Norbert Boettcher
ADuR4	Joshua Taron
ADuR5	Yuanyuan Sun
ADuR6	Joshua Taron and Florin Radu
ADuR7	Joshua Taron
ADuR8	Joshua Taron
ADuR10	Joshua Taron
ADuR11	Joshua Taron
ADuR12	Norihiro Watanabe
ADuR13	Yuanyuan Sun and Dmitri Naumov

10.2 Alternate numerical methods for advective transport in heterogeneous fractures (Benchmark ADuR6)

10.2.1 Finite elements and finite difference method

10.2.1.1 Motivation

This benchmark compares different numerical methods, and checks the correct codes implementation. It also shows the importance of confining different geological conditions to conservative transport.

10.2.1.2 Differences in transport

For these comparisons, OGS is utilized as the FEM software and TOUGH2 as the FDM software. TOUGH2, as with other FDM based simulators, requires upwinding to generate stable mass transport. The basic advection/diffusion equation in 1d is referred to,

$$\frac{\partial C}{\partial t} + u \frac{\partial C}{\partial x} = D \frac{\partial^2 C}{\partial x^2}. \tag{10.4}$$

For a finite-difference based spatial discretization, the local truncated error, neglecting higher order terms, is,

$$\varepsilon = u \Delta x \left[(\omega - 0.5) + \frac{u \Delta t}{\Delta x} \cdot (\theta - 0.5) \right] \cdot \frac{\partial^2 C}{\partial x^2}, \tag{10.5}$$

so that the numerical dispersion is, in non-dimensional terms,

$$\frac{1}{Pe_{num}} = [(\omega - 0.5) + C \cdot (\theta - 0.5)], \tag{10.6}$$

for the Courant number, $C = \frac{u \Delta t}{\Delta x}$, and the numerical dispersion based peclet number, $Pe_{num} = \frac{u \Delta x}{D_{num}}$, with the coefficient of numerical dispersion, D_{num}. If molecular diffusion or longitudinal dispersion is also in use, then the total dispersion results in a total Peclet number of,

$$\frac{1}{Pe_T} = \frac{1}{Pe_{num}} + \frac{1}{Pe}. \tag{10.7}$$

For optimal selection of parameters, theoretical zero-numerical dispersion can be guaranteed, such as $\theta = 0.5$ (central difference scheme) and $\omega = 0.5$ (central upwinding scheme). Stability is not always guaranteed in TOUGH2, which exhibits far greater stability for an implicit time difference scheme. Therefore, with an implicit scheme, theoretical zero numerical dispersion occurs for a given value of ω with a given Courant number. This can be guaranteed in smooth fractures. In rough fractures, however, the Courant number is variable and, therefore, so is the amount of numerical dispersion. It is only possible to seek parameters that meet a given numerical dispersion on the average.

10.2.1.3   Smooth transport

Fig. 10.1 shows the difference in tracer breakthrough between the FEM and FDM simulators for a single smooth fracture. Note that an exact solution is obtained for the FEM solution, but the FDM solution exhibits differences due to the degree of spatial upwinding that is utilized.
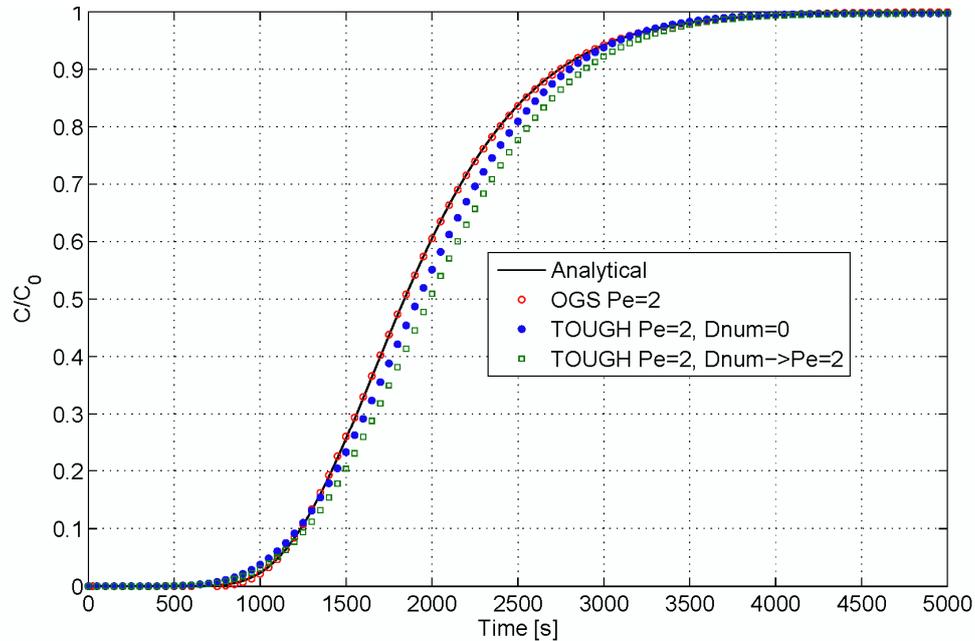
Fig. 10.1   Breakthrough curves for OGS and TOUGH2

> Analytical and numerical solutions for Pe = 2. The curve TOUGH Dnum=0 utilizes weighting parameters such that zero theoretical numerical dispersion exists (Pe = 2 is obtained with molecular diffusion). The curve TOUGH Dnum−>Pe = 2 utilizes zero molecular diffusion, and weighting parameters such that the numerical dispersion corresponds to Pe = 2.

10.2.1.4   Velocity fields in rough fractures

In remaining portions of the section the same real fracture is utilized as in Benchmark ADuR4 (see section 10.2.2). Here, first the differences in velocity produced by FEM and FDM approximation methods are examined. This is shown in Fig. 10.2. Note that while quite similar, differences arise due to assumptions made in both numerical methods. The FDM method utilizes harmonic averaging of permeability and mobility between adjacent cells, while the FEM method inherently operates on arithmetic averages.
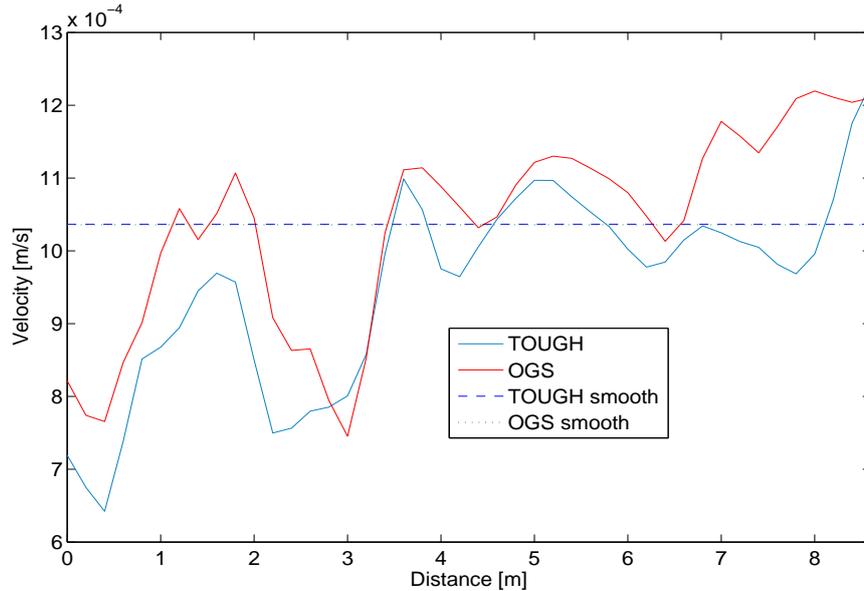
Fig. 10.2 Velocity differences between FEM and FDM for single rough fracture, stressed at 1 MPa

Smooth lines show also the velocity in a smooth fracture with the same effective permeability as the 1 MPa stressed rough fracture.

10.2.1.5   Tracer breakthrough in rough fractures

Now that differences in the smooth fracture due to mass transport assumptions, and differences in velocity of the rough fracture due to mobility assumptions are observed, differences in mass transport between the two methods for rough fractures at alternate states of stress (alternate degrees of roughness) will be illustrated. This is shown in Fig. 10.3. The 1 MPa stressed fracture utilizes an inlet boundary pressure of 1 MPa. The 5 MPa stressed fracture utilizes an inlet pressure of 4.30728 MPa, which, utilizing the effective permeability of the fracture, corresponds to generate the identical velocity of the 1 MPa stressed fracture. In other words, if the effective permeability were precisely accurate, both breakthrough curves would overlay identically. Of course, this is not the case, and the greater degree of roughness in the 5 MPa fracture generates different behavior altogether than the 1 MPa case. Differences are quite apparent between FEM and FDM for the velocity of breakthrough (see above) and also the amount and style of dispersion that is observed (see also above). Note that for the 1 MPa stressed fracture, the effective permeability correctly approximates the 50 % breakthrough, although a greater degree of dispersion is witnessed in the numerical solution.
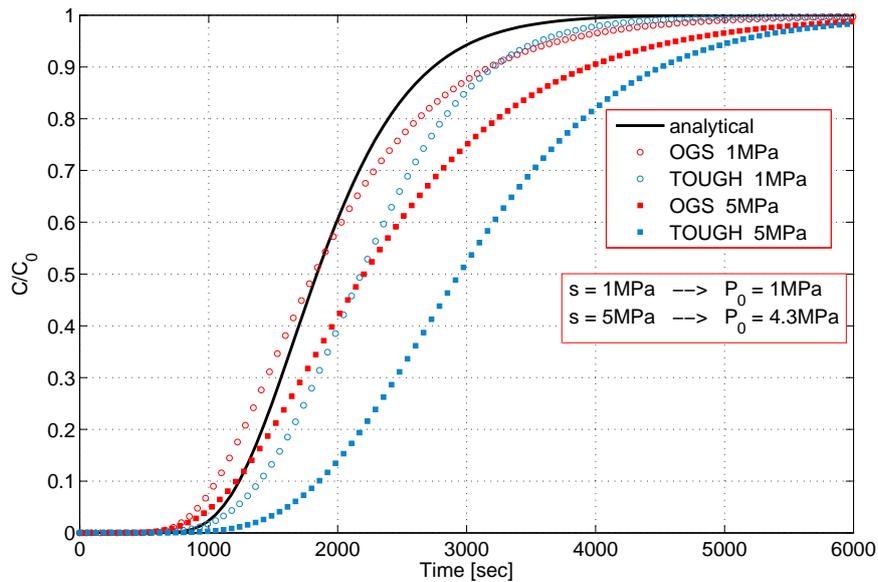
Fig. 10.3 Breakthrough curves for different states of stress for OGS and TOUGH2

10.2.2 Finite elements and random walk particle tracking (Benchmark ADuR4-1 and ADuR4-2)

In reality, all fractures undergo some form of mechanical compression. With an average lithostatic stress gradient of approximately 22 MPa/km and average hydrostatic gradient of near 10 MPa/km, the effective normal stress on a fracture in the Earth's upper crust increases at near 12 MPa/km. Even shallow aquifers ($< 1\,000$ m in depth for instance) may experience significant stress and, for reasonably compliant fractures, a degree of mechanical closure that can significantly impact hydraulic permeability. At greater depths the geothermal gradient becomes important, and thermally activated chemical-mechanical processes (such as pressure solution and sub-critical crack growth) become critical in determining the behavior of fluid flow in fractures. In the following, it is focused on only the hydro-mechanical behavior.

Although capable of simulating coupled hydro-mechanical processes, OpenGeoSys is utilized only for the hydraulic flow and mass transport problem, with mechanical calculations performed analytically prior to numerical simulation. This is done for ease of comparison to other simulators designed to handle the flow-transport problem alone. Roughness profiles of a real fracture are utilized to determine the permeability-stress state for a set of conditions, and this state utilized as input to the numerical simulator.

A single rough fracture of Arkansas novaculite (> 99.5 % quartz) /YAS 06/ was roughness profiled /MIT 03/ on each of its rough surfaces utilizing a 3d laser scanner. Aperture distribution within the fracture is determined from point-by-point subtraction of the two digitized surfaces. From the data it is possible to determine the area of contact between the surfaces after any vertical relative shift of the two surfaces (closure or opening of the fracture), and this will be taken advantage of below.

10.2.2.1   Mechanical compression

It is of significant interest and importance to examine the behavior of a fracture under alternate initial stress conditions. A fracture compressed at 10 MPa ($\approx$ 0.8 km depth) may exhibit largely different flow characteristics than one at 30 MPa ($\approx$ 2.5 km depth), for instance. As a fracture compresses, different areas of the surfaces will come into contact, altering the available area of flow and introducing the potential for flow channeling; an effect important for both mass transport and for chemical reaction.
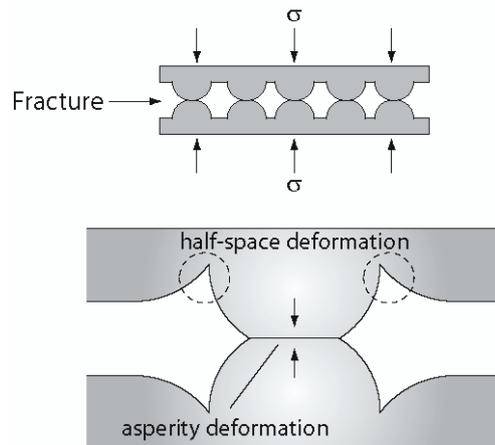
Fig. 10.4   Conceptualization of mechanical compression process, with asperity de-
formation and half-space compliance

The novaculite fracture is compressed (analytically) to various initial stress conditions, prior to the onset of simulation, and the resulting compressed permeability utilized as input to the finite element mesh. For aperture closure based on contact theory, deformation of each asperity is usually assumed to follow either Hertz's solution for the elastic contact of spherical bodies /JAE 07/, or a model for the deformation of cylindrical columns /PYR 00/. Asperity deformation alone has been shown to underestimate closure at low effective stress, and overestimate at higher stress, with

more accurate solutions obtained by considering also deformation of the (approximate) half-space surrounding each asperity. Here, compression occurs via elasticity theory, where contacting asperities of the fracture are treated as deforming cylinders and the area around these cylinders allowed to compress via a Boussinesq half-space approximation Fig. 10.4). The solution for the deformation length of a half-space from a circular contact of radius, r, is /COO 92/ (written in terms of elastic aperture change, Δb_{E1}),

$$\Delta b_{E1} \approx \frac{\sigma'}{ER_c}\left(\frac{4r}{1 - v^2}\right), \tag{10.8}$$

where v is Poisson ratio, E is Young's modulus, σ' is the effective normal stress, and R_c is contact area ratio (fraction of nominal area that is in contact). The deformation of a cylindrical column (asperity) is,

$$\Delta b_{E2} \approx \frac{\sigma'}{ER_c} b_v^i, \tag{10.9}$$

where b_v^i is the initial void aperture (mean aperture within the fracture of all points not in contact), used as an approximation of the potential deformation length. Combining these relationships, the total elastic aperture change is,

$$\Delta b_E = \frac{\sigma'}{ER_c}\left(\frac{4r}{1 - v^2} + b_v^i\right). \tag{10.10}$$

The unknown variable, R_c is obtained by numerical manipulation of the digital fracture profiles.

10.2.2.2 Conservative transport in a stressed fracture

Fig. 10.5 shows fracture permeability at three alternate stress states. Blue areas are open to flow, while increasing degrees of red indicate a greater degree of closure. Note a complete alteration in the fracture with respect to flow availability with increasing stress.
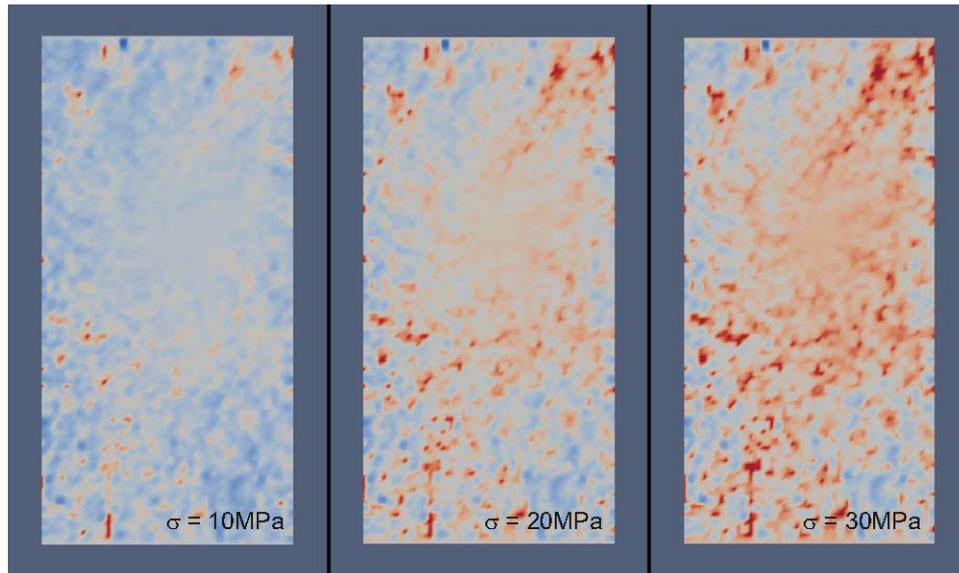
Fig. 10.5 Aperture of the (real) novaculite fracture compressed at different stress states

Blue indicates open space, while increasing red indicates fracture contact.

Fig. 10.6 shows the breakthrough curves for the three states of stress (10, 20, and 30 MPa). Analytical solutions are generated utilizing b_h. In all cases, a pressure drop of 1.0×10^5 Pa is utilized. Time step is governed dynamically with a Courant condition, where the Courant number, $C = v \cdot dt/dx$, is maintained beneath 0.8, for $dx =$ element size, and is controlled by the minimum occurring number within the FEM domain at each time step. Diffusion coefficient, D_f, is chosen based on the approximated b_h, to maintain a Peclet number of $Pe = v \cdot dx/D_f \approx 5$. The monitoring location is 25 % of the total flow length from the injection point, and centrally located perpendicular to flow. Note that OGS is quite stable at Peclet numbers in excess of (typical) 2. No trouble has been observed at Pe exceeding 10. Dashed lines in the figure represent the analytical solution to the 1d ADE equation, utilizing b_h and is only a reference. Note that the approximation made by utilizing a mean aperture is reasonable at lower values of roughness and diverges rapidly in rougher fractures. Note also that a single point in the domain is being monitored at, and thus the resulting value would differ not only due to general roughness, but due to the location and layout of this roughness.
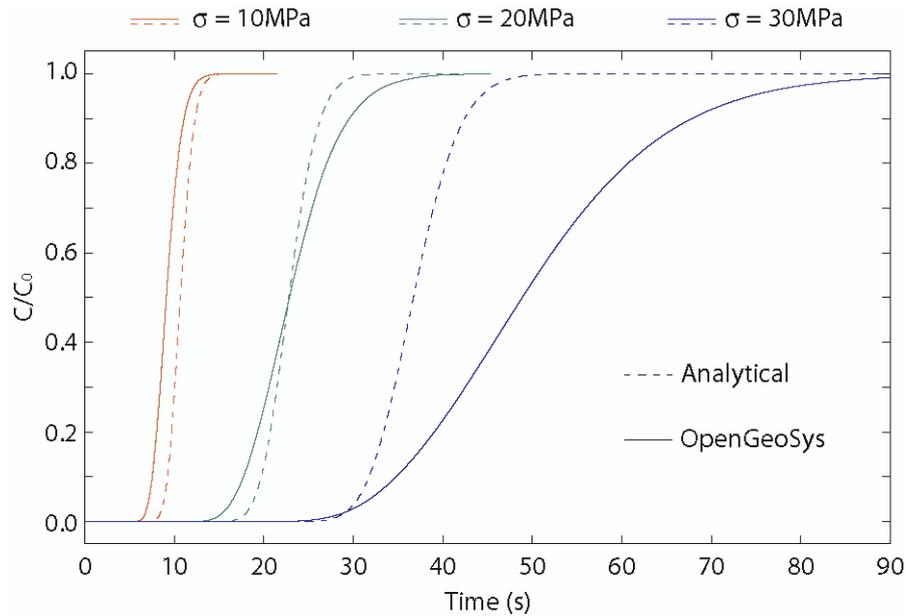
Fig. 10.6   Breakthrough curves at each increment of stress

Analytical solution utilizes the effective permeability (k).

10.2.2.3   Uncertainty in flow, Preferential flow: Random walk particle tracking (RWPT)

To examine changes to flow characteristics, two alternate forms of mass transport are utilized: the classical advection-dispersion equation (ADE) and random walk particle tracking (Fig. 10.7). The RWPT simulator within OGS is modified to allow a continuous source of particles (numerically approximate to a Neumann concentration boundary) for comparison with results from ADE simulations. For comparison, dispersion is not allowed within the RWPT simulation: particles are only advected with the flow. Therefore, particles represent the 50 % concentration breakthrough if particles are imagined as concentrations. The plot for each stress state is shown at a different absolute time, but each corresponds to the same dimensionless time, $t_D = v \cdot t/L$, where t is current time and L is total flow length, with v calculated from the mean b_h. Therefore, if b_h is a good approximation of behavior, the concentration advance in each plot should be approximately of the same extent. Note that this is true, but also that the increasing tendency for preferential flow with stress lends to increasingly less uniform concentration advance: with increasing stress, a given point in the geometry will record strongly different behavior than its neighbors. This is an observation that is apparent in Fig. 10.7, where the b_h at $\sigma = 30\ MPa$ is of lower quality.

199
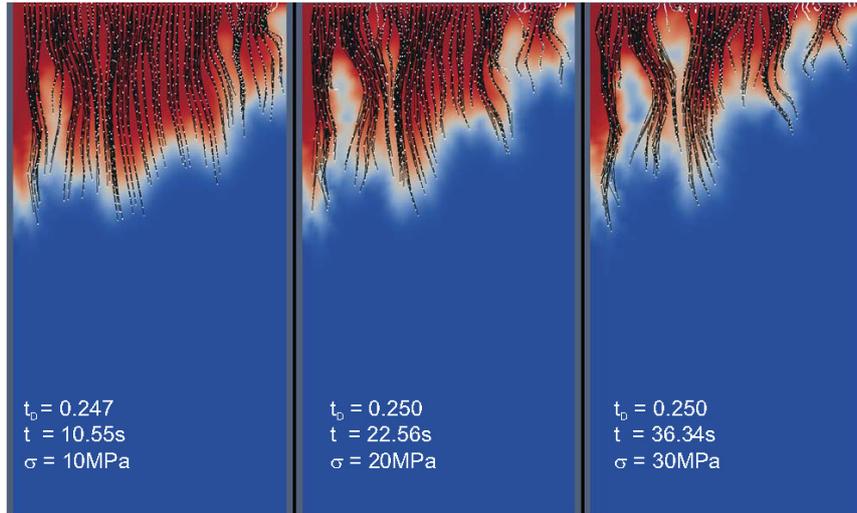
Fig. 10.7   RWPT vs. ADE at different stress states

Two separate simulations are conducted and overlay one another. Particle pathlines (black) and particles (white) are illustrated, and overlay contours (red = higher concentration) generated from the ADE simulation.

Aperture in the file apertures.txt was modified prior to simulation. It was multiplied uniformly by a factor of 10 000. This does not impact simulation results, where only the ratio between connecting element sizes is important, and benefits the simulation by increasing the size of values on the matrix diagonal. The values occurring in file apertures.txt have already undergone this transformation.

Tab. 10.3   Properties of the stressed fracture

k_v^*: mean permeability calculated from mechanical (void) aperture k: effective (hydraulic) permeability calculated from hydraulic aperture

σ	k_v^*	k	D_f
	$[m^2]$	$[m^2]$	$[m^2/s]$ for $Pe = 5$
10 MPa	2.10×10^{-12}	1.54×10^{-12}	2.83×10^{-7}
20 MPa	1.14×10^{-12}	7.19×10^{-13}	1.33×10^{-7}
30 MPa	7.97×10^{-13}	4.47×10^{-13}	8.22×10^{-8}

The 7 503 nodes comprise a structured FEM mesh of 7 320 elements. Each element is given a permeability based on its corresponding aperture value, calculated pointwise from $k_i = b_i^2/12$. Based on the mean calculated hydraulic aperture, b_h, the diffusion required to maintain a Peclet number $Pe = 5$ is calculated. For the first time steps, step

size is controlled with a Courant condition, maintaining the Courant number ≤ 0.8 at all points in the geometry to guarantee a stable velocity field (the element with the highest velocity/size ratio governs behavior at each time step).

10.3 Sorption in heterogeneous fractures (Benchmark ADuR7)

This benchmark shows the effect of roughness on mass transport with sorption process in the fracture.

10.3.1 Problem definition

The advection-dispersion equation is written as,

$$\frac{\partial C}{\partial t} = D\frac{\partial^2 C}{\partial x^2} - u\frac{\partial C}{\partial x} - \frac{\rho_b}{\phi}\frac{\partial q}{\partial C}\frac{\partial C}{\partial t} - \lambda C, \tag{10.11}$$

for the bulk solid density ρ_b, and a reactive source term expanded by the chain rule, $\frac{\partial q}{\partial C}\frac{\partial C}{\partial t}$, and a decay constant, λ. Rearranging produces,

$$R\frac{\partial C}{\partial t} = D\frac{\partial^2 C}{\partial x^2} - u\frac{\partial C}{\partial x} - \lambda C, \tag{10.12}$$

with the retardation coefficient, R. The retardation coefficient is, $R = 1 + \frac{\rho_b}{\phi}K_T$, for the sorption isotherm, K_T. If a linear isotherm is utilized, it may substitute, $K_T = K_d$. If a Freundlich isotherm is utilized, it may substitute $K_T = nK_F C^{n-1}$. To include decay in the equation, $\lambda = k_d C^{1-m}$ for the reaction order, m, and decay constant, k_d.

The analytical solution for a constant input is /VAN 81/:

$$C = \frac{1}{2}C_0\left[\exp\left(\frac{ux(1-\gamma)}{2D}\right)\mathrm{erfc}\left(\frac{Rx - u\gamma t}{2\sqrt{DRt}}\right)\right.$$
$$\left. + \exp\left(\frac{ux(1+\gamma)}{2D}\right)\mathrm{erfc}\left(\frac{Rx+u\gamma t}{2\sqrt{DRt}}\right)\right] \tag{10.13}$$

where

$$\gamma = \sqrt{1 + 4\lambda D/u^2} \tag{10.14}$$

10.3.2   Results

Fig. 10.8 shows breakthrough curves for the same fracture at 1 MPa and 5 MPa normal stress (same as in previous sections). Again, inflow pressure to the 5 MPa fracture is adjusted to match the same theoretical velocity as the 1 MPa stressed fracture, utilizing the effective permeability. In this figure, two smooth fractures are also generated, with permeabilities corresponding to the effective permeability for the 1 MPa and 5 MPa fracture. Linear sorption is utilized in all curves, with $R = 2$. The analytical solution is obtained by use of the 1d advection-dispersion equation, adjusted for the appropriate retardation in velocity and dispersion. In both smooth fractures, the numerical solution overlays the analytical identically, proving the numerical accuracy in the homogeneous case. With the introduction of roughness (mild for 1 MPa stress and greater for 5 MPa stress) the deviation is noticeable (as in previous sections), which may indicate some numerical inaccuracy due to incorrect heterogeneous velocity fields (see previous section) but also that the effective permeability approximation is not exact.
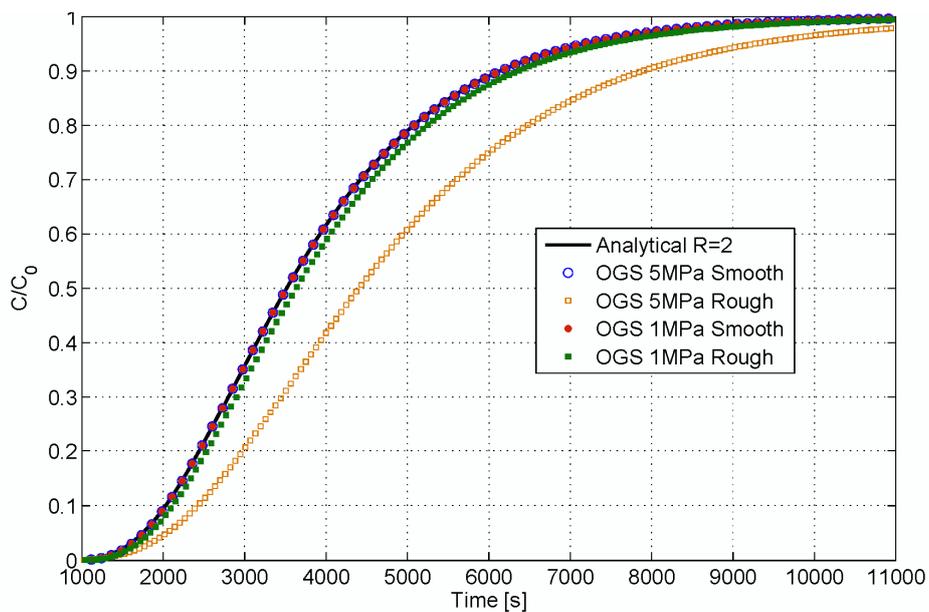
Fig. 10.8   Breakthrough curves for Pe = 2 and R = 2 for fracture at 1 MPa and 5 MPa

Fig. 10.9 breaks down the 1 MPa and 5 MPa solutions individually. Illustrated is the conservative solution ($R = 1$) and the sorption solution with both linear and Freundlich isotherms (both with $R = 2$).
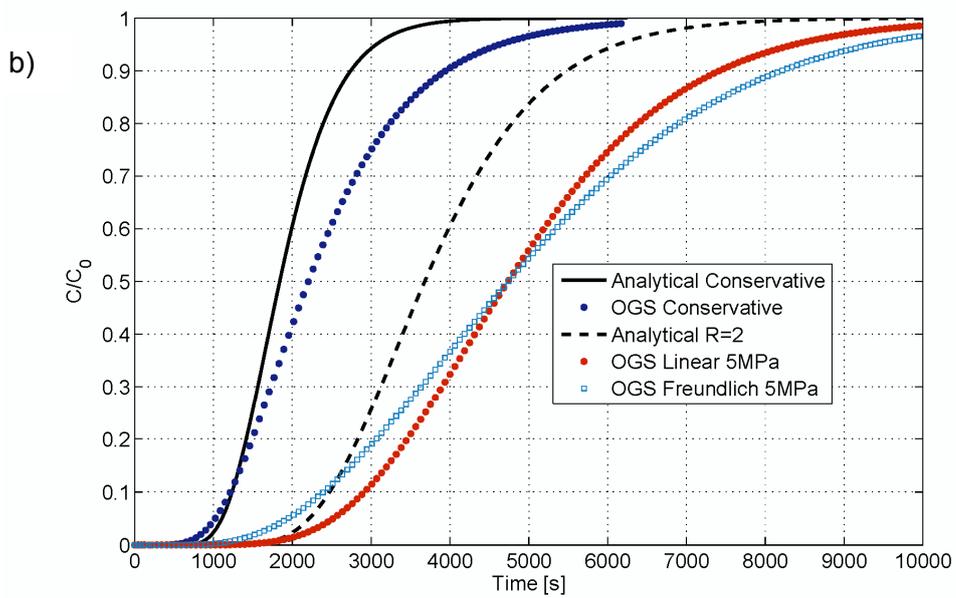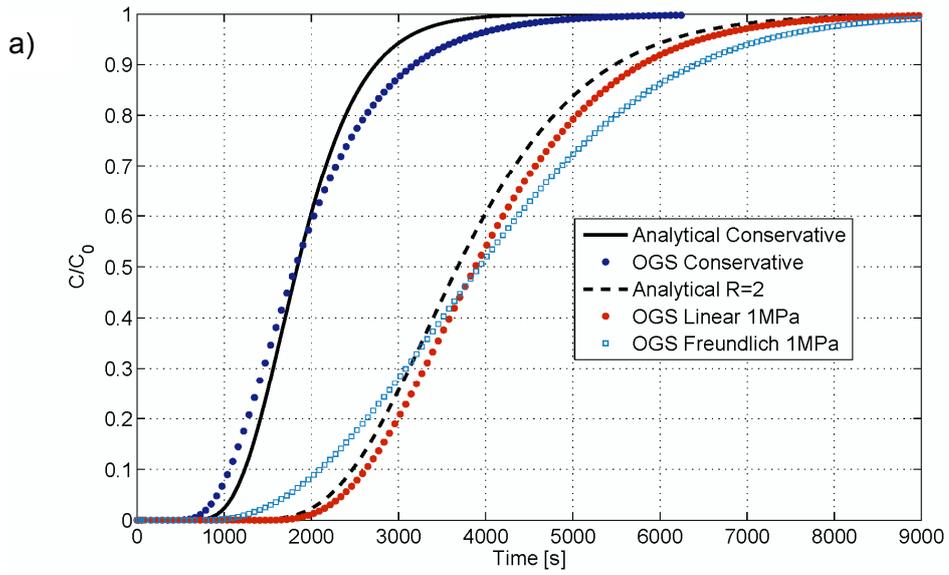
Fig. 10.9 Breakthrough curves for Pe = 2 and R = 2 for fracture at a) 1 MPa and b) 5 MPa

10.4   Matrix diffusion in fractured rock (Benchmarks ADuR1 and ADuR2)

10.4.1   Background

In many engineered geological environments (reservoirs for the sequestration of CO_2, nuclear waste repositories, engineered geothermal systems (EGS), etc.) fluid/mass/ thermal transport is controlled by high permeability fractures, situated within an intact rock matrix of significantly lower permeability. Typically, the intact matrix comprises a much larger volume fraction of the total system. Therefore, while flow characteristics are fracture dominated, the matrix volume serves as a storage site for pressure, chemical mass, and temperature, that may communicate with intersecting fractures and provide a buffer against rapid changes within the fractures.

In traditional reservoir modeling, such systems are referred to as *dual-porosity* or *dual-permeability*, and are modeled by introducing a separate grid discretization (matrix continuum) to a (FE) finite element (for instance) framework, that may communicate via exchange terms to the original (fracture continuum) element discretization. Dual-porosity refers to the case where global flow occurs across the entire fracture continuum, while the matrix continuum serves only as a storage site, with exchange allowed with fractures in corresponding elements. Dual-permeability is the more complex case applicable where the matrix may exhibit a slightly higher (non-negligible) permeability. Here, global flow is allowed in both continuums, in addition to exchange between them.

Because of the necessity of an additional grid discretization, the greater modeling accuracy that is introduced comes at the expense of computational efficiency. This drawback has lead researchers to introduce alternate methods to incorporate dual-porosity like behavior. The following benchmark examines one such method.

10.4.1.1 Problem definition
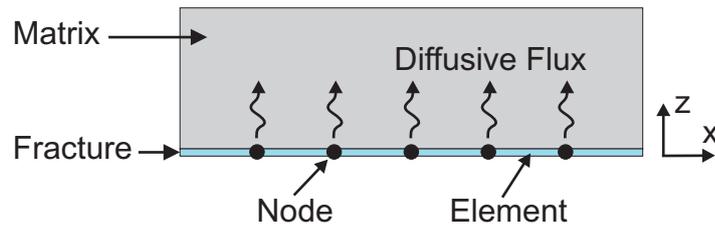
Fig. 10.10 Fracture-matrix diffusive exchange

This benchmark is introduced to examine mass transport interaction between an advection dominated planar fracture and a low permeability rock matrix (Fig. 10.10). In terms of mass transport, the system is similar to a construct of dual-porosity. Advective-dispersive transport of a non-reactive solute is simulated within a planer fracture using OpenGeoSys (OGS). Diffusion into the surrounding matrix occurs via an analytical solution for diffusion into an infinite medium. The approach mimics the composite analytical/numerical solution provided by /MCD 09/, with exchange between the fractures and matrix accommodated by source terms within the advection/ dispersion equation (ADE). The geometry and material parameters are chosen to fit data extracted from experiments conducted during the Colloid Radionuclide Retardation Experiment at Nagra's Grimsel test site /KOS 05/.

Simulations are conducted utilizing the ADE only (therefore no matrix contribution to fracture mass transport), ADE with matrix diffusion (ADE+MD), and ADE+MD with sorption of contaminant to the matrix structure (ADE+MD+sorption).

10.4.1.2 Numerical solution

OGS solves the general advection/dispersion equation (ADE) for mass transport in an effective fracture continuum,

$$\frac{\partial C}{\partial t} = -\nabla^T(D\nabla C) - v \cdot \nabla C + q_c, \tag{10.15}$$

where q_c is a source term establishing the connection between fracture and matrix domains and where the fluid velocity, v, is obtained from Darcy's law. Matrix diffusion is governed by the analytical solution to the diffusion equation,

$$\frac{\partial C}{\partial t} = D^* \frac{\partial^2 C}{\partial z^2}, \tag{10.16}$$

given here, for the effective diffusion coefficient D^*, as opposing pulses of concentration, C_j,

$$\frac{\partial C}{\partial z}(z = 0, t_n) = \frac{-C_n}{\sqrt{\pi D^*(t_n - t_{n-1})}} + \sum_{j=1}^{n-1} \left\{ \frac{-C_j}{\sqrt{\pi D^*(t_n - t_{j-1})}} + \frac{C_j}{\sqrt{\pi D^*(t_n - t_j)}} \right\}, \tag{10.17}$$

where the addition of opposing terms represents diffusion occurring over the current time step (first term, time step n), corrected for accumulations that have occurred over each of all previous time steps (remaining terms in summation, time step j). See /MCD 09/ for an explanation of this derivation. This result informs the source term as,

$$q_c = -\frac{D^*}{b_i} \frac{\partial C}{\partial z}, \tag{10.18}$$

where b$_i$ is fracture aperture at node i. Sorption into the solid matrix may also be considered by including retardation effects into the effective diffusion coefficient, $D^* = D/(R\tau)$, where D is the coefficient of molecular diffusion, τ is diffusive tortuosity, and R is a retardation factor given by,

$$R = 1 + \frac{K_d \rho}{\phi}, \tag{10.19}$$

for the sorption coefficient, K_d [m^3/kg], bulk rock density, ρ, and porosity, ϕ. Darcy's law is applied to the global FE system by utilizing the cubic law to obtain permeability at each computational element, $k_i = b_i^2/12$ and applying the appropriate elemental volume (including aperture contribution) to each element.

10.4.2 Solute transport through a smooth fracture with matrix diffusion (Benchmark ADuR1)

This benchmark is introduced to verify the matrix diffusion function. It simulates the advective dispersive transport of a solute in a one-dimensional fracture with constant aperture, with and without the effect of matrix-diffusion.
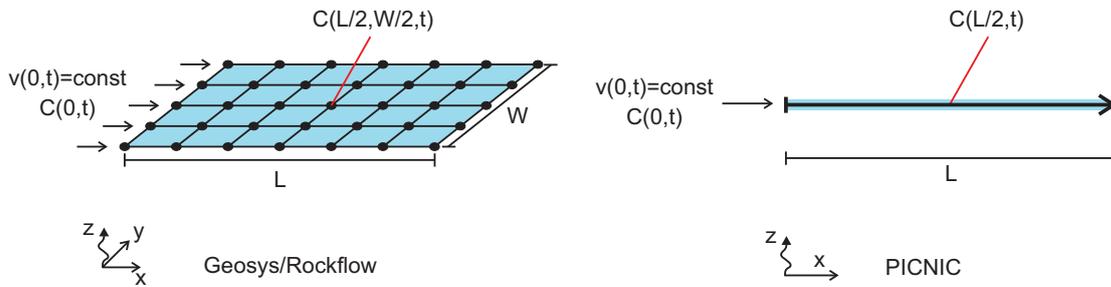
Fig. 10.11 Conceptual realizations in OpenGeoSys and PICNIC

For smooth fractures, benchmarking of the OGS numerical/analytical system was conducted against the analytical matrix diffusion code PICNIC (V 2.2, /BAR 01/). The geometry and material parameters in PICNIC and OGS are summarized in Tab. 10.4 and the conceptual model is shown in Fig. 10.11. PICNIC solves the one-dimensional problem, whereas in OGS a two-dimensional discretization was chosen. A rectangular domain of 5.2 m × 0.5 m was discretized with 1 155 nodes and 2 080 triangular elements. One of the shorter domain edges was chosen as inflow boundary and fluid was injected at the boundary-nodes in such a way that the resulting fluid velocity matches exactly the value from Tab. 10.4.

Tab. 10.4 Geometry and material properties for ADuR1 smooth fracture benchmark

Symbol	Unit	Description	Value
L	m	Distance source boundary to observation point	2.5
k	m^2	Uniform fracture permeability	2.52×10^{-8}
v	m/s	Fluid velocity	7.05×10^{-4}
α_L	m	Coefficient of longitudinal dispersion (OGS only)	0.078
Pe	−	Peclet number (PICNIC only)	25
ε_p	−	Matrix porosity	0.3
D_p	m^2/s	Diffusion coefficient in rock matrix	7.4×10^{-11}

As defining exactly the same transport boundary conditions in OGS and PICNIC is not possible, a special procedure was used to replicate as closely as possible the boundary conditions of PICNIC: 1) The PICNIC solution was obtained for a constant flux, 50s pulse of solute at the inflow boundary. Concentration vs. time was recorded at the inflow-leg, and 2) Concentrations vs. time extracted from PICNIC were applied (fixed) to the inflow boundary of the OGS system.

These procedures work, as long as advective fluxes are much higher than the dispersive-diffusive fluxes over the boundary. The breakthrough curve is recorded at a distance of 2.5 m down-gradient from the inflow boundary. In OGS the domain is set to 5 m, double the distance between inflow boundary and observation point; far enough away to avoid boundary influence of contaminant breakthrough.

Two cases are examined: 1) Advection/dispersion (ADE) only and 2) ADE plus matrix diffusion (MD). Results are agreeable between PICNIC and the OGS solution (Fig. 10.12). For this simulation very small time steps are required during the concentration injection phase. This is not due to numerical stability or accuracy but due to the concentration boundary which is a function of time. Larger time steps apply this (very special boundary case) inaccurately.
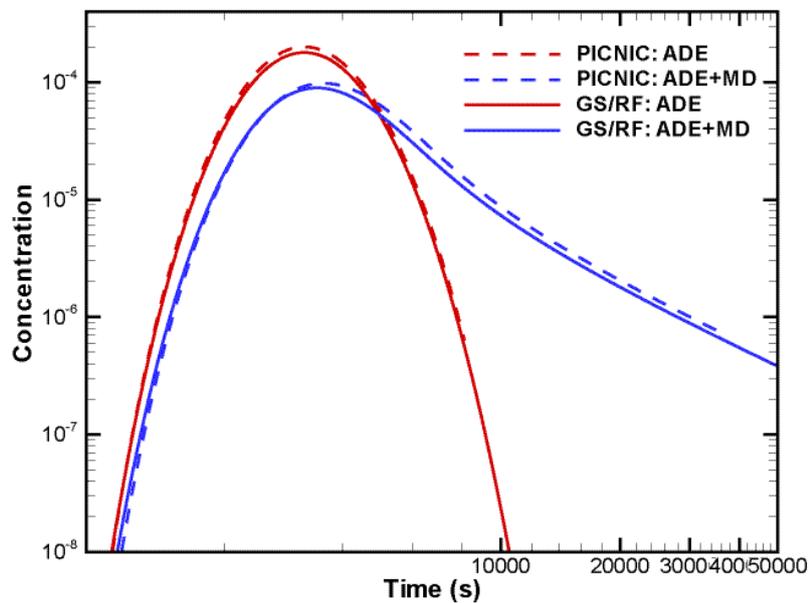
Fig. 10.12 Breakthrough of the ADE and the ADE+MD solutions calculated with PICNIC and OGS

10.4.3 Solute transport through a rough fracture with matrix diffusion (Benchmark ADuR2)

Real rock fractures are of course not parallel plates, but are comprised of two rough surfaces held apart at contacting asperities. Fluid pressure and velocity and solute distribution will vary locally, rather than representing a bulk value, as governed by location dependent fracture aperture and permeability. This benchmark examines the effect of fracture roughness on solute distribution.

Darcy's law is accommodated in the global FE system by applying the cubic law to obtain permeability at each computational element, $k_i = b_i^2/12$, and updating the elemental volume (including aperture contribution) of each element. In the previous benchmark (ADuR1) this was uniform across the geometry. Now variable aperture is introduced such that permeability and element volume will vary within each finite element.

Fracture apertures (in file apertures.txt) are generated utilizing a geostatistical fracture surface generator provided by Geraldine Pichot at U. du Havre (Le Havre, France). Permeabilities (in file permeabilities.txt) are generated directly from the aperture file through use of the cubic law. Two fractures are compared, one that is nearly smooth (FR1) and one with significant roughness (FR2). Characteristics are provided in Tab. 10.5.

Tab. 10.5 Fracture properties

All values represent the mean across the geometry. k_v^* is permeability calculated from the mean mechanical aperture (b_v), while k is effective mean permeability (from b_h).

Fracture	σ/b_v	b_v	k_v^*	b_h	k
	$-$	$[\mu m]$	$[m^2]$	$[\mu m]$	$[m^2]$
FR1	0.0236	0.418	1.46×10^{-14}	0.417	1.45×10^{-14}
FR2	0.458	0.459	2.12×10^{-14}	0.416	1.44×10^{-14}

Processes of diffusion are, of course, quite slow, and so matrix diffusion is only important as timescales increase relative to advective velocity. To illustrate the MD process, therefore, the permeability of these fractures is low in conjunction with a low pressure source and a high rate of diffusion into the porous matrix. The importance of

matrix diffusion relative to fluid velocity may be roughly defined with a parameter similar to the Peclet number,

$$Pe_m = \frac{v \cdot dx}{D_m} \approx 0.14, \quad\quad\quad (10.20)$$

for the diffusion coefficient within the rock matrix D_m, and with all parameters obtainable from Tab. 10.5 and Tab. 10.6. Therefore, matrix diffusion is significant relative to velocity, and a significant contribution from matrix diffusion on concentration within the fracture is expected. When fracture velocity is much higher relative to the rate of matrix diffusion the impact on fracture concentration is lower, but matrix diffusion will remain important if chemical processes are being examined in the rock matrix.

Fluid velocity will vary spatially to a larger degree in the rough fracture. Note, however, that while each fracture exhibits a different mean permeability (k_v^* in Tab. 10.5), both fractures exhibit nearly the same effective permeability (k in Tab. 10.5). For the same overall pressure drop, then, both fractures would be expected to show similar mean mass transport behavior (this can be seen approximately true in Fig. 10.14). Roughness itself, however, will alter behavior from the mean case; both with regard to fracture transport and the contribution from matrix diffusion. Differences in concentration breakthrough between the smooth and rough fracture and with and without matrix diffusion are shown in Fig. 10.13. Note firstly that mean permeability (mechanical) is a poor estimate of behavior (cubic law is not valid) in rough fractures. The effective permeability does a reasonable job of capturing behavior; but this too is limited. Simply changing the monitoring point (Fig. 10.13a, same downstream linear distance, but shifting very slightly transverse to flow) demonstrates somewhat different breakthrough characteristics.

Tab. 10.6 Geometry and material properties for ADuR2 rough fracture benchmark

Symbol	Description	Value
L	Linear distance from source to observation	$0.6\ m$
P	Applied boundary pressure	$5.0 \times 10^4\ Pa$
α_L	Coefficient of longitudinal dispersion	$0.01\ m^2$
Pe	Corresponding approximate Peclet number	2
	(utilizing k obtained from b_h)	
ϕ	Matrix porosity	0.3
D_m	Diffusion coefficient in rock matrix	$1.0 \times 10^{-7}\ m^2/s$
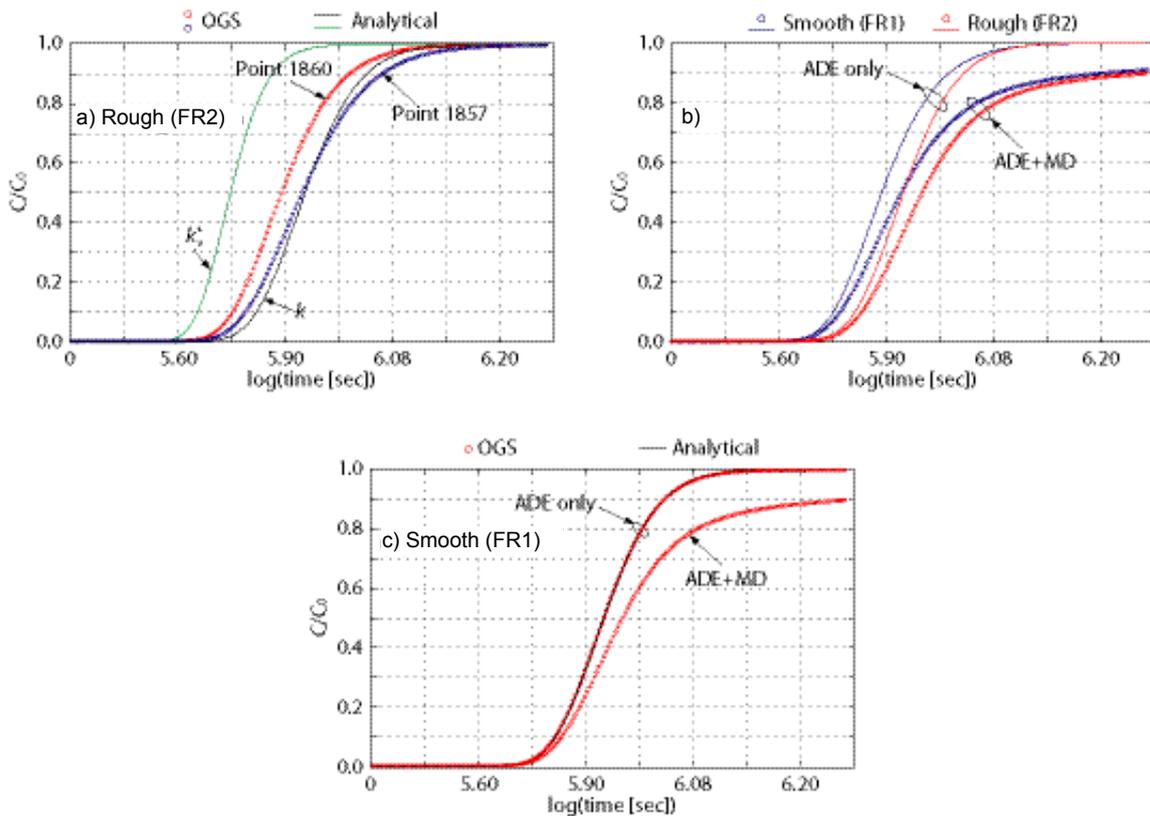
Fig. 10.13 Breakthrough curves 0.6m down-gradient

All curves at point 1860, point 1857 for comparison is also 0.6 m down-gradient, but shifted transverse to flow by three grid cells, or 0.006 m.

A more visual analysis of these results is provided in Fig. 10.14. Mean permeability of the rough fracture is 1/2 that of the smooth fracture (Tab. 10.6), but effective

permeability is nearly the same for both. Therefore, the mean concentration breakthrough is similar for both fractures. Note also that for these statistically generated fractures, the roughness is quite uniform (as opposed to real fractures such as those examined in ADuR4, see section 10.2.2).

The 3 150 nodes comprise a structured FEM mesh of 5 916 elements. Each element is given a permeability (file permeability.txt) based on its corresponding aperture value (file apertures.txt): calculated pointwise from $k_i = b_i^2/12$.
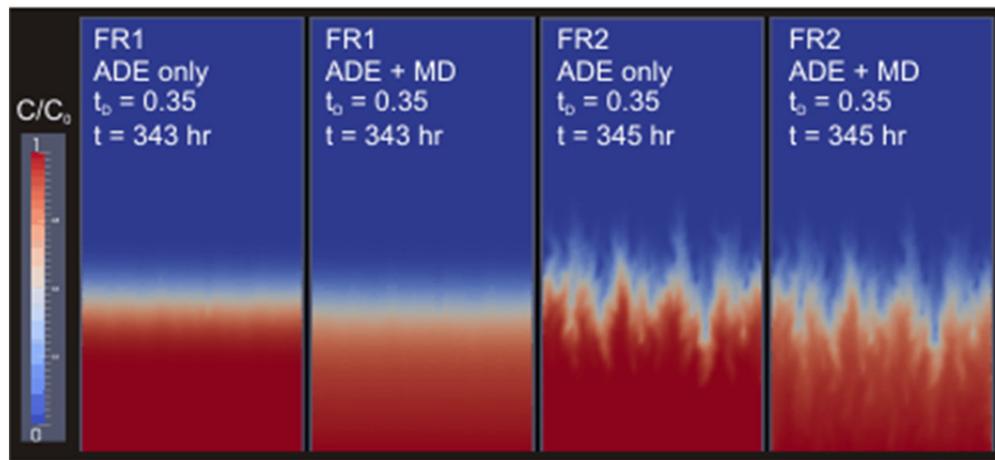
Fig. 10.14 Visual analysis of tracer breakthrough

Flow enters from bottom at constant pressure ($0.1\ MPa$); constant concentration at the bottom boundary

10.5   Numerical matrix diffusion: Transport in a coupled fracture-matrix system (Benchmark ADuR3)

10.5.1   Problem definition

The OGS benchmark for transport by advection and diffusion in a fracture-matrix system was provided by Norbert Böttcher (TU Dresden) and can be easily adopted to mass transport. This test problem is extended by heat diffusion through a rock matrix orthogonal to the fracture (Fig. 10.15) (cf. /KOL 95a/, /KOL 95b/, /TEN 09/).
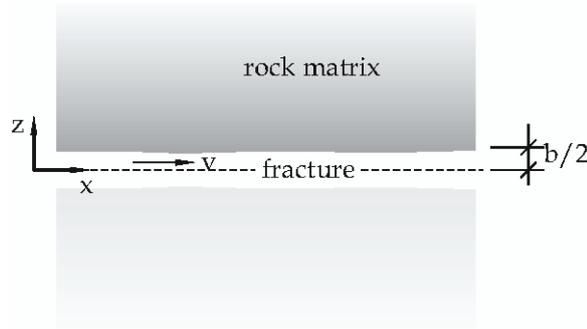
Fig. 10.15 Heat transport in a fracture-matrix system

10.5.2 Analytical solution

For this problem an analytical solution is given by Lauwerier (1955) /LAU 55/ with following restrictions: 1) In the fracture, heat is transported just by advection, and 2) in the rock matrix, heat transport takes place by diffusion (only along the z-axis). The Lauwerier equation is given by

$$T_D = \begin{pmatrix} 0, & t_D < x_D \\ erfc\left\{\dfrac{\beta}{\sqrt{\alpha(t_D - x_d)}}\left[x_D + \dfrac{1}{2\beta}\left(z_D - \dfrac{1}{2}\right)\right]\right\}, & t_D > x_D \end{pmatrix}, z_D \geq \dfrac{1}{2} \qquad (10.21)$$

with the following dimensionless parameters:

$$t_D = \frac{v_x}{b}t, \quad x_D = \frac{x}{b}, \quad z_D = \frac{z}{b}, \quad \alpha = \frac{\lambda^r}{c^r \rho^r}\frac{1}{bv_x}, \quad \beta = \frac{\lambda^r}{c^w \rho^w}\frac{1}{bv_x} \qquad (10.22)$$

where b is the fracture width, λ is the thermal conductivity, c is the heat capacity, ρ is the density and r and w are rock or water material parameters respectively.

10.5.3 Numerical solution

The Lauwerier-problem is formed as a coupling of advective 1d heat transport in x-direction and diffusive 1d heat transport in z-direction. This means, that nodes in the rock matrix are not influenced by their left or right neighbors. The matrix elements are connected to the fracture elements orthogonally. Fig. 10.16 shows a schematic description of the model setup. Because of the symmetry, the numerical model calculates just the domain above the x-axis.
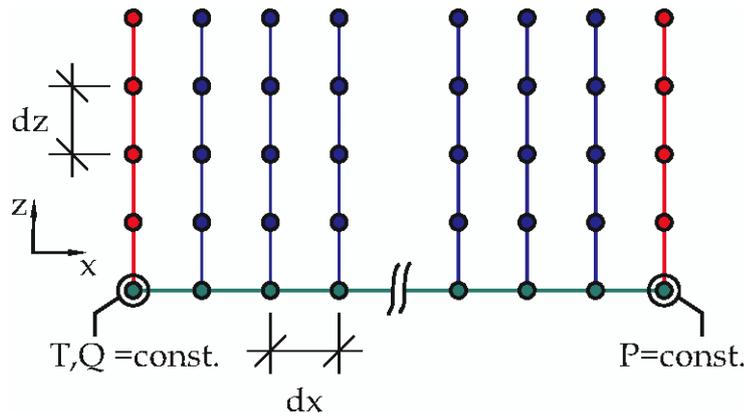
Fig. 10.16 Alignment of the grid for the numerical model
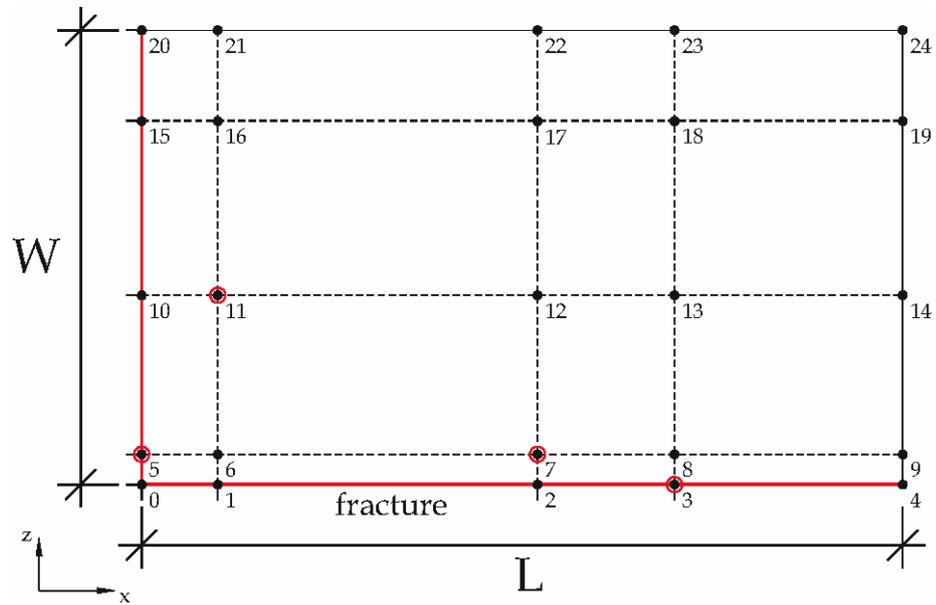
Fig. 10.17 Positions of observation points for temperature breakthrough curves

Fig. 10.17 shows the positions of observation points which were chosen to evaluate the numerical model by the comparison with analytical solutions. The chosen parameters and material properties for this solution are shown in Tab. 10.7.

Tab. 10.7 Model parameters for the Lauwerier-problem

Parameter	Value
Spatial discretization	
fracture length L	$[50]m$
matrix width W	$[63.25]m$
step size X Δx	$[2]m$
step size Z Δz	$[0.1265]m$
half of fracture width $b/2$	$[1.0 \cdot 10^{-3}]m$
groundwater velocity v_x	$[1.0 \cdot 10^{-4}]m/s$
Temporal discretization	
timesteps Δt	$[2.0 \cdot 10^5]s$
No. of timesteps	2 500
total time	$[5.0 \cdot 10^8]s$
Material properties – solid	
thermal conductivity λ	$[1]W \cdot m^{-1} \cdot K^{-1}$
heat capacity c	$[1\,000]J \cdot kg^{-1} \cdot K^{-1}$
density ρ	$[2\,500]kg \cdot m^{-3}$
Material properties – fluid	
heat capacity c	$[4\,000]J \cdot kg^{-1} \cdot K^{-1}$
density ρ	$[1\,000]kg \cdot m^{-3}$

10.5.4   Results

The quality of the numerical results can be shown by temperature distribution curves for several times in the rock matrix. Fig. 10.18 shows the temperature profiles for $x = [0]\,m$ at three moments t'. The numerical solution has a very good agreement to the analytical results. Temperature profiles along the fracture at $z = [0]\,m$ are plotted in Fig. 10.19. For long simulation times ($t' = 1\,000; t' = 600$) both solutions fits very well

together. For short simulation times, the numerical solution differs slightly from the analytical results. This discrepancy for short simulation times can be examined in Fig. 10.20, where temperature breakthrough cures for certain points (see Fig. 10.17) is plotted.
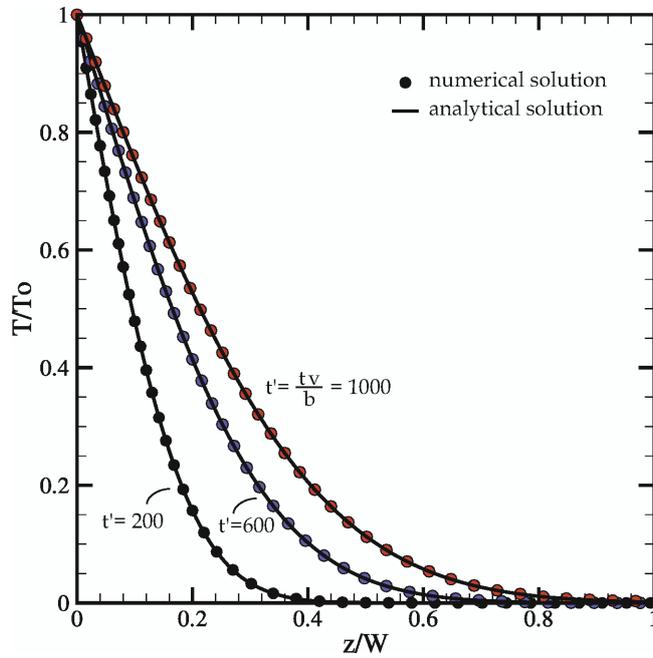
Fig. 10.18 Temperature distribution orthogonal to the fracture at x=0 at three different times
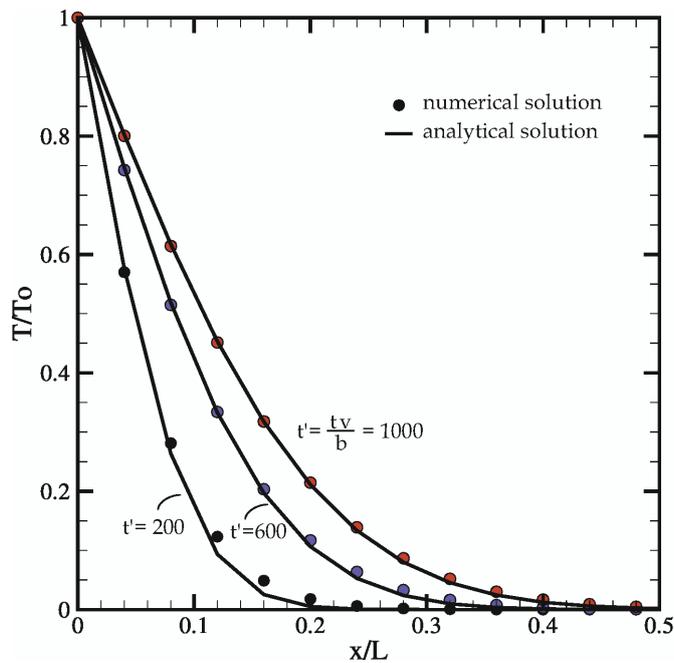
Fig. 10.19 Temperature distribution along the fracture at three different times
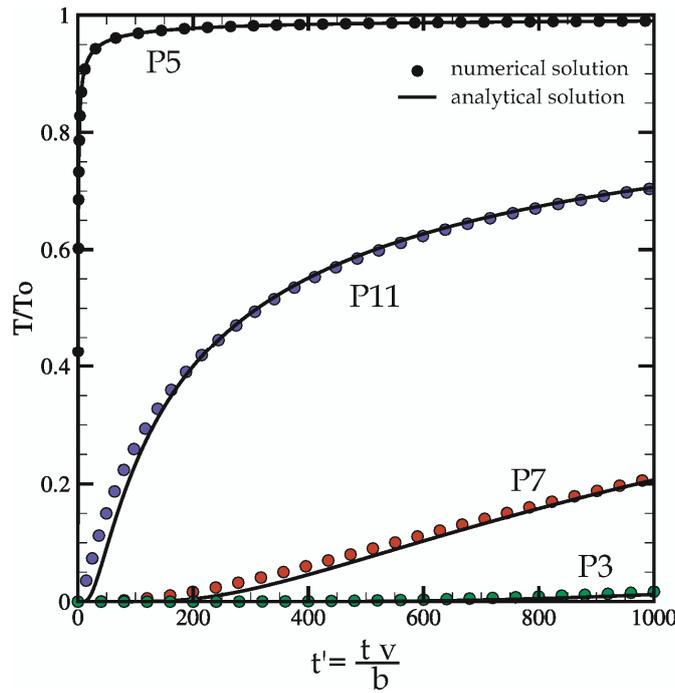
Fig. 10.20 Temperature breakthrough curves at certain points in the rock matrix

10.6 Flow in porous media with fractures (Benchmark ADuR12)

10.6.1 Problem definition

This example illustrates the disturbance of the uniform flow in porous media caused by the presence of a fracture. Consider a 2d infinite horizontal plane of porous media with an embedded fracture. Uniform flow with specific discharge q_0 occurs from the left side to the right of the domain. The fracture extends to infinity in the directions normal to the plane. The middle point of the fracture is placed at the center of the plane. The shape of the fracture is shown in Fig. 10.21. The fracture has a length of L and is inclined with angle β. The fracture aperture b may vary with positions. In this example, it is assumed that the shape corresponds to that obtained from the normal displacements of the sides of a pressurized crack in an elastic medium. This gives

$$b = b_{max}\sqrt{1 - {x'}^2}$$

(10.23)

where x' is the normalized local coordinate systems. b_{max} is the aperture at the center $x' = 0$. Assuming the volume of the fracture is sufficiently small as compared to that of porous media, the flow in the porous media can be modeled ignoring the width of the

fracture. The flow in the fracture is assumed to be laminar along the fracture surface. Hydraulic conductivity of the fracture is constant and independent of the aperture variation. The pressure variation across the fracture is neglected.
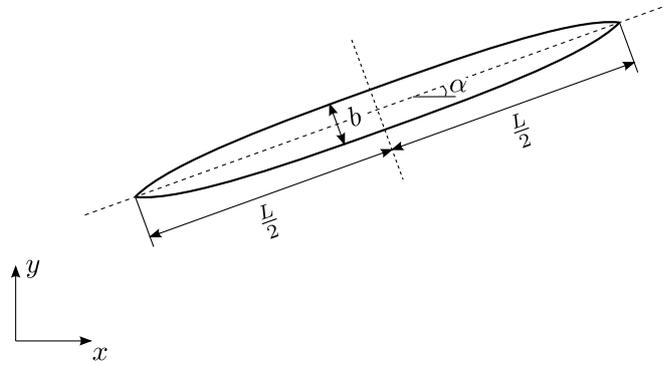
Fig. 10.21 Fracture geometry

Tab. 10.8 Model parameters

Symbol	Parameter	Value	Unit
α	fracture angle	45	°
$b_{\mathbf{max}}$	maximum fracture aperture	0.05	m
L	fracture length	2.0	m
K_f	fracture hydraulic conductivity	1.0×10^{-3}	m/s
K_m	porous medium hydraulic conductivity	1.0×10^{-5}	m/s
q_0	specific discharge	1.0×10^{-4}	m/s

10.6.2 Analytical solution

Strack /STR 82/ has derived an exact solution for this problem as the potential flow. The obtained complex potential Ω is given as

$$\Omega = -A\sqrt{(Z-1)(Z+1)} + AZ - \frac{1}{2}q_0 Le^{i\alpha}Z + C \tag{10.24}$$

for the dimensionless variable Z

$$Z = X + iY = \frac{z - \frac{1}{2}(z_1 + z_2)}{\frac{1}{2}(z_2 - z_1)} \qquad (10.25)$$

with the endpoints of the fracture z_1 and z_2. A is defined as

$$A = \frac{\frac{1}{2}K_f b_{\max}}{K_m L + K_f b_{\max}} q_0 L \cos\alpha \qquad (10.26)$$

and C is the integration constant. In this example, the constant is simply considered as zero.

10.6.3 Numerical solution

Numerical solution can be obtained by solving steady state liquid flow problem in a hybrid system of a discrete fracture model and continuum model (porous media). The fracture is represented as a 1d hydraulic conduit. The domain is set up in a finite space as a square with length of 10 m as depicted in Fig. 10.22. To compare numerical results with the analytical solution, pressure calculated by the analytical solution is utilized as prescribed pressure at the lateral boundaries, i. e. $p_{\text{in}} = 496\,465$ Pa and $p_{\text{out}} = -496\,465$ Pa. It is assumed that the fracture aperture does not vary with positions and has constant value even at the endpoints, $b = b_{\max}$.
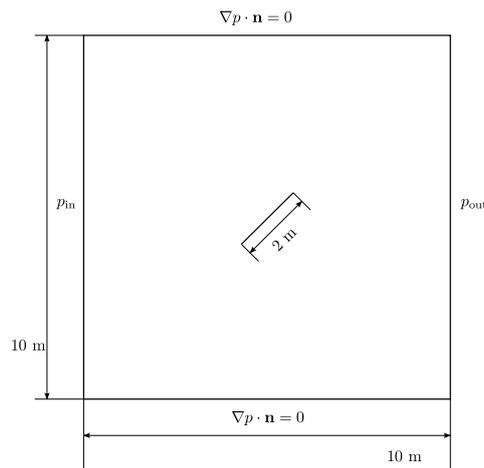
Fig. 10.22 Computational area

10.6.4 Results

Pressure distribution obtained by the analytical solution is shown in Fig. 10.23. Lateral uniform flow is disturbed in the vicinity of the inclined fracture where the flow is faster than in surrounding porous media. Fig. 10.24 presents the pressure profile along a diagonal line from the bottom-left to the top-right. Although the numerical solution adopts the idealized fracture geometry, results show good agreements between the numerical and the analytical solution.
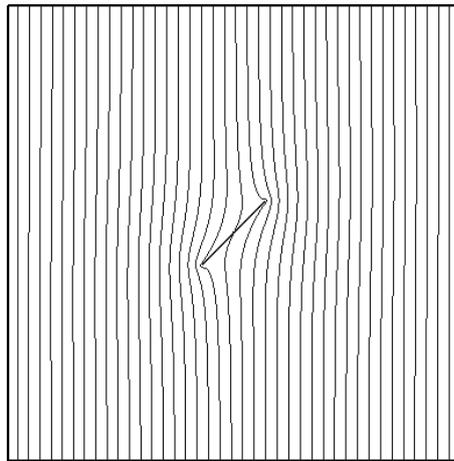
Fig. 10.23 Pressure distribution obtained by the analytical solution
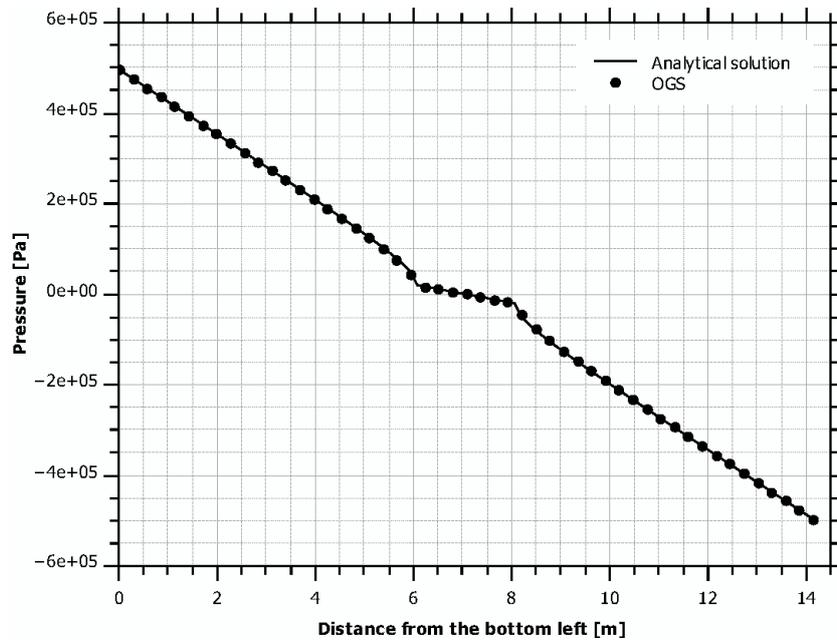
Fig. 10.24 Pressure profile along a diagonal line from the bottom-left to the top-right

10.7 Fracture networks: (Grimsel shear zone), flow and conservative transport (Benchmark ADuR8)

10.7.1 Problem definition

In this section conservative transport in a discrete fracture network is examined. A real fracture network is utilized. This network is constructed from data at the Grimsel shear zone /KAL 07/. A boundary pressure of 2.0×10^6 Pa is applied (Fig. 10.25). Aperture calculations show that $k = 1.11 \times 10^{-12}$, where k is calculated from b_h, as in the previous section.
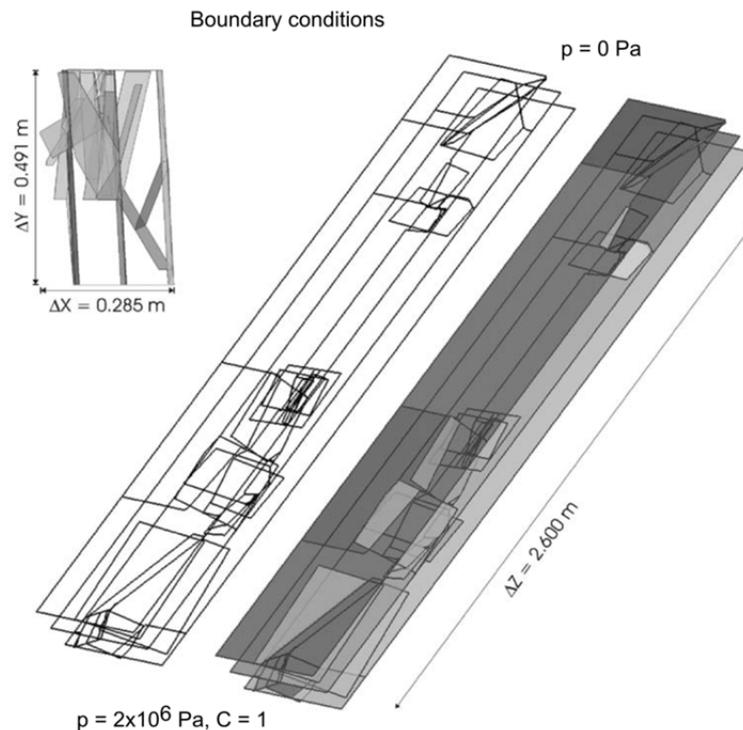
Fig. 10.25 Definition of the Grimsel fracture network benchmark

10.7.2 Numerical solution

The geometry consists of 12 802 nodes placed on an unstructured triangular mesh. Curvature of the real fracture network was modified in /KAL 07/ to make it more amenable to numerical simulation. In this benchmark, the fracture was further modified in that aperture across the entire network was decreased uniformly by a factor of 100.

This was done because the initial value led to very high permeabilities where a Darcy solution would become questionable.

10.7.3   Results

Fig. 10.26 shows two simulations, one conducted with a uniform aperture (b_h), and one with the true rough profiles. Note that b_h is a reasonable approximation of mean concentration breakthrough, but obviously fails at locations undergoing an increase or lack of preferential flow. Two times are illustrated in the figure.

The 12 802 nodes comprise a FEM mesh of 24 750 elements. Each element is given a permeability based on its corresponding aperture value, calculated pointwise from $k_i = b_i^2/12$. Based on the mean calculated hydraulic aperture, b_h the diffusion required to maintain a Peclet number $Pe = 2$ is calculated. A small additional amount of dispersion is applied via a longitudinal and transverse dispersion coefficient for stability. For the first timesteps stepsize is controlled by a Courant condition, maintaining the Courant number ≤ 0.8 at all points in the geometry (the element with the highest velocity/size ratio governs behavior at each time step) to guarantee a stable velocity field. Aperture was multiplied uniformly by a factor of 100 prior to simulation to increase the size of values on the matrix diagonal.
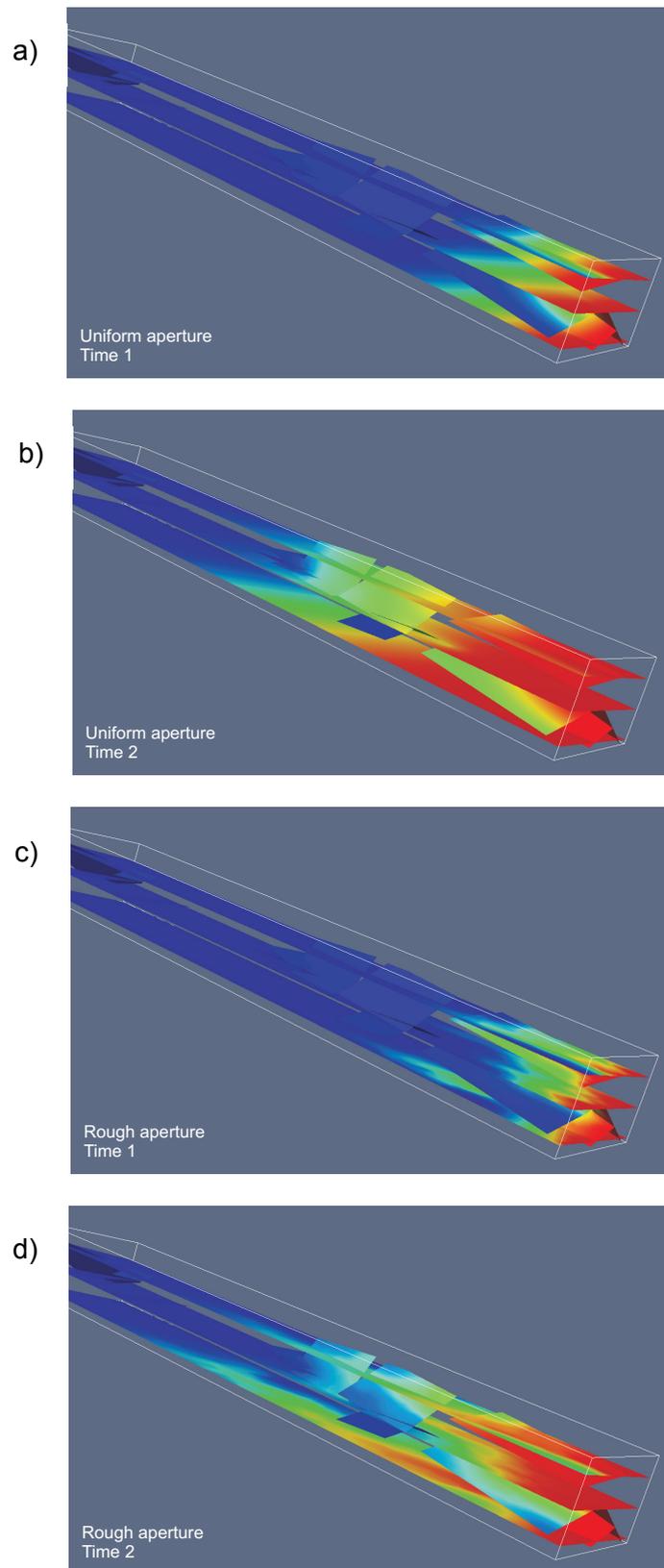
Fig. 10.26 Conservative transport in the Grimsel fracture network

Smooth fractures in a) and b), rough fractures in c) and d), aperture magnitude obtained by calculating b_h for the full network

10.8 Flow in discrete fracture-matrix systems: Flow and transport in the Grimsel 10-fracture network (Benchmark ADuR10 and ADuR11)

10.8.1 Motivation

In this benchmark begins the analysis of the Grimsel shear zone 10-fracture network. The first step is to examine pressure and velocity fields in the uniform fracture network. Meshing is conducted on the fracture network itself. Later, behavior will be examined utilizing combined fracture-matrix meshing and interaction. Additional complexities will also be added incrementally.

10.8.2 Independent fracture network - Uniform aperture (Benchmark ADUR10)

Geometry of the network is defined by the corner node coordinates of 10 planar fractures, and the locations of their intersections.

10.8.2.1 Numerical solution

For the fracture only simulations, meshing is straightforward and is conducted with *Gmsh*, a finite element mesh generator with build-in pre- and post-processing facilities /GEU 09/. Fig. 10.27 shows the conversion from geometry data to a 2d mesh with *Gmsh*.

Two alternate spatial discretizations are explored, one with 2 m discretization, and one with 5 m. The resulting fracture meshes are displayed in Fig. 10.28. For a 5 m spatial discretization (mean) the mesh comprises 1 363 elements, while the 2 m discretization contains 9 175 elements. The total geometry size $[x, y, z]$ is, in meters, $[139, 81, 67]$.
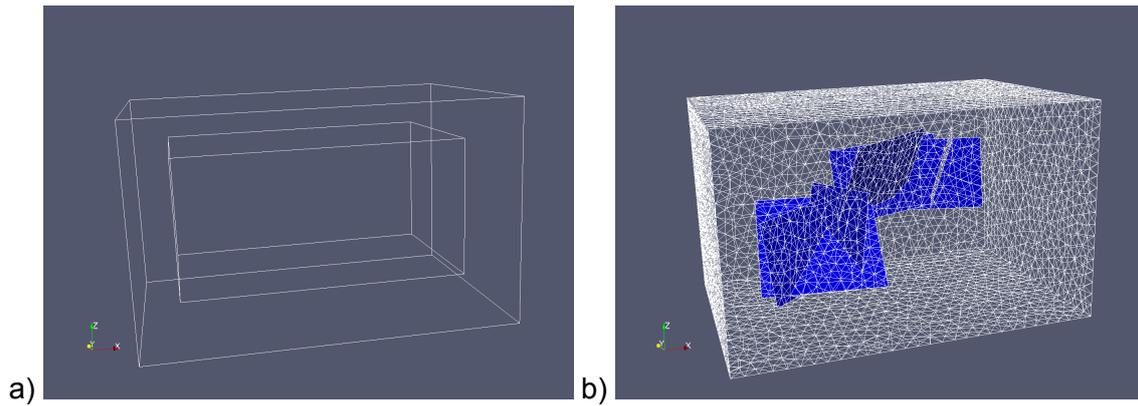
Fig. 10.27 Conversion from outline to 2d mesh with Gmsh
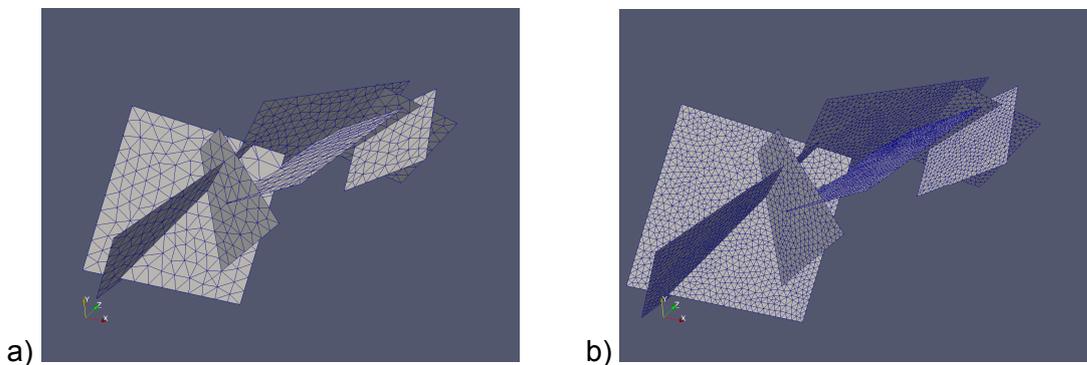
Fig. 10.28 Gmsh mesh results for the 5m (a) and 2m (b) discretisations

A boundary pressure of 1 MPa is prescribed at the western edge of the westernmost fracture, while a pressure of 0 MPa is maintained at the eastern boundary. Initial conditions are zero pressure.

The fractures are uniform with a permeability of $1.0 \times 10^{-12}\ m^2$, a porosity of 1.0, and no tortuosity. The fluid is prescribed a density of 1 000 kg/m^3 and a viscosity of $1.0 \times 10^{-3}\ Pa \cdot s$. Time stepping is controlled by a Courant condition.

10.8.2.2   Results

Results are explored qualitatively in Fig. 10.29, which shows the advance of a conservative tracer in the 2d network for the alternative meshes
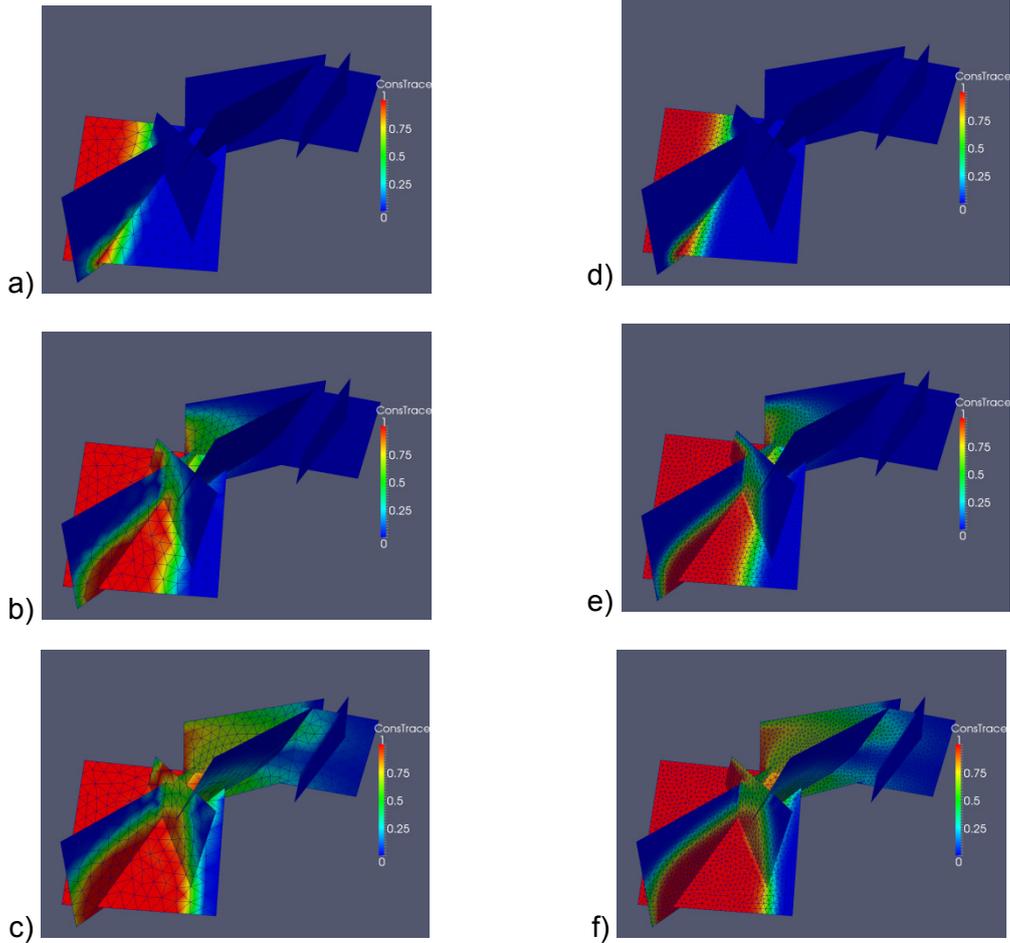
Fig. 10.29 Conservative ADE in Grimsel 10-fracture network for the 5m (a – c) and 2m (d – f) discretized meshes

The same simulations are explored with breakthrough curves in Fig. 10.30, where two points are selected in the geometry, and relative concentrations monitored in time. Points A and B are at $[x, y, z]$ coordinate locations $[346, 192, 170]$ and $[395, 232, 171]$ (in meters), respectively. As expected, the 5 m mesh is more dispersive so that at point A, closer to the injection boundary, there is little difference between the meshes, but this difference grows in time as evidence by point B, further from injection. A slight amount of instability is also evident in the larger discretization, where slight negative concentrations evolve in early times.
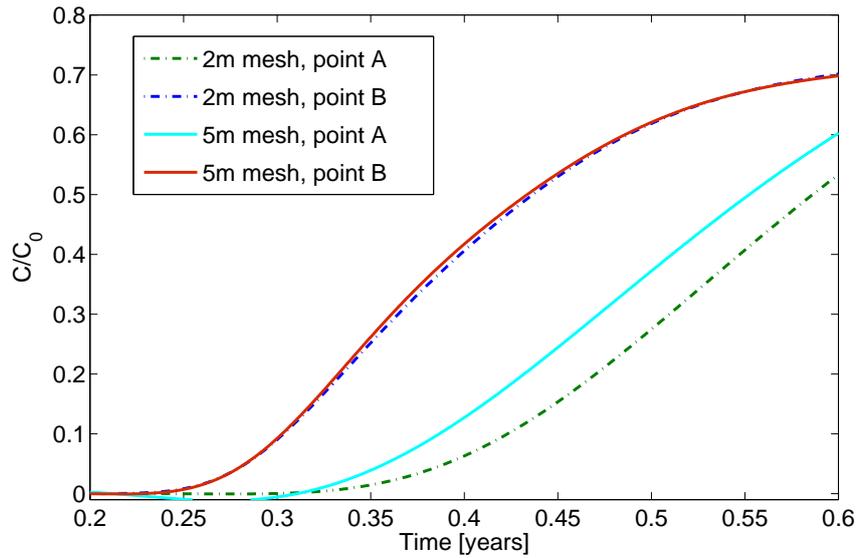
Fig. 10.30 Breakthrough curves for conservative tracer at two points

10.8.3   Fracture imbedded in low permeability matrix - Uniform aperture (Benchmark ADUR11)

Geometry of the network is defined by the corner node coordinates of 10 planar fractures, as before, and the locations of their intersections.

10.8.3.1   Numerical solution

Including the rock matrix mesh requires additional operations beyond those in the previous section. A 2d mesh is first constructed, as before, with *Gmsh*. *Tetgen* is then used to generate 3d elements across the entire domain corresponding to nodes of the 2d fracture mesh and the 2d boundaries of the rock matrix. *Tetgen* is a tetrahedral mesh generator and a 3d delaunay tiangulator /SI 04/.The result is then combined to a single mesh (Fig. 10.31).

>Gmsh>

>Tetgen>

+   =
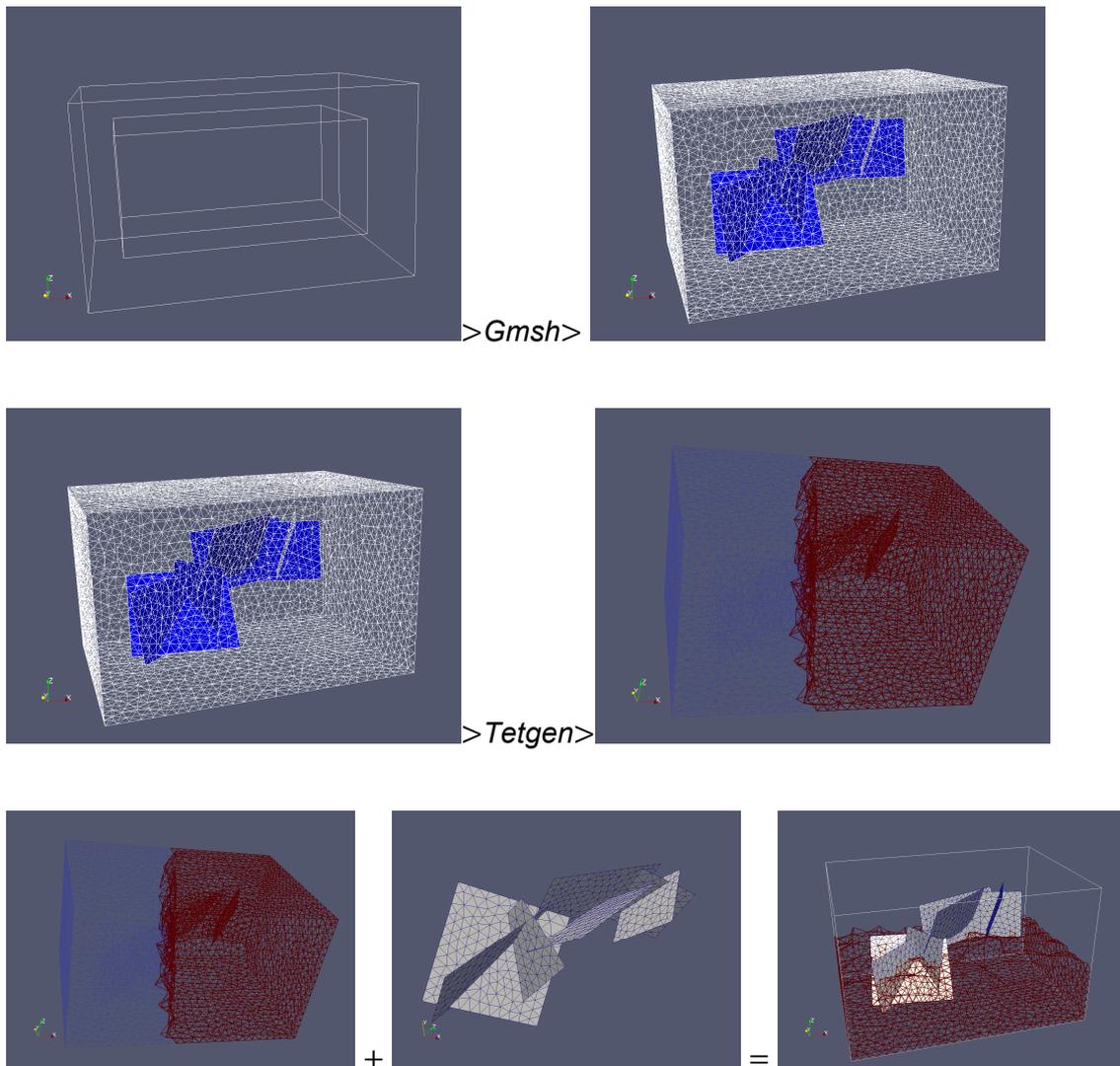
Fig. 10.31 Conversion to 2d fracture mesh imbedded in 3d rock matrix

For a 5 m spatial discretization (mean, on the planar fracture) the mesh comprises 20 818 elements. While a 3 m and 2 m discretization contain 36 867 and 66 890 elements, respectively. The total $[x, y, z]$ geometry size is, in meters, $[178,121,108]$.

A boundary pressure of 10 MPa is prescribed at the lower left edge of the block geometry while a pressure of 0 MPa is maintained at the upper right edge. Initial conditions are zero pressure.

The fractures are uniform with a permeability of $1.0 \times 10^{-12}\ m^2$, a porosity of 1.0, and no tortuosity (see file *ogs.mmp*). The lower permeability matrix is assigned a permeability of $1.0 \times 10^{-14}\ m^2$, a porosity of 0.3, and no tortuosity. The fluid is

prescribed a density of 1 000 kg/m^3 and a viscosity of $1.0 \times 10^{-3}\ Pa \cdot s$ (file ogs.mfp). Time stepping is controlled by a Courant condition.

10.8.3.2   Results

Results are explored qualitatively in Fig. 10.32, which shows the advance of a conservative tracer in the 2d network for a mesh with 2m discretization on the fractures and one of 3 m discretization, for a slice of the 3d geometry.
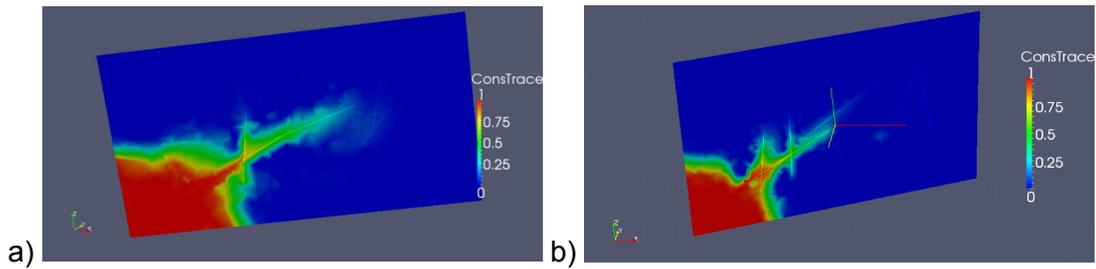
Fig. 10.32 ADE in slices of the 3d geometry for a) the 3 m discretization and b) the 2 m discretization

The full 3d advance is then displayed in Fig. 10.33 for a series of 5 snapshots in time in the 2 m mesh.

The same simulations are explored with breakthrough curves in Fig. 10.34, where two points are selected in the geometry, and relative concentrations monitored in time. Points A and B are at $[x, y, z]$ coordinate locations $[346,192,170]$ and $[395,232,171]$ (in meters), respectively. Now even points at the leftmost area of the fracture network (point A) diverge for the 5 m mesh. A slight amount of instability is also evident in the larger discretization, where slight negative concentrations evolve in early times.
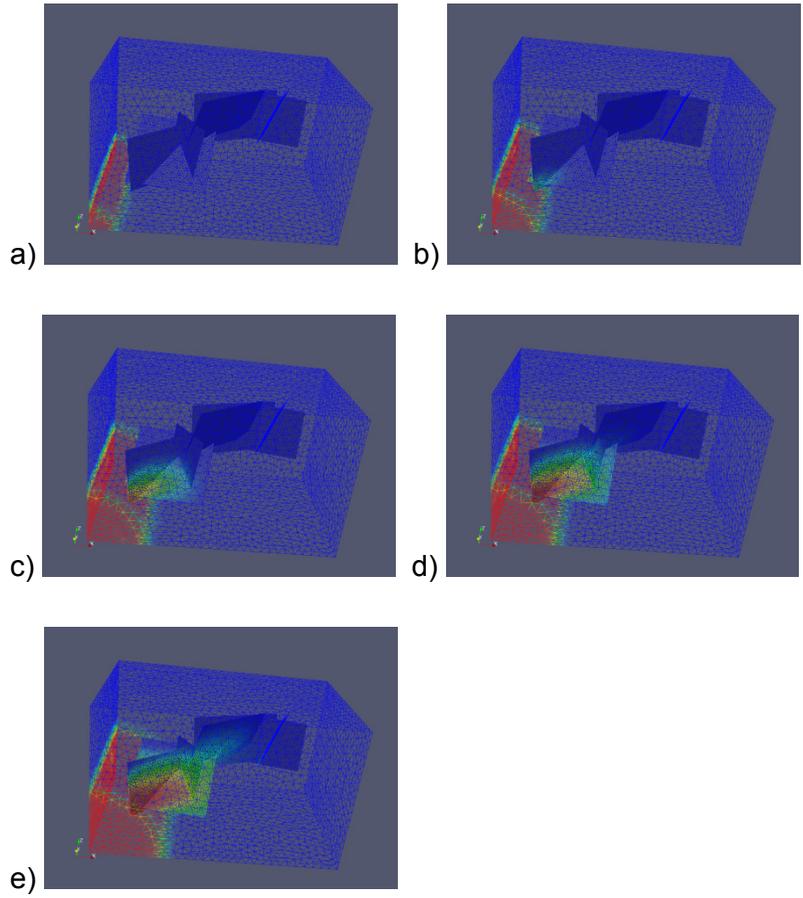
Fig. 10.33 Conservative transport in the 3d fracture-matrix geometry
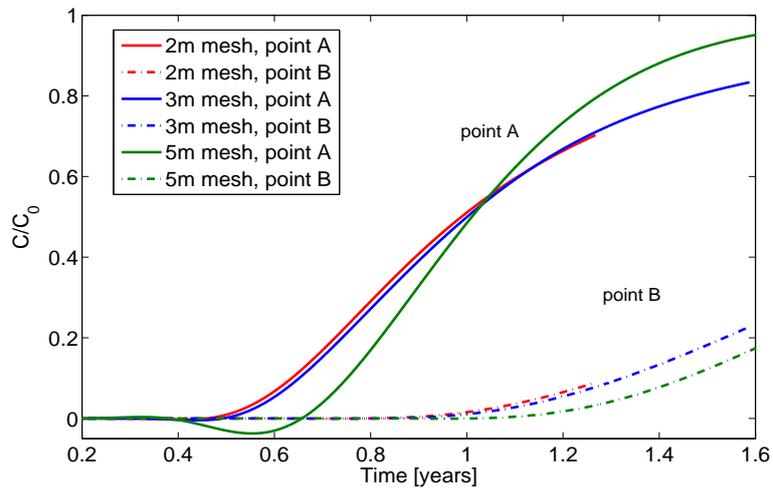
Fig. 10.34 Breakthrough curves for conservative tracer at two points in the 2d fracture

11 Code verification

11.1 Fractured Elder problem

The Henry problem cf. /HEN 64/ and section 6.4.1 and the Elder problem cf. /DEB 00/, /ELD 67/ are well-known benchmark problems for density-driven flow. In the Elder problem the originally thermally driven flow problem has been reformulated for density-driven flow by /VOS 87/, among others. Here the density differences are due to heavy brine. The geometry was modified to feature a fracture cf. /GRI 12a/, /STI 12/ and the boundary conditions can be found in Fig. 11.1. The parameters used in the simulations are listed in Tab. 11.1.
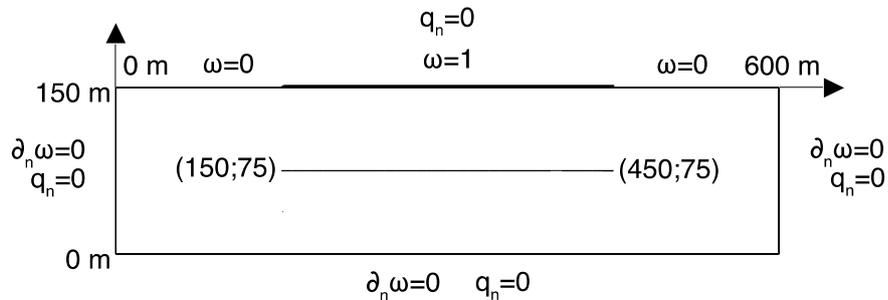
Fig. 11.1 Geometry and boundary conditions for the modified Elder problem featuring a fracture.

Tab. 11.1 Parameters for the Elder problem

Symbol	Quantity	Value
D_m	Diffusion coefficient in the medium	$3.565 \cdot 10^{-6}$ m^2 s^{-1}
D_f	Diffusion coefficient in the fracture	$10.695 \cdot 10^{-6}$ m^2 s^{-1}
g	Gravity	9.81 m s^{-2}
K_m	Permeability of the medium	$4.845 \cdot 10^{-13}$ m^2
K_f	Permeability of the fracture	$4.845 \cdot 10^{-10}$ m^2
ϕ_m	Porosity of the medium	0.1
ϕ_f	Porosity of the fracture	0.3
μ	Viscosity	10^{-3} kg m^{-1} s^{-1}
ρ^{pW}	Density of water	10^3 kg m^{-3}
ρ^{pB}	Density of brine	$1.2 \cdot 10^3$ kg m^{-3}

Symbol	Quantity	Value
$a_\alpha^t, a_\alpha^\ell$	Dispersivity lengths	0
A_α	Forchheimer coefficient	0

For a fracture of width $\epsilon = 0.1\,\text{m}$ the simulation results of the Elder problem using the d- and the $(d-1)$-dimensional model are compared at different points in the fracture (cf. Fig. 11.2). It can be observed that the main behaviour, including all peaks, is resembled by the $(d-1)$-dimensional simulation. Though, a little shift between the two results can be observed. As it is well known that the Elder problem has a history for its multiple solutions which are associated, e. g., with the number of fingers at its stationary solution (cf. e. g. /JOH 02/, /JOH 03/). Therefore, by keeping in mind, that the computational grids for the d- and the $(d-1)$-dimensional simulations are not the same, this result is satisfactory. Also, the in section 6.5.2 defined criterion indicates that the use of the $(d-1)$-dimensional model is adequate.

a) b)
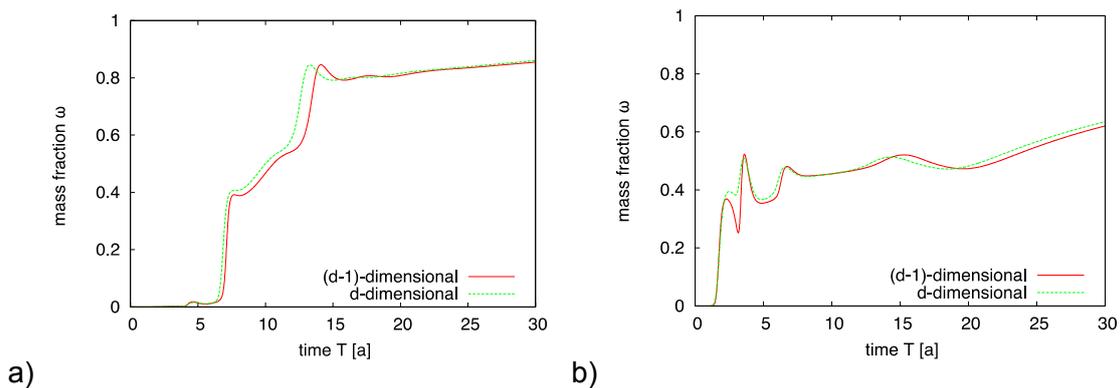
Fig. 11.2   Comparisons of d- and $(d-1)$-dimensional simulations of the Elder problem mass fraction in the fracture at $x = 300\,\text{m}$ (a) and $x = 440\,\text{m}$ (right) cf. /STI 12/.

11.2   Tests using the Forchheimer correction

In section 6.2 the original model using Darcy's law was extended by a Forchheimer correction of the velocity. In section 6.4.2 it was observed that, e. g., in the Henry problem there are vortices generated in fractures for increasing fracture width. The presence of vortices itself, implies not only the questionability of the validity of Darcy's law,

but also the question, if the use of Forchheimer's correction leads to better results for the $(d-1)$-dimensional model.

Therefore, the fractured Henry problem as it was described in section 6.4.1 is considered using four different sets of parameters for the Forchheimer correction (cf. /GRI 12b/ and Tab. 11.2), one corresponding to Darcy's law, two based on the work of /THA 98/ and one freely chosen to have a value in between.

Tab. 11.2 Parameter sets for the Forchheimer coefficient A_α

Case	$A_f \ [m^{-1} \ s]$	$A_m \ [m^{-1} \ s]$	Reference
1	0	0	Darcy's law
2	36	51	(/THA 98/, eq. 4)
3	$1 \cdot 10^3$	$1 \cdot 10^3$	-
4	$2.5 \cdot 10^6$	$2.2 \cdot 10^5$	(/THA 98/, eq. 2)

In Fig. 11.3 it can be seen that for increasing values of the Forchheimer coefficient A_α less saltwater is intruding into the domain and the influence of the fracture on the flow pattern is reduced. This observation can be explained as follows: In (6.12) the expression of the specific discharge, which includes the Forchheimer correction, is given by a product of the Darcy velocity and a factor depending among others on A_α. This factor tends towards zero when A_α tends to infinity and, therefore, the velocity including the Forchheimer correction is reduced for increased Forchheimer coefficient A_α. As the norm of the Darcy velocity in the fracture is bigger than in the medium, the fracture's influence is reduced.
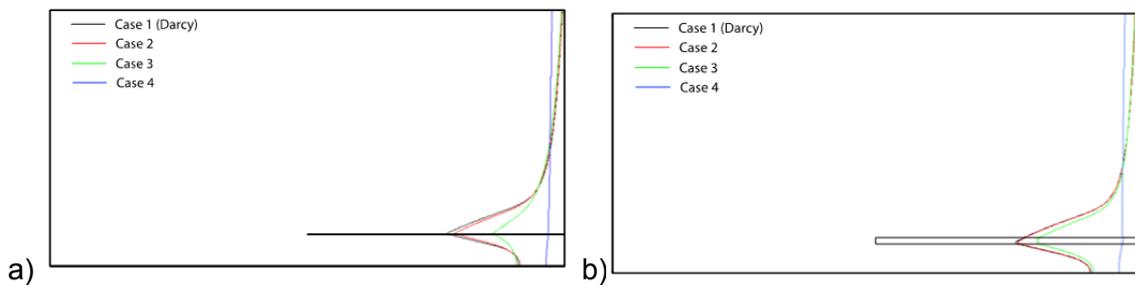
Fig. 11.3 Isolines of the mass fraction (corresponding to $\omega = 0.1$) of the d-dimensional simulation with different Forchheimer coefficients A_α for Henry's problem with a fracture of width $\epsilon = 0.003$ m (a) and $\epsilon = 0.024$ m (b) at time $t = 5$ min cf. /GRI 12b/.

By comparing the impact of the Forchheimer correction for the different fracture widths ϵ (cf. Fig. 11.3), we notice that the correction with finite values of A_α, e. g. with $A_f = A_m = 10^3$ m^{-1} s (case 3), slows down the flow even more in the case of the thin fracture. The correction with really big A_α (case 4: $A_f = 2.5 \cdot 10^6$ m^{-1} s, $A_m = 2.2 \cdot 10^5$ m^{-1} s) gives the same result in both cases and results in a flow pattern in which a relation to the original flow pattern of Henry's problem is no longer visible. Furthermore, it can be observed that in the case of the thicker fracture with width $\epsilon = 0.024$ m, the Forchheimer correction with $A_f = A_m = 10^3$ m^{-1} s (case 3) yields a more uniform distribution of the brine concentration along the fracture width. This observation is very important for this study because it implies that the $(d-1)$-dimensional model might yield better results for thicker fractures when the Forchheimer correction is used.

Comparisons between d- and $(d-1)$-dimensional simulations of the fractured Henry problem using the Forchheimer correction can be found in /GRI 12b/.

12 Preprocessing and graphical user interfaces for d³f and r³t

12.1 Introduction

VRL-Studio is an integrated development environment (IDE) based on the Java Platform that combines both visual and text-based programming. In contrast to many other development environments VRL-Studio Projects are fully functional programs that are developed at runtime. VRL-Studio is based on VRL (Visual Reflection Library) to enable declarative and fully automated creation of graphical user interfaces from Java objects. To accomplish that, VRL uses the information accessible via the Java Reflection API /HOF 11/.

The d³f/UG software is accessible in the VRL visualization framework using a C/C++ binding of the required functionality to the Java platform /SCH 12/. The d³f/UG code has been developed in a modular way using small, combinable components that allow the user to easily change and control its application. All functionality blocks are available as a graphical representation in the VRL and can be graphically reorganized and adapted in order to suit to the users need. However, many applications are of a very similar structure and it is useful to prepare and provide some template applications where users must only choose their specific needs (such as physical parameters, domain and grid, solver parameters and output requirements), but does need to setup the control flow of the project from scratch. This helps to avoid doubling of work and provides a fast and user-friendly usage of the d³f/UG package within the VRL framework.

12.2 Project Format

For VRL-Studio a new project format has been introduced that can contain multiple user-defined workflows. This makes it possible to exchange multiple workflows between different computes without having to consider workflow dependencies. That is, if user A sends a workflow to user B that consists of several sub-workflows user A can simply send the project file to user B.

12.3　　　　Improved UI-Generation

Components in complex workflows often need a large number of input parameters. Even though the interface generation provides a mechanism to use problem specific parameter visualizations it was necessary to improve the visualization possibilities.

The interface generation consists of three types of visual components (see Fig. 12.1). An object representation is a container, comparable to a program window that can group several child components. A method representation is a container component inside an object representation. It can also group child components and provides elements for calling the represented method. To represent variable data VRL provides type representations. In most cases they allow interaction with the visualised.
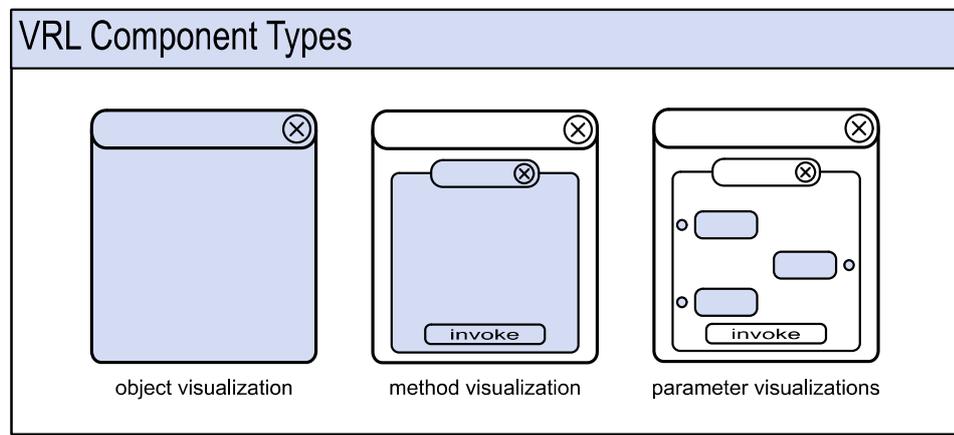
Fig. 12.1　Component Types

One important extension to those component types is the possibility to define parameter groups inside a method representation. Groups are container objects for parameter visualizations. Each group can be shrinked/expanded individually (see Fig. 12.2).
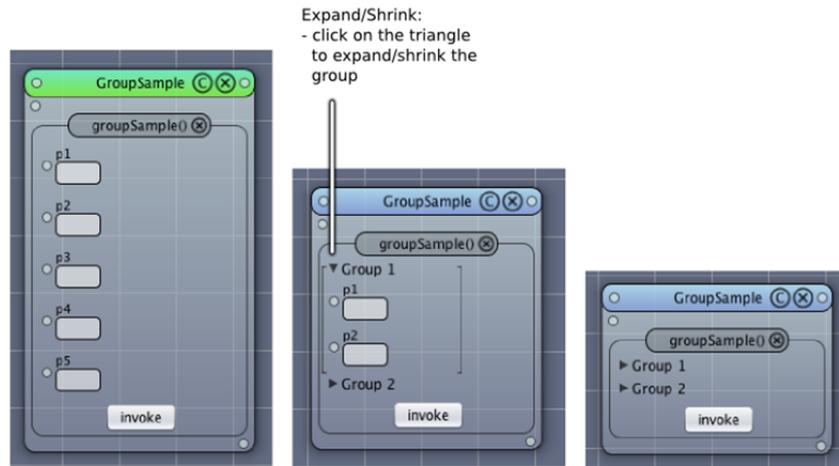
Fig. 12.2   Improved Parameter Groups

Except from grouping the parameters group containers do not influence the functionality of parameters and methods. The following code example shows how parameter groups can be defined:

Code Example:
```
@ComponentInfo(name="GroupSample", category="Custom")
public class GroupSample implements java.io.Serializable {
  private static final long serialVersionUID=1L;

  public void groupSample(
    @ParamGroupInfo(group="Group 1|true|no description")
    @ParamInfo(name="p1", style="default", options="") int p1,
    @ParamGroupInfo(group="Group 1")
    @ParamInfo(name="p2", style="default", options="") int p2,
    @ParamGroupInfo(group="Group 2|true|no description")
    @ParamInfo(name="p3", style="default", options="") int p3,
    @ParamGroupInfo(group="Group 2")
    @ParamInfo(name="p4", style="default", options="") int p4,
    @ParamGroupInfo(group="Group 2")
    @ParamInfo(name="p5", style="default", options="") int p5
  ) {
    //
  }
}
```

The first occurrence of `@ParamGroupInfo` defines a new parameter group „p1“. The Boolean „true“ defines that the group will be expanded. The string defines a tooltip description „no description“. The second occurrence of `@ParamGroupInfo` „p1“ specifies that the second parameter shall be added to group „p1“.

12.4 Dynamic Array Visualizations

12.4.1 Defining array visualizations

The type representations that have been discussed so far do not support a variable number of input parameters.

Therefore, a parameter visualization has been developed that can visualize fixed-size arrays as well as user defined arrays (the size can be chosen by the user).

```
Code Example:
public Integer add(
  @ParamInfo(style="array", options="minArraySize=2") Integer... values) {
    def result = 0
    values.each{it->result+=it}
    return result
}
```

The code shown above demonstrates how to visualize an integer array with user-defined size. The minimum number of elements is 2. Fig. 12.3 shows the corresponding VRL visualization.
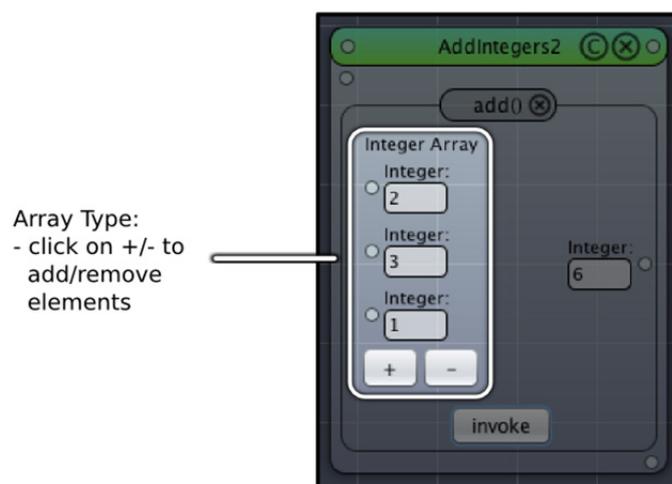
Fig. 12.3 Integer array with user-defined size

Except for array visualizations all available parameter visualizations can be used as element visualization. The next code example shows how to input a variable number of strings using the editor visualization:

```
public String add(
  @ParamInfo(style="array", options="elemStyle=\"editor\"") String... values){
    def result = ""
    values.each{it->result+=it+"\n"}
    return result
}
```

Fig. 12.4 shows an example visualization.
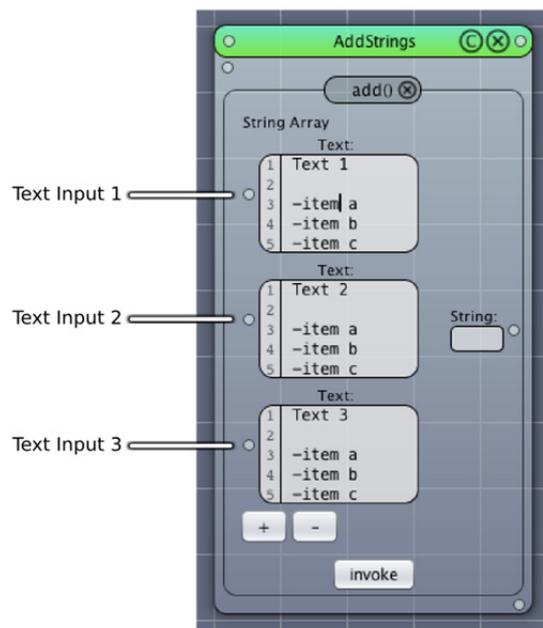
Fig. 12.4   String array using an editor component as element visualization

12.4.2   Array visualizations as container with variable element types

The previously shown array visualizations (Fig. 12.3) only use one element type for the entire array.

As arrays can also contain elements of different types a type representation container has been implemented that dynamically uses the class object of element types to

choose the correct element type visualization. This mechanism is equivalent to the visualization used for top-level containers.

12.4.3 Creating a new project from the d3f template application

In the following this template project, its user data setup and usage will be described in detail.

In order to create a new d³f project, the VRL-Studio containing the d³f/UG plugin (provided as a bundle) must be started. A new project from the d³f-template is created via "File" → "New Project from Template" → "UG – Density-Driven-Flow" (see Fig. 12.5).
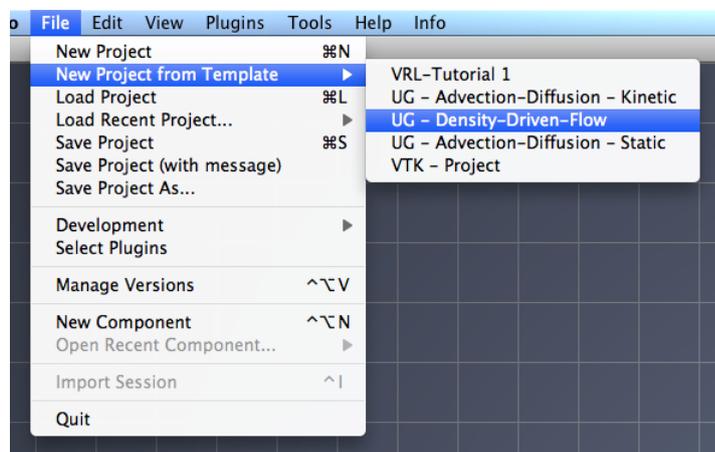
Fig. 12.5 Creating a new project from template

This will create a project as shown in Fig. 12.23. The control flow of the project consists of three components:

- **DensityDrivenFlow**: domain, physical parameter, boundary conditions, start values, discretization setup
- **KineticSolver**: time solver setup, linear solver setup, non-linear solver setup, data evaluation
- **VTUViewer**: live visualization, output setup

These three basic components are already connection into a control flow (yellow lines) and data dependencies between the components are established (grey lines). After choosing the appropriate, problem specific parameters the simulation can be run invoking the "Start" button.

12.4.4 DensityDrivenFlow component: physical user data

The DensityDrivenFlow component is used to setup the user-specific problem of the type

$$\frac{\partial}{\partial t}\left(\phi\rho_f\right) + \nabla\left(\boldsymbol{q}\,\rho_f\right) = 0, \tag{12.1}$$

$$\frac{\partial}{\partial t}\left(\phi\rho_f\chi_s\right) + \nabla\left(\boldsymbol{q}\,\rho_f\chi_s - \boldsymbol{D}_s\rho_f\nabla\chi_s\right) = 0, \tag{12.2}$$

with

$$\boldsymbol{q} = -\frac{K}{\mu}\left(\nabla p - \rho_f\boldsymbol{g}\right). \tag{12.3}$$

The unknown solution components are

p pressure

χ_s brine mass fraction.

All the other variables are user-defined and problem-specific data and must be specified by the user. Thus, the user must be able to enter the following data

ϕ porosity

ρ_f density

$\boldsymbol{D}_s$ molecular diffusion

K permeability

μ viscosity

$\boldsymbol{g}$ gravity

The following subsections describe how the user data can be specified in the d3f/UG template project within the VRL studio.

Domain: Grid and Subsets

All physical parameters are dependent on the physical domain used for the simulation. Specification of user data on different subsets of the domain as well as different

boundary conditions on parts of the domain rely on the partition of the domain into sub-sets. Therefore, the recommended data format to load a grid is the *.ugx file format. This format stores the plain grid together with the description of different subsets on this grid and can be easily created and/or processed using ProMesh (section 12.5.1). The *.ugx file used for the simulation is chosen in the section "Domain" → "Grid". Invoking the selection button a file-dialog appears where the file system can be navigated until the requested file is found.
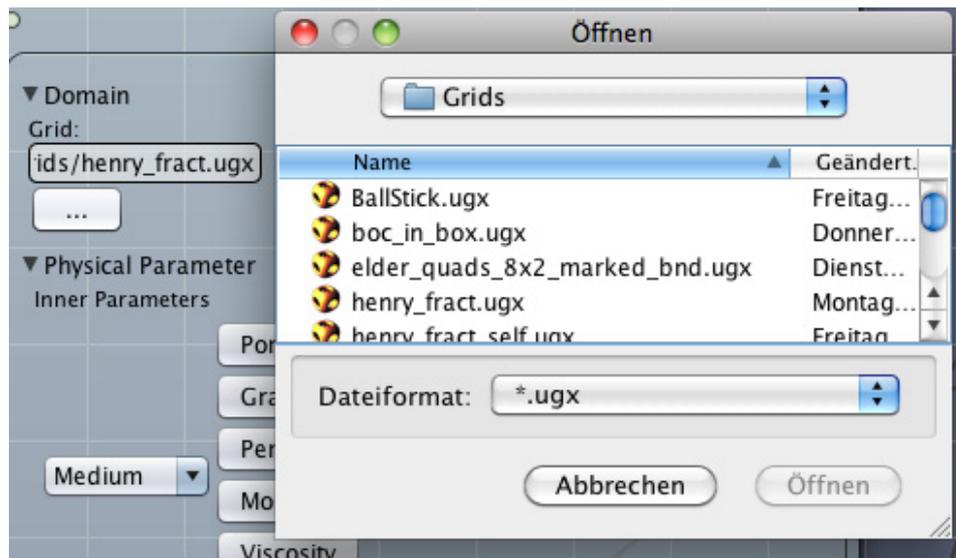
Fig. 12.6   Selection of the domain: Loading a *.ugx file

Physical Parameter: Inner domain parameter

Within the domain the system is modeled by the equations given in (12.1) – (12.3). It is assumed that the problem parameter may vary in space and time. Specially, the parameter set may be different in the subsets of the domain. Therefore, all user parameters are given subset by subset. The user can add and remove subset specifications using the "+/-"-button as shown in Fig. 12.7.
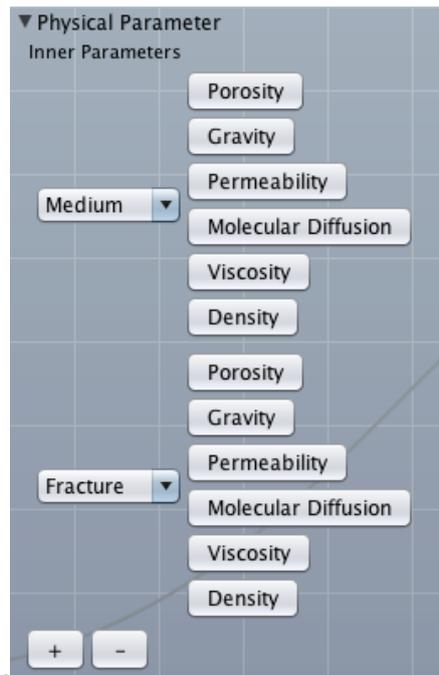
Fig. 12.7 User parameter for several subsets of the domain

On the left hand side the considered subset is chosen by a drop-down menu. The available subsets are according to the selected *.ugx file and automatically adjusted if the grid is changed.

The parameter input on each subset is changed by invocation of the associated button. This leads to a dialog window for the data. The input dialog varies from the required data format:

Scalar Data depending on space and time

The porosity and viscosity can be specified by a function of space and time. The simplest case is a constant value for the data. As shown in Fig. 12.8 this can be done entering the corresponding number. In addition for more evolved cases the data may be specified using a function given as Java code where the special coordinated, the time point and the subset are available as parameters for the function. In order to switch between the two types of possible data the radio button at the top is used.

```
                    Porosity              ⊗
              ○ Constant ⊙ Code
        Parameters: x, y, t, si
        Return: value (as double)
   1  │ // some spatially defined medium
   2⊟ │ if ( x < 1000) {
   3  │    return 0.25;
   4  │ }
   5  │ // some medium grid subset
   6⊟ │ else if (si == 2) {
   7  │    return  0.15;
   8  │ }
   9  │ // other regions
  10⊟ │ else {
  11  │    return 0.35;
  12  │ }
  13  │
```

```
     Porosity    ⊗
 ⊙ Constant ○ Code
      0.35
```
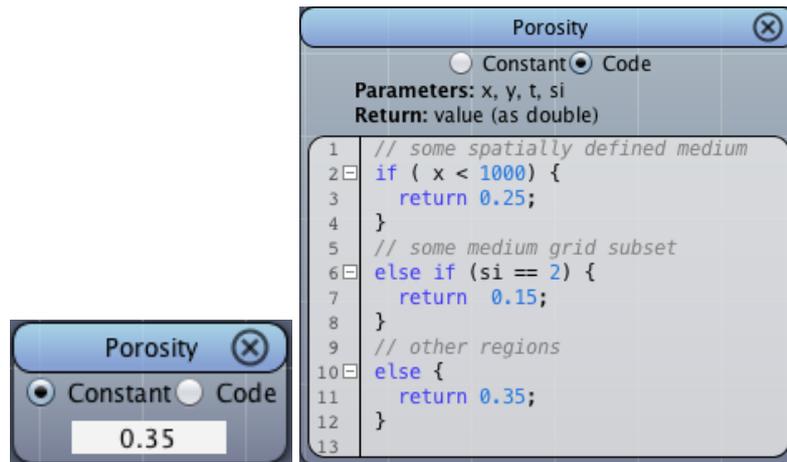
Fig. 12.8   Constant data (left) and user code (right)

Vector Data depending on space and time

The gravity is specified as a vector of the spatial dimension as shown in Fig. 12.9.
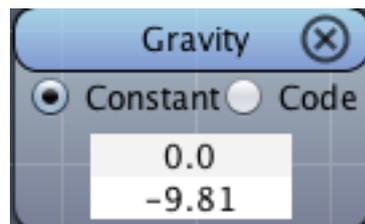
Fig. 12.9   Vector Data in 2d

Matrix Data depending on space and time

Permeability and molecular diffusion are given as matrices. The specification can be given as constant data or as user code. The data must be specified as a matrix according to the dimension of the physical world. The dialog for the constant case is shown in Fig. 12.10.
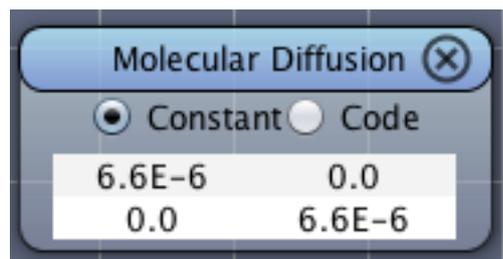
Fig. 12.10 Matrix Data in 2d

Solution dependent Data

The density is assumed to be a function of the brine mass fraction. Thus, in order to specify this relation a user code must be given. In addition the derivative of the relation has to be specified with respect to the brine mass fraction. This setup is shown in Fig. 12.11.
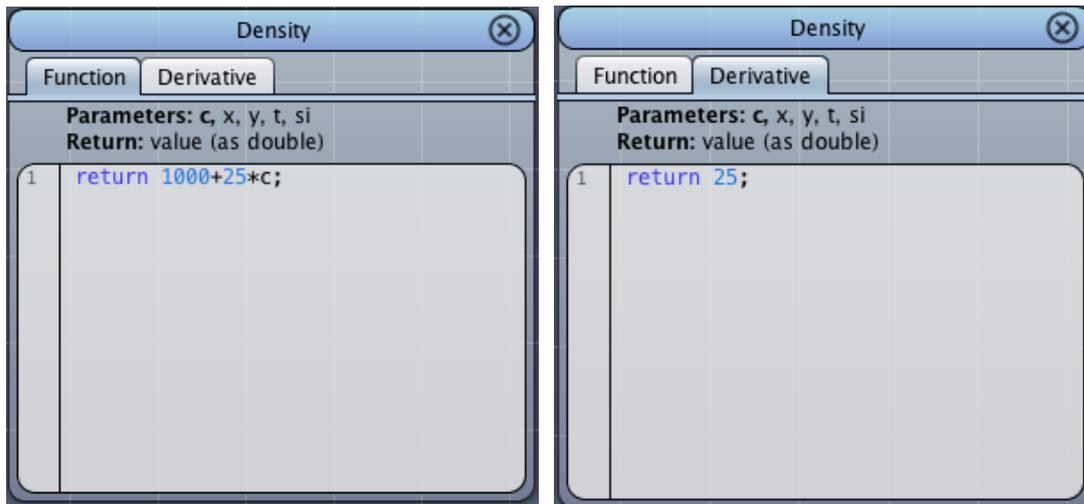
Fig. 12.11 Solution dependent data: function (left) and derivative (right)

All user specific data input options are intelligent in the way that the possible choices are related to the selected *.ugx file: dimension-related fields are adjusted in size and available subsets are displayed as present. Assistance is provided for the user once the domain (i. e. the *.ugx file) is changed: changing the domain dimension the data is adjusted in a logical way, e. g., defining a corresponding vector or matrix data for this dimension. This speeds up the usage when setting up simulations of several problems ©of similar type in different dimensions. In rare cases this is not possible and must be taken into account. Therefore, again a graphical assistance is provided. Once the *.file is changed the user data buttons appear in three different colors: grey (user proofed or auto-adjustment successful), yellow (no auto-adjustment available) and red (no reasonable choice available). In the yellow case the user is informed that a reasonable choice has been make but may be verified by the user. In the red case the user is required to adjust the data manually to the needs. This usually appears if no or an invalid domain has been chosen. An example is shown in Fig. 12.12.
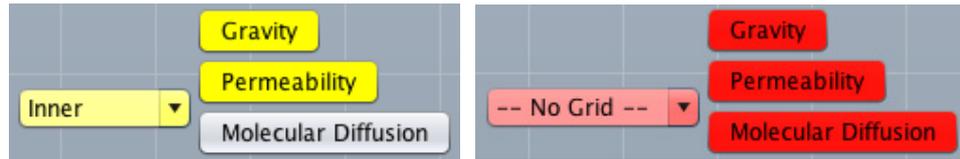
Fig. 12.12 Visual data validity: auto-adjusted (left) and incorrect data (right)

Boundary Conditions

Boundary conditions for the brine mass fraction and the pressure have to be specified subset-wise. Having selected a domain all available subsets are present in the drop-down-menus and additional boundary specifications can be added using the "+/-"-buttons. Two types of boundary conditions are offered: Dirichlet boundary conditions can be set prescribing the values as constant or user code. Flow boundary conditions are specified prescribing the normal flux. A negative value corresponds to an inflow boundary condition. All boundaries can dependent on the spatial coordinates, time and subset. If no boundary condition is prescribed for a boundary subset a no flux condition is used as default value. See Fig. 12.13 for an illustration.
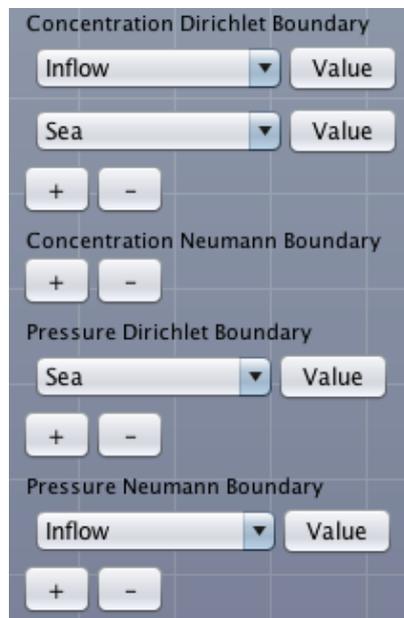
Fig. 12.13 Specification for the boundary conditions

Initial values

The start values for the brine mass fraction and the pressure at the beginning of the computed time interval are specified using scalar user data. Constant and code based versions are available.

Fig. 12.14 Setting the initial values for the solution components

Discretization setup

The system of partial differential equations is discretized on the given grid. In order to allow the user to influence the concrete discretization setup some of the choices are make available in the section "Discretization Setup".
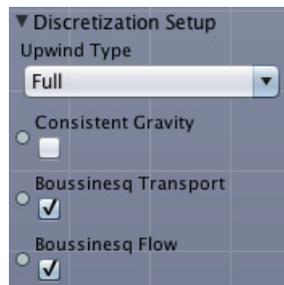
Fig. 12.15 Discretization setup management

12.4.5   KineticSolver component

Once the user problem has been specified as described in the previous section, this problem must be solved. To do so, the KineticSolver component is used that computes the solution for specified time points. The success of the solver and the progress of the computation can be observed in the output log at the bottom of the VRL window if required, see Fig. 12.16.
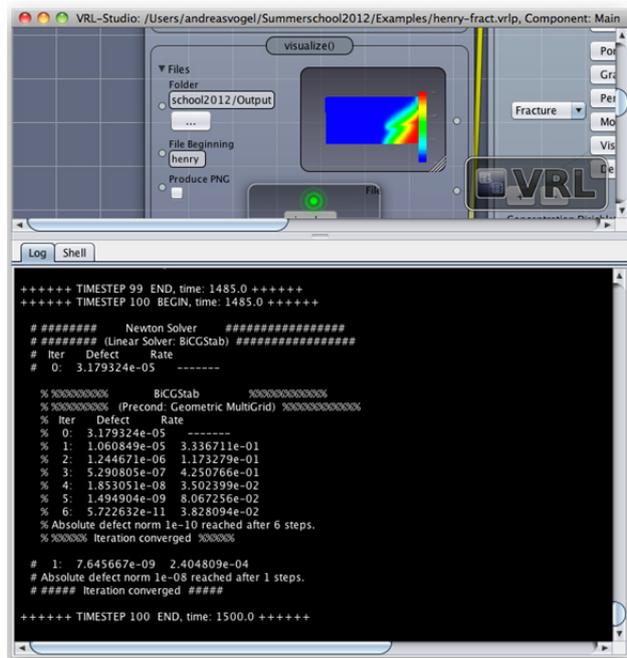
Fig. 12.16 Computation information displayed during a simulation

Time solver setup

The time solver is used to control the time discretization scheme. The available parameters are shown in Fig. 12.17.
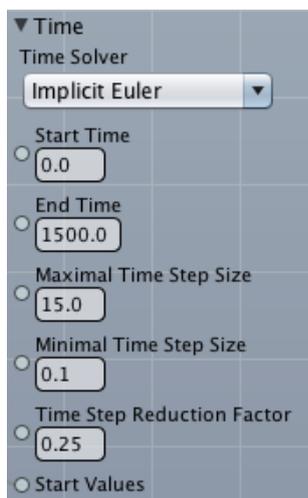
Fig. 12.17 Time solver setup

It is possible to choose between several schemes: implicit Euler, explicit Euler and Crank-Nicolson (implicit Euler is recommended). The start and end time point must be

specified. The maximal and minimal time step size is used to control the step size. Always trying the maximal step size this size will be reduced by the reduction factor until solvability of the time step is accounted. The solver fails if the minimal time step size is reached.

Linear and Nonlinear solver setup

The discretization of the partial differential equations leads to a large sparse matrix system that must be solved. Several matrix solvers are implemented for this task. The user can choose from iterative solvers such as LinearSolver, CG, BiCGStab or use an LU-factorization. The iterative solvers can be preconditioned using geometric multigrid, Jacobi, Gauss-Seidel or ILU preconditioner. A maximum number of iterations and a desired computational accuracy must be choose to control the linear solvers.
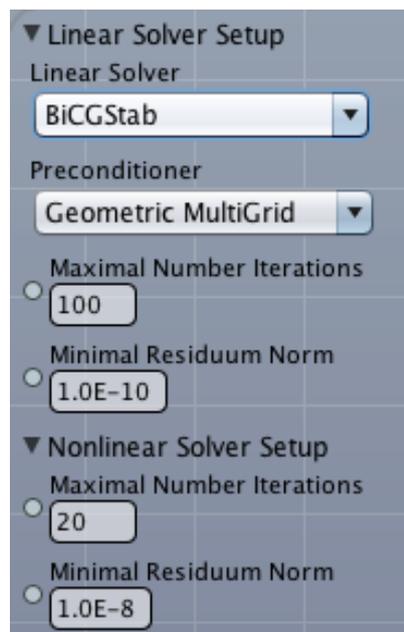
Fig. 12.18 Linear and Nonlinear solver setup

Since the solved problem is nonlinear a Newton method is used to solve the nonlinearity using an exact jacobian. The user can specify the maximum numbers of iterations and the desired accuracy.

Data evaluation

During the computation it is interesting to compute some data. The user might be interested in the integrated amount of brine mass fraction within some subset or the flux of brine over some boundary subset. This can be requested in the section "Data Evaluation" and is returned as a trajectory usable in a trajectory plotter.

Fig. 12.19 Integration of masses and mass fluxes over subsets

12.4.6   VTUViewer component

While a computation is running, it is interesting to see a live visualization of the current simulation status. Having performed a simulation it is interesting to review the computed solution. To this aim the component VTUViewer is integrated into the control flow.
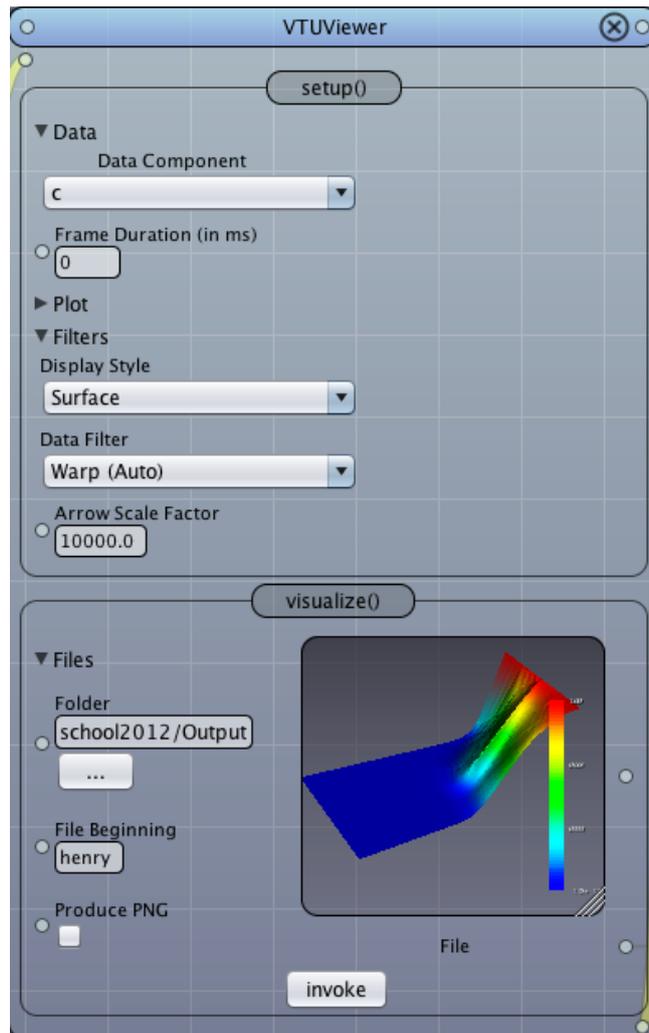
Fig. 12.20 Visualization component used for live and replay plots

The required display styles can be chosen in the "setup" field. The solution component (brine mass fraction or pressure) must be selected. In the "Plot" section several settings are available:

- **Title**: the title to be shown in the picture / video
- **Range**: the data range (user specified or automatic)
- **Data Legend**: controls the display of the data legend
- **Outline**: draws an outline around the plotted domain
- **Orientation**: displays an orientation triad

In the section "Filters" several filters can be selected in order to provide an easier data interpretation:

- **Display style**: controls which elements (volumes, faces, edges, points) of the grid are shown.
- **Data Filter**: A warp filter displays a 2d solution as a height profile. The contour filter shows contour lines / areas, i. e. regions of same value.
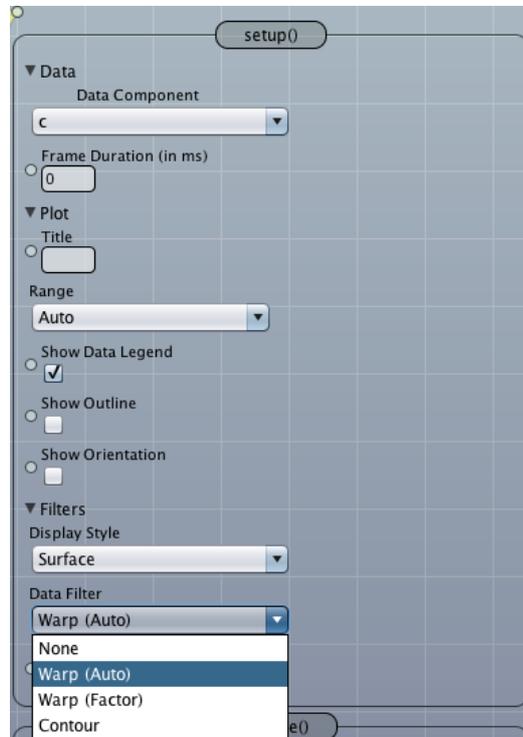
Fig. 12.21 Setup panel of the VTUViewer

The visualization of the selected data is displayed in the section "visualize". The view can be adjusted in size and the geometry can be shifted and zoomed in or out. A full screen visualization is available by double-click on the image.

The data selection is via the field in the section "Files". The user can choose to show just one time step by selection a file or can choose to visualize a whole time series by selecting a folder and specifying the file name beginning. In order to produce a png-file series (that may be converted to a video) this option can be selected.
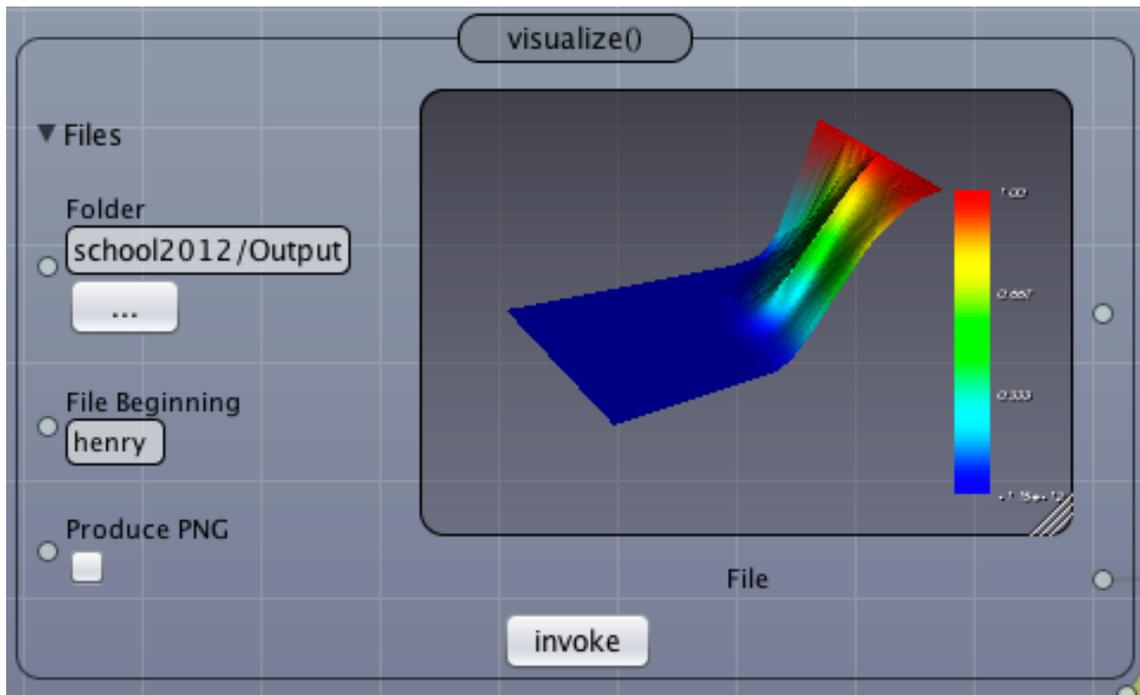
Fig. 12.22 View of a computed solution
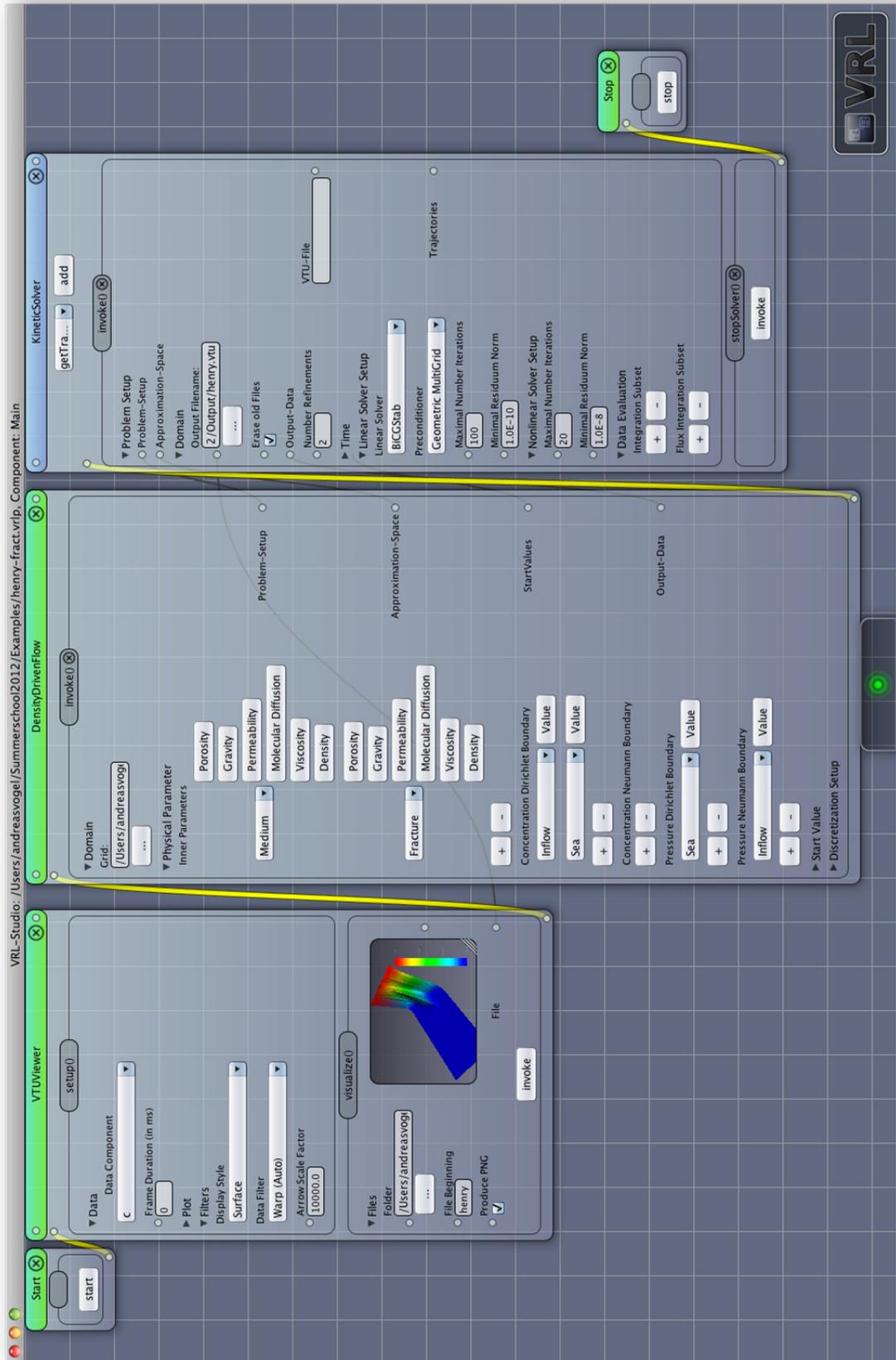
Fig. 12.23 Control flow of the d³f template

12.5 Preparing geometries for simulating density driven flow

In order to perform code verification through simulations, means of creating grids which represent the underlying domains are required. Since very specific demands on such grids arise especially in problems of fractured density driven flow, the grid generator ProMesh, a general-purpose meshing software cf. /REI 13/, has been enhanced in order to allow for the construction and inspection of related grids. In the following, a short introduction to ProMesh is given in section 12.5.1. Algorithms required for the construction of 2d and 3d grids are specified in sections 12.5.2 and 12.5.3. In Fig. 12.24 ProMesh's user interface is depicted.
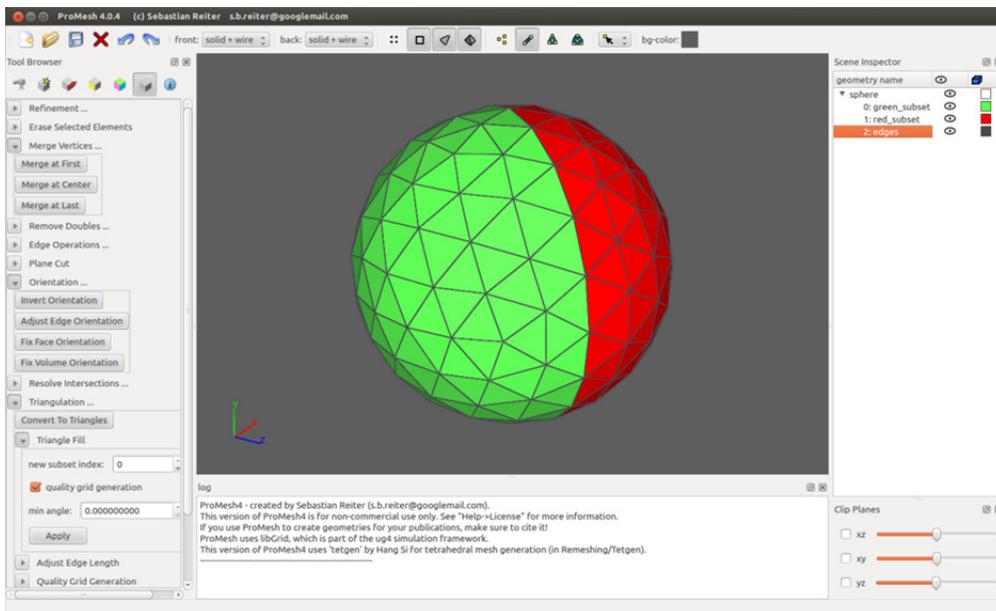
Fig. 12.24 ProMesh4 – Graphical User Interface

12.5.1 ProMesh

ProMesh is targeted at the generation of 1, 2 and 3 dimensional grids for numerical simulations using, e. g., finite element / finite volume or discontinuous Galerkin methods. It is capable to generate, visualize, and modify unstructured hybrid grids consisting of vertices, edges, faces (triangles or quadrilaterals), and volume elements (tetrahedrons, hexahedrons, prisms, and pyramids; cf. Fig. 12.25). Grids are constructed and transformed (both geometrically and topologically) by applying different algorithms featured in ProMesh. Those algorithms can be applied to the whole grid or to selected parts of a grid and involve the optimization of element aspect ratios, local anisotropic

refinement with hanging nodes or regular closure, triangle- and tetrahedral fill algorithms and more. Elements can furthermore be assigned to different subsets, allowing users to define specific boundary values during simulations, as well as parameters and equations for different parts of a grid.

An important feature of ProMesh is its fully interactive grid visualization, which lends itself to inspect even complex volume geometries both on a large scale (different subsets, general structure and geometry of the domain) as well as on very small scales, down to the shape and of individual elements. By hiding selected parts of a grid or by using different clip-planes, a grids interior can be inspected. The grid visualization is fully hardware accelerated and thus allows for a smooth user interaction.
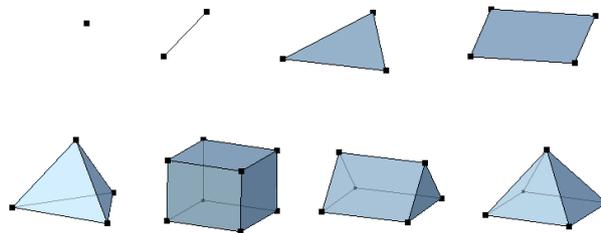
Fig. 12.25 Grid elements used by ProMesh (top: vertex, edge, triangle, quadrilateral; bottom: tetrahedron, hexahedron, prism, pyramid)

12.5.2   Construction of geometries for 2d fractured domains

In a first step, ProMesh is used to construct the outer boundary and low dimensional inner features of a discretization grid, like fractures or boundaries between inner layers. This is accomplished through ProMesh's grid generation and remeshing tools, which include, e. g., creation of polylines through extrusion, refinement, or scale-, rotate-, and move-transformations.

In a second step unresolved edge intersections can be automatically resolved by ProMesh by introducing new vertices at places where edges intersect and by splitting those edges using the new vertices.

The grid is then prepared for triangular grid generation. Such triangular grids have to represent the medium which is possibly split into different layers of rock/soil. Furthermore fractures have to be resolved by triangle sides. In order to create such grids, a

first coarse triangulation is constructed without introducing new vertices. Sides of those triangles are either edges which were already contained in the initial boundary geometry from step 1 or are newly introduced inner edges, which do not cross any other edges (neither newly introduced edges nor edges given from step 1). This triangulation algorithm is based on the "sweep line triangulation" algorithm described in /DEB 00/ and is capable of generating triangulations for any set of polygons and polygonal chains, as long as one closed polygon exists in the set which contains all other polygons and as long as no two edges of any polygon penetrate each other.

The resulting triangulation may contain triangles which are rather badly shaped. Those result from restrictions of the initial geometry or are a consequence from the fact that the triangulation algorithm may not introduce new inner vertices. ProMesh thus applies a "constrained Delaunay refinement" algorithm cf. /CHE 89/ on the geometry, which improves the triangle aspect ratios through vertex insertion and edge swapping, constructing a grid which fulfills the "constrained Delaunay" property.

After triangulation, fractures finally have to be expanded so that the full dimensional equations for density driven flow can be applied – until this point they are represented by line segments only. A similar algorithm as for the case of low-dimensional fracture approximation using degenerated elements given in /REI 12b/ is used. For the full dimensional case, however, new vertices are not introduced at the same position as the original fracture vertex, from which they were generated, but an offset along the normal to the fracture is added. By this quadrilateral elements are generated representing the full dimensional fracture. The grid structure in the fractures is thus similar to the case of degenerated elements – each degenerated element corresponds to a full dimensional fracture element and each vertex of the degenerated geometry built from the same base triangulation has a corresponding vertex in the full dimensional equivalent. This property is especially useful when it comes to performing the transition from a low dimensional to a full dimensional fracture representation during dimensional adaptivity.

A sample triangulation of a geometry with subsequent expansion of two intersecting fractures is depicted in Fig. 12.26.
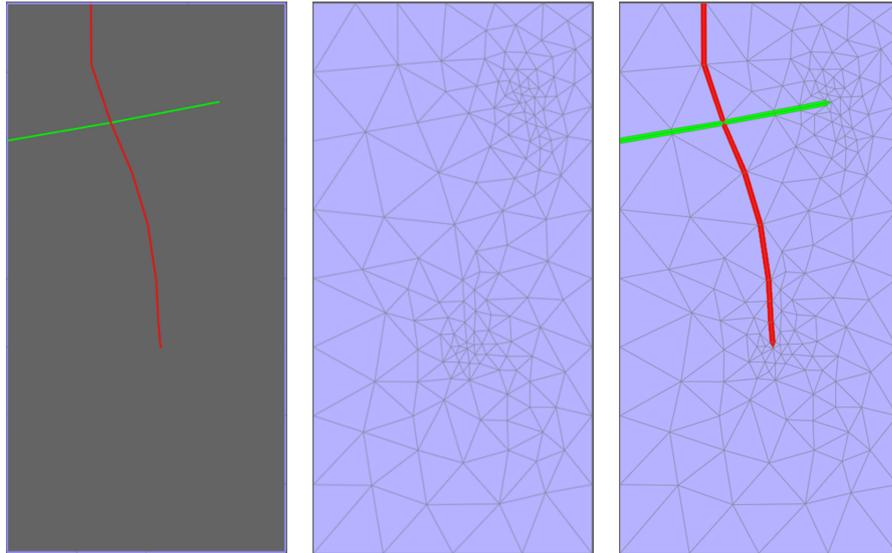
Fig. 12.26 Generation of a fractured domain in 2d. Low dimensional features, triangulation and expanded layers (from left to right)

12.5.3 Constructing geometries for 3d fractured domains

Construction of 3d fractured domains can be performed analogously to the 2d case. Instead of quadrilaterals, prisms are now used to build the two element layers in the fractures. The grid generation process is again similar to the process used for grids in which fractures are represented using two layers of degenerated elements. The reader is again referred to /REI 12b/ for a detailed description on how such grids are precisely constructed. Again, as in 2d, only the step in which fracture elements are generated differs. Instead of generating degenerated elements, newly introduced vertices are now moved along the fracture normal which points into the side to which the new vertex will be connected. Instead of degenerated prisms, normal prisms can now be used to connect old fracture vertices with new ones (cf. Fig. 12.27).
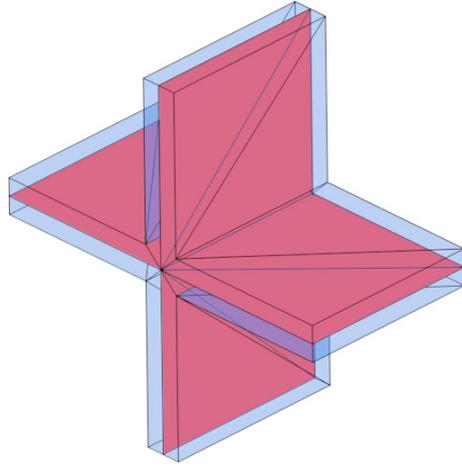
Fig. 12.27 Two layers of prisms (blue) generated around an initially low dimensional triangular fracture representation (red). Surrounding tetrahedrons omitted for clarity

13   Summary

One of the main challenges in flow and transport modelling are the different scales of the heterogeneities of the rock matrix. The matrix may comprise homogeneous and heterogeneous continuous parts, large deterministically known single fractures and s of small background fractures that can be described by geostatistical means only. Of special interest is the representation of tiny fissures that cannot be modelled discretely without neglecting the porous matrix because this would be too complex and too time-consuming.

Growing evidence had indicated in the past that the log hydraulic conductivity field of natural heterogeneity of fractured aquifers can be appropriately described with self-affine properties. The scale effects cause the longitudinal dispersion to increase with the travel distance as the solute follows the complex pathways provided by the hetrogeneities. The temporal behaviour of the longitudinal dispersion in fractal media developes differently to media with finite correlation lengths: The latter are characterised by an ergodic situation and the ensemble and effective quantities converge against the same limit value for infinite times while in fractal media, the longitudinal dispersion does not converge. Furthermore, the ensemble and effective quantities are different for all times. They describe two fundamentally different properties.

The behaviour of the transverse dispersion coefficients is similar to that in media with finite correlation lengths to first increase and then reduce with increasing travel distance. This is a consequence of the absence of divergence in the flow field and could imply a degradation of the contaminant. However, the timescale of changes in the transverse dispersion media with finite and with infinite correlation lengths differs considerably. This is a consequence of more branched and much longer pathways of the solute particles caused by the tiny fissures that remove any preferential scales. It was shown that the timescale increases with the degree of fractality. This corresponds to a high tortuosity and a much longer retention period of the contaminants in fractal media.

Thermohaline flow and transport are described by a system of partial differential equations. In order to solve these equations numerically, d³f and r³t use a vertex-centered finite volume discretisation. Here, beside of the set of discrete control volume, where

the conservation law is fulfilled numerically, the Ansatz space for the unknown solution has to be chosen.

The usual choice for the Ansatz functions in d³f is a set of linear trial functions, i. e. the unknown solution is represented by linear functions on each mesh element. This approach requires only degrees of freedom in the vertices. The generalization to higher orders is achieved by using a polynomial representation for the unknown solution on each element that uses functions of order greater than one. Lagrange finite elements are used and result in degrees of freedom on vertices, edges, faces and volumes in order to ensure the continuity of the solution.

In d^3f and r³t barycentric control volumes are used, constructed by taking the convex hull of the following points: a vertex of the mesh, all barycenters of adjacent edges and faces of the vertex and all barycenters of the adjacent elements. The generalization of this construction is related to the chosen Ansatz space. For each degree of freedom one control volume is constructed. This ensures that the resulting linear system remains quadratic. For this purpose, each element of the mesh is subdivided virtually into smaller elements of the same type, such that the finer partition corresponds to a distribution of degrees of freedom equivalent to the linear case, i. e. all virtual subelements carry exclusively degrees of freedom in their vertices. Now, the same barycentric construction procedure as used for the linear case can be applied to the virtually refined elements to produce control volumes related to the subelements.

This type of discretisation was applied to the equations of density driven flow and implemented in d³f. It was successfully tested using Henry's problem. Hereby, the use of quadratic and cubic Ansatz functions resulted in a formidable improvement in convergence rates even for coarser grids.

The discretisation of the thermohaline flow equations leads to large linear equation systems. Effective solvers are necessary to reduce the computational effort. Basically, d³f and r³t use classical (geometric) or algebraical multigrid solvers (MG and AMG) to overcome this problem. Multigrid methods solve the equations iterating among different refinement levels of the computational grid. On each level simple iterative solvers are used to reduce the high-frequency parts of the error ("smoothing"). The equation system is only on the coarse grid solved exactly. However, growing numbers of unknowns and higher grid resolution lead to larger and larger systems to be solved. Therefore, AMG methods were advanced to filtering algebraic multigrid methods (FAMG). These

methods are based on the idea of smoothing only parts of the equation system with re-duceable defect (high error frequencies). The other parts are directly restricted to the coarser grid. In the coarsening algorithm, FAMG methods choose fine- and coarse nodes by minimizing the number of coarse nodes while still maintaining a good interpo-lation for fine nodes. An FAMG solver was developed and implemented in d³f and r³t with the objective to speedup the solver especially in case of large numbers of un-knowns.

The development of d³f and r³t is based on the ug-toolbox. The codes have been com-pletely parallelised from the beginning, i. e. the computational grid may be decomposed into multiple parts that are distributed to different processors. Assembling and solving are performed on those distributed domains. Special concepts, algorithms and data structures are required to parallelize those tasks and to efficiently perform the required synchronization between different processes.To facilitate communication and to gain more efficiency and flexibility, the **p**arallel **c**ommunication **l**ayer (pcl) library has been developed and implemented as a part of the ug4 library. Numerical tests using the La-place equation and a geometric multigrid solver on up to more than 250 000 proces-sors resulted in a nearly ideal scaling.

The mesh size influences the dispersion coefficients. Therefore, grid-size dependent transport coefficients are needed for a realistic description of the situation. With the up-scaling method of coarse graining artificial mixing these effects can be quantified. This spatial filtering method allows the determination of the true mixing as a function of the local grid size.

For weakly heterogeneous media, it could be shown, that the coarse graining method reduces the artificial mixing effect in the ensemble quantities and filters out the fluctua-tions in the effective dispersion quantities. In media with finite correlation lengths, this effect is visible especially for small distances to the fracture, whereas the difference vanishes with growing distance. The same limit value is reached by both the effective quantities without and with the spatial filtering procedure.

In fractal media the coarse graining method reduces the artificial mixing effect especial-ly in the ensemble longitudinal quantity. A small value of the filter width results in a large cut-off effect and the corresponding grid-size dependent quantities will be small and reach the same limit value. The larger the filter width, the smaller is the cut-off ef-fect and the larger is the limit value. If the correct physical filter width is applied, the

corresponding grid-size dependent ensemble quantity recovers the values of the unfiltered effective coefficient, which reflects the dispersion more exactly. In the effective longitudinal quantity itself, the effect of this filter width persists at all times. Therefore, the coarse graining method improves the dispersion quantities, indeed, defining the true physical mixing.

The transverse dispersion in both media types is not signifycantly affected by the coarse graining method.

A d- and a $(d-1)$-dimensional approach for modelling fractured porous media were compared. The advantages of the $(d-1)$-dimensional approach are less computational costs and less numerical problems. It was shown though that it can not cover all phenomena that might happen inside the fracture and that its validity should be seriously questioned, especially for the case of large fracture apertures and high density contrasts. In order to solve this problem, a dimension-adaptive multigrid method improving the convergence of the numerical solver for the d-dimensional case was introduced. Furthermore, a criterion indicating the validity of the $(d-1)$-dimensional approach was developed. This criterion allows a dimension-adaptive approach that automatically switches between d- and $(d-1)$-dimensional fracture representations during run-time, depending on actual flow-conditions and fracture properties. The results of this approach show that the error made with the $(d-1)$-dimensional model can be kept small, while also keeping the numerical cost small.

A parameter estimation method is described, which has been implemented into d³f repository. A user manual is given describing all necessary details about the parameter estimation method. Furthermore, the functionality of the parameter estimation method is investigated by two examples. It is shown that the method works sufficiently well, as long as the parameter estimation problem is not ill-conditioned. This is not the case if sufficient data points are provided.

Generally, flow systems in fractured rocks can be characterised by a hierarchy of connected flow paths. The largest and most connected fractures contribute the major part to flow and transport. This highly transmissive flow system is embedded in a system of smaller-scale fractures and fissures that form a background system as well as the rock matrix both of which have a much smaller hydraulic conductivity. For a fast conservative simulation of solute transport in such a flow system analytical solutions were suggested. For this purpose the network of large connected fractures is focussed on and

the influence of the background system has to be estimated. Here is to be distinguished between the effective 1d-model for estimating first arrival times and the effective 1d-model for estimating peak concentrations because the first is built on the ensemble mixing, whereas the latter relies on the effective mixing behaviour of the plume.

Instead of solving the advection-dispersion equation, fast predictions in solute transport may be obtained using particle tracking methods. This alternative may be a time-saving alternative especially for advection-dominated problems.

In chapter 9 a random walk particle tracking (RWPT) method is explained and tested. The results of 1d and 3d test cases are compared to analytical solutions and in 1d additionally to measurements and numerical results got by a classical FEM simulation. Furthermore, 2d and 3d pore scale benchmarks are suggested.

For testing the newly implemented features, 12 benchmarks are suggested that enable the comparism of d³f and r³t results to analytical solutions, measurements or the results of other codes (OGS, TOUGH2, PICNIC and RWPT-methods).

The VRL-based graphical user interface was further developed and adopted to the needs arising in the course of the project. VRL-Studio is an integrated development environment (IDE) based on the Java Platform that combines both visual and text-based programming. It enables declarative and fully automated creation of graphical user interfaces from Java objects. The highly flexible graphical user interface permits numerical controlling as well as the input of physical parameters and other model data. To provide an integrated visualisation, a VTU Viewer is implemented.

The preprocessor ProMesh was considerably advanced to make it more user-friendly. Additionally, grid generation was improved and extended, and the grid quality inpection tools were enhanced.

References

/AAR 06/   Aarnes; Efendiev: An adaptive multiscale method for simulation of fluid flow in heterogeneous porous media. accepted SIAM MMS, 2006.

/ABS 84/   Abramowitz, M., Stegun, I. A.: Pocketbook of Mathematical Functions. Verlag Harri Deutsch, Frankfurt am Main, 1984.

/ALA 89/   Alabert, F. G.: Constraining description of randomly heterogeneous reservoirs to pressure test data: a Monte Carlo study. SPE paper 19600, presented at SPE Annual Technical Conference and Exhibition, 8-11 October 1989, San Antonio, Texas, Society of Petroleum Engineers, 1989.

/ANG 09/   Angot, P., Boyer, F., Hubert, F.. Asymptotic and numerical modelling of flow in fractured porous media. ESAIM: M2AN. Mathematical Modelling and Numerical Analysis 43, 239 – 275, 2009.

/ARB 02/   Arbogast, T.: Implementation of a Locally Conservative Numerical Subgrid Upscaling Scheme for Two-Phase Darcy Flow. Computational Geosciences, 6, 453 – 468, 2002.

/ARB 04/   Arbogast, T.: Analysis of a two-scale, locally conservative subgrid upscaling for elliptic problems. SIAM J. Numer. Anal., 42, 576 – 598, 2004.

/ATT 99/   Attinger, S., Dentz, M., Kinzelbach, H., Kinzelbach, W.: Temporal behaviour of a solute cloud in a chemically heterogeneous porous medium. Journal of Fluid Mechanics 386: 77 – 104, 1999.

/ATT 02/   Attinger, S.; Eberhard, J.; Neuss, N.: Filtering Procedures in Heterogeneous Porous Media: Numerical results,   Computing and Visualization in Science, 5, 67 – 72, 2002.

/ATT 03/   Attinger, S.: Generalized Coarse Graining Procedures in Heterogeneous Porous Media. Computational Geosciences , Vol 7, No 4, 253 – 273, 2003.

/ATT 04/   Attinger, S. Coarse grained ensemble and effective mixing parameters for solute transport. American Geophysical Union (0043-1397).

/ATT 04/   Attinger, S., Dentz, M.: Exact Transversal Macrodispersion Coefficients for Transport in Heterogeneous Porous Media. Stochastic Environmental Research and Risk Assessment 18 (No. 1): 9 – 15, 2004.

/BAR 60/   Barenblatt,G.I.; Zheltov, Y.P.; Kochina, I.N.: Basic concepts in the theory of seepage of homogeneous fluids in fissured rocks. Prikladnaya Matematika i Mekhanika, 24, 5, 852-864 (in Russian); J. Applied Mathematics and Mechanics (PMM), 24, 5, 1286 – 1303, 1960.

/BAR 97/   Barker, J. W., Thibeau, S.: A critical review of the use of pseudorelative permeabilities for upscaling. SPE Reservoir Engineering 12 (2): 138 – 143, 1997.

/BAR 01/   Barten, W., Robinson, P..Contaminant transport in fracture networks with heterogeneous rock matrices: The picnic code. Tech. Rep. 01-02, PSI, 2011.

/BAR 09/   Barrett, R., Berry, M., Chan, T. F., Demmel, J., Donato, J., Dongarra, J., Eijkhout, V., Pozo, R., Romine, C., van der Vorst, H.. Templates for the solution of linear systems: building blocks for iterative methods. SIAM, Philadelphia, PA, 1993.

/BAS 94/   Bastian, P., Wittum, G.. Robustness and adaptivity: The UG concept. In Hemker, P., Wesseling, P. (eds.): Multigrid Methods IV, proceedings of the Fourth European Multigrid Conference, Amsterdam 1993, Birkhäuser, Basel, 1994.

/BAS 00a/ Bastian, P., Birken, K., Johannsen, K., Lang, S., Reichenberger, V., Wieners, C., Wittum, G., Wrobel, C.. Parallel solution of partial differential equations with adaptive multigrid methods on unstructured grids. In: Jäger, W., Krause, E. (Eds.), High performance computing in science and engineering. Springer, Berlin, pp. 506 – 519, 2000.

/BAS 00b/   Bastian, P., Chen, Z., Ewing, R. E., Helmig, R., Jakobs, H., Reichenberger, V.. Numerical simulation of multiphase flow in fractured porous media. In: Chen, Z., et al. (Eds.), Numerical treatment of multiphase flows in porous media. Proceedings of the international workshop, Beijing, China, August 2–6, 1999. Vol. 552 of Lect. Notes Phys. Springer, Berlin, pp. 50 – 68, 2000.

/BAS 05/   Bastian P.; Droske, M.; Engwer, C.; Klöfkorn R.; Neubauer, T.; Ohlberger, M.; Rumpf, M. *In:* Kornhuber, R. (ed.) et al.: Domain decomposition methods in science and engineering. Selected papers of the 15th international conference on domain decomposition, Berlin, Germany, July 21-25, 2003. Berlin: Springer. Lecture Notes in Computational Science and Engineering 40, 167 – 174, 2005.

/BAT 49/   Batchelor, G. K.: Diffusion in a field of homogeneous turbulence: I. Eulerian analysis. Australian Journal of Scientific Research: Series A: Physical Sciences, 2: 437 – 450, 1949.

/BAT 52/   Batchelor, G. K.: Diffusion in a field of homogeneous turbulence. Mathematical Proceedings of the Cambridge Philosophical Society 48: 345 – 362, doi: 10.1017/S0305004100027687, 1952.

/BAT 88/   Bates, Douglas M., Watts, Donald G.: Nonlinear Regression Analysis and Its Applications, Wiley Series in Probability and Statistic, 1988.

/BAV 84/   Baveye, P., Sposito, G.: The operational significance of the continuum hypothesis in the theory of water movement through soils and aquifers. Water Resources Research 20 (5): 521 – 530, 1984.

/BEA 72/   Bear, J.: Dynamics of Fluids in Porous Media, Dover Publications, Inc., New York, 1972.

/BEA 77/   Bear, J.. On the aquifer's integrated balance equations. Adv. Water Resour. 1 (1), 15 – 23, 1977.

/BEA 79/   Bear, J.. Hydraulics of Groundwater. Dover Publications. Inc., Mineola, 1979.

/BEA 90/   Bear, J., Bachmat, Y.. Introduction to Modeling of Transport Phenomena in Porous Media. Kluwer Academic Publishers, Dordrecht, Boston, London, 1990.

/BEA 93/   Bear, J., Tsang, C.-F., deMarsily, G.. Flow and contaminant transport in fractured rocks. Academic Press, Inc., New York, 1993.

/BEC 94/   Beckie, R., Wang, B.: A numerical method to characterize the averaging process invoked by a slug test. X. International Conference on Computational Methods in Water Resources, Heidelberg, 703 – 710, 1994.

/BEC 96a/   Beckie, R., Aldama, A. A., Wood, E. F.: Modeling the large-scale dynamics of saturated groundwater flow using spatial filtering theory: 1. Theoretical development. Water Resources Research 32 (5): 1269 – 1280, 1996.

/BEC 96b/   Beckie, R., Aldama, A. A., Wood, E. F.: Modeling the large-scale dynamics of saturated groundwater flow using spatial filtering theory: 2. Numerical evaluation. Water Resources Research 32 (5): 1281 – 1288, 1996.

/BEC 02/   Beckie, R.; Harvery, C.F.: What does a slug test measure: An investigation of instrumenst response and the effects of heterogeneity. WRR, 10.1029/2001WR001072, 2002.

/BEL 96/   Bellin, A., Pannone, M., Fiori, A., Rinaldo, A.: On transport in porous formations characterized by heterogeneity of evolving scales. Water Resources Research 32 (12): 3485 – 3496, 1996.

/BEN 00/   Bennethum, L. S., Murad, M. A., Cushman, J. H.. Macroscale Thermodynamics and the Chemical Potential for Swelling Porous Media. Transport in Porous Media 39, 187 – 225, 2000.

/BER 93/   Berkowitz, B.; Balberg, I.: Percolation theory and ist application to groundwater hydrology. WRR, 29, 775 – 794, 1993.

/BER 06/   Berkowitz, B.; Cortis, A.; Dentz, M.; Scher, H.: Modeling non-Fickian transport in geological formations as a continuous time random walk. Reviews of Geophysics, 44, RG2003, 2006.

/BIR 94/ Birken, K. and Bastian, P.: Dynamic Distributed Data (DDD) in a parallel programming environment, specification and functionality. Citeseer, 1994.

/BIR 00/ Birthler, H.; Fein, E.; Schneider, A.: Validierung von Einzeleffekten in Grundwassermodellen. Gesellschaft für Anlagen- und Reaktorsicherheit (GRS) mbH, GRS-150, Braunschweig 2000.

/BOR 05/ Borzì, A.: On the convergence of the MG/OPT method, HUPAMM, 5(1), 735-736UH, 2005.

/BOR 07/ Borzì, A.: Smoothers for control- and state-constrained optimal control problems, HUComputing and Visualization in Science, 2007.U

/BOU 97/ Bour; Davy: Connectivity of random fault networks following a power law fault length distribution. WRR, 1997.

/BRU 06/ Brunskill, B.: Discussion of an option for geological storage of used nuclear fuel beneath the Williston Basin of Southern Saskatchewan. Summary of Investigations 1: 1 – 8, 2006.

/CAC 90a/ Cacas, M.C.; Ledoux, E.; de Marsily, G.; Barbreau, A.; Calmels, P.; Gaillard, B.; Margritta, R.: Modelling fracture flow with a stochastic discrete fracture network: calibration and validation. 1. The flow model. WRR, 26(3), 479 – 489, 1990.

/CAC 90b/ Cacas, M.C.; Ledoux, E.; de Marsily, G.; Barbreau, A.; Calmels, P.; Gaillard, B.; Margritta, R.: Modelling fracture flow with a stochastic discrete fracture network: calibration and validation. 2. The transport model. WRR, 26(3), 491 – 500, 1990.

/CAI 90/ Cai, Z.. On the finite volume element method. Numer. Math. 58 (1), 713 – 735, 1990.

/CAM 03/ Cameron, C.: Relative effeciency of Gaussian stochastic process sampling procedures. Journal of Computational Physics 192: 546 – 569, 2003.

/CHE 03/ Chen, Z.; Hou, T.Y.: A Mixed Multiscale Finite Element Method for Elliptic Problems with Oscillating Coefficients. Math. Comput. 72, 242 , 541 – 576, 2003.

/CHE 89/ Chew, L.P.. Constrained Delaunay triangulations. Algorithmica 4(1), pp. 97 – 108, 1989.

/CHR 96/ Christie, M. A.: Upscaling for reservoir simulation. Journal of Petroleum Technology 48 (11): 1004 – 1010, 1996.

/COO 92/ Cook, N.. Natural joints in rock: Mechanical, hydraulic and seismic behaviour and properties under normal stress. International Journal of Rock Mechanics and Mining Sciences 29 (3), 198 – 223, 1992.

/CUS 84/ Cushman, J. H.: On unifying the concepts of scale, instrumentation, and stochastics in the development of multiphase transport theory. Water Resources Research 20 (11): 1668 – 1676, 1984.

/CUS 86/ Cushman, J. H.: On measurement, scale, and scaling. Water Resources Research 22 (2): 129 – 134, 1986.

/DAG 84/ Dagan, G.: Solute transport in heterogeneous porous formations. Journal of Fluid Mechanics 145: 151 – 157, 1984.

/DAG 88/ Dagan, G.: Time-dependent macrodispersion for solute transport in anisotropic heterogeneous aquifers. Water Resources Research 24 (9): 1491 – 1500, 1988.

/DAG 89/ Dagan, G.: Flow and transport in Porous Formations. Springer-Verlag, New York, 1989.

/DAG 90/ Dagan, G.: Transport in heterogeneous porous formations: Spatial moments, ergodicity, and effective dispersion. Water Resources Research 26 (6): 1281 – 1290, 1990.

/DAG 91/   Dagan, G.: Dispersion of passive solutes in non ergodic transport by steady velocity fields in heterogeneous formations. Journal of Fluid Mechanics 233: 197 – 210, 1991.

/DAG 94/   Dagan, G.: The significance of heterogeneity of evolving scales to transport in porous formations. Water Resources Research 30 (12): 3327 – 3336, 1994.

/DAV 93/   Davy, P.: On the Frequency-Length Distribution of the San Andreas Fault System. Journal of Geophysical Research Letters 98 (No. B7): 12,141 – 12,151, 1993.

/DEB 00/   de Berg, M., van Kreveld, M., Overmars, M., Schwarzkopf, O.. Computational Geometry, Springer-Verlag, pp. 45-61, 2000.

/DEG 54/   De Groot, S., Mazur, P.. Non-Equilibrium Thermodynamics, 2nd reprint. North-Holland Publishing Company, 1954.

/DEN 97/   Dentz, M.: Zeitverhalten von Transportkoeffizienten in heterogenen porösen Medien. Diploma thesis, University of Heidelberg, Germany, 1997.

/DEN 00a/   Dentz, M., Kinzelbach, H., Attinger, S., Kinzelbach, W: Temporal behaviour of a solute cloud in a heterogeneous porous medium: 1. Point-like injection. Water Resources Research 36 (12): 3591 – 3604, 2000.

/DEN 00b/   Dentz, M., Kinzelbach, H., Attinger, S., Kinzelbach, W: Temporal behaviour of a solute cloud in a heterogeneous porous medium: 2. Spatially extended injection. Water Resources Research 36 (12): 3605 – 3614, 2000.

/DEN 02/   Dentz, M., Kinzelbach, H., Attinger, S., Kinzelbach, W: Temporal behaviour of a solute cloud in a heterogeneous porous medium: 3. Numerical simulations. Water Resources Research 38 (7), doi: 10.1029/2001WR000436: 23.1 – 23.13, 2002.

/DEN 03/   Dentz, M., Kinzelbach, H., Attinger, S., Kinzelbach, W: Numerical studies of the transport behaviour of a passive solute cloud in a two-dimensional incompressible random flow field. Physical Review E 67 (Nr. 046306): 1 – 10, 2003.

/DES 92/   Desbarats, A. J.: Spatial averaging of transmissivity in heterogenepous fields with flow toward a well. Water Resources Research 28 (3): 757 – 767, 1992.

/DES 94a/   Desbarats, A. J., Bachu, S.: Geostatistical analysis of aquifer heterogeneity from the core scale to the basin scale: A case study. Water Resources Research 30 (3): 673 – 684, 1994.

/DES 94b/   Desbarats, A. J.: Spatial averaging of hydraulic conductivity under radial flow conditions. Mathematical Geology 26 (1): 1 – 21, 1994.

/DEU 94/   Deutsch, C. V., Journel, A. G.: Integrating well test-derived effective absolute permeabilities in geostatistical reservoir modeling. Chapter 12 in CA3: Stochastic Modeling and Geostatistics ed. by Yarus, J. M. and R. L. Chambers. The American Association of Petroleum Geologists, 131 – 142, 1994.

/DIE 05/   Diersch, H.-J.-G., Kolditz, O.. Variable-density flow and transport in porous media: approaches and challenges. In: Wasy Software FEFLOW© - Finite Element Subsurface flow and Transport Simulation System. Vol. 2. Wasy GmbH, 2005.

/DIF 97/   Di Federico, V., Neuman, S. P.: Scaling of random fields by means of truncated power variograms and associated spectra. Water Resources Research 33 (5): 1075 – 1085, 1997.

/DUR 96/   Durlofsky, L. J., Behrens, R. A., Jones, R. C., Bernath, A.: Scale up of heterogeneous three dimensional reservoir descriptions. SPE Journal 1 (3): 313 – 326, 1996.

/DUR 97/   Durlofsky, L. J., Jones, R. C., Milliken, W. J.: A nonuniform coarsening approach for the scale-up of displacement processes in heterogeneous porous media. Advances in Water Research 20 (5-6): 335 – 347, 1997.

/EBE 04/ Eberhard, J.; Attinger, S.; Wittum, G.: Coarse graining for upscaling of flow in heterogeneous porous media. Multiscale Model. Simul. 2 (2), 269 – 301, 2004.

/EBE 05/ Eberhard, J.: Simulation of lognormal random fields with varying resolution scale and local average for Darcy flow. Comput. Vis. Sci. 8, 4, 2005.

/EFE 00/ Efendiev, Y., Durlofsky, L. J., Lee, S. H.: Modeling of subgrid effects in coarse-scale simulations of transport in heterogeneous porous media. Water Resources Research 36 (8): 2031 – 2041, 2000.

/ELD 67/ Elder, J.. Transient convection in a porous medium. J. Fluid Mech. 27, pp. 609 – 623, 1967.

/ELL 97/ Elliott, F. W. Jr., Horntrop, D. J., Majda, A. J.: A Fourier-wavelet Monte Carlo method for fractal random fields. Journal of Computational Physics 132 (2): 384 – 408, 1997.

/ENG 03/ Engquist, W.E.; Engquist, B.: The heterogeneous multi-scale method. Comm. Mat. Science, 1, 87 – 133, 2003.

/FEI 99/ Fein, E.; Schneider, A. (eds.): d^{3}f - ein Programmpaket zur Modellierung von Dichteströmungen. Abschlussbericht. Gesellschaft für Anlagen- und Reaktorsicherheit (GRS) mbH, GRS-139, Braunschweig 1999.

/FEI 04/ Fein, E. (ed.): Software Package r^{3}t. Model for Transport and Retention in Porous Media. Gesellschaft für Anlagen- und Reaktorsicherheit (GRS) mbH, GRS-192, Braunschweig 2004.

/FEI 08/ Fein, E.; Kröhn, K.-P.; Noseck, U.; Schneider, A.: Modelling of field-scale pollutant transport. Gesellschaft für Anlagen- und Reaktorsicherheit (GRS) mbH, GRS-231, Braunschweig 2008.

/FIO 01/ Fiori, A.: On the influence of local dispersion in solute transport through formations with evolving scales of heterogeneity. Water Resources Research 37 (2): 235 – 242, 2001.

/FLU 09/ Flügge, J., Radionuclide Transport in the Overburden of a Salt Dome – The Impact of Extreme Climate States, Verlag Dr.Hut, München (2009) 209 p.

/FRE 75/ Freeze, R. A.: A stochastic-conceptual analysis of one-dimensional groundwater flow in nonuniform homogeneous media. Water Resources Research 11 (5): 725 – 741, 1975.

/FRO 96a/ Frolkovič, P., Finite volume discretization of density driven flows in porous media. In "Finite Volumes for Complex Applications" (Benkhaldoun F., Vilsmeier, R., Eds.), Hermes, Paris, 433 – 440, 1996.

/FRO 96b/ Frolkovič, P., Knabner, P.. Consistent velocity approximations in finite element or volume discretizations of density driven flow. In: Aldama, A. A., et al. (Eds.), Computational Methods in Water Resources XI. Computational Mechanics Publication, Southhampten, pp. 93–100, 1996.

/FRO 98a/ Frolkovič, P., Consistent velocity approximation for density driven flow and transport. In: Van Keer, R., at al. (Eds.), Advanced Computational Methods in Engineering, Part 2: Contributed papers. Shaker Publishing, Maastricht, pp. 603 – 611, 1998.

/FRO 98b/ Frolkovič, P., Maximum principle and local mass balance for numerical solutions of transport equation coupled with variable density flow. Acta Mathematica Universitatis Comenianae 1 (68), 137 – 157, 1998.

/GEL 83/ Gelhar, L. W., Axness, C. L.: Three-dimensional stochastic analysis of macrodispersion in aquifers. Water Resources Research 19 (1): 161 – 180, 1983.

/GEL 86/ Gelhar, L. W.: Stochastic subsurface hydrology: From theory to applications. Water Resources Research 22 (9): 135S – 145S, 1986.

/GEL 93/ Gelhar, L. W.: Stochastic Subsurface Hydrology, Prentice Hall, Englewood Cliffs, New Jersey, 1993.

/GER 93/ Gerke, H.H.; van Genuchten, M.T.: Evaluation of a First-Order Water Transfer Term for Variably Saturated Dual-Porosity Flow Models. WRR, 29(4), 1225 – 1238, 1993.

/GEU 09/ Geuzaine C. and Remacle J.-F.. Gmsh: a three-dimensional finite element mesh generator with built-in pre- and post-processing facilities. International Journal for Numerical Methods in Engineering 79(11), 1309 – 1331, 2009.

/GRA 07/ Gradshteyn, I. S., Ryzhik, I. M.: Table of Integrals, Series and Products. Elsevier, Amsterdam, 2007.

/GRA 05/ Graf, T., Therrien, R.. Variable-density Groundwater Flow and Solute Transport in Porous Media Containing Nonuniform Discrete Fractures. Adv. Water Resour. 28, 1351 – 1367, 2005.

/GRA 09/ Graf, T., Therrien, R.. Stable-unstable flow of geothermal fluids in fractured rock. Geofluids 9, 138 – 152, 2009.

/GRA 01/ Granet, S., Fabrie, P., Lemmonier, P., Quintard, M.: A two-phase flow simulation of a fractured reservoir using a new fissure element method. Journal of Petroleum Science and Engineering 32: 35 – 52, 2001.

/GRA 82/ Gray, W. G.. Derivation of vertically averaged equations describing multiphase flow in porous media. Water Resources Research 18, 1705 – 1712, 1982.

/GRA 83/ Gray, W. G.. Constitutive Theory for Vertically Averaged Equations Describing Steam-Water Flow in Porous Media. Water Resources Research 19, 1501 – 1510, 1983.

/GRI 10/ Grillo, A., Logashenko, D., Stichel, S., Wittum, G.. Simulation of Density-Driven Flow in Fractured Porous Media. Adv. Water Resour., 33(12), 1494 – 1507, 2010.

/GRI 12a/ Grillo, A., Lampe, M., Logashenko, D., Stichel, S., Wittum, G.. Simulation of salinity- and thermohaline-driven flow in fractured porous media. Journal of Porous Media 15 (5), 439 – 458, 2012.

/GRI 12b/ Grillo, A., Logashenko, D., Stichel, S., Wittum, G.. Forchheimers corrections in modelling flow and transport in fractured porous media. Comput. Vis. Sci. (accepted), 2012.

/GRI 13/ Grillo, A., Logashenko, D., Stichel, S., Wittum, G.. Forchheimers corrections in modelling flow and transport in fractured porous media. Comput. Vis. Sci. (accepted), 2013.

/GRO 99/ Gropp, W.; Lusk, E.; Skjellum, A.: Using mpi: portable parallel programming with the message passing interface, 1999.

/HAC 85/ Hackbusch, W., Multi-grid methods and applications, vol. 4 of springer series in computational mathematics, 1985.

/HAE 92/ Häfner, F., Sames, D., Voigt, H.-D.: Wärme- und Stofftransport: mathematische Methoden. Berlin: Springer, 1992.

/HAR 00/ Harter, T., Wagner, S.. Colloid transport and filtration of *Cryptosporidium parvum* in sandy soils and aquifer sediments. Environ. Sci. Technol. 34, 62 – 70, 2000.

/HAR 92/ Harvey, C. F.: Interpreting parameter estimates obtained from slug tests in heterogeneous aquifers. M. S. Thesis, Stanford University, Department of Applied Earth Sciences, 1992.

/HAS 89a/ Hassanizadeh, S. M., Gray, W. G.. Boundary and Interface Conditions in Porous Media. Water Resources Research 25 (7), 1705 – 1715, 1989.

/HAS 89b/ Hassanizadeh, S. M., Gray, W. G.. Derivation of Conditions Describing Transport Across Zones of Reduced Dynamics Within Multiphase Systems. Water Resources Research 25, 529 – 539, 1989.

/HAZ 02/ Hazra, S. B.; Schulz, V.: Numerical Parameter Identification in Multiphase Flow through Porous Media. Computing and Visualization in Science, Vol. 5, pp. 107 – 113, 2002.

/HEL 05/ Held, R., Attinger, S., Kinzelbach, W.: Homogenization and effective parameters for the Henry problem in heterogeneous formations. Water Resources Research 41: W11420, doi:10.1029/2004WR003674, 2005.

/HEN 00/ Henn, N., Bourbiaux, B., Quintard, M., Sakthikumar, S.: Modelling fluid flow in reservoirs crossed by multiscale fractures: a new approach. 7th European Conference on the Mathematics of Oil Recovery, ECMOR7, Baveno, Lago Maggiore, Italy, 5-8 September 2000: 1 – 16.

/HEN 64/ Henry, H. R.. Effects of dispersion on salt encroachment in coastal aquifers. In: Sea water in coastal aquifers. USGS Water Supply Paper 1613-C, pp. 70 – 84, 1964.

/HEP 12/ Heppner, I.; Lampe, M.; Nägel, A.; Reiter, S.; Rupp, M.; Vogel, A.; Wittum, G.: Software Framework ug4: Parallel Multigrid on the Hermit Supercomputer. High Performance Computing in Science and Engineering '12, Transactions of the High Performance Computing Center, Stuttgart (HLRS) 2012, Nagel, W. E.; Kröner, D. H.; Resch, M. M. (Editors), pp. 435 – 449, Springer Heidelberg New York Dordrecht London, in press, Springer-Verlag Berlin Heidelberg, 2013.

/HES 13/ Heße, F., Prykhod'ko, V., Schlüter, S., Attinger, S.: On the numerical simulation of random fields with a truncated power-law variogram. 2013. In review.

/HES 90/ Hestir, K.; Long, J.: Analytical expressions fort he permeabilit of random two-dimensional Poisson fracture networks based on regular lattice percolation and equvalent media theories. J. of Geophysical Search, 95(B13),1990.

/HOF 11/ Hoffer, M., Poliwoda, P., Wittum, G.. Visual Reflection Library – A Framework for Declarative GUI Programming on the Java Platform. Computing and Visualization in Science, 2011, in press.

/HOR 96/   Hornung, U.: Models for flow and transport through porous media derived by homogenization. Institute for Mathematics and Ist Applications, Vol. 79, p. 201, 1996.

/HOT 02/   Hoteit, H., Mose, R., Younes, A., Lehmann, F., Ackerer, P.. Three-dimensional modeling of mass transfer in porous media using the mixed hybrid finite elements and the random-walk methods. Mathe. Geology 34 (4), 435 – 456, 2002.

/HOU 97/   Hou, T.Y.; Wu, X-H.: A Multiscale Finite Element Method for Elliprtic Problems in Composite Materials and Porous Media. J. of Computational Physics, 134, 169 – 189, 1997.

/HUY 83a/   Huyakorn, P.S.; Lester, B.H.; Faust, C.: Finite Element Techniques for Modlling Ground Water Flow in Fractured Aquifers. WRR, 19(4), 1019 – 1035, 1983.

/HUY 83b/   Huyakorn, P.S.; Lester, B.; Mercer, J.W.: An efficient finite-element technique for modelling transport in fractured porous media. 1. Single species transport. WRR, 19(3), 841 – 854, 1983.

/ITO 51/   Ito, K.. On stochastical differential equations. American Mathematical Society 4, 289 – 302, 1951.

/JAE 07/   Jaeger, J., Cook, N., Zimmerman, R.. Fundamentals of Rock Mechanics, 4th Edition. Blackwell Publishing, Malden, MA, 2007.

/JAN 99/   Jansen, D.: Identifikation des Mehrkontinuum-Modells zur Simulation des Stofftransportes in multiporösen Festgesteinsaquiferen. Bericht IWW, RWTH Aachen, 1999.

/JEN 03/   Jenny, P.; Lee, S.H.; Tchelepi, H.: Multi-scale finite-volume method for elliptic problems in subsurface flow simulations. J. Computational Physics, 187(1), 47 – 67, 2003.

/JOH 02/   Johannsen, K.. The Elder problem - Bifurcations and steady state solutions. In: Hassanizadeh, S.M., et al. (ed.) Comptational Methods in Water Resources, vol. 47(1), pp. 485 – 492, 2002.

/JOH 03/   Johannsen, K.. On the validity of the Boussinesq approximation for the Elder problem. Comput. Geosci. 7(3), 169 – 182, 2003.

/JOH 06a/   Johannsen,K.: A Symmetric Smoother for the Nonsymmetric Interior Penalty Discontinuous Galerkin Discretization. Numerical Linear Algebra with Applications. to appear, 2006.

/JOH 06b/   Johannsen, K.: Multigrid Methods for Nonsymmetric Interior Penalty Discontinuous Galerkin Methods. Computing and Visualization in Science. to appear, 2006.

/JOH 95/   Johnson, W. P., Blue, K. A., Logan, B. E.. Modeling bacterial detachment during transport through porous media as a residence-time-dependent process. Water Resour. Res. 31, 2649 – 2658, 1995.

/JUT 08/   Juanes, R., Tchelepi, H. A..: Special Issue on multiscale methods for flow and transport in heterogeneous porous media. Computational Geosciences 12 (3): 255 – 256, 2008.

/KAL 07/   Kalbacher, T., Mettier, R., McDermott, C., Wang, W., Kosakowski, G., Taniguchi, T., Kolditz, O.. Geometric modelling and object-oriented software concepts applied to a heterogeneous fractured network from the grimsel rock laboratory. Computational Geosciences 11, 9 – 26, 2007.

/KAR 95/   Karimian, S. M., Schneider, G. E.. Pressure-based control-volume finite element method for flow at all speeds. AIAA Journal 33 (9), 1611 – 1618, 1995.

/KEM 94/   Kempers, L. J. T. M., Haas, H.: The dispersion zone between fluids with different density and viscosity in a heterogeneous porous medium. Journal of Fluid Mechanics 267: 299 – 324, 1994.

/KEE 05/   Keesmann, S.; Noseck, U.; Buhmann, D.; Fein, E., Schneider, A.: Modell-rechnungen zur Langzeitsicherheit von Endlagern in Salz- und Granitforma-tionen. FKZ-02 E 9239. Ges. f. Anlagen- und Reaktorsicherheit (GRS) mbH, GRS-206, Braunschweig 2005.

/KEV 03/   Kevrekidis,I.G.; Hummer, G.: Coarse molecular dynamics of a peptide fragment: free energy, kinetics, and long time dynamics computations. J. Cem. Phys., 118(23), 10762 – 10773, 2003.

/KIM 04/   Kim, J., Schwartz, F. W., Smith, L., Ibaraki, M.: Complex dispersion in sim-ple fractured media. Water Resources Research 40: W05102, 2004.

/KIN 86/   Kinzelbach, W.. Groundwater Modelling. Elsevier, Amsterdam, 1986.

/KIN 88/   Kinzelbach, W.. The random-walk method in pollutant transport simulation. NATO ASI Ser Ser. (C224), 227 – 246, 1988.

/KIT 88/   Kitanidis, P. K.: Prediction by the method of moments of transport in a het-erogeneous formation. Journal of Hydrology 102: 453 – 473, 1988.

/KOL 95a/   Kolditz, O.. Modelling flow and heat transfer in fractured rocks: Conceptual model of a 3-d deterministic fracture network. Geothermics 24 (3), 451 – 470, 1995 a.

/KOL 95b/   Kolditz, O.. Modelling flow and heat transfer in fractured rocks: dimensional effect of matrix heat diffusion. Geothermics 24 (3), 421 – 437, 1995 b.

/KOE 00/   Köngeter, J.; Lagendijk, V.; Jansen, D.; Vogel, T.: Forschungsvorhaben bei der DFG: Festgesetins-Aquiferanalog: Experimente und Modellierung, Teil-projekt 4 – Arbeitsbericht – 2. Projektphase: Einsatz von äquivalenten Mo-dellansätzen (Ko 1573/2-2). Aachen: Lehrstuhl und Institut für Wasserbau und Wasserwirtschaft der RWTH Aachen, 2000.

/KOS 96/   Kosakowski G.: Modellierung von Strömungs- und transportprozessen in geklüfteten Medien: Vom natürlichen Kluftsystem zum numerischen Gitter-netzwerk. Doctoral Thesis. Fortschritt-Berichte, 7(304), VDI Verlag, Düs-seldorf, 1996.

/KOS 05/ Kosakowski, G., Smith, P.. Modelling the transport of solutes ans colloids in the grimsel migration shear zone. Tech. Rep. 05-03, Paul Scherrer Institut, Villigen, Switzerland, 2005.

/KOS 06/ Kosakowski, G.: Transport in fractured media: Concepts, models, and applications. Habilitationsschrift, Geowissenschaftliche Fakultät, Universität Tübingen, 2006.

/KRA 07/ Kramer, P. R., Kurbanmuradov, O., Sabelfeld, K.: Comparative analysis of multiscale Gaussian random field simulation algorithms. Journal of Computational Physics 226 (1): 897 – 924, 2007.

/KRO 91/ Kröhn, K.-P.: Simulation von Transportvorgängen im klüftigen Gestein mit der Methode der Finiten Elemente. Dissertation, Institut für Strömungsmechanik, Bericht Nr. 29, 1991.

/LAB 96/ LaBolle, E. M., Fogg, G. E., Tompson, A. F. B.. Random-walk simulation of transport in heterogeneous porous media: Local mass-conservation problem and implementation methods. Water Resources Research 32 (3), 583 – 593, 1996. /LAM 07/ Lampe, M.; Wittum, G.: New Benchmarks for massively parallel computing. SiT-Report 11/07, Technische Simulation, Universität Heidelberg, 2007.

/LAN 95a/ Lang, U.; Helmig, R.: Numerical modeling in fractured media – identification of measured field data. In Krasny, J., Groundwater Quality: remediation and Protection, S. 203 – 212, 1995.

/LAN 95b/ Lang, U.: Simulation regionaler Strömungs- und Transportvorgänge in Karstaquiferen mit Hilfe des Doppelkontinuum-Ansatzes: Methodenentwicklung und Parameteridentifikation. Dissertation, Universität Stuttgart,1995.

/LAN 05/ Lang, S., Wittum, G.. Large-scale density-driven flow simulations using parallel unstructured Grid adaptation and local multigrid methods. Concurrency Computat.: Pract. Exper. 17, 1415 – 1440, 2005.

/LOG 01/ Logashenko, D.; Maar, B.; Schulz, V.; Wittum, G.: Optimal geometrical design of Bingham parameter measurement devices. International Series of Numerical Mathematics (ISNM), Vol. 138, pp. 167 – 183, 2001.

/LON 82/ Long, J.C.S.; Remer, J.S.; Wilson, C.R., Witherspoon, P.A.: Porous media equivalents for networks of discontinuous fractures. WRR, 18(3), 1982.

/LON 83/ Long, J.C.S.: Investigation of equivalent porous medium permeability in networks of discontinuous fractures. Technical Report, LBL-16259, Lawrence Berkely Laboratory, 1983.

/LON 85/ Long, J.C.S; Witherspoon, P.A.: The relationship of the degree of interconnection to permeability in fracture networks. J. Geophys. Res., 90B, 3087-3098, 1985.

/LAU 55/ Lauwerier H.A.. The transport of heat into an oil layer caused by the injection of hot fluid, Journal of Applied Sciences Research, Section A, 5(2-3), 145 – 150, 1955.

/MAC 89/ Mackay, D.M.; Cherry, J.A.: Groundwater contamination: Pump-and-treat remediation. Environmental Science & Technology, 23(6), 630-636,1989.

/MAJ 99/ Majda, A. J., Kramer, P. R.: Simplified models for turbulent diffusion: Theory, numerical modelling, and physical phenomena. Physics Report 314 (4-5): 237 – 574, 1999.

/MAL 97/ Malkovsky, V. I., Pek, A. A.. Conditions for the onset of thermal convection of a homogeneous fluid in a vertical fault. Petrology 5, 381 – 387, 1997.

/MAN 68/ Mandelbrot, B. B., van Ness, J. W.: Fractional Brownian motions, fractional noises and applications. SIAM Review 10 (4): 422 – 437, 1968.

/MAR 98/ Margolin, G.; Berkowitz, B.; Scher, H.: Structure, Flow and generalized Conductivity scaling in fracture network. WRR, 98WR01648,34(9), 2103, 1998.

/MAR 06/ Martinez-Landa, L., Carrera, J.. A methodology to interpret crosshole tests in a granite block. Journal of Hydrogeology 325(1-4), 222 – 240, 2006.

/MCC 90/ McComb, W. D., Watt, A. G.: Conditional averaging procedure for the elimination of the small-scale modes from incompressible fluid turbulence at high Reynolds numbers. Physical Review Letters 65 (26): 3281 – 3284, 1990.

/MCD 09/ McDermott, C., Walsh, R., Mettier, R., Kosakowski, G., Kolditz, O.. Hybrid analytical and finite element numerical modeling of mass and heat transport in fractured rocks with matrix diffusion. Computational Geosciences 13 (8), 349 – 361, 2009.

/MCD 06/ McDermott, Cl.: Reservoir engineering and system analysis: Hydraulic, thermal and geomechanical coupled processes in geosystems. Habilitationsschrift, Geowissenschaftliche Fakultät, Universität Tübingen, 2006.

/MCD 07/ McDermott, Cl.; Walsh, R.; Mettier, R.; Kosakowski, G.; Kolditz, O.: Influence of matrix diffusion on mass transport in fractured rock: Application to the Grimsel shear zone. Ground Water, submitted, 2007.

/MET 99/ Metzger, D., Kinzelbach, H., Neuweiler, I., Kinzelbach, W.: Asymptotic transport parameters in a heterogeneous porous medium: Comparison of two ensemble-averaging procedures. Stochastic Environmental Research and Risk Assessment 13 (6): 396 – 415, 1999.

/MIT 03/ Mitani, Y., Esaki, T., Zhou, G., Nakashima, Y.. Experiments and simulation of shear-flow coupling properties of a rock joint. In: Culligan, P., Einstein, H., Whittle, A. (Eds.), Proc. 39th US Rock Mech. Symp. Cambridge. pp. 1459 – 1464, 2003.

/MOL 97/ Molz, F. J., Liu, H. H., Szulga, J.: Fractional Brownian motion and fractional Gaussian noise in subsurface hydrology: A review, presentation of fundamental properties and extensions. Water Resources Research 33 (10): 2273 – 2288, 1997.

/MUH 12/ Muha, I.. Modellierung und Simulation von Biogasreaktoren, Dissertation, Universität Frankfurt, 2012.

/MUR 79/   Murphy, H. D.. Convective Instabilities in Vertical Fractures and Faults. Journal of Geophysical Research 84, 6121 – 6130, 1979.

/MUS 11a/ Musuuza, J. L., Radu, F. A., Attinger, S.: The effect of dispersion on the stability of density-driven flows in saturated homogeneous porous media. Advances in Water Resources 34: 417 – 432, 2011.

/MUS 11b/ Musuuza, J. L., Radu, F. A., Attinger, S.: The stability of density-driven flows in saturated heterogeneous porous media. Advances in Water Resources 34 (11): 1464 – 1482, 2011.

/NAE 10/   Nägel, A.: Schnelle Löser für große Gleichungssysteme mit Anwendungen in der Biophysik und den Lebenswissenschaften. Dissertation, University Heidelberg, 2010.

/NÄG 12/   Nägel, A.: Algebraic multigrid solvers for density driven flow. Enhancement of the Codes d^{3}f and r^{3}t, Chapter 8.2, GRS-Report 292, ISBN 978-3-939355-68-7, 2012.

/NAR 82/   Narasimhan, T.N.: Recent trends in hydrogeology. Symposium on recent trends in hydrogeology; Berkely, CA, USA. Geol. Soc. Am., Spec. Pap.; 189, Geological Society of America, Inc.; Boulder, CO, 1982.

/NEU 90/   Neuman, S. P.: Universal scaling of hydraulic conductivities and dispersivities in geologic media. Water Resources Research 26 (8): 1749 – 1758, 1990.

/NEU 95/   Neuman, S. P.: On advective transport in fractal permeability and velocity fields. Water Resources Research 31 (6): 1455 – 1460, 1995.

/NEU 05/   Neuman, S. P.: Trends, prospects and challenges in quantifying flow and transport through fractured rocks. Hydrogeology Journal 13: 124 – 147, 2005.

/NEU 08/   Neuman, S. P. Riva, M., Guadagnini, A.: On the geostatistical characterization of hierarchical media. Water Resources Research 44: W02403, doi:10.1029/2007WR006228: 1 – 16, 2008.

/NEU 97/   Neunhäuser, L.; Hemminger; Helmig, R.: Festgestein-Aquiferanalog: Experimente und Modellierung, Teilprojekt 3: Einsatz von diskreten Modellansätzen. Fortschrittsbericht zum DFG-Projekt, Institut für Wasserbau, Universität Stuttgart, in Zusammenarbeit mit Fachgebiet für Numerische Methoden und Informationsverarbeitung, Technische Universität Braunschweig, 12/1997. – Nr.:1, Heft 2531/1-1, -05/1996 – 10/1997.

/NEU 99/   Neunhäuser, L.; Hemminger, A.; Helmig, R.: Influence of Fracture-Matrix-Interaction on Flow and Transport Processes and the Resulting Effective Parameters in Fractured Porous Media. In: Hydraulic Engineering for Sustainable Water Resources Management at the Turn of the Millenium. Graz, Austria, 1999.

/NEU 00/   Neunhäuser, L.; Hemminger; Helmig, R.: Festgestein-Aquiferanalog: Experimente und Modellierung, Teilprojekt 3: Einsatz von diskreten Modellansätzen. Arbeitsbericht zum DFG-Projekt 11/1997-03/2000. Institut für Computeranwendungen im Bauingenieurwesen, Technische Universität Braunschweig, 2000.

/NEU 03/   Neunhäuser, L.: Diskretisierungsansätze zur Modellierung von Strömungs- und Transportprozessen in geklüftet-porösen Medien. Mitteilungsheft Nr. 119, Promotionsschrift, Institut für Wasserbau, Universität Stuttgart, ISBN: 3-933761-22-0, 2003.

/NEU 01/   Neuss, N.; Jäger, W.; Wittum, G.: Homogenization and multigrid, Computing, 66 (1), pp. 1 – 26, 2001.

/NOC 06/   Nocedal, J., Wright S.J.: Numerical optimization, Springer, Heidelberg, New York, 2006.

/NOE 00/   Noetinger, B., Estebenet, T.: Up-scaling of double porosity fractured media using continuous-time random walks methods. Transport in Porous Media 39: 315 – 337, 2000.

/NOR 09/   Nordbotton, J. M.: Adaptive variational multiscale methods for multiphase flow in porous media. Multiscale Modelling and Simulation 7 (3): 1455 – 1473, 2009.

/NOS 13/   Noseck, U., Brendler, V., Flügge, J., Stockmann, M., Britz, S., Lampe, M., Schikora, J., Schneider, A.: Realistic integration of sorption processes in transport codes for long-term safety assessments. FKZ 02 E 10518 and 02 E 10528. Gesellschaft für Anlagen- und Reaktorsicherheit (GRS) mbH, GRS-297, Braunschweig, 2013.

/ODE 98/   Oden, J.T.;Babuska, I.; Baumann, C.E.: A discontinuous hp finite element method for diffusion problems. Journal of Computational Physics, v146 n .2., p. 491 – 519, 1998.

/OGA 61/   Ogata, A., Banks, R. B.. A solution of the differential equation of longitudinal dispersion in porous media. Tech. rep., U.S. Geological Survey, Washington, D.C, 1961.

/OLD 98/   Oldenburg, C. M., Pruess, K.. Layered Thermohaline Convection in Hypersaline Geothermal Systems. Transport in Porous Media 33, 29 – 63, 1998.

/OLI 90/   Oliver, D. S.: The averaging process in permeability estimation from well-test data. SPE Formulation Evaluation 5 (3): 319 – 324, 1990.

/PAP 78/   Papanicoulaou, G.; Bensoussan, A.; Lion, J.L.: Asymptotic Analysis for Periodic Structures. North Holland, Amsterdam, 1978.

/PEI 88/   Peitgen, H.-O., Saupe, D. (eds.): The Science of Fractal Images. Springer-Verlag, New York, 1988.

/PHI 86/   Philip, J. R.: Issues in flow and transport in heterogeneous porous media. Transport in Porous Media 1: 319 – 338, 1986.

/PIC 81/   Pickens, J. F., Grisak, G. E: Scale-dependent dispersion in a stratified granular aquifer. Water Resources Research 17 (4): 1191 – 1211, 1981.

/PIG 93/   Piggott, A., Elsworth, D.. Laboratory assessment of the equivalent apertures of a rock fracture. Geophysical Research Letters 20 (13), 1387 – 1390, 1993.

/PRU 85/ Pruess, K.; Narasimhan, T.N.: A practical method for modelling fluid and heat flow in fractured porous media. Society of Petroleum Engineers Journal, 25, 14 – 26, 1985.

/PYR 00/ Pyrak-Nolte, L., Morris, J.. Single fractures under normal stress: The relation between fracture specific stiffness and fluid flow. International Journal of Rock Mechanics and Mining Sciences 37, 245 – 262, 2000.

/QUE 07/ Queisser, G.: Simulation of Signal Processing in Neurons, Dissertation, Mathematik, Universität Heidelberg, 2007.

/RAJ 93a/ Rajaram, H., Gelhar, L. W.: Plume scale-dependent dispersion in heterogeneous aquifers: 1. Lagrangian Analysis and Three-Dimensional Aquifers. Water Resources Research 29 (9): 3261 – 3276, 1993.

/RAJ 93b/ Rajaram, H., Gelhar, L. W.: Plume scale-dependent dispersion in heterogeneous aquifers: 2. Eulerian Analysis in a Stratified Aquifer. Water Resources Research 29 (9): 3249 – 3260, 1993.

/REE 08a/ Reeves, D. M., Benson, D. A., Meerschaert, M. M.: Transport of conservative solutes in simulated fracture networks: 1. Synthetic data generation. Water Resources Research 44, W05404, doi: 10.1029/2007WR006069, 2008.

/REE 08b/ Reeves, D. M., Benson, D. A., Meerschaert, M. M., Scheffler, H.-P.: Transport of conservative solutions in simulated fracture networks: 2. Ensemble solute transport and the correspondence to operator-stable limit distributions. Water Resources Research 44, W05410, doi: 10.1029/2008WR006858, 2008.

/REI 04/ Reisiger, C.; Wittum, G.: Multigrig methods for anisotropic equations and variational inequalities. Computing and Vizualisation in Science, 7(3-4), 189 – 197, 2004.

/REI 12a/ Reiter, S.; Vogel, A.; Heppner, I.; Rupp, M.; Wittum, G.: A massively parallel geometric multigrid solver on hierarchically distributed grids. Comp. Vis. Sci., in press, 2012.

/REI 12b/   Reiter, S., Logashenko, D., Stichel, S., Wittum, G., Grillo, A.. Models and simulations of variable-density flow in fractured porous media. Int. J. Computational Science and Engineering (in print), 2012.

/REI 13/   Reiter, S., Wittum, G.. 'ProMesh – a flexible interactive meshing software for unstructured hybrid grids in 1, 2 and 3 dimensions'. (in preparation), 2013.

/REN 97/   Renard, PH.; de Marsily, G.: Calculating the equivalent permeability: a review. Advances in Water Resources, 20(5-6), 253 – 278, 1997.

/REN 99/   Renshaw, C. E.: Connectivity of joint networks with power law length distributions, Water Resources Research 35 (No. 9): 2661 – 2670, 1999.

/RIT 04/   Ritzi, R. W., Dai, Z., Dominic, D. F. Rubin, Y. N.: Spatial correlation of permeability in cross-stratified sediment with hierarchical architecture. Water Resources Research 40: W03513, doi:10.1029/2003WR002420: 1 – 14, 2004.

/RUB 99/   Rubin, Y., Sun, A. Maxwell, R. Bellin, A.: The concept of block-effective macrodispersivity and a unified approach for grid-scale- and plume-scale-dependent transport. Journal of Fluid Mechanics 395: 161 – 180, 1999.

/RUG 87/   Ruge, J. W.; Stüben, K., Multigrid Methods, volume 3 of Frontiers in Applied Mathematics, chapter Algebraic multigrid (AMG), pages 73 – 130. SIAM, Philadelphia, PA, 1987.

/SCH 74/   Scheidegger, A. E.. The Physics of Flow through Porous Media, 3rd Edition. University of Toronto Press, Toronto, 1974.

/SCH 04a/   Schneider, A.; Birthler, H.: Modellrechnungen zur großräumigen dichteabhängigen Grundwasserbewegung. Gesellschaft für Anlagen- und Reaktorsicherheit (GRS) mbH, GRS-191, Braunschweig 2004.

/SCH 12/   Schneider, A., Enhancement of the codes d^{3}f and r^{3}t, GRS, Braunschweig 292, 2012.

/SCH 06/ Schneider, C.; Attinger, S.: Beyond Thiem – submitted to WRR, 2006.

/SCH 07a/ Schneider, C.; Attinger, S.: Beyond Thiem – Interpretation of large scale pumping tests in heterogeneous porous formations, WWR accepted, 2007.

/SCH 98/ Schulz, V.; Wittum, G.: Multigrid optimization methods for stationary parameter identification problems in groundwater flow. In Hackbusch, W., Wittum, G. (eds.): Multi-Grid Methods V. Lecture Notes in Computational Science and Engineering, Vol. 3, Springer, Heidelberg, 1998.

/SCH 04b/ Schulz, V.: Simultaneous solution approaches for large optimization problems, Journal for Computational and Applied Mathematics, Vol. 164-165, pp. 629 – 641, 2004.

/SCH 07b/ Schulz, V.; Wittum, G.: Transforming smoothers for Optimization Saddle-point Problems. Comput Vis Sci, to appear, 2007.

/SCH 83/ Schwartz, F.W.; Smith, L.; Crowe, A.S.: A Stochastic Analysis of Macroscopic Dispersion in Fractured Media. WRR; 19(5), 1253 – 1265, 1983.

/SCU 10/ Suciu, N.: Spatially inhomogeneous transition probabilities as memory effects for diffusion in statistically homogeneous random velocity fields. Physical Review E 81 Nr. 056301: 1 – 7, 2010.

/SDG 54/ Scheidegger, A. E.: Statistical hydrodynamics in porous media. Journal of Applied Physics 25 (8): 994 – 1001, 1954.

/SHA 09/ Sharp, J. M. J., Shi, M.. Heterogeneity effects on possible salinity-driven free convection in low-permeability strata. Geofluids 34, 263 – 274, 2009.

/SHI 98/ Shikaze, S. G., Sudicky, E. A., Schwartz, F. W.. Density-dependent solute transport in discretely-fractured geologic media: is prediction possible? Journal of Contaminant Hydrogeology 34, 273 – 291, 1998.

/SI 04/ Si H.. TetGen, A Quality Tetrahedral Mesh Generator and Three-Dimensional Delaunay Triangulator, v1.3 User's Manual. WIAS Technical Report No. 9, 2004.

/SIM 04/   Simpson, M., Clement, T.. Improving the worthiness of the Henry problem as a benchmark for density-dependent groundwater flow models. Water Resources Research 40, 2004.

/SMI 84/   Smith, L.; Schwartz, F.W.: Analysis of the Influence of Fracture Geometry on Mass Transport in Fractured Media. WRR, 20(9), 1241 – 1252, 1984.

/SNO 65/   Snow, D.T.: A prallel plate modell of fractured permeable media. Dissertation, Institut für Wasserbau, Universität Stuttgart, 1965.

/SOR 01/   Sorek, S., Borisov, V., Yakirevich, A.. A two-dimensional Areal Model for Density Dependent Flow Regime. Transport in Porous Media 43, 87 – 105, 2001.

/SPO 86/   Sposito, G., Jury, W., Gupta, V. K.: Fundamental problems in the stochastic convection-dispersion model of solute transport in aquifers and field soils. Water Resources Research 22 (1): 77 – 88, 1986.

/STI 12/   Stichel, S., Logashenko, D., Grillo, A., Reiter, S., Lampe, M., Wittum, G.. Numerical Methods for Flow in Fractured Porous Media. Accepted for publication in J. M. P. Q. Delgado (ed.), Heat and Mass Transfer in Porous Media, Advanced Structured Materials 13, 83 – 113, Springer-Verlag, 2012.

/STR 82/   Strack, O.D.L.. Assessment of effectiveness of geologic isolation systems. Analytic modeling of flow in a permeable fissured medium. Technical report, Pacific Northwest Lab., Richland, WA, 1982.

/SUD 86/   Sudicky, E. A.: A natural-gradient experiment on solute transport in a sand aquifer: spatial variability of hydraulic conductivity and its role in the dispersion process. Water Resources Research 22 (13): 2069 – 2082, 1986.

/TAR 00/   Tartakovsky, D. M., Guadagnini, A., Guadagnini, L.: Effective hydraulic conductivity and transmissivity for heterogeneous aquifers (Short Note). Mathematical Geology 32 (6): 571 – 579, 2000.

/TEN 09/ Tenzer, H., Park, C.-H., Kolditz, O.and McDermott, C.. Application of the geomechanical facies approach and comparison of exploration and evaluation methods used at soultz-sous-forets (france) and spa urach (germany) geothermal sites. Environmental Earth Sciences, 1 – 28, 2009.

/TEU 88/ Teutsch G.: Grundwassermodelle im Karst: Praktische Ansätze am Beispiel zweier Einzugsgebiete in Tiefen und Seichten Malmkarst der Schwäbischen Alb. Dissertation, Universität Tübingen, 1988.

/THA 98/ Thauvin, F., Mohanty, K.K.. Network modeling of non-darcy flow through porous media. Transport in Porous Media 31, pp. 19 – 37, 1998.

/TID 99a/ Tidwell, V. C., Gutjahr, A. L., Wilson, J. L.: What does an instrument measure? Empirical spatial weighting functions calculated from permeability data sets measured on multiple sample supports. Water Resources Research 35 (1): 43 – 54, 1999.

/TID 99b/ Tidwell, V. C., Wilson, J. L.: Upscaling Experiments conducted on block of volcanic tuff: Results for a bimodal permeability distribution. Water Resources Research 35 (11): 3375 – 3387, 1999.

/TOM 90/ Tompson, A. F. B., Gelhar, L. W.. Numerical simulation of solute transport in three-dimensional randomly heterogeneous porous media. Water Resources Research 26 (10), 2451 – 2562, 1990.

/TRA 02/ Trangenstein, J. A.: Multi-scale iterative techniques and adaptive mesh refinement for flow in porous media. Advences in Water Resources 25: 1175 – 1213, 2002.

/VAN 81/ van Genuchten, M.. Analytical solutions for chemical transport with simultaneous adsorption, zero-order production and first order decay. Journal of Hydrology 49, 213 – 233, 1981.

/VEL 70/ Vela, S., McKinley, R. M.: How areal heterogeneities affect pulse-test results. SPE Journal 10 (2): 181 – 191, 1970.

/VOG 10/   Vogel, A.; Xu, J.; Wittum, G.: A generalization of the vertex-centered finite volume scheme to arbitrary high order. Computing and Visualization in Science, 13, 221 – 228, 2010.

/VOG 12/   Vogel, A.; Reiter, S.; Rupp, M.; Nägel, A.; Wittum, G.: UG4 – A novel flexible software system for simulating PDE based models on high performance computers. Comp. Vis. Sci., in press, 2012.

/VOS 87/   Voss, C., Souza,W.. Variable density flow and solute transport simulation of regional aquifers containing a narrow freshwater-saltwater transition zone. Water Resources Research 26, pp. 2097 – 2106, 1987.

/WAG 00/   Wagner, C.: On the algebraic construction of multilevel transfer operators. Computing, 65:73 – 95, 2000.

/WAR 63/   Warren, J.E.; Root, P.J.: The Behaviour of Naturally Fractured Reservoirs. Society of Petroleum Engineers Journal. Transactions, AIME, 228, 245 – 255, 1963.

/WES 92/   Wesseling, P.: An introduction to multigrid methods. Edwards, 1992.

/WIL 70/   Wilson, C.R.: An investigation for laminar flow in fractured reservoirs. Soc. of Petroleum Engeneers Journal. Transactions, AIME 228, 245 – 255, 1970.

/WIT 80/   Witherspoon, PA.; Wang, JSY.; Iwai, K.; Gale, JE.: Validity of cubic law for fluid flow in a deformable rock fracture. Water Res. Research, Vol. 16 No. 6, pp. 1016 – 24, 1980.

/WIT 03/   Wittum, G.; Schulz, V.; Maar, B.; Logashenko, D.: Numerical methods for parameter estimation in Bingham-fluids. In Jäger, W.; Krebs, H.-J.: (eds.): Mathematics - Key Technology for the Future, pp. 204 – 215, Springer Berlin, Heidelberg, 2003.

/WOL 90/   Wollrath, J.: Ein Strömungs- und Transportmodell für klüftiges Gestein und Untersuchungen zu homogenen Ersatzsystemen. Dissertation, Institut für Strömungsmechanik, Universität Hannover, Bericht Nr.: 28, 1990.

/YAS 06/   Yasuhara, H., Polak, A., Mitani, Y., Grader, A., Halleck, P., Elsworth, D.. Evolution of fracture permeability through fluid-rock reaction under hydro-thermal conditions. Earth and Planetary Science Letters 244, 186 – 200, 2006.

/ZEN 06/   Zeng, Z. Grigg, R, 2006. A criterion for non-darcy flow in porous media. Transport in Porous Media 63, 57 – 69, 2006.

/ZHA 96a/ Zhan, H., Wheatcraft, S. W.: Macrodispersivity tensor for nonreactive solute transport in isotropic and anisotropic fractal porous media: Analytical solutions. Water Resources Research 32 (12): 3461 – 3474, 1996.

/ZHA 96b/ Zhang, Y., Zhang, D.: Nonergodic solute transport in three-dimensional heterogeneous istropic aquifers. Water Resources Research 32 (9): 2955 – 2963, 1996.

/ZHA 97/   Zhang, Y., Zhang, D.: Time-dependent dispersion of nonergodic plumes in two-dimensional heterogeneous aquifers. Journal of Hydrologic Engineer-ing 2: 91 – 94, 1997.

Table of figures

List of tables

A   Notation

The most general notations used in this report are given below. Where different authors used different symbols for the same quantity the referring chapter is also cited.

$\boldsymbol{q}$	flow velocity vector [m s^{-1}]
$\boldsymbol{u}$	flow velocity vector [m s^{-1}] (chapter 3, 5, 7)
V	flow velocity vector [m s^{-1}] (chapter 9, 10)
$\boldsymbol{k}$	permeability tensor [m²]
K	permeability constant [m²]
k	permeability constant [m²] (chapter 9, 10)
ρ	density [kg m^{-3}]
ρ_f	density [kg m^{-3}] (chapter 4)
ρ^{pW}	density of water [kg m^{-3}] (chapter 6, 8)
ρ^{pB}	density of brine [kg m^{-3}] (chapter 6, 8)
μ	viscosity [Pa s]
ϕ	porosity [-]
n	porosity [-] (chapter 9, 10)
τ	tortuosity [-]
ω	solute mass fraction [-] (chapter)
c	volumetric solute concentration [kg m^{-3}] (chapter 3,5,7)
C	volumetric solute concentration [kg m^{-3}] (chapter 9,10)
χ_s	solute mass fraction [-] (chapter 4)
p	hydraulic pressure [Pa]
$\boldsymbol{g}$	gravitational acceleration [m s^{-2}]
D_m	molecular diffusion coefficient [m² s^{-1}]
D_m	molecular diffusion coefficient in the medium [m² s^{-1}] (chapter 6)

D_f	molecular diffusion coefficient in the fracture [m² s⁻¹] (chapter 6)
D	Diffusion coefficient [m² s⁻¹] (chapter 9, 10)
$\boldsymbol{D}$	dispersion tensor [m² s⁻¹]
$\boldsymbol{D^d}$	dispersion tensor [m² s⁻¹] (chapter 8)
D	local dispersion coefficient [m² s⁻¹] (chapter 3, 5, 7)
α^l, α^t	longitudinal & transverse dispersions coefficients [m² s⁻¹] (chapter 6, 8)
α_L, α_T	longitudinal & transverse dispersions coefficients. [m² s⁻¹] (chapter 9, 10)
D_{11}, D_{22}	longitudinal & transverse dispersions coefficients [m² s⁻¹] (chapter 3, 5, 7)
$\widetilde{(...)}$	Fourier transformed variables
$\widehat{(...)}$	quantities related to fractal media
CL	correlation length [m]
D^{ens}, D^{eff}	ensemble & effective dispersion coefficients, resp. [m² s⁻¹]
D_{11}, D_{22}	longitudinal & transverse dispersions coefficients, resp. [m² s⁻¹]
$D^{ens,\ CG}, D^{eff,\ CG}$	grid-size dependent dispersion coefficients [m² s⁻¹]
$\mathbf{x}$	vector of coordinates in j dimensions [m]
$\mathbf{k}$	vector of spatial coordinates in the Fourier space [m⁻¹]
$f = \ln(K(\mathbf{x}))$	log-normally distributed hydraulic conductivity [m s⁻¹]
$C^{ff}(\mathbf{x})$	correlation function [-]
$p_i(\mathbf{k})$	projector, ensures the incompressibility of the flow [-]
$\theta(t)$	Heaviside step function [-]
$c(\mathbf{x}, t)$	spatial concentration distribution of the solute [kg m⁻³]
$v = \mathbf{u}/\phi$	specific discharge of the groundwater [m s⁻¹]
σ_{ff}^2	variance of the velocity fluctuations [-]
λ	characteristic length scale related to fractal media [m]
ℓ	correlation scale [m]
$\hat{L}$	correlation scale in fractal media [m]
$\ell_{\langle f \rangle}$	scale-dependent correlation length [m]

$\hat{L}_{\langle f \rangle}$	scale-dependent correlation length in fractal media [m]
τ_u, τ_D	advective & dispersive timescales, resp. [s]
$\epsilon = \dfrac{\tau_u}{\tau_D}$	inverse Peclet number [-]
d	Euclidean dimension [-]
d_f	fractal dimension [-]
H	Hurst coefficient [-]
β	degree of fractality [-]
ξ	spatial filter width [m]
ω	a constant depending on the minimum fracture length [-]
a	power-law exponent
ADE	advection-dispersion-equation
FADE	fractional advection-dispersion-equation

B Explicit expressions for the dispersion coefficients without coarse graining for finite correlation lengths

In this appendix, the explicit expressions in media characterised by finite correlation lengths of the heterogeneities in an isotropic situation are listed as defined in /DEN 00a/.

B.1 Longitudinal ensemble dispersion coefficient

The longitudinal ensemble dispersion coefficient has the form:

$$\delta^{uu}\{D_{11}^{ens}(t)\} \tag{13.1}$$

$$= \bar{u}\,\ell\,\sigma_{ff}^2\,\sqrt{\frac{\pi}{2}}\left\{ \text{erf}(s(T)) + \frac{1}{\sqrt{\pi}}\exp(-s^2(T)) \right.$$

$$\cdot\left[\frac{1}{s(T)} + \frac{4\varepsilon^2 h(T)}{s^2(T)} - \frac{3}{2s^3(T)}\right] + \text{erf}(s(T))$$

$$\cdot\left[\frac{4\varepsilon^2 h(T)}{s(T)} + \frac{8\varepsilon^4 h(T)}{s(T)} - \frac{1}{s^2(T)} - \frac{2\varepsilon^2 h(T)}{s^3(T)} + \frac{3}{4s^4(T)}\right] - 8\varepsilon^4$$

$$\left. \cdot\exp\left(\frac{1}{2\varepsilon^2}\right)\left[\text{erfc}\left(\frac{1}{\sqrt{2\varepsilon^2}}\right) - \text{erfc}(h(T))\right] - \frac{4\sqrt{8}\varepsilon}{3\sqrt{\pi}} - \frac{4\sqrt{8}\varepsilon^3}{\sqrt{\pi}} \right\}$$

with σ_{ff}^2 denoting the variance of the log-hydraulic conductivity and

$$\tau_u = \frac{\ell}{\bar{u}}; \quad \tau_D = \frac{\ell^2}{D}; \quad \varepsilon = \frac{\tau_u}{\tau_D} \tag{13.2}$$

$$h(T) = \frac{1}{\sqrt{2}}\frac{\frac{1}{\varepsilon}+\frac{t}{\tau_u}}{\sqrt{1+\frac{2t}{\tau_D}}}; \quad s(T) = \frac{1}{\sqrt{2}}\frac{\frac{t}{\tau_u}}{\sqrt{1+\frac{2t}{\tau_D}}} \tag{13.3}$$

B.2 Transverse ensemble dispersion coefficient

The transverse component of the ensemble dispersion coefficient reads:

$$\delta^{uu}\{D_{22}^{ens}(t)\} = \bar{u}\,\ell\,\sigma_{ff}^2\sqrt{\frac{\pi}{8}}\left\{\frac{1}{\sqrt{2\pi}}\exp\left(-s^2(T)\right)\left[-\frac{8\varepsilon^2 h(T)}{s^2(T)}+\frac{3}{s^3(T)}\right]\right.$$

$$+\,\mathrm{erf}\big(s(T)\big)$$

$$\cdot\left[-\frac{2\varepsilon^2 h(T)}{s(T)}-\frac{8\varepsilon^4 h(T)}{s(T)}+\frac{1}{2s^2(T)}-\frac{2\varepsilon^2 h(T)}{s^3(T)}-\frac{3}{4s^4(T)}\right]$$

$$-\,(8\varepsilon^4-2\varepsilon^2)\exp\left(\frac{1}{2\varepsilon^2}\right)\left[\mathrm{erfc}\big(h(T)\big)-\mathrm{erfc}\left(\frac{1}{\sqrt{2}\varepsilon}\right)\right]+\frac{\sqrt{8}\varepsilon}{3\sqrt{\pi}}$$

$$\left.+\,\frac{4\sqrt{8}\varepsilon^3}{\sqrt{\pi}}\right\}$$

(13.4)

with τ_u, τ_D and ε given in (13.2) and $h(T)$ and $s(T)$ in (13.3).

B.3 Longitudinal effective dispersion coefficient

The explicit form of the longitudinal effective dispersion coefficient reads:

$$\delta^{uu}\{D_{11}^{eff}(t)\} = \delta^{uu}\{D_{11}^{ens}(t)\} - D_{11}^{eff}(t)$$

(13.5)

with the effective longitudinal contribution $D_{11}^{eff}(t)$:

$$D_{11}^{eff}(t) = \bar{u}\,\ell\,\left(-\sigma_{ff}^2\right)\sqrt{\frac{\pi}{2}}(1+2b)^{-2}\left\{\mathrm{erf}\big(g(-T)\big)+\frac{1}{\sqrt{\pi}}\exp\left(-g^2(-T)\right)\right.$$

$$\cdot\left[\frac{1}{g(-T)}+\frac{4\varphi^2 w(T)}{g^2(-T)}-\frac{3}{2g^3(-T)}\right]+\mathrm{erf}\big(g(-T)\big)$$

$$\cdot\left[\frac{4\varphi^2 w(T)}{g(-T)}+\frac{8\varphi^4 w(T)}{g(-T)}-\frac{1}{g^2(-T)}-\frac{2\varphi^2 w(T)}{g^3(-T)}+\frac{3}{4g^4(-T)}\right]$$

$$-\,8\varphi^4\cdot\exp\left(\frac{1}{2\varphi^2}\right)\left[\mathrm{erfc}\left(\frac{1}{\sqrt{2\varphi^2}}\right)-\mathrm{erfc}\big(w(T)\big)\right]-\frac{4\sqrt{8}\varphi}{3\sqrt{\pi}}$$

$$\left.-\,\frac{4\sqrt{8}\varphi^3}{\sqrt{\pi}}\right\}$$

(13.6)

and $\delta^{uu}\{D_{11}^{ens}(t)\}$ as defined in (13.6), τ_u, τ_D and ε in (13.2) and

$$b = \frac{2t}{\tau_D}; \qquad \varphi = \frac{\varepsilon}{\sqrt{1 + 2b}} \tag{13.7}$$

$$w(T) = \frac{1}{\sqrt{2}} \frac{\frac{1}{\varepsilon} + \frac{t}{\tau_u}}{\sqrt{(1 + 2b) + \frac{2t}{\tau_D}}}; \qquad g(-T) = \frac{1}{\sqrt{2}} \frac{-\frac{t}{\tau_u}}{\sqrt{(1 + 2b) + \frac{2t}{\tau_D}}} \tag{13.8}$$

In order to reproduce the results of /DEN 00a/ and /DEN 02/, the sign of w(t) had to be changed (instead of w(-T)) and the exponent in the pre-coefficient $(1+2b)^{-2}$ (instead of "-1") as described after equation (3.99).

B.4   Transverse effective dispersion coefficient

The transverse effective dispersion coefficient is given by the difference

$$\delta^{uu}\{D_{22}^{eff}(t)\} = \delta^{uu}\{D_{22}^{ens}(t)\} - D_{22}^{eff}(t) \tag{13.9}$$

with the effective transverse contribution $D_{22}^{eff}(t)$:

$$\begin{aligned} D_{22}^{eff}(t) = \bar{u}\,\ell\,(-\sigma_{ff}^2)\sqrt{\frac{\pi}{8}}(1 + 2b)^{-2} \Bigg\{ &\frac{1}{\sqrt{2\pi}}\exp(-g^2(-T))\left[-\frac{8\varphi^2 w(T)}{g^2(-T)}\right. \\ &\left. +\frac{3}{g^3(-T)}\right] + \mathrm{erf}(g(-T)) \\ &\cdot\left[-\frac{2\varphi^2 h(T)}{g(-T)} - \frac{8\varphi^4 w(T)}{g(-T)} + \frac{1}{2g^2(-T)} - \frac{2\varphi^2 w(T)}{g^3(-T)}\right. \\ &\left. -\frac{3}{4g^4(-T)}\right] \\ &- (8\varphi^4 - 2\varphi^2)\exp\left(\frac{1}{2\varphi^2}\right)\left[\mathrm{erfc}(w(T)) - \mathrm{erfc}\left(\frac{1}{\sqrt{2}\varphi}\right)\right] \\ &+ \frac{\sqrt{8}\varphi}{3\sqrt{\pi}} + \frac{4\sqrt{8}\varphi^3}{\sqrt{\pi}}\Bigg\} \end{aligned} \tag{13.10}$$

σ_{ff}^2 denotes the variance of the log-hydraulic conductivity, $\delta^{uu}\{D_{22}^{ens}(t)\}$ is defined in (13.4), τ_u, τ_D and ε in (13.2), b and φ in (13.7) and w(t) and g(-T) in (13.8).

C   Explicit expressions of the scale-dependent dispersion coefficients with finite correlation lengths (CL)

For infinite times the scale-dependent asymptotic value reads:

$$\delta^{uu}\{D_{11}^{macro,CG}(\xi)\} \equiv \lim_{t\to\infty} \delta^{uu}\{D_{11}^{ens,CG}(t,\xi)\} = \lim_{t\to\infty} \delta^{uu}\{D_{11}^{eff,CG}(t,\xi)\} \tag{13.11}$$

$$= \delta^{uu}\{D_{11}^{macro}\}$$

$$- \sigma_{ff}^2\, \bar{u}\, \frac{\ell}{\left(1 + \frac{\xi^2}{4\ell^2}\right)^{(d-1)/2}} \sqrt{\frac{\pi}{2}} \left\{ 1 \right.$$

$$- 8\epsilon_\xi^4 \exp\left(\frac{1}{2\epsilon_\xi^2}\right) \mathrm{erfc}\left(\frac{1}{\sqrt{2\epsilon_\xi^2}}\right) + 8\epsilon_\xi^4 - \frac{16}{\sqrt{2\pi}}\epsilon_\xi^3 + 4\epsilon_\xi^2$$

$$\left. - \frac{16}{3\sqrt{2\pi}}\epsilon_\xi \right\}$$

where erfc(z) denotes the error-function as defined by /ABS 84/ and

$$\delta^{uu}\{D_{11}^{macro}\} \equiv \sigma_{ff}^2\, \bar{u}\, \ell\, \sqrt{\frac{\pi}{2}} \left\{ 1 - 8\epsilon^4 \exp\left(\frac{1}{2\epsilon^2}\right) \mathrm{erfc}\left(\frac{1}{\sqrt{2\epsilon^2}}\right) + 8\epsilon^4 - \frac{16\epsilon^3}{\sqrt{2\pi}} \right. \tag{13.12}$$

$$\left. + 4\epsilon^2 - \frac{16\epsilon}{3\sqrt{2\pi}} \right\}$$

given in /DEN 00a/ with

$$\epsilon = \frac{\tau_u}{\tau_D} > \epsilon_\xi = \frac{\tau_{u,\xi}}{\tau_{D,\xi}} = \frac{\epsilon}{\sqrt{1 + \frac{\xi^2}{4\ell^2}}} = \frac{\epsilon}{\ell_{\langle f\rangle}} \tag{13.13}$$

The following explicit expressions are derived for situations characterised by finite inverse Peclet numbers $\epsilon_\xi \ll 1$ corresponding to realistic aquifer situations /GEL 83/.

317

C.1 Scale-dependent coefficients with finite correlation lengths

The complete expression of the grid-size dependent effective coefficient consists of four parts: Two for the corresponding grid-size dependent ensemble quantity and two more for the grid-size dependent effective contribution. The explicit grid-size dependent expressions in a 3-dimensional isotropic system have the form:

$$\delta^{uu}\{D_{ii}^{ens,CG}(t,\xi)\} = \delta^{uu}\{D_{ii}^{ens}(t)\} - \left(\frac{\ell^2}{\ell_{\langle f\rangle}^2}\right)^{d/2} \bar{u}\,\ell_{\langle f\rangle}\, M_i^{CG,-}(T_\xi, 0, 0) \tag{13.14}$$

$$\delta^{uu}\{D_{ii}^{eff,CG}(t,\xi)\} = \delta^{uu}\{D_{ii}^{ens,CG}(t,\xi)\} \tag{13.15}$$
$$- \left\{\{D_{ii}^{eff}(t)\} - \left(\frac{\ell^2}{\ell_{\langle f\rangle}^2}\right)^{d/2} \bar{u}\,\ell_{\langle f\rangle}\, M_i^{CG,+}(T_\xi, b_\xi, b_\xi)\right\}$$

with $\{D_{ii}^{eff}(t)\}$ given in (13.6) and (13.10) and the auxiliary functions $M_i^{CG,\pm}$ due to the coarse graining procedure:

$$M_1^{CG,\pm}(T_\xi, b_\xi, b_\xi) = (\mp\sigma_{ff}^2)\sqrt{\frac{\pi}{2}}(1+2b_\xi)^{-2}\left\{\mathrm{erf}\left(g(\mp T_\xi)\right)\right. \tag{13.16}$$

$$+ \frac{1}{\sqrt{\pi}}\exp\left(-g^2(\mp T_\xi)\right)\cdot\left[\frac{1}{g(\mp T_\xi)} + \frac{4\varphi_\xi^2 w(T_\xi)}{g^2(\mp T_\xi)} - \frac{3}{2g^3(\mp T_\xi)}\right]$$

$$+ \mathrm{erf}\left(g(\mp T_\xi)\right)$$

$$\cdot\left[\frac{4\varphi_\xi^2 w(T_\xi)}{g(\mp T_\xi)} + \frac{8\varphi_\xi^4 w(T_\xi)}{g(\mp T_\xi)} - \frac{1}{g^2(\mp T_\xi)} - \frac{2\varphi_\xi^2 w(T_\xi)}{g^3(\mp T_\xi)}\right.$$

$$\left. + \frac{3}{4g^4(\mp T_\xi)}\right] - 8\varphi_\xi^4$$

$$\cdot\exp\left(\frac{1}{2\varphi_\xi^2}\right)\left[\mathrm{erfc}\left(\frac{1}{\sqrt{2\varphi_\xi^2}}\right) - \mathrm{erfc}\left(w(T_\xi)\right)\right] - \frac{4\sqrt{8}\varphi_\xi}{3\sqrt{\pi}}$$

$$\left. - \frac{4\sqrt{8}\varphi_\xi^3}{\sqrt{\pi}}\right\}$$

and

318

$$M_2^{CG,\pm}(T_\xi, b_\xi, b_\xi) = M_3^{CG,\pm}(T_\xi, b_\xi, b_\xi) \tag{13.17}$$

$$= (\mp\sigma_{ff}^2)\sqrt{\frac{\pi}{8}}(1 + 2b_\xi)^{-2}\left\{\frac{1}{\sqrt{2\pi}}\exp\left(-g^2(\mp T_\xi)\right)\right.$$

$$\cdot\left[-\frac{8\varphi_\xi^2 w(T_\xi)}{g^2(\mp T_\xi)} + \frac{3}{g^3(\mp T_\xi)}\right] + \text{erf}\left(g(-T_\xi)\right)$$

$$\cdot\left[-\frac{2\varphi_\xi^2 w(T_\xi)}{g(-T_\xi)} - \frac{8\varphi_\xi^4 w(T_\xi)}{g(\mp T_\xi)} + \frac{1}{2g^2(\mp T_\xi)} - \frac{2\varphi_\xi^2 h(T_\xi)}{g^3(\mp T_\xi)}\right.$$

$$\left.-\frac{3}{4g^4(\mp T_\xi)}\right] - (8\varphi_\xi^4 - 2\varphi_\xi^2)\exp\left(\frac{1}{2\varphi_\xi^2}\right)$$

$$\left.\cdot\left[\text{erfc}\left(w(T_\xi)\right) - \text{erfc}\left(\frac{1}{\sqrt{2\varphi_\xi^2}}\right)\right] + \frac{\sqrt{8}\varphi_\xi}{3\sqrt{\pi}} + \frac{4\sqrt{8}\varphi_\xi^3}{\sqrt{\pi}}\right\}$$

with $\ell_{\langle f\rangle}$ given in (5.16), the correct physical filter width of ξ in (5.50), ϵ_ξ in (13.13), $\tau_{u,\xi}$ in (5.45), $\tau_{D,\xi}$ in (5.46), σ_{ff}^2 denotes the variance of the log-hydraulic conductivity and

$$T_\xi = \frac{t}{\tau_{u,\xi}} = \frac{t}{\tau_u \ell_{\langle f\rangle}}; \qquad b_\xi = \frac{2t}{\tau_{D,\xi}} = \frac{2t}{\tau_D \ell_{\langle f\rangle}^2}; \qquad \varphi_\xi = \frac{\epsilon_\xi}{\sqrt{1 + 2b_\xi}} \tag{13.18}$$

$$w(T_\xi) = \frac{1}{\sqrt{2}}\frac{(1 + 2b_\xi)\frac{1}{\epsilon_\xi} + \frac{t}{\tau_{u,\xi}}}{\sqrt{(1 + 2b_\xi) + \frac{2t}{\tau_{D,\xi}}}} \tag{13.19}$$

$$g(\mp T_\xi) = \frac{1}{\sqrt{2}}\frac{\mp\frac{t}{\tau_{u,\xi}}}{\sqrt{(1 + 2b_\xi) + \frac{2t}{\tau_{D,\xi}}}} \tag{13.20}$$

C.2   Grid-size dependent longitudinal ensemble coefficient with finite CL

The scale-dependent ensemble dispersion approaches its constant long-time value on timescales larger than $t \gg \tau_u$. The explicit expression has the form:

$$\delta^{uu}\{D_{11}^{ens,CG}(t,\xi)\} = \delta^{uu}\{D_{11}^{ens}(t)\} - \left(\frac{\ell^2}{\ell_{\langle f \rangle}^2}\right)^{d/2} \bar{u}\, \ell_{\langle f \rangle}\, M_1^{CG-}\left(\frac{t}{\tau_{u,\xi}}, 0, \ldots, 0\right) \tag{13.21}$$

with $\delta^{uu}\{D_{11}^{ens}(t)\}$ given in (13.1) and M_1^{CG-} in (13.16).

Situations with infinite Peclet numbers for $\delta^{uu}\{D_{11}^{ens,CG}(t,\xi)\}$

For infinite Peclet numbers the time-independent expression holds

$$\delta^{uu}\{D_{11}^{ens,CG}(\xi)\} = \bar{u}\, \ell\, \sigma_{ff}^2 \sqrt{\frac{\pi}{2}}\left(1 - \frac{1}{\left(1 + \frac{\xi^2}{4\ell^2}\right)^{(d-1)/2}}\right) \tag{13.22}$$

If small-scale mixing is present and the width of filter is chosen according to $\xi \sim \sqrt{16\, D_T\, t}$, the results for effective mixing without coarse graining are recovered

$$\delta^{uu}\{D_{11}^{ens,CG}(t,\xi = \sqrt{16\, D_T\, t})\} = \bar{u}\, \ell\, \sigma_{ff}^2 \sqrt{\frac{\pi}{2}}\left(1 - \frac{1}{\left(1 + \frac{D_T t}{\ell^2}\right)^{(d-1)/2}}\right) \tag{13.23}$$

$$= \delta^{uu}\{D_{11}^{eff}(t)\}$$

C.3   Grid-size dependent transverse ensemble coefficient with finite CL

The explicit expression of the grid-size dependent transverse ensemble coefficient reads:

$$\delta^{uu}\{D_{22}^{ens,CG}(t,\xi)\} = \delta^{uu}\{D_{22}^{ens}(t)\} - \left(\frac{\ell^2}{\ell_{\langle f \rangle}^2}\right)^{d/2} \bar{u}\, \ell_{\langle f \rangle}\, M_2^{CG-}\left(\frac{t}{\tau_{u,\xi}}, 0, \ldots, 0\right) \tag{13.24}$$

with $\delta^{uu}\{D_{22}^{ens}(t)\}$ given in (13.4) and M_2^{CG-} in (13.17).

C.4 Scale-dependent longitudinal effective coefficient with finite CL

The explicit scale-dependent longitudinal effective dispersion coefficient reads:

$$\delta^{uu}\{D_{11}^{eff,CG}(t,\xi)\} = \delta^{uu}\{D_{11}^{ens,CG}(t,\xi)\} \tag{13.25}$$

$$-\left\{\{D_{11}^{eff}(t)\} - \left(\frac{\ell^2}{\ell_{\langle f\rangle}^2}\right)^{d/2}\bar{u}\,\ell_{\langle f\rangle}\,M_1^{CG,+}\left(T_\xi, b_\xi, b_\xi\right)\right\}$$

with $\delta^{uu}\{D_{11}^{ens}(t)\}$ given in (13.1), $\{D_{11}^{eff}(t)\}$ in (13.6) and $M_1^{CG,+}$ in (13.16). The scale-dependent effective longitudinal coefficient reaches its constant long-time value for times $t \gg \tau_{D,\xi}$. This value is identical to that of the corresponding ensemble quantity.

Situations with infinite Peclet numbers for $\delta^{uu}\{D_{11}^{eff,CG}(t,\xi)\}$

The difference between the grid-size dependent ensemble and effective coefficients vanishes – similar to the behaviour in situations without the filtering procedure – after the plume has sampled dispersively a sufficiently large region of the heterogeneities, which is determined by the spatial filter width ξ: If the plume has spread over ξ, the filtering procedure will display no artificial mixing anymore and hence, the grid-size dependent quantities become identical. The corresponding time is given by the scale $\tau_{D,\xi}$, that becomes large in cases of a small local dispersion. With increasing widths ξ, the timescales split according to $\tau_u < \tau_{u,\xi} \ll \tau_D < \tau_{D,\xi}$. For times $t \gg \tau_{u,\xi} > \tau_u$ it is:

$$\delta^{uu}\{D_{11}^{eff,CG}(t,\xi)\} = \delta^{uu}\{D_{11}^{ens,CG}(t,\xi)\} \tag{13.26}$$

$$-\bar{u}\,\ell\,\sigma_{ff}^2\sqrt{\frac{\pi}{2}}\left\{\left(1 + 4\frac{t}{\tau_D}\right)^{-\frac{d-1}{2}} - \left(1 + \frac{\xi^2}{4\ell^2} + 4\frac{t}{\tau_D}\right)^{-\frac{d-1}{2}}\right\}$$

C.5 Scale-dependent transverse effective coefficient with finite CL

The explicit expression of the scale-dependent transverse effective quantity reads:

$$\delta^{uu}\{D_{22}^{eff,CG}(t,\xi)\} = \delta^{uu}\{D_{22}^{ens,CG}(t,\xi)\}$$

$$-\left\{\{D_{22}^{eff}(t)\} - \left(\frac{\ell^2}{\ell_{\langle f\rangle}^2}\right)^{d/2} \bar{u}\,\ell_{\langle f\rangle}\,M_2^{CG,+}\left(T_\xi, b_\xi, b_\xi\right)\right\} \tag{13.27}$$

with $\delta^{uu}\{D_{22}^{ens,CG}(t,\xi)\}$ given in (13.24), $\{D_{22}^{eff}(t)\}$ in (13.10) and $M_2^{CG,+}$ in (13.17).

D   Inverse modelling and parameter estimation

D.1   Submitted Files

The following files and folders were submitted to the d³f Repository:

- dfpp/gen/solver/l2_param.c
- dfpp/gen/solver/l2_param.h
- dfpp/gen/solver/fit
- dfpp/2d/gorleben_left_fit/
- dfpp/2d/saltdome_fit/

Hereby, saltdome_fit and gorleben_left_fit contain an example for the estimation of permeability. The files l2_param.c and l2_param.h contain the UG 3 numproc "l2_param_est", which is needed for parameter estimation and the folder fit contains the Perl module used for parameter estimation. More information can be found in Section 8.4 and Section 8.5.

D.2   Implementation and Parallelization

The implementation of the Quasi-Newton method described in section 8.3 is divided into a main process and sub processes and can be found in dfpp/gen/solver/fit. The main steps of the algorithm are described in detail in this section and are depicted in Fig. 8.1. Furthermore, a user manual for parameter estimation and the numproc "l2_param_est" can be found in section D.5.

D.3   Implementation and parallelisation of the Quasi-Newton Method

The main process starts with an initial set of parameters and is responsible for setting up all variations of the parameter vector, which are needed for the computation of the search direction. After preparing all necessary information, the main process starts a separate subprocess for every variation. With this technique the computation can be performed very efficient on parallel computers as each subprocess can be easily distributed to a single or even multi CPUs.

Each subprocess is then responsible for the computation of the parameter estimation function. This is performed by the UG3 numproc "l2_param_est" which is described in detail in Section D.5. On termination of the processes the value of the parameter estimation function is returned to the main process and is then used to compute a search direction.

Afterwards, the main process prepares all necessary information for the line search steps and starts separate subprocesses for every step. Again, the subprocesses can be easily distributed to CPUs leading to an optimal parallelization of the algorithm.

When the computations are finished the subprocesses return the values of the parameter estimation function to the main process. With this information at hand, the main process chooses a new parameter vector. If an abort criterion is reached the main process terminates and returns the new parameter vector as optimal parameter vector. Otherwise, the main process starts over with the new parameter vector as initial parameter vector (cf. Fig. 8.1).

D.4   Unser manual for parameter estimation

In order to use the provided Perl module "gaussnewton.pm" (in dfpp/gen/solver/fit/bin) with d^{3}f problems a Perl script and a Perl module providing all problem dependent information need to be created.

Furthermore, the following script files need to be included in the script directory of the d^{3}f problem:

- ddf_after_comput.scr
- ddf_at_ts.scr
- ddf_before_ts.scr
- ddf_init_sol.scr
- ddf_prepare_grid.scr
- ddf_problem_specific.scr
- ddf_solver.scr
- run_ddf_fit.scr

Hereby, the script run_ddf_fit.scr should be created from run_ddf.scr by adding the numproc "l2_param_est" (cf. section D.5).

The Perl script needs to provide information about the initial parameters, upper and lower parameter bounds, total number of Quasi-Newton steps, number of line search steps, and a folder, where the results are stored. An example can be found in dfpp/gen/solver/fit/bin/gaussnewton.gorleben.pl.

The Perl module needs to provide the following information about the d^3f problem:

- problem directory (function `getAppDirectory`)
- config file name (function `getConfigFilename`)
- necessary information to create a config file (function `create_config_file`)
- system dependent information on how to create a batch file (function `create_batch_file`)
- system dependent information on how to execute a batch file (function `launch`)

An example can be found in dfpp/gen/solver/fit/bin/UG3/gorlebentask.pm.

Executing the created Perl script then launches parameter estimation.

D.5 Implementation of the UG3 numproc "l2_param_est"

The main purpose of the subprocesses is the efficient computation of the parameter estimation function. This is performed by a simulation of an a priori defined mathematical problem with the set of parameters given by the main process and a comparison of simulational data, e. g., concentration, pressure etc., at certain coordinates and times with experimental or estimated data.

In the case of density driven flow the simulation is typically performed with the framework UG by using efficient multigrid methods for solving large systems of linear equations cf. /BAS 94/, /FEI 99/, and /LAN 05/.

In this context, experimental data can be entered with help of the UG3 numproc "l2_param_est" (cf. example below). The numproc then writes all necessary information about the parameter estimation function into the files "l2.dat" and "l2sum.dat".

Example

The numproc "l2_param_est" needs to be created and initialized before the actual computation. This is performed within the script file "run_ddf_fit.scr" with the following code:

```
npcreate l2error $c l2_param_est; //numproc is created
npinit l2error //numproc is initialized
        $n 2 //number of data points
        $p2d 0 100 13000.0 200.0 0.86
        $p2d 0 110 13000.0 200.0 0.85;
npdisplay l2error;
```

Hereby, `$p2d` is used for 2d-Datapoints. It needs to be followed by the component of the solution in UG (in the example 0 is the first component and corresponds to mass fraction), the time, the x-coordinate, the y-coordinate, and the measured/desired value for the solution.

Furthermore, `$p3d` can be used for 3d-Datapoints. It needs to be followed by the component of the solution in UG (in the example 0 is the first component and corresponds to mass fraction), the time, the x-coordinate, the y-coordinate, the z-coordinate, and the measured/desired value for the solution.

After each time step the numproc needs to be executed. This is done by the following command.

```
npexecute l2error $t @time;
```

Hereby, `@time` is the current time in the simulation.

Testcases

The example Gorleben can be found in the folder dfpp/2d/gorleben_left_fit/,
the saltdome example in dfpp/2d/saltdome_fit/.

E   Publications

Papers

Frolkovič, P., Logashenko, D., Wittum, G.: Flux-based level set method for two-phase flows. In R. Eymard and J.-M. Herard, editors, Finite Volumes for Complex Applications, pages 425 – 422. ISTE and Wiley, 2008.

Frolkovič, P., Lampe, M., Wittum, G.: Numerical simulation of contaminant transport in groundwater using the software tool r³t, submitted.

Grillo, A., Logashenko, D., Stichel, S., Wittum, G.: Simulation of Density-Driven Flow in Fractured Porous Media. Advances in Water Resources, Volume 33, Issue 12, Pages 1494 – 1507, 2010.

Grillo, A., Lampe, M., Wittum, G.: Three-dimensional simulation of the thermohaline-driven buoyancy of a brine parcel. Comput Vis Sci, Comput Vis Sci Volume 13, Number 6, 287 – 297, 2010.

Grillo, A., Lampe, M., Wittum, G.: Modelling and Simulation of Temperature-Density-Driven Flow and Thermodiffusion in Porous Media. Journal of Porous Media, v14.i8.20, pages 671 – 690, 2011.

Grillo, A., Lampe, M., Logashenko, D., Stichel, S., Wittum, G.: Simulation of salinity- and thermohaline-driven flow in fractured porous media. Journal Porous Media, 15(5):439 – 458, 2012.

Grillo, A., Federico, G., Wittum, G.: Growth, mass transfer, and remodeling in fiber-reinforced multi-constituent materials. International Journal of Non-Linear Mechanics, 47(2), 388 – 401, 2012.

Grillo, A., Logashenko, D., Wittum, G.: Study of a transport problem in a two-dimensional porous medium. Cosserrat +100, International Conference on the legacy of Théorie des Corps Déformables by Eugene and Francois Cosserat in the centenary of its publication, 15-17 July 2009.

Grillo, A., Logashenko, D., Stichel, S., and Wittum, G. (2012b). Forchheimers corrections in modelling flow and transport in fractured porous media. Comput. Vis. Sci. Volume 15, Issue 1, Springer, 2013.

Heppner, I., Lampe, M., Nägel, A., Reiter, S., Rupp, M., Vogel, A., Wittum, G.: Software framework ug4: Parallel multigrid on the hermit supercomputer. In Wolfgang. E. Nagel, Dietmar H. Kröner, and Michael M. Resch, editors, High Performance Computing in Science and Engineering 2012, pages 435 – 449. Springer Berlin Heidelberg, 2013.

Heße, F., Prykhod'ko, V., Attinger, S.: Assessing the validity of a lower-dimensional representation of fractures for numerical and analytical investigations, scientific paper, FKZ 02 E 10578, Advances in Water Resources 56, 35 – 48, 2013.

Heße, F., Prykhod'ko, V., Schlüter, S., Attinger, S.: On the numerical simulation of random fields with a truncated power-law variogram, scientific paper in review, FKZ 02 E 10578, submitted to Environmental Science & Modelling, 2013.

Hoffer, M., Poliwoda, C., Wittum, G.: Visual Reflection Library. A Framework for Declarative GUI Programming on the JAVA Platform, Computing and Visualization in Science, 2011, in press.

Kolditz, O. and Shao, H. (eds.): OpenGeoSys – Developer Benchmark Book 5.0.04, Internet Report, available through www.opengeosys.net, Helmholtz Centre for Environmental Research, AESA TU Dresden, 2011.

Kolditz, O., Görke, U.-J., Shao, H. (eds.): OpenGeoSys – Developer Benchmark Book 5.0.12, Internet Report, available through www.opengeosys.net, Helmholtz Centre for Environmental Research, Applied Environmental System Analysis, TU Dresden, 2011.

Kolditz, O., Shao, H., Görke, U.-J., Wang, W. (eds): Thermo-hydro-mechanical/chemical processes in porous media. Lecture Notes in Computational Science and Engineering, Vol. 86, Springer, Heidelberg, ISBN 978-3-642-27176-2, 2012.

Kosakowski G. Transport in fractured media: Concepts, Models, and Applications. Habilitation: GeoHydrology and HydroInformatics, Center for Applied Geosciences, Tübingen University, 2007.

Kröhn, K.-P.: Qualifying a computer program for simulating fracture flow. Computing and Visualization in Science, Volume 15, Issue 1, Page 29 – 37, Springer, DOI 10.1007/s00791-013-0191-6, 2013.

Micunovic, M. V., Grillo, A., Muha, I., Wittum, G.: Two dimensional plastic waves in quasi rate independent viscoplastic materials. 7th Euromesh Solid Mechanics Conference, J. Ambrosio et.al. (eds.), Lisbon, Portugal, 7 – 11 September 2009.

Muha, I., Stichel, S., Attinger, S., Wittum, G.: Coarse graining on arbitrary grids. Multiscale Model. Simul. Volume 8, Issue 4, pp. 1368 – 1382, 2010.

Musuuza, J. L., Attinger, S., Radu, F. A.: An extended stability criterion for density-driven flows in homogeneous porous media, Advances in Water Res. 32 (6), 796-808, 2009.

Musuuza J., Radu F., Attinger, S.: The stability of density-driven flows in saturated heterogeneous porous media, Advances in Water Res. 34, 1464 – 1482, 2011

Musuuza J., Radu F., Attinger, S.: The effect of dispersion on the stability of density-driven flows in homogeneous porous media, Advances in Water Res., 34 (3): 417 – 432, 2011.

Musuuza, J. L., Radu, F. A., Attinger, S.: Predicting predominant thermal convection in thermohaline flows in saturated porous media, scientific paper, FKZ 02 E 10578, Advances in Water Resources 49 , 23 – 36, 2012.

Nägel A., Falgout R., Wittum G.: Filtering algebraic multigrid and adaptive strategies. Computing and Visualization in Science, 11(3):159 – 167, 2008.

Radu, F. A., Wang, W., Kolditz, O.: Convergence analysis for a mixed finite element scheme for flow in strictly unsaturated porous media, J Nonlinear Analysis, SI Real World Applications, submitted, 2011.

Reiter, S., Logashenko, D., Stichel, S., Wittum, G., and Grillo, A.: Models and simulations of variable-density flow in fractured porous media. International Journal of Computational Science and Engineering. In press, 2012.

Reiter, S., Logashenko, D., Grillo, A., and Wittum, G.: Preparation of grids for simulations of groundwater flow in fractured porous media. Comput. Vis. Sci., Vol. 15, Issue 1, Springer, 2013.

Reiter, S. and Wittum, G.: Promesh - a flexible interactive meshing software for unstructured hybrid grids in 1, 2 and 3 dimensions. in preparation, 2013.

Reiter, S., Vogel, A., Heppner, I., Rupp, M., Wittum. G.: A massively parallel geometric multigrid solver on hierarchically distributed grids. Computation and Visualisation in Science, Volume 15, Issue 1, Springer, 2013.

Schneider, A., Kröhn, K.-P., Püschel, A.: Developing a modelling tool for density-driven flow in complex hydrogeological structures. Computation and Visualisation in Science, Volume 15, Issue 4, Springer, 2012.

Stichel, S., Logashenko, D., Grillo, A., Reiter, S., Lampe, M., and Wittum, G.: Numerical methods for flow in fractured porous media. In Delgado, J., editor, Heat and Mass Transfer in Porous Media, volume 13 of Advanced Structured Materials, pages 83–113. Springer Berlin Heidelberg, 2012.

Sun, Y. Y., Park, C.-H., Wang, W., Kolditz, O.: Simulation of solute transport in porous media using random walk particle tracking method. PARTICLES 2011, Thematic ECCOMAS Conference, 26-28.2011, Barcelona, accepted, 2011

Sun, Y. Y.: Random-Walk-Particle-Tracking (RWPT) methods for non-linear flows in porous and fractured media, PhD thesis, in preparation, TU Dresden, 2012.

Sun, Y. Y., Naumov D, Fischer T, Taron J, Watanabe N, Kolditz O: Abbildung von Inhomogenitäten bei der Strömungs- und Transportmodellierung. 6th A-DuR Progress Report. Helmholtz Centre for Environmental Research UFZ, 2012.

Taron, J., Park, C.-H., Kolditz, O.: A-DuR Project Progress Report. Technical Report, UFZ, Environmental Informatics, 2010.

Taron, J., Elsworth, D., Kolditz, O.: Pressure solution models for quartz materials: Micromechanical development and potential impact in fractured reservoirs. ARMA Paper 10-422, 44th US Rock Mechanics Symposium and 5th U.S.-Canada Rock Mechanics Symposium, Salt Lake City, UT June 27–30, 2010.

Taron, J., Elsworth, D., Kolditz, O.: Mechanisms for permeability evolution in fracture networks: hydrothermal effects in enhanced geothermal systems. ARMA Paper 10-423, 44th US Rock Mechanics Symposium and 5th U.S.-Canada Rock Mechanics Symposium, Salt Lake City, UT June 27–30, 2010.

Taron., J., Watanabe, N., Sun, Y. Y., Park, C.-H., Kolditz, O.: 3. A-DuR Project Progress Report. Technical Report, UFZ, Environmental Informatics, 2011, https://svn.ufz.de/svn/ogs/branches/josh/Projects/ADuR/A_DuR_Project

Vogel, A., Wittum, G., Xu, J.: A generalization of the vertex-centered Finite Volume scheme to arbitrary order. Comput. Vis. Sci. Volume 13 Issue 5, June 2010.

Vogel, A., Reiter, S., Rupp, M., Nägel, A., Wittum, G.: UG 4 - a novel flexible software system for simulating pde based models on high performance computers. Computation and Visualisation in Science, Volume 15, Issue 1, Springer, 2013.

Watanabe, N.: Semi extended FEM (XFEM) approach for modeling coupled HM processes in rock joints, Kieler Scientific Computating Seminar, 16.06.2010, Kiel, 2010.

Watanabe, N., Wang, W., Kolditz, O.: Flow and mechanics in discrete fracture-matrix rock systems: Hydromechanical behavior utilizing an extended Finite Element Method, SIAM. Mathematical and Compuational Issues in Geosciences, Long Beach, 21.-24.03.2011, accepted, 2011.

Watanabe, N., Wang, W., Taron, J., Gorke, U.-J., Kolditz, O.: Lower-dimensional interface elements using local enrichments and application for a coupled hydromechanical problem in fractured rock. International Journal for Numerical Methods in Engineering, DOI: 10.1002/nme.3353., 2011.

Watanabe, N.: Finite element method for coupled thermo-hydro-mechanical processes in discretely fractured and non-fractured porous media. Dissertationsschrift, einge-

reicht an der Fakultät für Forst-, Geo- und Hydrowissenschaften an der Technischen Universität Dresden, 2012.

Posters and Presentations

Attinger, S.: Mixing processes in heterogeneous porous media without separated scales, Conference on Modelling Storage in Deep Layers (MSDL), Schwetzingen, 2011.

Berkels, B., Linkmann, G., Rumpf, M.: An SL(2) invariant shape median. Journal of Mathematical Imaging and Vision, 37(2):85-97, June 2010.

Frolkovic, P.: Some advances in numerical modelling of groundwater flow and contaminant transport, Conference on Modelling Storage in Deep Layers (MSDL), Schwetzingen, 2011.

Grillo, A., Lampe, M., Logashenko, D., Reiter, S., Stichel, S., Wittum, G.: An Overview of Models on Variable-Density Flow in Fractured Porous Media, Conference on Modelling Storage in Deep Layers (MSDL), Schwetzingen, 2011.

Hoffer, M.: A software for the automated mapping of program functionality to intuitive user interfaces in the context of technical simulation, Conference on Modelling Storage in Deep Layers (MSDL), Schwetzingen, 2011.

Kröhn, K.-P.: Qualifying a code for simulating fracture flow, Conference on Modelling Storage in Deep Layers (MSDL), Schwetzingen, 2011.

Lenz, M., Nemadjieu, S. F., Rumpf, M.: A convergent finite volume scheme for diffusion on evolving surfaces. SIAM Journal on Numerical Analysis, 49(1):15-37, 2011.

Logashenko, D., Grillo, A., Lampe, M.: Simulation of density and temperature driven flow and contaminant transport in fractured porous media using d3f and r3t, Talk on SIAM Geosciences, Leipzig, June 2009

Musuuza, J. L: A Stability Criterion for Homogeneous Density-driven Flows. Poster EGU Konferenz, Wien, Apr. 2008.

Musuuza, J. L: A Stability Criterion for Density-driven Flows in Heterogeneous Media. Poster. NUPUS Konferenz, Stuttgart, Okt. 2009.

Musuuza, J. L: The Stability of Density-driven Flows in Heterogeneous Porous Media. Poster. DBG Jahrestagung, Bonn, Sept. 2009.

Musuuza, J. L: The Effect of Dispersion on Flow Stability. Poster Mai 2009 SIAM Konferenz, Leipzig. A Stability Criterion for Heterogeneous Density-driven Flows. Gastvortrag. EGU Konferenz, Wien, Apr. 2009.

Musuuza, J. L: The Stability of Density-driven Flows in Heterogeneous Media. Vortrag. EGU Konferenz, Wien, Mai 2010.

Musuuza, J. L.: The Application of Homogenization Theory to Study Instabilities in Saturated Heterogeneous Media. Gastvortrag. SIAM Konferenz, Long Beach, USA, März 2011.

Musuuza, J. L., Radu, F., Attinger, S.: The application of homogenization theory to predict the onset of thermal convection in thermohaline systems, Conference on Modelling Storage in Deep Layers (MSDL), Schwetzingen, 2011.

Reiter, S., Logashenko, D.: Topological Expansion of Low Dimensional Fractures in Porous Media, Conference on Modelling Storage in Deep Layers (MSDL), Schwetzingen, 2011.

Rumpf, M.: Variational methods in image matching and motion extraction. In M. Burger and S. Osher, editors, Level Set and PDE based Reconstruction Methods: Applications to Inverse Problems and Image Processing, Lecture Notes in Mathematics. to appear as CIME course notes, Springer, 2009.

Rupp, M.: On Algebraic Multigrid for Density Driven Flow in Porous Media, Conference on Modelling Storage in Deep Layers (MSDL), Schwetzingen, 2011.

Schneider A.: Developing a modelling tool for density-driven flow in complex hydrogeological structures. Conference on Modelling Storage in Deep Layers (MSDL), Schwetzingen, 2011.

Stichel, S., Logashenko, D., Grillo, A. and Wittum, G.: Numerical methods for flow in fractured porous media. 6th International Conference on Diffusion in Solids and Liquids, Paris, 2010

Stichel, S., Logashenko, D., Grillo, A., Wittum, G.: Comparison of models for flow in fractured porous media. Conference on Modelling Storage in Deep Layers (MSDL), Schwetzingen, 2011.

Stichel, S., Logashenko, D., Grillo, A. and Wittum, G.: Dimension-adaptive approaches for flow in fractured porous media. European Multigrid Conference 2012, Schwetzingen, 2012

Master Thesis

Föhner, M.: Geometry Visualization & Modification Toolkit (GVMT), ein Werkzeug zur Ein-/Ausgabe und Modifikation von UG-Geometrien und UG-Gittern mit der 3d-Grafiksoftware Blender, 2008.

Hoffer, M.: Methoden der visuellen Programmierung, 2010.

Muha, I.: Coarse Graining auf beliebigen Gitterhierarchien, 2008.

Poliwoda, C.: Erstellung von Bedienoberflächen zur Steuerung von ausgewählten UG-Komponenten mit VRL, 2011.

Reiter, S. (2008). Glatte Randapproximation in hierarchischen Gittern. Diplomarbeit, Universität Heidelberg.

Rupp, M.: Filternde Algebraische Mehrgitterverfahren zur Berechnung großer Eigenwertprobleme, 2008.

Stepniewski, M.: Approximation glatter Ränder und Volumengittergenerierung zur alternativen Erzeugung von 3d-Gitterhierarchien für Mehrgitterverfahren, 2011.

Stichel, S.: Numerisches Coarse-Graining in UG, 2008.

Vogel, A.: Ein Finite-Volumen-Verfahren höherer Ordnung, 2008.

Wehner, C.: Numerische Verfahren für Transportgleichungen unter Verwendung von Level-Set-Verfahren, 2008.

PhD thesis

Feuchter, D.: Geometrie- und Gittererzeugung für anisotrope Schichtengebiete, Heidelberg, 2008.

Hauser, A.: Large Eddy Simulation auf uniform und adaptiv verfeinerten Gittern, Heidelberg 2009.

Musuuza, J. L.: Scaling Haline Flows in Heterogeneous Formations, PhD Thesis, Friedrich-Schiller-Universität Jena, 2010.

Nägel, A.: Schnelle Löser für große Gleichungssysteme mit Anwendungen, Heidelberg, 2010.

Ross, K.: Multi-Scale Model for Transport Coefficients in Heterogeneous Fractured Media, dissertation, FKZ 02 E 10578, Friedrich-Schiller-Universität Jena, 2013.

F   Meetings

Regular project meeting	Date	Location	Organizer
1.	February 27, 2009	Leipzig	Prof. Kolditz
2.	October 29, 2009	Frankfurt	Prof. Wittum
3.	April 20, 2010	Leipzig	Prof. Attinger
4.	November 09, 2010	Braunschweig	GRS
5.	May 06, 2011	Frankfurt	Prof. Wittum
6.	November 21, 2011	Jena	Prof. Attinger
7.	April 20, 2012	Braunschweig	GRS